

# Modelling and Sensors for Magnetically-Levitated Disc Drives

Présentée le 7 février 2022

Faculté des sciences et techniques de l'ingénieur  
Laboratoire d'actionneurs intégrés  
Programme doctoral en robotique, contrôle et systèmes intelligents

pour l'obtention du grade de Docteur ès Sciences

par

**Juan Patricio Tomás PERALTA FIERRO**

Acceptée sur proposition du jury

Prof. J. A. Schiffmann, président du jury  
Prof. Y. Perriard, directeur de thèse  
Prof. C. Espanet, rapporteur  
Prof. E. Lomonova, rapporteuse  
Prof. A. Karimi, rapporteur





A good traveler has no fixed plans  
and is not intent on arriving.  
— Lao Tzu

The part of life we really live is small.  
For all the rest of existence is not life, but merely time.  
— Lucius Annaeus Seneca

A mi polola Anna, nuestro bebé, y nuestras familias en Chile y Suiza ...

# Acknowledgements

The present work is the result of many actors that played decisive roles during my sojourn at the Integrated Actuators Laboratory (LAI) of EPFL. I am deeply humbled for their involvement over the last four years.

I am grateful of Professor Yves Perriard, who offered me a chance to take on a doctoral thesis at LAI. The confidence he deposits on my colleagues and me proves invaluable for the generation of knowledge within the laboratory.

Similarly, I am also grateful of Prof. Elena Lomonova, Prof. Christophe Espanet and Prof. Alireza Karimi for the revision and jury duty of this thesis. I also thank the students that contributed to my thesis and scientific publications with their projects.

The agreeable work conditions is daily fostered by the senior collaborators of LAI. I would like to thank Christian, for leading the corrections of this thesis and his advice regarding electric motors; Alexis, for his wise counsel; Paolo, for organizational efforts and his building of team spirit; and Yoan, for his boundless good humor and motivation. A big thanks go to Magda and Aline that keep the lab running.

I would equally like to thank Olivier Pajot and Matthieu Gani for coordinating the partners within this thesis. I am also indebted to Innosuisse (ex CTI Suisse) and Sonceboz SA for making this project possible. I am equally grateful to Douglas for setting the foundations of the research project; to Morgan for his technical knowledge; and for the support of Guillaume Verez in manifold technical aspects.

My day-to-day research and grind was made brighter by my office colleagues: first Guillaume and Louis, then Camilo and Sean. I immensely cherish their good spirits, their bizarre jokes, their availability to help, and their contagious effusiveness.

All the like, I deeply treasure the discussions and joyous moments spent with Adrien, Guzmán, Raphaël, Xiaotao, Kenny, Florian, Xinchang, Jonathan, Sofia, Pooneh, Armando, Thomas, Trung, Valentin, Jasha, Stefania, David, Marjan, Quentin, Francesco, and Silje.

A big thanks to all my friends in Switzerland and Chile. Their cheerfulness and love always kept me looking forward, backward, and sideways, and provided a golden distraction from non-working magnetic bearings.

Finally, I thank my family for always being there: my parents Mónica and Patricio for ingraining

in me the value of education, and my siblings Ximena and Ignacio for their cheerful and juvenile backing. And of course, an enormous thanks to my girlfriend Anna, who introduced me to Switzerland, who was always present during the rough patches of the doctorate, who accompanied me from Torino, to Zürich and to Neuchâtel, and with whom we are starting a family. Thank you for your unconditional support in this faraway adventure.

*Bern, December 17, 2021*

Patricio Peralta

# Abstract

The development of new industrial applications has diverted the focus of research towards compacter and faster rotatory drives. These requirements push the classical ball-bearings of electric motors to the limits in terms of operational lifetime and friction losses.

Advances in sensor systems, electronics, and semiconductors have thus rendered contactless, magnetically-levitated drives as a compelling alternative for the miniaturization of drives and the striving towards high rotational speeds. The possibility of hermetically sealing the rotor and stator has also opened new industrial applications in which high purity and robust operation are required.

In this thesis, the conceptualization of a compact yet simple magnetically-levitated electric drive is approached, from its analytical basis to the constitution of sensor systems, until the fabrication of two operating prototypes. One of the prototypes is ultimately deployed as a functioning actuator at high rotatory speeds.

This thesis thus tackles the different subjects that epitomize the complexity of a magnetically-levitated drive. In this regard, literature research is initially performed to investigate which structures of electric motors have successfully integrated magnetic bearings. A focused analysis upon small magnetically-levitated drives shows that few small flat drives—deemed as "disc drives"—have been tested with a mechanical load. The lack of documented electric motors at this scale and speed, working with a mechanical load, thus represents a novel, untasted research opportunity.

This work treats the electromagnetic principles that enable the magnetic levitation and spinning of drives. For better accuracy, the computational modelling of magnetically-levitated disc drives, along with an assessment of their passive, active, and power loss characteristics is proposed. A framework and a parametric analysis for the evaluation of these characteristics are provided.

Followingly, an analysis of different contactless sensor possibilities is supplied. The composition of an adjustable, low-cost system for the estimation of rotor position is presented. This that can be easily integrated into existing magnetic levitation systems.

The correct electromagnetic design of the drives and its relevant sensor system, coupled to readily available electronics result in two working prototypes. One of these is deployed as an axial blower, which can turn at speeds of 10000 rpm, blow airflows of  $40 \text{ liter} \cdot \text{min}^{-1}$ , and attain differential pressures of 10 Pa.

Finally, the lessons drawn from this manuscript are summarized, and future research work—that can improve the existing hardware, validate the electromagnetic design framework, or ameliorate alternative sensor systems—is proposed.

**Keywords:** magnetic levitation, disc drive, sensor systems, motion control, optimization, axial blower, high speed, small scale motors, experimental validation.

# Résumé

Le développement de nouvelles applications industrielles a orienté l'attention de la recherche vers des entraînements rotatifs plus compacts et plus rapides. Ces exigences poussent les roulements à billes des moteurs électriques à leurs limites en termes de durée de vie et de pertes par frottement.

Les progrès réalisés dans le domaine des systèmes de capteurs, de l'électronique et des semi-conducteurs ont fait des entraînements sans contact et à lévitation magnétique une alternative éloquent pour la miniaturisation des entraînements et la recherche de vitesses de rotation élevées. La possibilité de sceller hermétiquement le rotor et le stator a également ouvert de nouvelles applications industrielles dans lesquelles un environnement à grande pureté et un fonctionnement robuste sont requis.

Dans cette thèse, la conception d'un entraînement électrique compact et simple à lévitation magnétique est abordée, depuis sa base analytique, en passant par la construction d'un système de capteurs, jusqu'à la fabrication de deux prototypes opérationnels. L'un des prototypes est finalement mis en service comme un actionneur fonctionnel à des vitesses de rotation élevées.

Cette thèse aborde donc les différents sujets qui caractérisent la complexité d'un entraînement à lévitation magnétique. À cet égard, une recherche bibliographique est d'abord effectuée afin de déterminer quels types de moteurs électriques ont réussi à intégrer des paliers magnétiques. Une analyse approfondie des petits entraînements à lévitation magnétique montre que peu de petits entraînements à géométrie plate — appelés "disc drives" — ont été testés avec une charge mécanique. L'absence de moteurs électriques documentés à cette échelle et à cette vitesse, fonctionnant dans le cadre d'une véritable application, représente donc une opportunité de recherche nouvelle et inexploitée.

Ce travail traite des principes électromagnétiques qui permettent la lévitation magnétique et la rotation des disc drives. Il propose une modélisation numérique des disc drives à lévitation magnétique, ainsi qu'une évaluation de leurs caractéristiques passives, actives et de perte de puissance. Une structure et une analyse paramétrique pour l'évaluation de ces caractéristiques sont fournis.

Ensuite, une analyse des différentes possibilités de capteurs sans contact est fournie. La composition d'un système réglable et peu coûteux pour l'estimation de la position du rotor, facilement intégrable dans les systèmes de lévitation magnétique existants est présentée.

La dimensionnement électromagnétique correcte des entraînements et du système de capteurs correspondant, associée à une électronique facilement disponible, a permis de créer deux prototypes fonctionnels. L'un d'entre eux est déployé en tant que ventilateur axial, capable de tourner à des vitesses de  $10000 \text{ tr}\cdot\text{min}^{-1}$ , de souffler des flux d'air de  $40 \text{ litre}\cdot\text{min}^{-1}$  et d'atteindre des pressions différentielles de 10 Pa.

Enfin, les leçons tirées de ce manuscrit sont résumées. Des travaux de recherche future — pouvant améliorer le hardware existant, valider le cadre de design électromagnétique, ou améliorer les systèmes de capteurs alternatifs— sont proposés.

**Mots clés :** lévitation magnétique, disc drive, systèmes de capteurs, contrôle du mouvement, optimisation, ventilateur axial, haute vitesse, caractérisation, moteurs à petite échelle, validation expérimentale.

# Zusammenfassung

Die Entwicklung neuer industrieller Anwendungen hat den Fokus der Forschung auf kompaktere und schneller rotierende Antriebe gerichtet. Diese Anforderungen bringen die klassischen Kugellager von Elektromotoren in Bezug auf Lebensdauer und Reibungsverluste an ihre Grenzen.

Fortschritte in der Sensorik, in der Elektronik und in der Halbleitertechnik haben daher berührungslose, magnetgelagerte Antriebe zu einer überzeugenden Alternative für die Miniatürisierung von Antrieben und das Streben nach hohen Drehzahlen gemacht. Die Möglichkeit, Rotor und Stator hermetisch zu verschliessen, hat neue industrielle Anwendungen eröffnet, bei denen hohe Reinheit und robuster Betrieb gefordert sind.

In dieser Dissertation wird die Konzeption eines kompakten und schlichten magnetgelagerten Elektroantriebs von der analytischen Grundlage über den Aufbau der Sensorik bis hin zur Herstellung von zwei funktionsfähigen Prototypen angegangen. Einer der Prototypen wird schliesslich als funktionierender Aktuator, bzw. als Ventilator bei hohen Drehzahlen eingesetzt.

Diese Arbeit befasst sich also mit den verschiedenen Themen, die die Komplexität eines magnetgelagerten Antriebs verkörpern. Hierzu wird zunächst eine Literaturrecherche durchgeführt, um zu untersuchen, in welchen Bauformen Magnetlager in Elektromotoren erfolgreich integriert wurden. Ein Forschungsüberblick von kleinen magnet-gelagerten Antrieben zeigt, dass nur wenige kleine, flache Elektromotoren —als "Scheibenläufer" bezeichnet— mit einer mechanischen Belastung getestet wurden. Das Fehlen von dokumentierten Elektromotoren in dieser Größenordnung und mit dieser Geschwindigkeit, die mechanische Last treiben, stellt somit eine neue, unausgeschöpfte Forschungsmöglichkeit dar.

Diese Studie behandelt die elektromagnetischen Prinzipien, die das magnetische Schweben und Drehen von Antrieben ermöglichen. Zur Verbesserung der Genauigkeit wird die computerunterstützte Modellierung von magnetgelagerten Scheibenläufer zusammen mit einer Bewertung ihrer passiven und aktiven Eigenschaften sowie der Verlustleistung vorgestellt. Ein Rahmenkonzept und eine parametrische Analyse für die Bewertung dieser Eigenschaften wird aufgezeigt.

Anschliessend wird eine Analyse verschiedener berührungsloser Sensormöglichkeiten geliefert. Der Aufbau eines einstellbaren, kostengünstigen Systems zur Schätzung der Rotorposition, das leicht in bestehende Magnetschwebesysteme integriert werden kann, wird vorgestellt.

Die korrekte elektromagnetische Konzeption der Antriebe und der zugehörigen Sensorik,



gekoppelt an gebrauchsfertige Elektronik, führen zu zwei funktionierenden Prototypen. Einer davon wird als Axialventilator eingesetzt, der mit einer Drehzahl von  $10000 \text{ U} \cdot \text{min}^{-1}$  drehen, Luftmengen von  $40 \text{ liter} \cdot \text{min}^{-1}$  ausblasen und Differenzdrücke von 10 Pa erreichen kann.

Abschliessend werden die aus diesem Manuskript gezogenen Erkenntnisse zusammengefasst und für künftige Forschungsarbeiten —zur Verbesserung der vorhandenen Hardware, zur Validierung des elektromagnetischen Designrahmens oder zur Verbesserung alternativer Sensorsysteme— vorgeschlagen.

**Schlüsselwörter:** Magnetisches Schweben, Scheibenläufer, Sensorsysteme, Bewegungssteuerung, Optimierung, Axialgebläse, hohe Geschwindigkeit, Mikromotoren, experimentelle Validierung.

# Riassunto

Lo sviluppo di nuove applicazioni industriali ha concentrato l'attenzione della ricerca verso azionamenti rotativi più compatti e veloci. Questi requisiti spingono i classici cuscinetti a sfera dei motori elettrici ai limiti in termini di durata di vita e di perdite per attrito.

I progressi nei sistemi di sensori, nell'elettronica e nei semiconduttori hanno quindi reso gli azionamenti senza contatto e a levitazione magnetica un'alternativa convincente per la miniaturizzazione degli azionamenti e la ricerca di alte velocità di rotazione. La possibilità di sigillare ermeticamente il rotore e lo statore ha anche aperto nuove applicazioni industriali in cui sono richieste elevata purezza e funzionamento robusto.

In questa tesi, la concezione di un azionamento elettrico compatto a levitazione magnetica viene affrontata, dalla sua base analitica, alla costituzione del sistema di sensori, fino alla fabbricazione di due prototipi funzionanti. Uno dei prototipi viene infine utilizzato come attuatore funzionante, cioè come ventilatore assiale ad alte velocità di rotazione.

Questa tesi tratta quindi i diversi argomenti che incarnano la complessità di un azionamento a levitazione magnetica. A questo proposito, viene inizialmente effettuata una ricerca di letteratura per indagare quali tipi di strutture di motori elettrici si sono integrate con successo con i cuscinetti magnetici. Un'analisi focalizzata sui piccoli azionamenti a levitazione magnetica mostra che pochi piccoli azionamenti a geometria piatta —i cosiddetti "disc drives"— sono stati testati con un carico meccanico. La mancanza di motori elettrici documentati in questa scala e velocità, che funzionano nell'ambito di un'applicazione vera, rappresenta quindi un'opportunità di ricerca nuova e non sfruttata.

Questo lavoro esamina i principi elettromagnetici che permettono la levitazione magnetica e la rotazione degli azionamenti. Per una migliore accuratezza, viene proposta la modellazione computazionale dei disc drive a levitazione magnetica, insieme a una valutazione delle loro caratteristiche passive, attive e di perdite di potenza. Viene fornito un quadro d'analisi parametrica per la valutazione di queste caratteristiche.

In seguito, un'analisi prende in considerazione diverse possibilità di sensori senza contatto. Viene presentata la composizione di un sistema regolabile e a basso costo per la stima della posizione del rotore che può essere facilmente integrato nei sistemi di levitazione magnetica già esistenti.

La corretta concezione elettromagnetica degli azionamenti e il sistema di sensori, accoppiato ad'elettronica reperibile, porta a due prototipi funzionanti. Uno di questi è utilizzato come

un soffiatore assiale, che può girare a velocità di  $10000 \text{ giri} \cdot \text{min}^{-1}$ , soffiare flussi d'aria di  $40 \text{ l} \cdot \text{min}^{-1}$ , e raggiungere pressioni differenziali di 10 Pa.

Infine, le lezioni tratte da questo manoscritto sono riassunte, e ed è proposto il futuro lavoro di ricerca —che potrebbe migliorare l'hardware esistente, convalidare il quadro di progettazione elettromagnetica, o potenziare i sistemi di sensori alternativi—.

**Parole chiave:** levitazione magnetica, disc drives, sistemi di sensori, controllo del movimento, ottimizzazione, soffiatore assiale, alta velocità, motori su piccola scala, validazione sperimentale.

# Contents

## Acknowledgements

Abstract (English/Français/Deutsch/Italiano)	ii
--	----

List of Figures	xiv
-----------------	-----

List of Tables	xvii
----------------	------

Notation	xviii
----------	-------

<b>1 Introduction</b>	<b>2</b>
1.1 Background in Electric Drives . . . . .	2
1.1.1 Electric Drives . . . . .	2
1.1.2 Towards High-Speed Drives . . . . .	3
1.2 Motivations of Magnetic Levitation . . . . .	4
1.2.1 Advantages . . . . .	5
1.2.2 Challenges . . . . .	5
1.3 Outline of the Thesis . . . . .	6
1.4 Conclusion . . . . .	8
<b>2 State of the Art</b>	<b>9</b>
2.1 Introduction . . . . .	9
2.2 Rotatory Drives . . . . .	9
2.2.1 Topologies . . . . .	10
2.2.2 Miniaturization of Drives . . . . .	11
2.3 Topologies for Magnetic Levitation . . . . .	12
2.3.1 Types of Magnetic Levitation . . . . .	12
2.3.2 Disc Drives in Magnetic Levitation . . . . .	14
2.4 Application of Magnetically-Levitated Drives . . . . .	16
2.5 Miniaturized High-Speed Magnetic Levitation . . . . .	18
2.5.1 Towards high-speed . . . . .	18
2.5.2 Leveraging small, magnetically-levitated drives . . . . .	19
2.6 Sensor Systems . . . . .	20
2.7 Conclusion . . . . .	21

<b>3</b>	<b>Electromagnetic Modelling for Magnetic Bearings</b>	<b>22</b>
3.1	Introduction . . . . .	22
3.2	Electromagnetics . . . . .	22
3.2.1	Reluctance Forces . . . . .	22
3.2.2	Lorentz Forces . . . . .	25
3.2.3	Torque Generation . . . . .	27
3.3	Force and Torque Build-up in Rotatory Drives . . . . .	29
3.3.1	Passive Forces . . . . .	29
3.3.2	Drive Excitation . . . . .	32
3.3.3	Spatial and Electric Distribution of Windings . . . . .	38
3.4	Power Losses . . . . .	39
3.4.1	Joule losses . . . . .	40
3.4.2	Eddy-current losses . . . . .	40
3.4.3	Hysteresis losses . . . . .	44
3.4.4	Current ripple losses . . . . .	44
3.5	Conclusion . . . . .	46
<b>4</b>	<b>Conceptualization of Compact Disc Drives</b>	<b>47</b>
4.1	Introduction . . . . .	47
4.2	Comparison of Drives with Interior and Exterior Rotor . . . . .	48
4.2.1	Implementation of Axial Ventilator . . . . .	48
4.2.2	Solution Portfolio . . . . .	51
4.2.3	Electromagnetic Performance Analysis for Same Impeller Diameter . . .	53
4.2.4	Practical Considerations of Drive Realization . . . . .	55
4.3	Enhancing the Performance of Disc Drives . . . . .	57
4.3.1	Motivation . . . . .	57
4.3.2	Modelling of the Disc Drive . . . . .	57
4.3.3	Material Selection and Mechanical Considerations . . . . .	58
4.3.4	Parametric Study . . . . .	59
4.3.5	Scenarios for the Characterization of Disc Drives . . . . .	61
4.4	Comparison of Slotless and Slotted Topologies . . . . .	64
4.4.1	Effect of Drive Geometry upon Performance . . . . .	65
4.4.2	Trade-offs in Slice Drives . . . . .	70
4.4.3	Inequality Constraints upon Design Space . . . . .	72
4.4.4	Head-to-head Comparison . . . . .	72
4.5	Conclusion . . . . .	75
<b>5</b>	<b>Contactless Sensor Systems for Rotor Position Estimation</b>	<b>76</b>
5.1	Introduction . . . . .	76
5.2	Contactless Sensor Technology . . . . .	77
5.2.1	Performance of Sensor Systems . . . . .	77
5.2.2	Physical Principles . . . . .	77
5.3	Eddy-Current Based Estimation of Rotor Radial Position . . . . .	82

## Contents

---

5.3.1	Modelling . . . . .	82
5.3.2	Placement of Sensor . . . . .	85
5.4	Hall-Effect Sensor Estimation of Rotor Angular and Radial Position . . . . .	86
5.4.1	Placement of Sensor . . . . .	86
5.4.2	Modelling of Rotor Fields . . . . .	87
5.4.3	Estimation of Angular Rotor Position . . . . .	89
5.4.4	Estimation of Radial Rotor Position . . . . .	89
5.4.5	Estimation of Axial Rotor Position . . . . .	90
5.4.6	Compensation of Coil Currents . . . . .	91
5.5	Conclusion . . . . .	93
<b>6</b>	<b>Control and Compact System Integration in Magnetically-levitated Drives</b>	<b>94</b>
6.1	Introduction . . . . .	94
6.2	Motor Control . . . . .	94
6.2.1	Control Schemes . . . . .	95
6.2.2	Rotor Position Control . . . . .	95
6.2.3	Rotational Speed Control . . . . .	98
6.2.4	Current Control . . . . .	99
6.2.5	Microcontrollers . . . . .	101
6.2.6	Power Converter . . . . .	102
6.3	Sensor Electronics . . . . .	102
6.3.1	Eddy-Current Sensing Excitation . . . . .	103
6.3.2	Integration of Eddy-Current Sensing Coils and their Shielding . . . . .	105
6.3.3	Hall-Effect Sensor PCB . . . . .	107
6.4	Conclusion . . . . .	108
<b>7</b>	<b>Disc Drive Prototypes</b>	<b>109</b>
7.1	Introduction . . . . .	109
7.2	Compact PCB-based Axial Assembly of the System . . . . .	111
7.3	Experimental Validation of the Eddy-Current-Based Estimation of Rotor Position . . . . .	114
7.3.1	Testing of Sensor Coils . . . . .	114
7.3.2	Single and Differential Sensor Characteristic . . . . .	117
7.3.3	Sensor Resolution Characteristic . . . . .	118
7.3.4	Sensor Noise Characteristic . . . . .	119
7.4	Experimental Validation of the Hall-Effect-Based Estimation of Rotor Position . . . . .	124
7.4.1	Rotor Angle Estimation . . . . .	124
7.4.2	Radial Rotor Position Estimation . . . . .	125
7.4.3	Axial Rotor Position Estimation . . . . .	128
7.4.4	Current Compensation for Hall-Effect Sensors . . . . .	130
7.5	Measurement of Forces of the Prototypes . . . . .	132
7.5.1	Test Bench . . . . .	132
7.5.2	Passive Forces . . . . .	132
7.5.3	Active Forces and Torque . . . . .	137

7.5.4	Active Torque . . . . .	140
7.6	Commissioning . . . . .	141
7.6.1	Drive and Ventilator Test Bench . . . . .	141
7.6.2	Bearing Start-Up . . . . .	143
7.6.3	Rotation . . . . .	144
7.6.4	Hall-Effect vs. Eddy-Current-Based Position Estimation . . . . .	146
7.7	Experimental Validation of an Axial Ventilator . . . . .	150
7.7.1	Measurement Rig . . . . .	150
7.7.2	Results . . . . .	152
7.8	Conclusion . . . . .	153
<b>8</b>	<b>Conclusion and Outlook</b>	<b>155</b>
8.1	Summary . . . . .	155
8.2	Original contributions . . . . .	157
8.3	List of Publications . . . . .	158
8.4	Outlook . . . . .	159
<b>A</b>	<b>Metglas Stator Material</b>	<b>162</b>
	<b>Bibliography</b>	<b>164</b>
	<b>Curriculum Vitae</b>	<b>180</b>

# List of Figures

1.1	Energy conversion scheme . . . . .	3
1.2	Diagram of ball-bearing vs. magnetic bearing drive . . . . .	5
1.3	Main features and advantages of mag-lev . . . . .	6
2.1	Motor topologies for high speeds. . . . .	10
2.2	Diagram of types of magnetic levitation. . . . .	12
2.3	PM and iron structures for disc drives. . . . .	13
2.4	Drive with magnetic bearings for six DoF control. . . . .	15
2.5	Schematic of disc drives. . . . .	15
2.6	Overview of magnetically-levitated drives and their industrial application. . . .	16
2.7	Application examples of magnetically-levitated disc drives. . . . .	17
2.8	Documented speed of small, magnetically-levitated PMSM drives. . . . .	18
2.9	Cooled PPE concept for the fight against infectious diseases. . . . .	19
2.10	Documented radial position sensitivities of EC-based systems. . . . .	21
3.1	Magnetic levitation based on reluctance forces. . . . .	23
3.2	Voice coil actuator based on Lorentz forces. . . . .	26
3.3	Torque generation in slotted drives. . . . .	28
3.4	Geometric disturbances for the study of passive characteristics in disc drives. .	30
3.5	Radial disturbances for diametrical rotor magnetization. . . . .	31
3.6	Axial and tilting restoring effects in disc drives. . . . .	32
3.7	Equivalence of surface current density to linear current density. . . . .	33
3.8	Electromagnetic generation of Lorentz and reluctance forces. . . . .	36
3.9	Electromagnetic generation of torque based on Lorentz forces. . . . .	37
3.10	Coil interconnection of the slotless and slotted motor. . . . .	39
3.11	Eddy-currents inside a conducting object due to alternating magnetic field. . .	40
3.12	Magnetic flux density in the coils of the slotless and slotted drives. . . . .	41
3.13	Simulated current density inside the rotating rotor of a slotted stator. . . . .	42
3.14	Effects of lamination for the constriction of eddy-currents in conductive materials.	43
3.15	Alternating magnetic flux density in the stator of a slotted drive. . . . .	44
4.1	Integration possibilities for magnetization disc drives with axial ventilators. . .	48
4.2	Slotless and slotted stators with interior and exterior rotor configurations. . . .	52



4.3	Magnetic flux density in the air gap of the compared electrical machines for axial ventilators. . . . .	53
4.4	Radial stiffnesses resulting from FE models of the compared electrical machines. . . . .	54
4.5	Axial and tilting stiffnesses resulting from FE models of the compared drives. . . . .	54
4.6	Torque and force obtained from FE models of the compared electrical machines. . . . .	55
4.7	Effects of design parameters upon drive geometry. . . . .	60
4.8	Flow diagram to determine comparable slotless and slotted drives with correctly-biased stator iron. . . . .	61
4.9	Effects of design parameters upon the slotless disc drives. . . . .	67
4.10	Effects of design parameters upon the slotted disc drives. . . . .	69
4.11	Performance of compliant and non-compliant slotless and slotted drives for different rotor sizes. . . . .	71
4.12	Vis-à-vis comparison of optimal variants for different rotor sizes. . . . .	73
4.13	To-scale sketch of optimal drives. . . . .	74
5.1	Capacitive position measurement principle. . . . .	78
5.2	Optical position measurement principle. . . . .	79
5.3	Hall-effect position measurement principle. . . . .	79
5.4	Inductive and eddy-current-based position measurement principle. . . . .	80
5.5	Modelling of EC sensing coil and its coupling to a conductive target. . . . .	82
5.6	Real and imaginary part of the impedance of a eddy-current sensing coil as a function of target distance $x$ . . . . .	83
5.7	Effect of the magnetic field's frequency upon eddy-currents inside target. . . . .	84
5.8	Effect of sensing probe to target distance upon eddy-currents inside the target. . . . .	84
5.9	Possible locations of EC sensing coils inside a disc drive. . . . .	85
5.10	Hall-effect sensors are placed around the stator to sense magnetic stray fluxes from PM rotor. . . . .	86
5.11	Drive's cross-section with Hall-effect sensor array and an uncentered rotor. . . . .	87
5.12	Symmetric sensor and coil array for the simplification of motor current compensation in the Hall-effect sensor signals. . . . .	92
6.1	Digital control, analogical conversion, sensors, electric and mechanical models for magnetic levitation. . . . .	96
6.2	Microcontroller and power stage for the prototypes. . . . .	102
6.3	LCR resonant tank for the generation and tracking of the frequency of a eddy-current sensing coil. . . . .	103
6.4	LDC coupled to four sensing coils and their message transmission over I <sup>2</sup> C. . . . .	104
6.5	Cross-section of the installation of the EC sensor probes and their shielding. . . . .	106
6.6	Shielding for EC sensor probes, made out of Flex PCB. . . . .	107
6.7	PCB for the mounting of axial or radial Hall-effect sensors. . . . .	107
7.1	Axial mount concept for the drive prototypes. . . . .	112
7.2	Pictures of the mounted prototypes and their stators. . . . .	113

## List of Figures

---

7.3	Tested sensing coils and their impedance. . . . .	114
7.4	Test bench and pieces for the characterization of the eddy-current sensors. . .	115
7.5	Single and differential sensor data. . . . .	117
7.6	Sensitivity, noise, and resolution of the sensing coils as a function of the frequency. . . . .	119
7.7	Flex PCB strip with four eddy-current sensor probes. . . . .	120
7.8	Estimated position signals disturbed by bearing's magnetic fields. . . . .	121
7.9	Frequency spectrum of picked-up noise in the sensor signals due to motor excitations. . . . .	122
7.10	Influence of the magnetic fields of the bearing and drive excitations for slotless and slotted upon the eddy-current estimation system. . . . .	123
7.11	Test bench for the characterization of radially and axially-mounted HES. . . . .	124
7.12	Hall-effect sensor signals for turning rotor. . . . .	125
7.13	Hall-effect signals for radially-displacing rotor. . . . .	126
7.14	Rotor position estimated by axially and radially-mounted Hall-effect sensors. . .	127
7.15	Experimentally-calculated radial rotor position sensitivity for axially and radially-mounted Hall-effect sensors. . . . .	128
7.16	Hall-effect sensor signals for axially-moving rotor. . . . .	129
7.17	Experimentally-calculated axial rotor position sensitivity for axially and radially-mounted Hall-effect sensors. . . . .	129
7.18	Influence of motor coil excitation upon Hall-effect sensor signal. . . . .	130
7.19	Effect of calibration and compensation of motor current upon Hall-effect sensors. . .	131
7.20	Test rig for the characterization of forces and active torque of the prototypes. . .	133
7.21	Measured radial forces of the prototypes. . . . .	134
7.22	Estimated radial stiffnesses of the prototypes. . . . .	134
7.23	Measured axial forces and estimated axial stiffnesses. . . . .	136
7.24	Measured active radial forces. . . . .	138
7.25	Rating of the magnetic bearing and its levitation effort. . . . .	140
7.26	Measured active torque and motor constant. . . . .	141
7.27	Mounted test bench of magnetically-levitated disc drives. . . . .	142
7.28	Picture of prototype levitating and spinning with a mounted impeller. . . . .	142
7.29	Soft start-up procedure of the magnetic bearing. . . . .	143
7.30	Rotor position and current of the magnetic bearing at startup. . . . .	145
7.31	Comparison of HES and EC-based estimated position for a rotor rolling in the mechanical clearance. . . . .	146
7.32	Rotor position estimated by the EC and HES systems at different speeds. . . . .	148
7.33	Test bench for differential pressure and flow measurement of the axial fan. . . . .	151
7.34	Example of an axial impeller. . . . .	151
7.35	Measured airflow and pressure difference of the slotless drive deployed as an axial ventilator. . . . .	152
A.1	<i>BH</i> curve and power losses of <i>Metglas</i> . . . . .	162

# List of Tables

1.1	Challenging aspects of high-speed rotatory drives. . . . .	4
1.2	Challenging aspects of magnetic levitation. . . . .	6
2.1	Qualitative comparison of motor topologies for miniaturization. . . . .	11
3.1	Approaches for the reduction of current-ripple losses. . . . .	46
4.1	Scaling of drive and bearing performance as a function of rotor radius . . . . .	49
4.2	Qualitative comparison of motor-ventilator assembly possibilities. . . . .	50
4.3	Geometric parameters and materials of the motors to deploy as axial ventilator. . . . .	52
4.4	Qualitative comparison of interior and exterior rotor configurations deployed as rim-driven axial ventilators. . . . .	56
4.5	Magnetic and mechanical constants for the comparison of slotless and slotted drives. . . . .	59
4.6	Variation of parameters common to slotted and slotless motors. . . . .	60
4.7	Results of stator dimensioning for the comparison between slotted and slotless drives. . . . .	61
4.8	FE simulation scenarios for the characterization of passive properties. . . . .	62
4.9	FE simulation scenarios for the characterization of active properties. . . . .	63
4.10	FE simulation scenarios for the characterization of power losses. . . . .	64
4.11	Geometry of optimal variants of slotted and slotless motors. . . . .	74
4.12	Design concerns for ratings of magnetically-levitated disc drives . . . . .	75
5.1	Qualitative comparison of position sensor technology. . . . .	81
7.1	Geometric dimensions and materials of the prototypes. . . . .	113
7.2	Paired capacitors and resonant frequencies of the different sensing coils tested. . . . .	117
A.1	Loss parameters for stator material <i>Metglas</i> . . . . .	163

# Notation

## Acronyms

2D	Two-dimensional
3D	Three-dimensional
AC	Alternating Current
ADC	Analog to Digital Converter
bng	Bearing
CAN	Controller Area Network communication protocol
CAS	Cumulated Amplitude Density
CCD	Charge Coupled Device
DAC	Digital to Analog Converter
DC	Direct Current
DoF	spatial Degree of Freedom
drv	Drive
EC	Eddy-Current
FE	Finite Element
Fe	Ferromagnetic material
FFT	Fast Fourier Transform
FOC	Field Oriented Control
GUI	Graphic User Interface
HES(s)	Hall-Effect Sensor (plural)
HM	Homopolar Machine
HP	High-Purity
IC	Integrated Circuit
I <sup>2</sup> C	Inter Integrated Circuit communication protocol
IM	Induction Machine
LC	Inductance-capacitance
LCR	Inductance-capacitance-resistance
MTPA	Maximum Torque Per Ampere
NdFeB	Neodymium Ferro Boron
PCB	Printed Circuit Board
PID	Proportional Integral Derivative (controller)
PM	Permanent Magnet
PMSM	Permanent Magnet Synchronous Motor

PPE	Personal Protection Equipment
PWM	Pulse Width Modulation
RMS	Root Mean Square
rpm	Revolutions Per Minute
SPI	Serial Peripheral Interface
SRF	Self-Resonant Frequency
SRM	Switched Reluctance Machine
TI	Texas Instruments

## Symbols

$A_i$	Area of surface $i$	$[m^2]$
$B$	Magnetic flux density	$[T]$
$B_{rem.}$	Remanence magnetic flux density of a PM	$[T]$
$\vec{B}$	Vector of magnetic flux density	$[T]$
$\chi_{bng}$	Bearing effort	$[W^{1/2} \cdot mm^{-1}]$
$C$	Capacitance	$[F]$
$C_{tank}$	Capacitance of resonance tank for ECS	$[F]$
$c_i$	Magnetic flux loss coefficients of ferromagnetic materials	$[-]$
$c_i$	Mass loss coefficients of ferromagnetic materials	$[-]$
$d_{rot.}$	Rotor diameter	$[m]$
$d_{i,k}$	Compensation factor of HES $i$ for current of coil $k$	$[T \cdot A^{-1}]$
$\delta$	Thickness	$[m]$
$\vec{e}_i$	Unitary vector in $i$ direction	$[-]$
$\vec{E}$	Vector of Electric Field	$[V \cdot m^{-1}]$
$\eta$	Power efficiency	$[-]$
$\vec{F}_{Lor}$	Vector of Lorentz Force	$[N]$
$F_{act.}$	Active magnetic force	$[N]$
$F_{pass.}$	Passive magnetic force	$[N]$
$F_{rel.}$	Magnetic reluctance force	$[N]$
$F_r.$	Magnetic radial force	$[N]$
$f$	Frecuency	$[Hz]$
$\gamma$	Angular coordinate	$[rad]$
$h$	Height (or axial length)	$[m]$
$\vec{H}$	Vector of magnetic field strength	$[A \cdot m^{-1}]$
$H$	Magnetic field strength	$[A \cdot m^{-1}]$
$H_i$	ADC value of $i$ -th Hall-Effect Sensor	$[counts]$
$\iota$	Signal lag	$[samples]$
$I$	Current	$[A]$
$I_i$	Current in phase $i$	$[A]$
$I_{bng.,i}$	Bearing current in phase $i$	$[A]$
$I_{drv.,i}$	Drive current in phase $i$	$[A]$

## Notation

$i_{F,x}$	FOC bearing current for force in $x$ direction	[A]
$i_{F,y}$	FOC bearing current for force in $y$ direction	[A]
$i_{T,d}$	FOC direct drive current	[A]
$i_{T,q}$	FOC quadrature drive current	[A]
$\vec{I}_F$	FOC current force vector $(i_{F,x}, i_{F,y})^T$	[A]
$\vec{I}_T$	FOC current torque vector $(i_{T,d}, i_{T,q})^T$	[A]
$\vec{j}$	Volumetric current density	$[\text{A}\cdot\text{m}^{-3}]$
$J$	Surface current density	$[\text{A}\cdot\text{m}^{-2}]$
$J_{\text{bng.st.}}$	Magnetic bearing's start-up current density	$[\text{A}\cdot\text{m}^{-2}]$
$k_{\text{Cu.}}$	Filling factor of winding	[—]
$k_\alpha$	Tilting stiffness parallel to mag. direction	$[\text{Nm}\cdot\text{deg}^{-1}]$
$k_\beta$	Tilting stiffness perpendicular to mag. direction	$[\text{Nm}\cdot\text{deg}^{-1}]$
$k_r$	Radial stiffness	$[\text{N}\cdot\text{m}^{-1}]$
$k_x$	Radial stiffness parallel to mag. direction	$[\text{N}\cdot\text{m}^{-1}]$
$k_y$	Radial stiffness perpendicular to mag. direction	$[\text{N}\cdot\text{m}^{-1}]$
$k_z$	Axial stiffness	$[\text{N}\cdot\text{m}^{-1}]$
$k_{j-B}$	Current-to-mag. flux density prop. constant	$[\text{T}\cdot\text{A}^{-1}\cdot\text{m}^2]$
$k_F$	Total force-current gain	$[\text{N}\cdot\text{A}^{-1}\cdot\text{Turns}^{-1}]$
$k_T$	Torque-current gain	$[\text{Nm}\cdot\text{A}^{-1}\cdot\text{Turns}^{-1}]$
$k_{F/J}$	Total force-current density gain	$[\text{N}\cdot\text{A}^{-1}\cdot\text{m}^2]$
$k_{F,\text{Lor.}}$	Force-current gain of Lorentz forces	$[\text{N}\cdot\text{A}^{-1}\cdot\text{Turns}^{-1}]$
$k_{F,\text{rel.}}$	Force-current gain of reluctance forces	$[\text{N}\cdot\text{A}^{-1}\cdot\text{Turns}^{-1}]$
$k_{M,F}$	Efficacy of active bearing	$[\text{N}\cdot\text{W}^{-1/2}]$
$k_{M,T}$	Motor drive constant	$[\text{Nm}\cdot\text{W}^{-1/2}]$
$k'_{F,\text{rel.}}$	Non-linear force-current gain of reluctance forces	$[\text{N}\cdot\text{m}^2\cdot\text{A}^{-2}]$
$K_p, K_I, K_D$	Gain parameters of a PID	[—, $\text{s}^{-1}$ , s]
$\lambda$	Rotor to stator height ratio	[—]
$l$	Length of magnetic path	[m]
$L_{\text{th.}}$	Length of stator teeth	[m]
$L$	Inductance	[H]
$m$	Mass	[kg]
$M$	Mutual inductance	[H]
$\mu$	Magnetetic permeability	$[\text{H}\cdot\text{m}^{-1}]$
$\mu_r$	Relative magnetetic permeability	[—]
$\mu_i$	Motor merit criterion	[—]
$n$	Rotatory speed	[rpm]
$\vec{n}$	Vector normal to ferromagnetic surface	[—]
$N_{\text{Turns}}$	Number of turns of a coil	[Turns]
$p$	Number pole pairs	[—]
$\Phi$	Magnetic flux	[Wb]
$\phi$	Phase angle of current excitation	[rad]
$\psi$	Angle of rotor orientation	[rad]

$\Psi$	Overall motor merit criterion	[—]
$\omega$	Rotational speed	[rad·s <sup>-1</sup> ]
$P_{\text{mech.}}$	Mechanical Power	[W]
$P_i$	Power losses	[W]
$r$	Radius	[m]
$r_s$	Sensor resolution	[m]
$\rho$	Volume charge density	[C·m <sup>-3</sup> ]
$\rho_{\text{Cu.}}$	Resistivity of copper	[Ω·m]
$\sigma$	Standard deviation of sensor samples	[counts]
$s$	Laplace's transform frequency parameter	[Hz]
$s_{\text{pos}}$	Sensitivity of sensor system	[counts·m <sup>-1</sup> ]
$s_r$	Sensitivity of magnetic flux density to radial displacement	[m <sup>-1</sup> ]
$s_z$	Sensitivity of magnetic flux density to axial displacement	[m <sup>-1</sup> ]
$S_z$	Signal of rotor's axial position estimated by the HESs	[—]
$S_{i_{\text{rot.}}}$	Rotor position estimated by the HES on rot. coord. system	[—]
$S_{i_{\text{st.}}}$	Rotor position estimated by the HES on st. coord. system	[—]
$T$	Torque	[Nm]
$T_z$	Rotatory torque	[Nm]
$\tau$	Magnetic flux density's phase shift	[—]
$\tau_{\text{bng.}}$	Time constant of magnetic bearing	[s]
$\Theta$	Magnetomotive Force	[A]
$u_{\text{ind.}}$	Back EMF voltage at a phase	[V]
$U_{\text{DC.}}$	DC voltage of power electronics	[V]
$v_T$	Tangential speed	[m·s <sup>-1</sup> ]
$v_{\text{d/q}}$	Direct/quadrature drive voltages of FOC	[V]
$v_{\text{x/y}}$	x/y bearing voltages of FOC	[V]
$v_{\text{bng } \alpha/\beta}$	Biphase bearing voltage equivalent	[V]
$v_{\text{drv } \alpha/\beta}$	Biphase drive voltage equivalent	[V]
$W$	Width	[m]
$X/Y_{\text{POS}}$	Estimated differential position on $x$ or $y$ axis	[m]
$\xi$	Ratio of rotor height to rotor diameter	[—]





# 1 Introduction

The need for higher rotatory speeds runs into intrinsic lifetime and power loss issues of classical ball-bearings, rendering magnetic bearings a compelling alternative. This type of contactless levitation also brings advantages in terms of bearing controllability and encapsulation possibilities, fostering the deployment of electric drives in novel scientific applications. The advantages of magnetic levitation come at a cost, which is sketched out and approached in this work.

## 1.1 Background in Electric Drives

In this section, the relevance of electric motors in the conversion of energy is introduced. The trends of energy conversion that push motors to become smaller are also presented.

### 1.1.1 Electric Drives

Electric machines are defined as actuators capable of transforming energy from one form to another, with at least one of them being electrical. A *motor* transforms electrical energy into mechanical energy, whereas a *generator* transforms mechanical energy into electrical energy [141]. For rotatory machines, this energetic transformation is usually performed by a torque  $T$  upon a shaft rotating at  $\omega$  as shown in Fig. 1.1.

As societies become richer, they simultaneously increase their energy consumption. It is estimated that electric drives are involved in up to 60% of the total energy conversion in western countries [15], in applications such as ventilation, air-conditioning, drills, and air compression.

Rendering energy conversion more efficient has become an international priority. Energy savings can be translated into monetary savings, less greenhouse gas emissions, and increased energetic independence [86, 161].

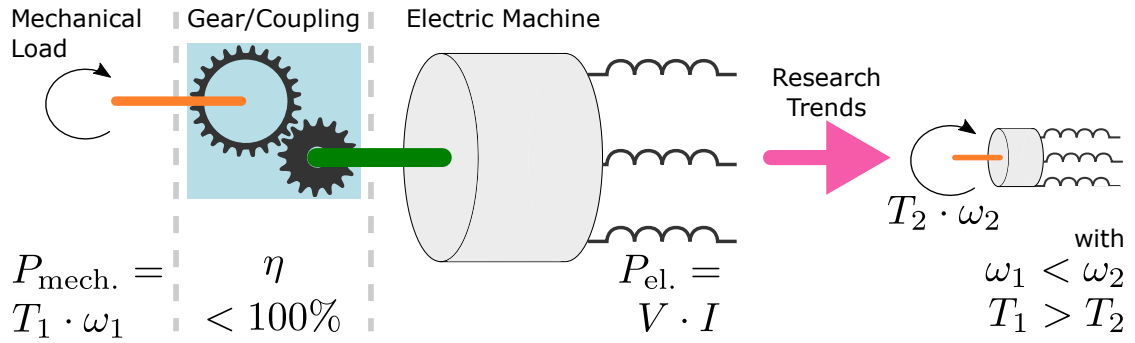


Figure 1.1: Diagram of classical and more compact energy conversion schemes. The energy can from the mechanical side to the electric or vice-versa.

Such energy savings are pursued by conceiving *integrated* drives. Matching an electric motor with its loads and electronics at a design phase means relinquishing from valves, gears, and couplings between the drive and the load [66, 162] in applications in which this is *meaningful* and more *energetically efficient*. Optimizing the complete drive system in this way can amount to up to energy savings that dominate over solely improving the efficiency of the electric motor [163].

The quest for more efficient energy exploitation funnels scientific interest towards more integrated drive solutions [149]. Along these lines, this thesis researches high-efficiency drives intended to *directly* drive a mechanical load.

### 1.1.2 Towards High-Speed Drives

The increasing demand for energy and its efficient conversion has led to technological breakthroughs in the domains of magnetic materials. This, along with preciser fabrication methods have thereto contributed to the *miniaturization* of electric drives, all the while attempting to augment the power these can yield; that is, increasing their power density [55, 143, 204].

Decreasing motor sizes —while trying to attain high-power densities— naturally steer scientific endeavors towards high-rotational speeds [16], as mechanical power cannot be leveraged from the rapidly-decaying torque of a smaller motor [136]. As a consequence, motor components are pushed to the limits of their mechanical resistance and fabrication feasibility [20, 186].

At the same time, novel applications intrinsically require high speeds, such as micro drills [172], beam choppers for optical systems [31], or miniaturized energy storage [182]. As an example, weight reductions of factor  $10^2$  are foreseen within the scope of turbocompressors for electric airplanes [203].

Along these lines, the miniaturization of electric drives can also enable the concept of *portable* systems. Some examples are turbines that power air micro-vehicles [80] or that compress gas [47]. This thesis proposes a high-speed drive that could —exemplarily— be exploited as a

micro blower for personal cooling purposes.

All in all, the conceptualization and subsequent deployment of small, high-speed actuators pose numerous challenges in the domains of magnetics and electronics but also thermal management and mechanics. The most common are listed in Table 1.1. Correctly tackling all these fields and fabricating a reliable, small motor is still a sophisticated scientific venture.

Table 1.1: Challenging aspects of conceiving small, high-speed rotatory drives.

Domain	Challenges	Approached in
Ball Bearings	Power losses, lifetime	[27, 97]
Magnetics	Materials for low power losses	[34, 107]
Material Science	Less brittle magnets, rotor bandaging	[17, 187]
Mechanics	Resonances, rotordynamical analysis	[21, 26, 41]
Power Electronics	Compact volume, low current ripple	[99, 108]
Sensors	Sensor miniaturization, sensorless schemes	[40, 64, 75, 83]
Thermal	Limited heat transfer, cooling systems	[73, 183]

### 1.2 Motivations of Magnetic Levitation

Technological progress has effectively tackled the problematics presented in Table 1.1. As a consequence, there are now various off-the-shelf drives that provide rotatory speeds above 100 krpm [30, 102].

Despite the availability of such solutions, this domain is nevertheless far from being dominated. Novel medical applications that demand high-speeds must be frequently sterilized; yet, the available ball-bearings and their seals can tolerate a limited number of sterilization cycles [30, 1, 58]. This limits the settling of micro-motors at a market level.

Simultaneously, the friction losses [136] and their resulting thermal cycling limit the lifetime of high-speed bearings [23]. For these reasons, ball-bearing failure accounts for 40 % of motor breakdowns for medium-sized machines [196] and is believed to be even more critical for low-voltage drives [18, 117].

These problematics can be circumvented by refraining from ball bearings, and aiming towards the *contactless* levitation of the rotor. This can be achieved by either gas-lubricated bearings [51] or magnetic bearings [81], among others. The latter alternative is investigated in this thesis, due to its adaptability, dampening characteristics, and operative robustness [101].

The principal components of a drive with ball bearings and magnetic bearings are portrayed in a simplified manner by Fig. 1.2. The former relies on seals to separate the shaft from the electrical components and ball bearings, yet abrasion at these locations cannot be ruled out. Magnetic levitation fosters simpler encapsulation concepts—free of abrasion—for the rotor and drive, but requires contactless sensors that estimate the position of the rotor.

The encapsulation of the rotor and its stator can render motor assembly easier at the expense of extra control and hardware effort needed to sustain the rotor in position. The advantages that the control of rotor position and its encapsulation promote are explained in the next subsection.

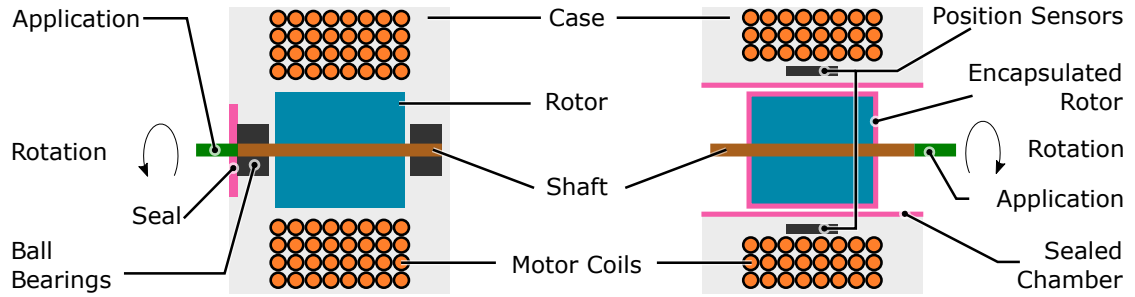


Figure 1.2: Simplified diagram of a motor with ball bearings (left) and magnetic bearings (right).

### 1.2.1 Advantages

The most distinct feature of magnetic levitation is its contactless operation principle, which eliminates abrasion, reduces friction losses due to ball-bearings, and permits encapsulation.

In the context of high-speed, the accurate control of the rotor's position is of further advantage. Magnetic bearings make rotor position—and its stiffness—modifiable, so that vibrations can be actively dampened and system resonances better circumvented [147, 198]. These rotordynamic phenomena—which often arise in high-speed drives [74, 194]—otherwise shorten the lifespan of ball-bearings.

The distinct advantages of magnetic levitation and their impact upon different applications are portrayed in Fig. 1.3. The particular application tackled in this thesis is highlighted.

### 1.2.2 Challenges

Magnetic levitation requires the stabilization of *multiple* Degrees of Freedom (DoFs) of an actuator, so it is fundamentally more complex than only energizing the spinning motion of a ball-bearing-fixed rotor. Magnetically-levitated devices are—at the time being—more expensive, as their correct operation requires larger efforts in the domains enunciated in Table 1.2. The chapters that treat the extra efforts are also indicated.

Despite their higher complexity, the reliability and low maintenance intrinsic to magnetic bearings render them already convenient for certain applications [4, 35, 45].

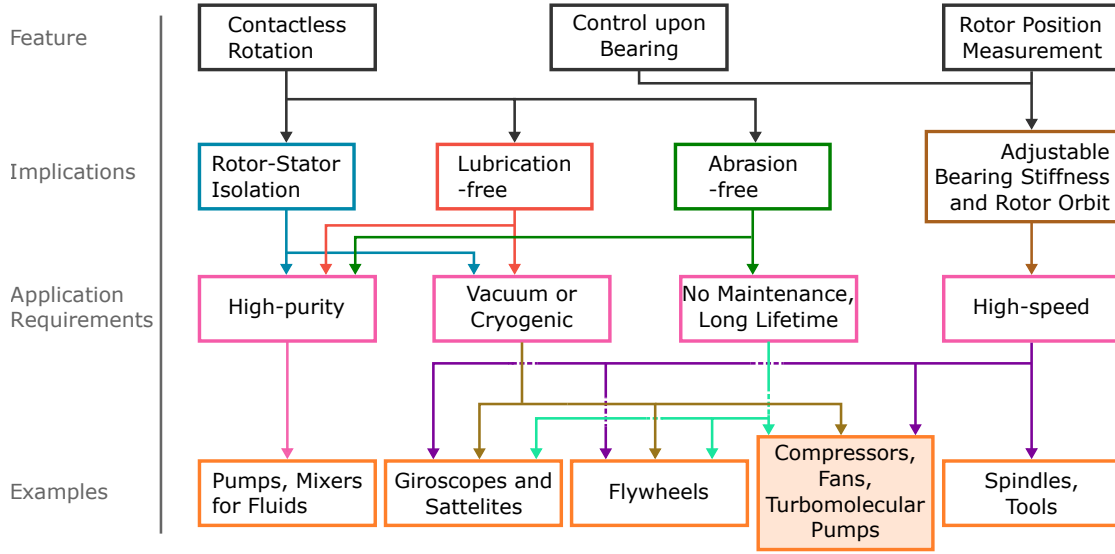


Figure 1.3: Schematic of the main features of magnetic levitation and its ensuring consequences in terms of technological applications, as in [111].

Table 1.2: Challenging aspects of magnetic levitation.

Domain	Requirements	Treated in Chp.
Electromagnetics	More PMs or coils	3
	Bearing and drive performance trade-offs	4
Sensors	Contactless position measurement	5
	Fast sampling rates, high resolution	6, 7
Power Electronics	More semiconductors	3, 6
Control	Extra control loops for extra DoFs	2, 3
	Fast response needed	5, 6

### 1.3 Outline of the Thesis

To effectively tackle the deployment of the magnetically-levitated system, the thesis is structured as follows:

- *State of the Art*

The chapter reviews which motor structures have enabled high-rotatory speeds and magnetic levitation, along with their pros and cons. The "disc drive" is picked out as a compelling contender for miniaturization due to its compactness and simplicity.

Subsequently, a survey classifies magnetically-levitated drives in terms of size, power, speed, and industrial application. This survey validates the drives conceived in this thesis amongst the *smallest disc drives* to demonstrably work with a mechanical load as a ventilator.

Ultimately, the eddy-current-based rotor position sensing system conceptualized in this thesis is described along with its advantages. Its sensitivity is compared to other

documented approaches.

- *Electromagnetic Modelling for Magnetic Bearings*

The electromagnetic principles that enable force and torque generation in rotatory drives are presented. Thereafter, the physical effects that spawn the passively-stable DoFs in disc drives are described.

The chapter then explains how the introduced concepts are exploited to generate both torque *and* force upon a rare-earth permanent magnet. It is demonstrated how both of these can be generated using a combined coil system and off-the-shelf semiconductor technology.

- *Conceptualization of Compact Disc Drives*

This chapter provides a framework for the design of disc drives. Such analysis tackles the consideration of active and passive characteristics, as well as power losses, and the trade-offs among such performances.

To this end, a solution portfolio composed of four magnetically-levitated disc drives is presented. A preliminary analysis sorts out the best contender within the scope of a given application and its constraints.

Thereafter, a parametric analysis for the suitable drive variants is performed. Their performance is mathematically pondered, resulting in optimal motors for different rotor sizes. These are compared head-to-head, so their pros and cons are highlighted.

- *Contactless Sensor Systems for Rotor Position Estimation*

In this chapter, the contactless sensor concepts for magnetic levitation are introduced. The exploitation of the eddy-current (EC) effect for the measurement of the radial position of the rotor is explained. Thereafter, the chapter illustrates how the measurement of magnetic flux density in the vicinity of the rotor allows for the estimation of its angular position *but also* its radial and axial displacement inside a mechanical clearance.

- *Control and Compact System Integration in Magnetically-Levitated Drives*

The control schemes implemented for the control of the levitation and speed of the drive are described. The hardware that runs the electric drives and the semiconductors that energize them are also portrayed. Thereafter, the PCB-based hardware that supports the sensing systems required by magnetic levitation is illustrated.

- *Disc Drive Prototypes*

The compact integration of the prototypes and the measurements that validate their operation are shown in this chapter. The sensor systems are characterized, and the active and passive forces of the prototypes are gauged. Thereafter, their bearing start-up procedures and rotatory operation and vibrations are documented. Ultimately, one prototype is deployed as a fan, whose blowing performance is rated for different impeller geometries.

- *Conclusion and Outlook*

Finally, the scientific lessons and concrete outcomes from the present work are summa-

rized. The chapter additionally proposes future work that can scoop out the potential of the fabricated prototypes, push the miniaturization of magnetically-levitated disc drives and expand their applications.

### 1.4 Conclusion

In this chapter, the relevance of electric motors within the scope of energy conversion is highlighted. The motivations behind the trend towards higher rotatory speeds and compacter actuators are described.

The significance of magnetic levitation is outlined as a pivotal approach in the quest towards higher rotatory speeds. Contactless magnetic levitation offers longer lifetimes and no rotational friction, and the controllability of the rotor position enables to avoid vibrations that are inevitable if ball-bearings are employed. The benefits proper to magnetic bearings are listed, as well as the aspects by which it renders an actuator more complex and —to this date— more expensive.

## 2 State of the Art

### 2.1 Introduction

In this chapter, the latest scientific and industrial developments of high-speed motors and magnetic levitation are presented. Various types of rotatory electric drives are described, along with the rotatory performances that these have achieved in literature.

The electromagnetic principles that enable contactless magnetic levitation are displayed. Out of these, permanent-magnet-based topologies are favored for their controllability and miniaturization potential. The geometric disposition of Permanent Magnets (PMs), electromagnets and ferromagnetic material that enable magnetic levitation for compact actuators are presented.

Thereafter, the novel scientific applications that are made possible by magnetically-levitated rotatory devices below 5 kW of power are classified. This survey on the magnetically-levitated drives is further refined, focussing on high rotational speeds.

As seen in these literature studies, the drives conceived in this thesis are located among the *smallest* actuators that have been tested with a mechanical load, i.e. an impeller. Its remaining potential in terms of higher rotational speeds is also highlighted. The suitability of compact disc drives is emphasized in terms of portability, robustness, and long lifetime operation in the context of an application.

Finally, the performance and advantages of the conceived sensor system for rotor radial position are compared to its counterparts.

### 2.2 Rotatory Drives

Various arrangements of ferromagnetic materials, electromagnets (coils), and PMs give way to different motor *topologies* or electric machine structures. These topologies leverage *Maxwell's equations* in different fashions to generate rotatory motion. The technological application,



its constraints, and fabrication costs must be ultimately matched to the pros and cons of the topology of an electric drive.

### 2.2.1 Topologies

Figure 2.1 sketches four different electric motors. Their different working principles have enabled high-speed rotation [28] *and* have been commissioned with magnetic levitation. These are the Permanent Magnet Synchronous Motor (PMSM), Induction Motor (IM), Synchronous Reluctance Motor (SRM), and Homopolar Motor (HM). Other drive topologies are not depicted because they are fundamentally a combination of the depicted ones.

Homopolar motors are conceived so that a single magnetic pole (north or south) biases one of the cross-sections of the drive, which is further energized by motor coils. This renders their magnetic bearing particularly easy to control [199]. The magnetic bias can be generated by an excitation coil [159] or by a permanent magnet, mounted on the stator [5], rotor [6], or on the stator *and* rotor [150].

The fluctuation of magnetic flux density in the air gap of HM motors is small, so their power losses are also feeble. At the same time, this small variation in magnetic flux density limits the torque generation potential—and thus mechanical power—of this motor type. Their limited power density is thus a disadvantage for motor miniaturization purposes.

Synchronous reluctance motors rely on *reluctance* forces for their operation; that is, on the tendency of the rotor poles to align themselves towards magnetically-excited stator teeth. The ferromagnetic rotors make these drives very robust against heat and mechanical stress [87] and have been implemented as magnetically-levitated drives [43, 60, 100].

Nevertheless, these motor types are intrinsically noisy [191] and their electromechanical characteristic makes them challenging to control [29, 193]. Moreover, any magnetic bias required to levitate a rotor must be provided by the electromagnets, and if a miniature drive is desired, a very limited magnetic bias (and thus bearing stability) can be supplied without overheating the coils. The two latter issues become difficult for small drives.

Induction motors also provide robust and high-temperature operation. Like the SRM, the

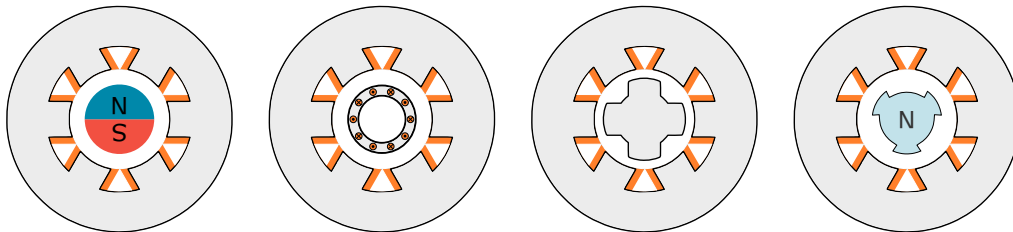


Figure 2.1: From left to right, diagrams of PMSM, IM, SRM, and HM; all with a slotted stator and radially-oriented concentric windings.

rotor is magnetized by electromagnets fixed on the stator, so their operation point can be finely tuned [36].

As a drawback, IMs require very narrow air gaps for good magnetic coupling between the stator and the rotor. This requirement constraints mechanical clearances for magnetic levitation to a minimum. Moreover, the rotor of an IM and its inductances are laborious to miniaturize. They must also be carefully designed to avoid high temperatures since the rotor cannot easily dispense its internal power losses [37]. These features, plus the need for strong magnetic biases of small stator coils (as in the previous case), render the IM unfit for high power-density compact drives.

Tackling high rotatory speeds has been mainly a task of the PMSM [16, 28]. This motor type outperforms the rest within the scope of small, high-speed drives, as the magnetic bias inside the air gap —proportional to the output power of the drive— is independent of rotor radius [14, 20]. This is not the case for the other drives, which usually rely on coils —and their consequent thermal challenges— to bias the drive’s air gap [204].

Moreover, PMSMs can be designed to yield magnetic fields that result in smooth torque and force characteristics [38, 112]. Nevertheless, the rare-earth rotor material is brittle, can hold relatively weak mechanical stress, and can start demagnetizing at circa 150 °C [46].

Table 2.1: Qualitative comparison of motor topologies in the context of miniaturization. (+) indicates is a good performance, (✓) an average performance, and (-) a rather weak performance.

	PMSM	IM	SRM	HM
Robustness	-	✓	+	✓
Controllability	+	✓	-	+
Power-density	+	✓	-	✓
Energy consumption	+	-	-	✓

### 2.2.2 Miniaturization of Drives

As rotatory drives become smaller, their components do as well. The increasing cost of the miniaturization and the complexity of miniature mechanical parts suggests magnetic bearings —and its lack of small abbrasive components— as a alternative in the pursuit of conceiving small actuators that can yield reliable, long lifetime operation.

Particularly, contactless levitation considerably reduces friction losses in the drives —significant in high-speed drives [20, 204]—, and extends the lifetime of a system by renouncing to components that experience abrasion —and its correspondent production of particles—. Applications that must avoid contamination due to particles match well with the encapsulation concepts and no-abrasion operation enabled by contactless levitation.

2.3 Topologies for Magnetic Levitation

Actuators with electromagnetically-levitated structures can rely on different principles for their contactless operation. Such principles are described in Fig. 2.2.

There are also degrees of freedom upon how the different PMs, coils, and ferromagnetic structures can be spatially arrayed, as seen in Fig. 2.3. Both of these considerations are studied in this section.

2.3.1 Types of Magnetic Levitation

Figure 2.2 classifies different principles that enable magnetic levitation. Among these, passive levitation concepts need no (direct) levitation control for their operation. They are shown in green and are fit for drives that

- seldom encounter disturbance forces (LC Resonant, unstable PMs),
- rarely turned off (levitation only at high speeds),
- or can be constantly energized (superconducting bearings, AC current bearings).

These three arguments render passive levitation concepts *unsuitable* for miniaturization, especially within the scope of portability. Portable actuators must be capable of handling vibrations during operation and are usually connected to limited energy sources.

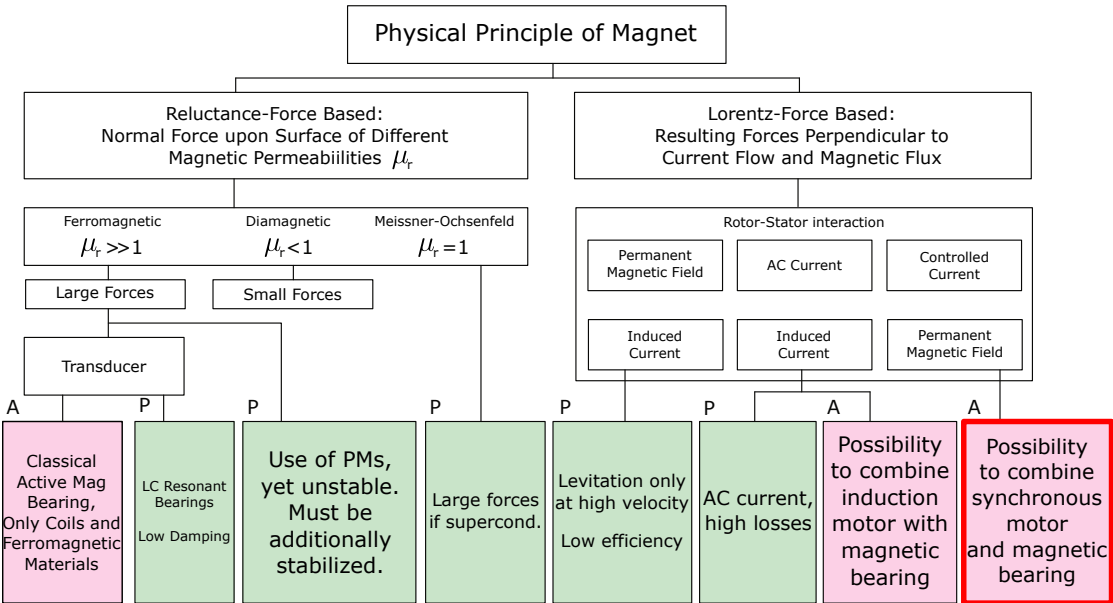


Figure 2.2: Diagram with types of active (red) and passive (green) magnetic levitation, as in [156].

These reasons make active magnetic bearings —red in Fig. 2.2—preferable for small actuators. Among these, those having a PM-biased magnetic flux yield higher power densities and have lower power expenditure than induction or reluctance-based motors.

With the type of magnetic bearing chosen, the arrangement of the PMs and iron, as proposed in Fig. 2.3, must be defined. A magnetic bearing actuator can be made out of multiple of the arrays shown in this picture, or solely out of one, as explained hereafter. This determines which DoFs are passively stable, and as a consequence, which must be stabilized, either by electromagnets or by other mechanical supports (not shown in the schematic).

The choice of stability and instability directions depends on the requirements upon the system's actuation and its desired dynamics. The instability must be ultimately controlled, which means that the levitation of the rotor on this axis can be conveniently *corrected* and its stiffness modified.

As mentioned before, research trends towards miniaturization strive towards high speeds to attain a high power density. The high rotatory speeds necessarily spawn radial forces upon the rotor, due to mass inevitable imbalances.

These centrifugal forces scale with rotatory speed  $n^2$  [54], and for most applications, are larger than the axial forces that the drive might encounter. In ball-bearing drives, these lead solely to vibrations, whereas a magnetic bearing must ensure levitation despite these forces. To this end, it is wiser to control the radial position of the rotor, as this enables minimizing system vibrations [21] and avoiding natural resonances in the system [109].

Out of the axially stable configurations of Fig. 2.3, the attractive ones are preferable. They are axially compacter and offer more axial mechanical clearance than the repellent magnetic bearings.

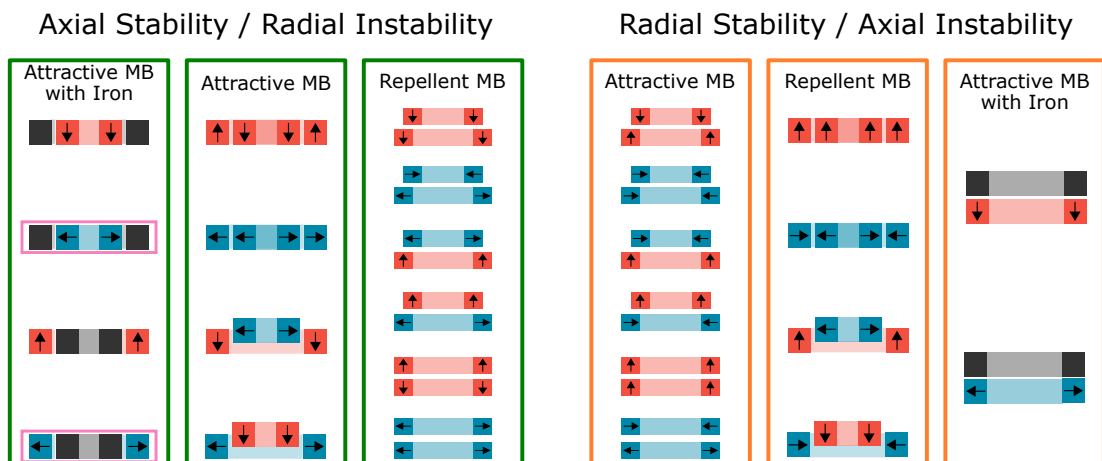


Figure 2.3: PM and iron structures that can lead to magnetic levitation [120]. Coils and mechanical supports are not shown.

For the remaining axially stable, attractive bearings, there is the option to either have an iron yoke or solely utilize PMs for the axial stability and the radial instability. An exclusive PM array strengthens both axial and radial pull [195]; yet incurs high power losses for high-speed rotation due to the conductive magnet material.

On the contrary, iron yokes provide weaker axial and radial pulls. If the axial force is correctly dimensioned for a given application, a feebleness radial pull is desired, so that the control of the radial position can be slower and disturbances can have a slower impact [156]. Moreover, the iron yoke materials can be sheeted to cap the losses in the actuator which become critical for decreasing sizes [20].

Out of the axially stable configurations with an attractive magnetic bearing and iron, variants with radially-oriented magnetizations are studied. They provide shorter reluctance paths between the PM and iron, thus yielding higher power densities.

In the context of this thesis, configurations with outer yoke and inner PMs, and with inner yoke and outer PMs are studied for miniaturization and high-speed purposes. These are highlighted in red in Fig. 2.3.

Ultimately, two stator prototypes of similar geometric dimensions are conceived with the same *design framework* and commissioned with the *same sensor types*. This validates how a combination of both reluctance and Lorentz forces can result in compact, magnetically-levitated drives.

### 2.3.2 Disc Drives in Magnetic Levitation

Multiple stages of those depicted in Fig. 2.3 can be employed to have a fine control upon *all* the DoFs of an actuator. A classic example of magnetic bearings for radially magnetized rotors is depicted in Fig. 2.4.

The depicted actuator is composed of a long spindle rotor. Provided there is enough distance between each actuation stage to ensure electromagnetic decoupling—depicted in Fig. 2.4—each one can be designed and controlled independently. The long axial lengths of each stage allow for analytical modelling methods in which stray fluxes are neglected [21].

Nevertheless, each actuation stage requires its sensor and power electronics. Although complete control of the displacement of the rotor is ensured, such drives are challenging to miniaturize and are elaborate from the electronics point of view. Attempts to render such drive configurations more compact have resulted in *bearingless* or *self-bearing* machines [22, 94], in which some actuation stages can be shared for force and torque generation purposes.

A simpler alternative to magnetic levitation is the "disc drive", first proposed in [19] and shown in Fig. 2.5a. If a ferromagnetic yoke and diametrically-magnetized (or radially) PM configuration are designed to be flat enough relative to its total radius—resembling a disk—,

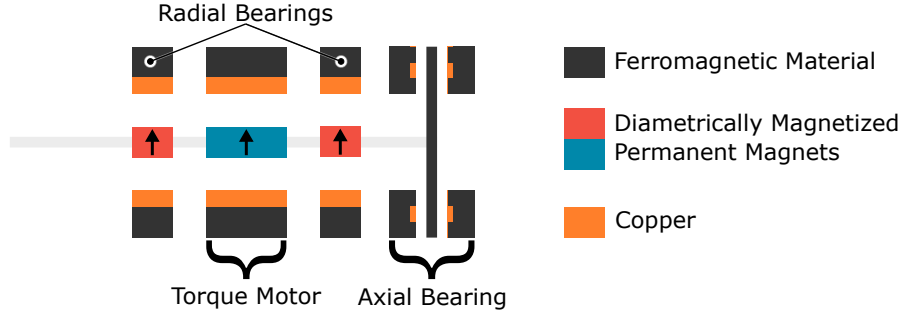


Figure 2.4: Radial-flux drive with classic magnetic bearings for the control of all six DoFs. Referred to as spindle drives in this thesis.

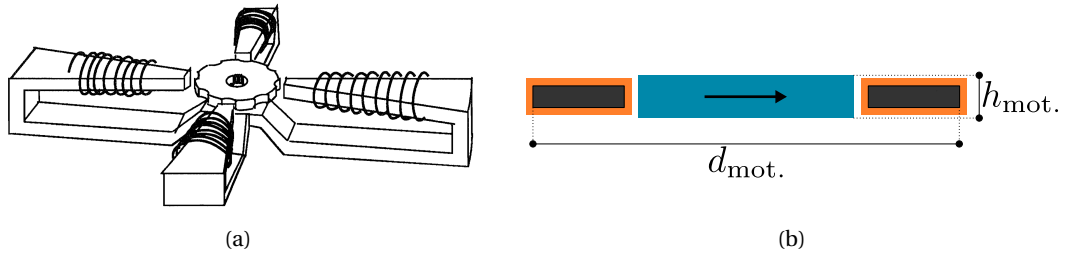


Figure 2.5: (a) Original schematic of the bearingless "disc drive" [19] and (b) general representation of "disc drive", in which  $d_{\text{mot.}} \gg h_{\text{mot.}}$ .

passive forces arise due to their interaction, without the need for energization. They stabilize the axial and tilting position of the rotor, for a total of 3 *passive* DoFs. Thus, *only* the radial positions of the rotor in  $x$  and  $y$  direction (2 DoFs) and its torque for rotatory operation (1 DoF) must be actively controlled. Due to their shared magnetic circuit, they indeed qualify as *bearingless* motors.

In the sizing of disc drives, trade-offs arise between the rotatory and bearing performance of the actuators. The correct modelling of the active drive and radial bearing functions and the passive effects commonly makes use of computational Finite Element (FE) simulations for high result accuracy. This thesis also considers power losses during operation and offers a framework that weights different performance aspects of the actuator that takes into account hard constraints.

Disc drive topologies are thus compacter and need fewer sensor and power electronics than their classical magnetic bearing counterparts. This makes them suitable for cost-sensible applications. As a downside, vibrations and disturbances upon the passively-stable DoFs cannot be controlled nor dampened, and this curbs the diversity of their possible applications. Moreover, for a given rotor radius, the complete disc drive is axially short (or flat), so it can produce limited torque; and it cannot be commissioned for applications with limited radial space. Despite these limitations, disc drives have established themselves in a wide range of applications due to their compactness and simplicity.

## 2.4 Application of Magnetically-Levitated Drives

A literature survey upon the actual state of PMSM, magnetically-levitated drives (of up to 5 kW power) is conducted, resulting in Fig. 2.6. The available motors are classified according to their area of application, rotor size, and mechanical power. Magnetic levitation that *does not* rely on disc drive geometry, i.e. spindle drives, has black borders.

Most of the sorted motors are conceived to drive compressors. A closer look at these reveals that approximately half of them are disc drives, designed to leverage the encapsulation and lubrication-free operation of magnetic levitation for high-purity applications.

One of the drives commissioned for this thesis is ultimately deployed as a fan, so it relates to these applications. The output of this thesis is thus marked as a thick line under 'This Work', for rotor diameters of 20 mm.

The other half of the actuators for compressor and blower purposes corresponds to spindle bearingless drives. They tackle high-speed compression applications with more stringent specifications upon the stability of the bearing and the desire for fewer vibrations.

The High-Purity (HP) Applications englobe pumps, tank mixers, and wafer production tools. Such applications benefit from the hermetic encapsulation of the stator from the rotor, so the latter spins —uninterruptedly— in a high-purity environment where maintenances and downtimes are contaminating and expensive. Disc drives can tackle this segment particularly well as relatively weak forces upon the rotor can be stabilized by their passive magnetic effects.

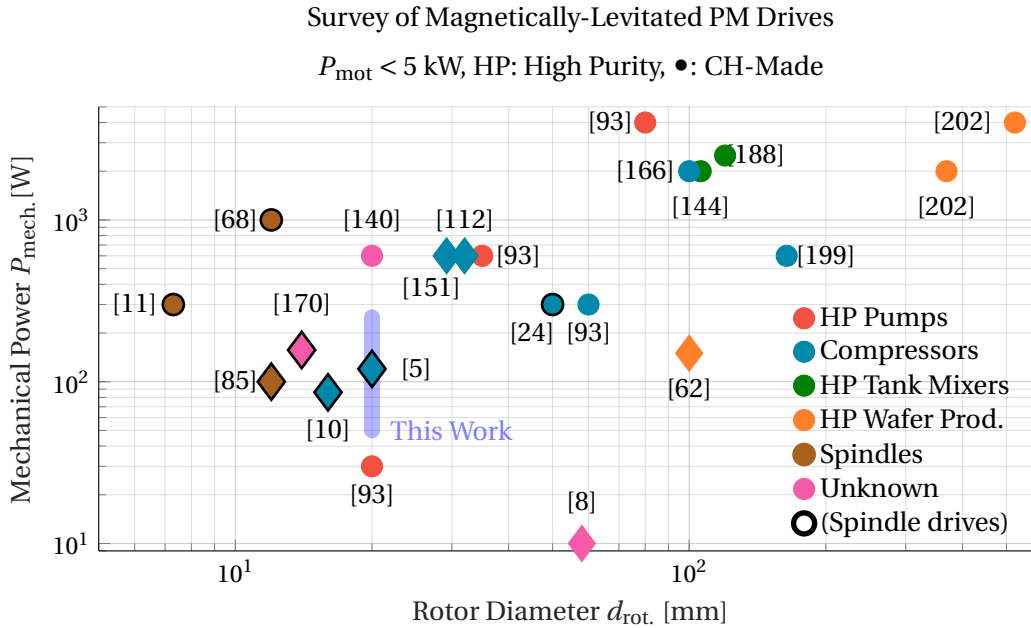


Figure 2.6: Overview of magnetically-levitated drives and their industrial application.

## 2.4 Application of Magnetically-Levitated Drives

Lastly, fabrication tools can positively benefit from magnetic levitation. Spindle tools intended for cutting or beam-chopping [204] can benefit from the vibration-suppressing capabilities of magnetic bearings. This type of application is better approached with spindle bearingless drives that provide complete control upon the axial load on the bearing and the rotor's tilting.

Some of the applications portrayed by Fig. 2.6 are shown in Fig. 2.7.

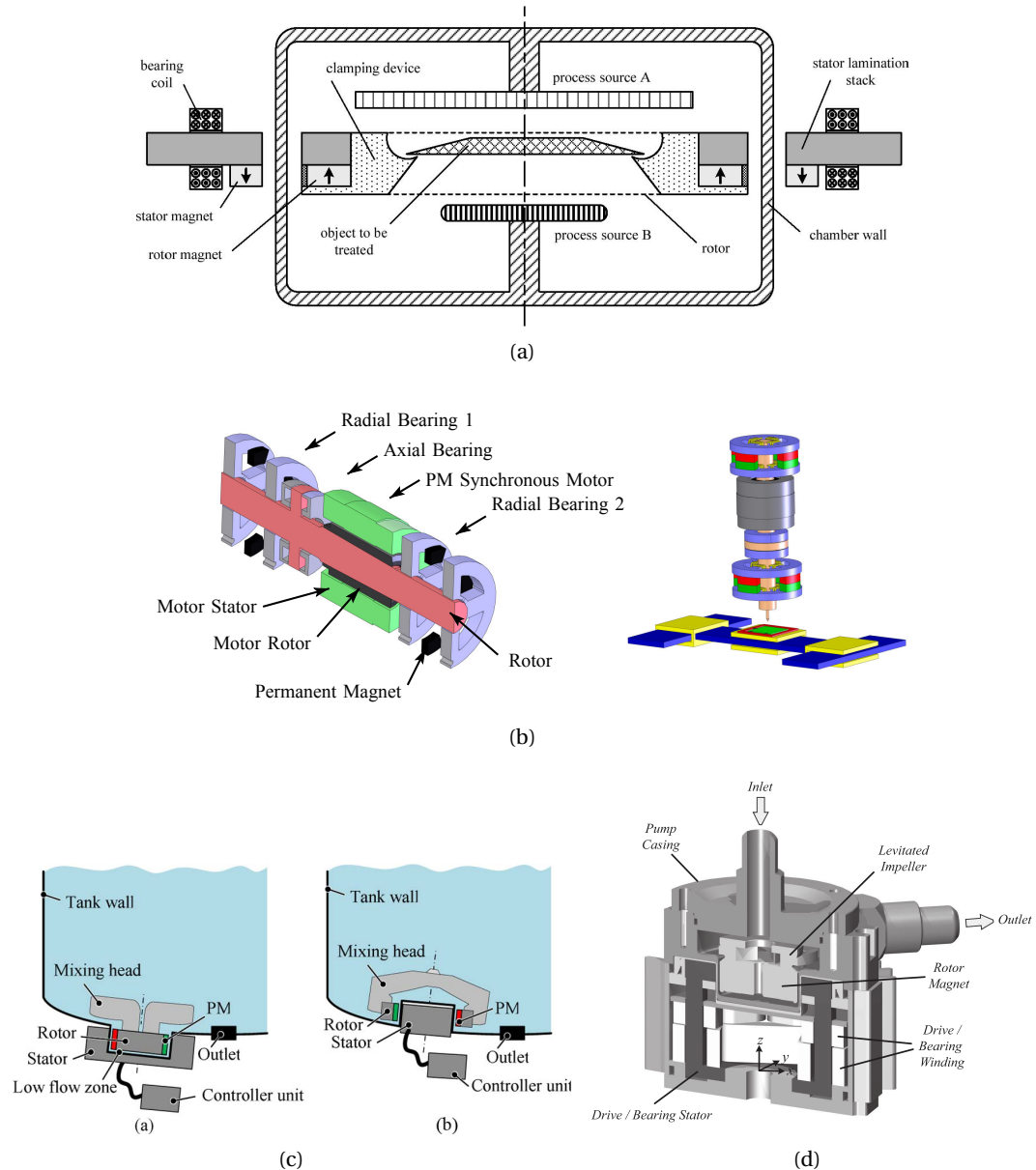


Figure 2.7: Application examples of magnetically-levitated disc drives: wafer handling for the semiconductor industry [150], spindles for precision cutting and optical applications [85], high purity mixers for bioreactors, pharma industry [145], and high purity pumps for the chemical and pharma industry [9].



## 2.5 Miniaturized High-Speed Magnetic Levitation

### 2.5.1 Towards high-speed

The literature survey is refined focussing on the documented rotational speeds of magnetically-levitated drives with small rotor diameters. This results in Fig. 2.8, on which the tensile strength limits of NdFeB—which ultimately limits rotational speed [91]—are indicated. This tensile strength limit is drastically reduced if the rotor is bored, so rotor bandaging techniques may be required to safely approach the zone delimited by this tensile strength [11, 112].

Both disc drives and spindle drives populate the strive towards high speeds, with records being 424 krpm [153] and 500 krpm [11], respectively. Yet, no actuation example is documented at such speeds.

The actuator presented in this thesis belongs to the few miniaturized magnetically-levitated drives whose working principle has been trialed with a mechanical load, i.e. a real-world application. This disc drive is validated within the scope of *blower applications* until 10 krpm, and is experimentally tested until 12 krpm. Smaller disc drives propelling a mechanical load have not been documented.

Nonetheless, the presented drive can be theoretically driven until speeds of 105 krpm, which corresponds to the tensile strength of a NdFeB ring without reinforcement [165]. The zone delimited by these operational points is marked in the graph.

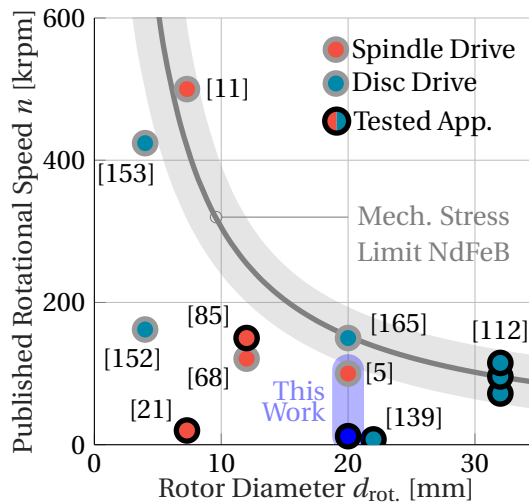


Figure 2.8: Documented rotational speed of small, magnetically-levitated PMSM drives. Tested drives have a black border.

### 2.5.2 Leveraging small, magnetically-levitated drives

The researched motor sizes render the output of this thesis suitable for *portable actuators* that must comply with *special requirements*. Miniaturized, high power density drives can become useful for air-cooling applications that must be wearable. Such demand might arise in the context of medical field-work in the fight against infectious diseases —for example, Ebola [32, 104] — in places with feeble infrastructure.

From the contamination point of view, a hermetical separation between medical personal and patients is demanded [184]. This can be provided by readily available Personal Protection Equipment (PPE) [123], as exemplarily shown in Fig. 2.9.

Nonetheless, if medical professionals work *outside* temperature-regulated facilities or outdoors, the temperature inside their enclosed PPE rises dramatically. Long, hot working shifts may thus lead to sickness and dehydration.

To circumvent these issues, medical professionals must undress from their PPEs and take mandatory pauses to cool and refresh themselves. Unfortunately, pauses lead to downtimes for *patient treatment*, and increases the exposure of the *medical staff* to an infectious environment. To tackle contamination issues, used PPE must be exchanged for newly-sterilized PPE between shifts.

To diminish the frequency of PPE removal, a blower can be integrated into the suit and force air into it. Such an approach fosters forced convection and gives the user a cooling sensation. Such a cooling system may indeed be assembled out of off-the-shelf drives [44, 50, 102, 138]

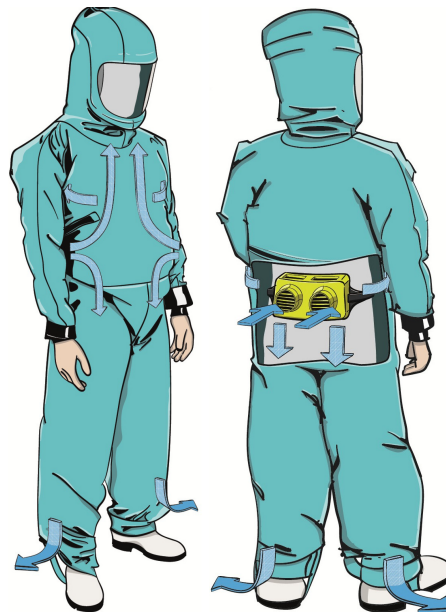


Figure 2.9: PPE concept for the fight against infectious diseases, cooled by wearable, miniaturized fans.

and components.

At any rate, rudimentary sterilization processes—a water-chlorine solution [33]—negatively affect the oil-lubricated ball-bearings. Moreover, the outdoor environments for medical attention also have considerable amounts of suspended dust that eventually penetrates into the ball bearings. These two factors rapidly shorten the lifetime of high-speed actuators if there is a lack of in situ, specialized motor-maintenance personnel.

These environmental hazards require robust actuators that can repeatedly deal with chemicals, dust and *still* provide long lifetime operation. Such requirements demand the encapsulation potential, frictionless operation of magnetic bearings, and their capacity to yield high power-density systems.

### 2.6 Sensor Systems

Magnetically-levitated actuators are intrinsically more complex than their ball-bearing counterparts. The position of the rotor must be continually and rapidly measured for levitation purposes, to assure proper operation at all times.

The research on robust, contactless sensor technologies is a cornerstone in the domain of magnetic levitation. Among these, eddy-current-based position measurement principles rate as one of the best in terms of noise immunity and resolution [38, 156].

Nonetheless, off-the-shelf position measurement solutions that exploit this principle are bulky, thus curtailing their integration potential in small actuators. In such cases, probes may require constructive measures that either take up excessive volume or need target structures that must be extended from the rotor. These issues finally interfere with the electromagnetic design of a drive, enlarge the volume of the overall system and raise its price.

Alternatively, tailored position measurement systems based on ECs with low footprint have been deployed to enable magnetic levitation even at high speeds. The implementation of their electronics is documented, yet involves the tuning of electronics, i.e. op-amps and capacitors, as a function of the sensing coils. Such efforts are thus highly system-specific.

In this thesis, a stand-alone measurement system, composed of one integrated circuit, and four sensing coils is proposed. The advantages of this sensor system rely on its

- flexibility, as it can exploit (practically) any given coil to work as an EC sensor probe, needing minimal, digital adjustment effort;
- integrability, as it can communicate via I<sup>2</sup>C communication protocol, available in most traditional microcontrollers;
- cost, because it relies on market-ready technology, and is validated with sensing probes printed on Flex-PCBs (whose cost rapidly descends with piece number);

- and low-footprint, as the  $150\text{ }\mu\text{m}$ -thin, PCB-printed probes can be easily integrated into thin slits or spaces and does not require extra supporting structures.

The arrangement of the proposed sensor system indeed enabled the magnetic levitation and spinning of two working prototypes. Its sensitivity to rotor displacements is documented and compared to other EC-based position-estimation systems in Fig. 2.10.

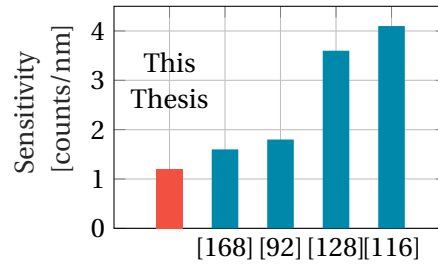


Figure 2.10: Sensitivities of EC-based contactless position sensors in the literature.

Despite offering lower sensitivities than its contenders, this performance indicator lays within the order of magnitude of the customized position measurement systems shown. However, the latter are system-specific, heavily rely on analogical (and thus noise-prone) electronics, and do not offer the indicated advantages.

## 2.7 Conclusion

In this chapter, a technical overview of the types of motors and types of magnetic levitation is provided. The advantages and disadvantages of different actuator topologies are described.

For high power-density purposes, actuators with a PM rotor are preferred. The deployment areas in which PM-biased actuators have enabled magnetic levitation and tackled industrial challenges are displayed on a literature survey. Among magnetically-levitated rotatory drives, disc drive motors, offer passively-stabilized DoFs, which makes them suitable for cost-sensitive applications and compact systems.

A closer look is given to high-speed motors with small rotor diameters. The disc drives conceived in this thesis establish themselves among the smallest drives which have been documented to handle a mechanical load. Regarding the latter, the motivations behind the implementation of an exemplary micro-blower for long lifetimes are described.

Finally, the rating of the stand-alone, rotor position estimation system is compared to its counterparts, along with its qualitative advantages.

## 3 Electromagnetic Modelling for Magnetic Bearings

### 3.1 Introduction

In this chapter, the physical laws that determine the conceptualization and functioning of magnetically-levitated electric drives are introduced.

Firstly, the laws that enable the *motion* of magnets, ferromagnetic materials, and electromagnets are detailed. Two fundamental mechanisms that spawn forces are exemplified, explained, and modelled. These principles are applied to rotatory electric drives, focussing on how force and torque can be *simultaneously* generated.

The operation of the bearingless drives also produces power losses. How the losses arise and how they are estimated is explained.

The concepts reviewed here are recalled in Chapter 4, where the drive and bearing performance of the drive is analyzed as a function of its geometry and an all-around performance is aimed to.

### 3.2 Electromagnetics

#### 3.2.1 Reluctance Forces

The surfaces of the ferromagnetic body ( $\mu_r \gg 1$ ), surrounded by vacuum ( $\mu_r = 1$ ), experience an attractive force if they are penetrated by a magnetic field. The magnetic field can be generated by an electromagnet, i.e. a coil with flowing current, or a PM. This force appears due to the change in magnetic permeability at the interface of the surfaces, and it is called *reluctance force*.

### Derivation

The magnitude of the reluctance force, denoted with  $F_{\text{rel.}}$ , can be derived using the principle of virtual displacement. For this, the energy of a volume that *enables* motion must first be calculated. In electric drives, this volume traditionally coincides with the air gap.

The magnetic system depicted in Fig. 3.1 is considered. In this actuator, the ferromagnetic cylinder can be pulled towards the ferromagnetic C-core by exciting the coil. Such motion would deform the air gap along its thickness  $s$ . To determine the force, the energy  $W_a$  stored in the air gap is calculated as

$$W_a = \frac{1}{2} \int \vec{B} \cdot \vec{H} \cdot dV, \quad (3.1)$$

with  $\vec{B}$ ,  $\vec{H}$  and  $V$  the magnetic flux density, the magnetic field strength, and the volume of the air gap.

Given the simplicity of the magnetic circuit, magnetic vectors  $\vec{B}$  and  $\vec{H}$  can be approximated as constants  $B_a$ ,  $H_a$  inside air gap volume  $V_a$ . The volume of both air gaps  $V_a$  is deconstructed as

$$V_a = A_a \cdot 2s, \quad (3.2)$$

with  $A_a$  the marked area of one pole and  $s$  the length of the air gap in Fig. 3.1, normal to its pink surfaces. The energy in the latter is thus computed as

$$\begin{aligned} W_a &= \frac{1}{2} B_a H_a V_a \\ &= \frac{1}{2} B_a H_a (A_a \cdot 2s). \end{aligned} \quad (3.3)$$

From the principle of virtual displacement [156, 90], it follows that an elongation  $ds$  of the air gap ensures an increase in energy  $dW_a$ . It follows that the magnitude of the attracting force

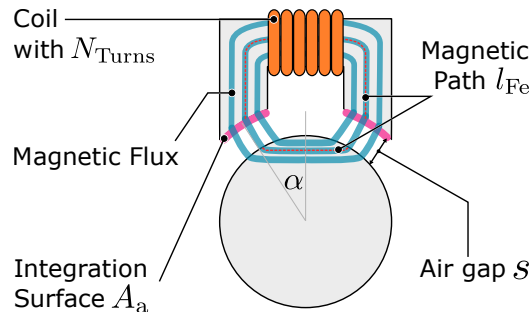


Figure 3.1: Example of basic magnetic levitation based on reluctance forces. Controlling the current of the coil permits to magnetically-levitate the cylinder in a controlled fashion.

between the cylinder and the coils equals

$$\begin{aligned} F_{\text{rel.}} &= \frac{\partial W_a}{\partial s}, \\ &= B_a H_a A_a, \\ &= B_a \left( \frac{B_a}{\mu_0} \right) A_a = \frac{B_a^2 A_a}{\mu_0}, \end{aligned} \quad (3.4)$$

that  $H_a = B_a / \mu_0$ , for the force upon the *two* air gaps. This formula can also be expressed for a single air gap in its differential and more popular form as

$$\vec{F}_{\text{rel.}} = \frac{1}{2\mu_0} \left( \int B^2 \cdot \vec{n} \cdot dA \right) \quad (3.5)$$

with  $B$ ,  $\vec{n}$  the magnetic flux density at the interface between ferromagnetic and vacuum, and  $\vec{n}$  the normal to this surface, respectively. It must be noted that reluctance forces are *always* attractive, and this is ensured by  $\vec{n}$ .

#### Reluctance Force-Based Actuator

The electromagnetic system of Fig. 3.1 is analyzed in terms of magnetic quantities and its force generation. With a fixed C-core, the current  $I$  circulating in the coil is used to generate an upward pulling force on the cylinder. The current can be precisely controlled to bring the latter to levitation.

Using Ampere's law [53] in the magnetic circuit of 3.1, it applies that

$$l_{\text{Fe}} \cdot H_{\text{Fe}} + 2 \cdot s \cdot H_a = N_{\text{Turns}} \cdot I, \quad (3.6)$$

with  $H_{\text{Fe}}$ ,  $l_{\text{Fe}}$ ,  $H_a$ ,  $I$  the magnetic field intensity in the iron, the length of its path, the magnetic field intensity in the air gap, and the current of the coil. If the iron and air have permeability  $\mu_r \gg 1$  and  $\mu_r = 1$  respectively, Eq. (3.6) becomes

$$l_{\text{Fe}} \cdot \frac{B}{\mu_0 \mu_r} + 2 \cdot s \cdot \frac{B}{\mu_0} = N_{\text{Turns}} \cdot I. \quad (3.7)$$

To calculate the force upon the cylinder, using Eq. (3.4), the magnetic flux density  $B$  is required. Equation (3.7) is thus solved in terms of  $B$ , rendering

$$B = \mu_0 \cdot \frac{N_{\text{Turns}} \cdot I}{(l_{\text{Fe}} / \mu_r + 2 \cdot s)}, \quad (3.8)$$

which permits the calculation of the force in the two air gaps with normals  $\vec{n}_1$  and  $\vec{n}_2$  as

$$\begin{aligned} \vec{F}_{\text{rel.}} &= \left( \frac{B_a^2 A_a}{2\mu_0} \right) \cdot (\vec{n}_1 + \vec{n}_2) \\ &= \frac{1}{2} \cdot \mu_0 \cdot \left( \frac{N_{\text{Turns}} \cdot I}{l_{\text{Fe}} / \mu_r + 2 \cdot s} \right)^2 \cdot A_a \cdot (\vec{n}_1 + \vec{n}_2). \end{aligned} \quad (3.9)$$

Thanks to the symmetry of the system, the horizontal components of the force upon the cylinder counteract each other. The vectorial sum  $\vec{n}_1 + \vec{n}_2$  has only a vertical component, which is relevant for vertical levitation. Ultimately, the vertical component  $F_{\text{rel.}}^y$  of  $\vec{F}_{\text{rel.}}$  results in

$$F_{\text{rel.}}^y = \mu_0 \cdot \left( \frac{N_{\text{Turns}} \cdot I}{l_{\text{Fe}} / \mu_r + 2 \cdot s} \right)^2 \cdot A_a \cos \alpha \quad (3.10)$$

which in the case of high iron magnetic permeability  $\mu_r \gg 1$  can be further simplified into

$$\begin{aligned} F'_{\text{rel.}} &= \mu_0 \left( \frac{N_{\text{Turns}} \cdot I}{2 \cdot s} \right)^2 \cdot A_a \cos \alpha, \\ &= \left[ \frac{1}{2} \mu_0 \cdot N_{\text{Turns}} \cdot A_a \cos \alpha \right] \left( \frac{I}{s} \right)^2 = k'_{F, \text{rel.}} \cdot \left( \frac{I}{s} \right)^2, \end{aligned} \quad (3.11)$$

with  $k'_{F, \text{rel.}}$  the force-current gain of the reluctance forces in  $\text{N} \cdot \text{m}^2 \cdot \text{A}^{-2}$ .

Thus the force-current relationship of Eq. (3.11) is fundamentally non-linear, even if the magnetic circuit has a permanent magnet. This is not desirable from the control perspective. Yet in the domain of magnetic bearings, the change in air gap  $s$  is small, and the magnetic circuit is either biased by a current or PM. The proper design of magnetic bearings thus strives for the linearization of Eq. (3.11) around an operating point, often with good accuracy and operational performance.

### 3.2.2 Lorentz Forces

*Lorentz forces* are another type of force that are exploited in electric drives. Moving charged particles experience a Lorentz force when they travel inside an electric and magnetic field. In contrast to reluctance forces, they act perpendicular to both magnetic fields and currents and are not exclusively attractive.

#### Derivation

The Lorentz force  $\vec{F}_L$  acts upon a volume  $V$  of moving charges. Given a spatial current density  $\vec{J}$  inside a magnetic flux density  $\vec{B}$ , or a charge density  $\rho$  in the electric field  $\vec{E}$ , the conductor experiences a *tangential force* which is estimated as follows

$$\vec{F}_L = -\vec{F}_{L, \text{mag}} = \int (\rho \vec{E} + \vec{J} \times \vec{B}) dV. \quad (3.12)$$

By the action-reaction principle, the source of the magnetic flux density, e.g. a PM, experiences a force  $\vec{F}_{L, \text{mag}} = -\vec{F}_L$ .

In electric drives, electric fields are neglectable, so Eq. (3.12) is simplified to only the magnetic term. Proper drive design strives toward a constant  $\vec{B}$  and  $\vec{J}$  along the *axial length*  $h_{\text{ax.length}}$  of



the drive, to further simplify Eq. (3.12) into

$$\begin{aligned}\vec{F}_L &= \int (\vec{J} \times \vec{B}) dV, \\ &= h_{\text{ax.length}} \cdot \int (\vec{J} \times \vec{B}) dA,\end{aligned}\quad (3.13)$$

so that the integral of Eq. 3.13 has to be calculated only inside the surface of the conductors, whose length is already accounted for. It must be noted that the longer the axial length of a drive, the more accurate Eq. (3.13) becomes, as stray fluxes compose a smaller proportion of the total magnetic flux of a drive.

Equation (3.13) can be further simplified for structures such as the voice coil depicted in Fig. 3.2. In this structure, the vertically-magnetized magnets ensure a uniform magnetic flux density  $B_\delta$  in the air gap. A movable coil with  $N_{\text{Turns}}$  can slide onto the center of the E-core, and can be arbitrarily excited with current  $I$  (in the direction of  $h_{\text{ax.length}}$ ). Current  $I$  flows perpendicular to the magnetic flux density  $B_\delta$ , so the Lorentz force is thus horizontal, and its direction depends on the sign of current  $I$ . The magnitude of the force upon *one side* of the coil is determined as

$$\begin{aligned}|\vec{F}_L| &= h_{\text{ax.length}} \cdot B_\delta \cdot \int J dA \\ &= h_{\text{ax.length}} \cdot B_\delta \cdot (N_{\text{Turns}} \cdot I)\end{aligned}\quad (3.14)$$

To obtain a close expression of the force, the magnitude of  $B_\delta$  must yet be obtained. Due to the symmetry, only the upper half of the voice coil of Fig. 3.2 is analyzed.

The magnetic flux closes by passing through three reluctances: the permanent magnet, air, and iron, with relative magnetic permeabilities  $\mu_{\text{PM}}$ ,  $\mu_r = 1$  and  $\mu_{\text{Fe}}$ , respectively. If the latter is considered infinite, the magnetic circuit can be simplified into two reluctances. Using Ampere's law, with a null current in the coil, becomes

$$H_\delta \cdot l_\delta + H_{\text{PM}} \cdot l_{\text{PM}} = \Sigma N \cdot I = 0 \quad (3.15)$$

To obtain the magnetic flux density  $B_\delta$  in the air gap, a linear  $BH$  curves inside air and the

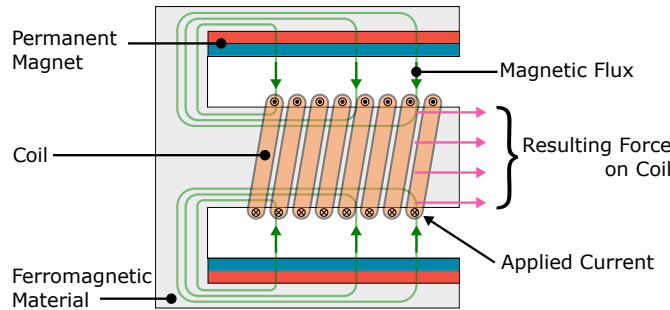


Figure 3.2: Voice coil actuator of thickness  $h_{\text{ax.length}}$ . The interaction of the magnetic flux in the air gap with the current in the moving coil spawns a force  $\vec{F}_L$  upon the coil. This force is perpendicular to the current and magnetic flux and thus pushes it horizontally.

permanent magnets,

$$\begin{aligned} B_\delta &= \mu_0 H_\delta, \\ B_{PM} &= B_{rem.} + \mu_0 \mu_r H_{PM}, \end{aligned} \quad (3.16)$$

are considered. Moreover, the magnetic flux into the air gap  $\Phi_\delta = B_\delta \cdot A_\delta$  is equal to the one into the permanent magnet  $\Phi_{PM} = B_{PM} \cdot A_{PM}$ , with  $A_\delta = A_{PM}$ . Combining these equations with Eq. (3.16) yields

$$B_\delta = B_{PM} = \frac{B_{rem.}}{1 + \mu_r \cdot \frac{\delta}{l_{PM}}}, \quad (3.17)$$

so that Eq. (3.14) is completed as

$$|\vec{F}_L| = 2 \cdot h_{ax.length} \cdot \left( \frac{B_{rem.}}{1 + \mu_r \cdot \frac{\delta}{l_{PM}}} \right) \cdot (N_{Turns} \cdot I) = k_{F, Lor.} \cdot I, \quad (3.18)$$

with factor 2 because the coil is pierced two times (from below and above) by the magnetic flux. In contrast to Eq. (3.11), the force is linear with the current.

### 3.2.3 Torque Generation

Torque generation enables the spinning motion in rotatory electric drives, and this is how they deliver mechanical energy. The torque can be derived from the force calculation of Lorentz and reluctance forces as

$$\begin{aligned} \vec{T}_L &= \int_V \vec{r} \times d\vec{F}_L \\ &= \int_V \vec{r} \times (\vec{J} \times \vec{B}) dV, \end{aligned} \quad (3.19)$$

and

$$\begin{aligned} \vec{T}_{rel.} &= \int_A \vec{r} \times d\vec{F}_M \\ &= \int \vec{r} \times \left( \frac{1}{2\mu_0} B^2 \cdot \vec{n} \right) dA, \end{aligned} \quad (3.20)$$

respectively.

In electric drive design, the torque is generated by a magnetic flux density inside an air gap  $\vec{B}$  which is –by design– perpendicular to the current-density  $\vec{J}$  of the conductors. According to Eq. (3.13), these results in the tangential forces, which are perpendicular to  $\vec{r}$  and thus amount to a rotatory motion. Therefore, if  $\vec{B}$ ,  $\vec{J}$  and  $\vec{r}$  are perpendicular,  $\vec{T}_L$  lays parallel to  $\vec{J}$  and its magnitude can be simplified as [28]

$$|\vec{T}_L| = \int r \cdot J \cdot B_{\delta r} dV_C, \quad (3.21)$$

with  $r$  the radius of rotation of the coil and  $V_C$  its volume.

It is noteworthy to mention that, if this formula were to be applied separately to the upper and lower cut of the coils of Fig. 3.2, they would result in the equal and opposing torques, so that  $\Sigma T = 0$  and  $\Sigma F \neq 0$ . Yet, if the magnetization direction of one PM were to be inverted, the

net force would become 0, and the net torque would become non-null. This is the working principle behind the simultaneous force and torque generation of the combined coil concept described in subsection 3.3.3.

Reluctance forces have another effect. As they are always attractive and normal to a surface, e.g. the interior of a drive stator, their torque generation mechanism is not evident. In rotatory machines, the radial vector  $\vec{r}$  is parallel to the normal of the stator iron surface  $\vec{n}$ , so

$$\begin{aligned}\vec{T}_{\text{rel.}} &= \int \vec{r} \times \left( \frac{1}{2\mu_0} B^2 \cdot \vec{n} \right) dA \\ &= \vec{0}\end{aligned}\tag{3.22}$$

so the contribution of the reluctance forces to torque generation is none.

This opens up the question of how slotted motors build up torque. In them, conductors are wound around high-permeability ferromagnetic material. As a result, the conductors are pierced by a negligible magnetic flux density, as seen in Fig. 3.3a and Fig. 3.3c. According to Eq. (3.19), torque generation is not possible and the windings are installed in the (practically) magnetic field-free grooves, so no Lorentz forces are possible.

Yet it is a fact that slotted motors *can* generate torque. The excitation of a conductor in the slots contributes to a distortion of the magnetic field at the surface of the teeth: at its tips or its lateral flanks. If the groove for the coils is wide and open, a current in the conductor generates an *uneven distribution* of the reluctance forces upon the flanks of the teeth, c.f. Fig. 3.3b. Analogously, by closed grooves, the excitation of the conductor warps the distribution of magnetic flux density at the tips of the teeth, c.f. Fig. 3.3d.

Therefore, the torque build-up mechanism of slotted motors is *physically* different from that of slotless motors. Nevertheless, [89] demonstrates how torque calculation for slotless and slotted motors is *mathematically* equivalent and can be done with the aid of the Lorentz force formula, e.g. Eq. (3.19).

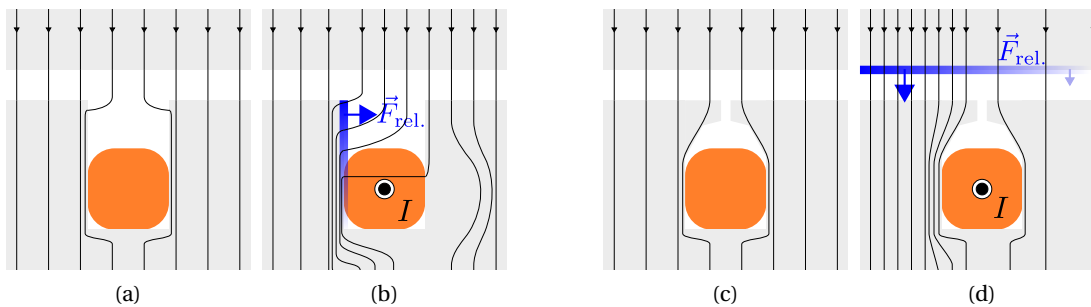


Figure 3.3: In slotted motors, conductors are installed in magnetic field-free grooves. The current  $I$  of the buried conductors distorts the magnetic field when excited; the latter represented as a (blue) gradient at (b) the slot flanks or (d) the slot tips. These fields result in reluctance forces that exert a net torque upon the stator (or on the rotor as a reaction).

## 3.3 Force and Torque Build-up in Rotatory Drives

The presence of a ferromagnetic material inside a magnetic field, coming from a permanent magnet or coil, suffices for the development of reluctance forces, determined by Eq. (3.5).

The reluctance forces in a classical, ball-bearing motor are not evident. The translation of the rotor is fixed, and it only spins if the coils are correctly excited. Yet without the mechanical bearings, a PM rotor is attracted to its stator iron towards an instability position [195].

Different magnetic configurations spawn different force directions, as seen in Fig. 2.3. In this section, the forces of the marked drives of Fig. 2.3 are analyzed; that is, of an inner, diametrically-magnetized rotor with stator iron.

For flat drive proportions, i.e. disc drives, this leads to *stabilizing* axial forces and tilting torques upon the rotor, and to *destabilizing* radial forces. The passive forces are quantified by studying the effect of disturbances of the DoFs depicted in Fig. 3.4 and the stator-rotor interaction.

The attractive forces between the stator iron and the PM rotor originate *without* coil excitation and are thus denominated *passive* forces. It is only with the proper excitation of coils that controlled radial forces are spawned upon the rotor for its controlled levitation in the  $x$  and  $y$  axes.

This force generation is composed of Lorentz and reluctance forces. These are *active* forces, as they require energizing the coils. With stable magnetic levitation ensured, further coil excitation is required to generate torque upon the rotor to start rotatory motion.

The following subsections detail how these forces are spawned and how they can be quantified. It is depicted how the restoring passive features —proper to the disc drives— are enhanced due to the overall flatness of the drive. This slenderness gives way to magnetic fluxes that penetrate the stator in a non-radial fashion, especially if the rotor is longer than the stator.

To accurately portray how position displacements of the rotor —in radial, axial and tilting directions— change the magnetic field distribution around the *entire* drive, the sizing of the drive is aided by the 3D Finite Element (FE) Method. This computational tool can likewise correctly evaluate the active properties of disc drives, considering non-radial fluxes. The potential and exactitude of this tool are verified in Chapter 7 .

### 3.3.1 Passive Forces

The passive forces and torques described hold —in principle— non-linear relationships with the linear magnitude of the disturbance  $x_i$  [156]. For radial pulls, or tilting disturbances, it

follows that the forces  $F_{\text{pass.}}$  at the surface of the stator with air gap  $\delta$  to a PM scale as in [156]

$$F_{\text{pass.}} \propto \frac{1}{(\delta - x_i)^2} - \frac{1}{(\delta + x_i)^2}. \quad (3.23)$$

For  $\delta \gg x_i$ , Eq. (3.23) can be approximated as  $F_{\text{pass.}} \propto x_i$ . Careful motor design strives towards operation in such succinct disturbance ranges.

To this end, if a *small* displacement is imposed upon the rotor, stiffnesses can be defined upon the disturbed geometric DoF of Fig. 3.4 as,

$$k_i = \frac{dF_i}{dx_i}, \quad (3.24)$$

$$= \frac{dT_i}{dx_i},$$

with  $F_i$  the  $i$ -th component of the passive reluctance forces,  $T_i$  a passive reluctance torque, and  $x_i$  the magnitude of the disturbance in this direction. The studied disturbance directions are highlighted in blue and orange in Fig. 3.4.

The passive effects described in this section rise, in part, due to the interaction of stray fluxes that *bend* and unevenly snatch the stator surface, see Fig. 3.6.

For the sake of conceiving a system, and obtaining accurate modelling of it, the passive effects are evaluated with the aid of 3D FE computational software, in this case, Flux 3D [2]. The modelling of the magnetic problem—with non-symmetric magnetic configurations and eccentric rotors—has been approached in literature [65, 160, 171], for 2D structures and slight disturbances to the DoFs. Their analytical model remains out of the scope of the thesis.

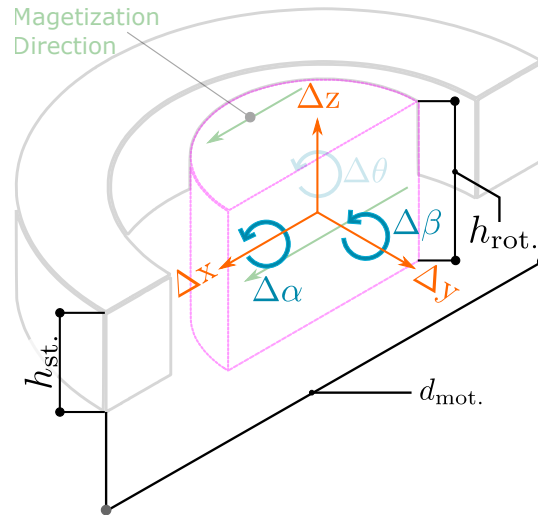


Figure 3.4: Disturbances in  $x$  and  $y$  direction (radial),  $z$  direction (axial), and tiltings in  $\alpha$  and  $\beta$  spawn forces upon the rotor and are therefore studied. Directions  $x$  and  $\alpha$  are defined as movements in the direction or around the diametral magnetization of the PM, whereas  $y$  and  $\beta$  are perpendicular to them.

#### Destabilizing Forces

With the diametrically magnetized PM rotor, radial forces are destabilizing, so the rotor is always pulled towards the stator. The magnitude of these pull depends on the geometry of each drive. The magnitude can be calculated using Eq. (3.5), using  $A$  as the stator surface *inside* the air gap. This surface is marked in blue in Fig. 3.5.

With the geometry of the drive fixed, the magnitude of the pull depends on the magnitude of the rotor displacement and also on its direction, i.e. parallel or perpendicular to rotor magnetization of Fig. 3.4. These pulls are  $F_x$  and  $F_y$ , and result in stiffnesses  $k_x$ , and  $k_y$ , respectively. These stiffnesses have different values, yet they resemble each other for multipolar rotor configurations [110].

The direction of the radial force  $F_x$  and  $F_y$  ensures that the radial stiffnesses defined in Eq. (3.24) are always positive. This intrinsic instability is to be counteracted and controlled by proper excitation of the motor coils.

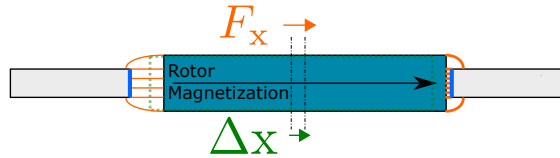


Figure 3.5: An eccentric rotor leads to a larger flux density at one side (right) of the air gap, and a smaller (left) on the opposite side, thus generating a radial force that tends to further displace the rotor. In blue, surface  $A$  for the reluctance force calculation.

#### Stabilizing Forces

The emergence of *passive* stabilizing forces in magnetically-levitated drives is not evident. These properties are a consequence of stray fluxes and only arise if the electric drive is designed to be flat, with  $d_{\text{mot.}} \gg h_{\text{st.}}$  and  $d_{\text{mot.}} \gg h_{\text{rot.}}$ . This classifies the drives studied here as *disc drives*.

The disc drive geometry benefits from the diametrically-exiting stray PM magnetic flux for the stabilization of additional DoFs. Stray fluxes of the PM enter the stator *vertically*, thus generating restoring forces or tilting torques. They appear as a result of evaluating Eq. (3.24) in the blue-marked surfaces of Fig. 3.6.

In practice, displacing the rotor vertically generates a restoring force  $F_z$  *against* the displacement, as shown in Fig. 3.6a. It can be thus said that the configuration is axially stable.

The axial force is initially linear to the vertical  $z$  displacement, so the axial stiffness  $k_z$  can be defined. As it is always stabilizing, it is always negative. Nevertheless, seen as the axial displacement of the rotor is unconstrained, restoring force  $F_z$  plateaus at a maximal force to

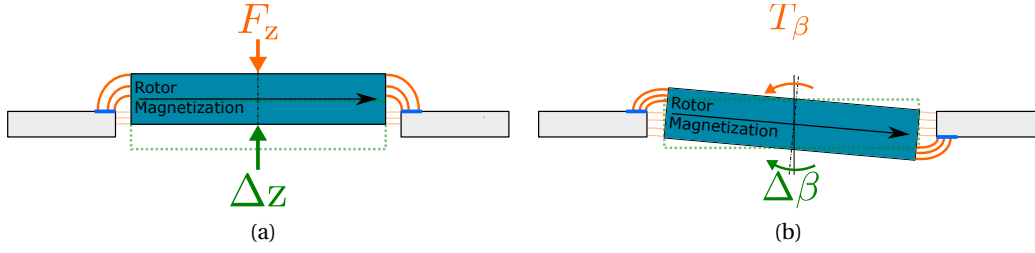


Figure 3.6: (a) An axial deflection of the rotor spawns an opposite, restoring force. Analogously, an (b) angular deflection of the rotor i.e. tilting, generates an opposing, restoring torque. In blue, surface  $A$  for the reluctance force calculation.

then start decreasing. This is a consequence of the increasing stator-rotor reluctance, which in turn diminishes the magnitude of the magnetic flux density.

Analogously, tilting the rotor leads to the counteracting, stabilizing torque. This effect can be appreciated in Fig. 3.6b.

As in the case of the radial pull, the magnitude of the tilting stiffnesses can vary. If the rotor is tilted along an axis perpendicular to its magnetization, i.e. axis  $\beta$  of Fig. 3.6b, the restoring torque  $T_\beta$  is strong. If the rotor is tilted along with its magnetization, i.e. axis  $\alpha$ , a weaker restoring torque  $T_\alpha$  emerges. This leads to two stiffnesses, as in the radial stiffness case,  $k_\alpha$  and  $k_\beta$ .

### 3.3.2 Drive Excitation

For the successful commissioning of the mentioned disc drive magnetic structure, the destabilizing radial pull must be counteracted. The proper energization of the coils leads to Lorentz and reluctance forces that help bring the rotor to levitation. Once successful levitation is achieved, a rotatory motion may be started by a torque.

The build-up of the previously mentioned physical quantities, for a rotatory motor, is explained in this section.

It is assumed that the magnetic flux density  $\vec{B}_{\text{rot.}}$  in the air gap due to the diametrically-magnetized PM rotor has the form [14]

$$\begin{aligned}\vec{B}_{\text{rot.}} &= \hat{B}_r \cos(p_{\text{rot.}}\gamma - \psi) \cdot \hat{e}_r + \hat{B}_\gamma \sin(p_{\text{rot.}}\gamma - \psi) \cdot \hat{e}_\gamma, \\ &\approx \hat{B}_r \cos(p_{\text{rot.}}\gamma - \psi) \cdot \hat{e}_r\end{aligned}\tag{3.25}$$

with  $p_{\text{PM}}$  the pole-pair number of the rotor,  $\gamma$  the angular coordinate on the perimeter of the rotor, and  $\psi$  the magnetization direction of the rotor. Given the diametrical magnetization of the rotor, it also follows that the amplitude of its radial components is larger than the tangential, i.e.  $\hat{B}_r > \hat{B}_\gamma$ , so the latter may be neglected. This is valid as the perimeter of the

rotor shows a larger reluctance than the air gap, so the magnet poles hardly short-circuit.

Along the stator perimeter, coils are to be placed and excited. The current flows axially inside the coils so the current-density distribution resembles block waves.

To simplify calculations, it is assumed that the coil is thin. This leads to a linear current density at the *mean* radius of the coil. The total magnetomotive force  $\Theta$  is calculated and can be related to the surface and linear current density  $J_{\text{lin.}}$  and  $J_{\text{surf.}}$  as

$$\begin{aligned}\Theta &= J_{\text{surf.}} \cdot A_{\text{coil}} \\ &= J_{\text{lin.}} \cdot l_{\text{coil}} \\ N_{\text{Turns}} \cdot I &= J_{\text{surf.}} \cdot \left( \frac{1}{2} \cdot \gamma_{\text{coil}} \cdot (r_{\text{coil,out}}^2 - r_{\text{coil,in}}^2) \right) \\ &= J_{\text{lin.}} \cdot (\gamma_{\text{coil}} \cdot \bar{r})\end{aligned}\tag{3.26}$$

with  $\gamma_{\text{coil}}$  the angular span of a single coil,  $r_{\text{coil,out}}$  and  $r_{\text{coil,in}}$  its outer and inner radius, and  $\bar{r} = \frac{r_{\text{coil,out}} + r_{\text{coil,in}}}{2}$  their mean. It follows that the current densities can be more directly related as

$$J_{\text{surf.}} \cdot (r_{\text{coil,out}} - r_{\text{coil,in}}) = J_{\text{lin.}}\tag{3.27}$$

The block-wise current densities lead to high order harmonics of  $\vec{J}$  in the air gap [14, 167]. Only its fundamental component of amplitude  $\hat{J}_{z,1}$  generates either force or torque, and is modelled with the spatial distribution

$$\vec{J}_{\text{lin., st.}} = \hat{J}_{z,1} \sin(p_{\text{st.}}\gamma - \psi - \phi_{\text{st.}}) \cdot \hat{e}_z,\tag{3.28}$$

with  $p_{\text{st.}}$  the number of pole-pairs of its spatial distribution, and  $\phi_{\text{st.}}$  an arbitrary phase angle. Current density  $\vec{J}_{\text{lin., st.}}$  generates Lorentz forces in combination with the magnetic flux density  $\vec{B}_{\text{rot.}}$  of the PM.

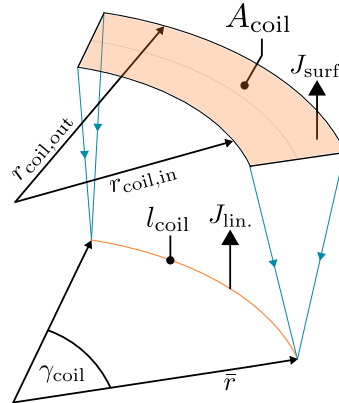


Figure 3.7: Equivalence of surface current density  $J_{\text{surf.}}$  to linear current density  $J_{\text{lin.}}$  of Eq. (3.26). This transformation simplifies the calculation of force and torque.



Furthermore, stator excitation  $\vec{J}_{\text{lin., st.}}$  induces a magnetic flux density  $\vec{B}_{\text{st.}}$  in the air gap. This induced magnetic flux density lags  $\vec{J}_{\text{lin., st.}}$  by  $\pi/2$  and is thus defined as

$$\vec{B}_{\text{st.}} = \hat{B}_{\text{st}} \cos(p_{\text{st.}}\gamma - \psi - \phi_{\text{st.}}) \cdot \hat{e}_r, \quad (3.29)$$

with  $\hat{B}_{\text{st}} = k_{\text{J-B}} \cdot \hat{J}_{z,1}$  the amplitude of the induced flux density in and  $k_{\text{J-B}}$  a proportionality constant in  $\text{T} \cdot \text{A}^{-1} \cdot \text{m}^2$ .

#### Active Force

For the calculation of the bearing force, it is

Lorentz forces upon the coil are calculated in the coil volume *inside* the air gap. Neglecting stray fluxes, proper to disc drives, the height of this volume coincides with that of the stator  $h_{\text{st.}}$ . Then, considering a linear current density, it follows

$$\begin{aligned} \vec{F}_{\text{L,coil}} = -\vec{F}_{\text{L,mag}} &= h_{\text{st.}} \cdot \int (\vec{J}_{\text{surf.}} \times \vec{B}_{\text{rot.}}) dA = h_{\text{st.}} \cdot \int (\vec{J}_{\text{lin., st.}} \times \vec{B}_{\text{rot.}}) dl \\ &= h_{\text{st.}} \cdot \int (\vec{J}_{\text{lin., st.}} \times \vec{B}_{\text{rot.}}) \cdot \vec{r} d\gamma. \end{aligned} \quad (3.30)$$

Assuming  $\phi_{\text{st.}} = \phi_{\text{bng.}}$  and  $p_{\text{st.}} = p_{\text{bng.}}$  from Eq. (3.28), Eq. (3.25) and Eq. (3.28) are inserted into Eq. (3.30) resulting in

$$\begin{aligned} \vec{F}_{\text{L,mag}} &= h_{\text{st.}} \cdot (\hat{J}_{z,1} \hat{B}_r \vec{r}) \cdot \int_0^{2\pi} \sin(p_{\text{bng.}}\gamma - \psi - \phi_{\text{bng.}}) \cdot \cos(p_{\text{rot.}}\gamma - \psi) \cdot (-\hat{e}_\gamma) d\gamma \\ &= h_{\text{st.}} \cdot (\hat{J}_{z,1} \hat{B}_r \vec{r}) \cdot \int_0^{2\pi} \frac{1}{2} \left\{ \sin((p_{\text{bng.}} + p_{\text{rot.}})\gamma - \psi - \phi_{\text{bng.}}) + \sin((p_{\text{bng.}} - p_{\text{rot.}})\gamma - \psi) \right\} \begin{pmatrix} \sin \gamma \\ -\cos \gamma \end{pmatrix} d\gamma. \end{aligned} \quad (3.31)$$

Integrated over a whole period, the vectorial result of the integral in Eq. (3.31) is non-zero only when its argument becomes a constant. This occurs for  $p_{\text{bng.}} = p_{\text{rot.}} \pm 1$ . In this case, the calculation becomes

$$\vec{F}_{\text{L,mag}} = \begin{cases} \frac{\pi \bar{r} h_{\text{st.}} \hat{B}_r \hat{J}_{z,1}}{2} \cdot \begin{pmatrix} \cos \phi_{\text{bng.}} \\ \sin \phi_{\text{bng.}} \end{pmatrix} & \text{for } p_{\text{bng.}} = p_{\text{rot.}} + 1 \\ \frac{\pi \bar{r} h_{\text{st.}} \hat{B}_r \hat{J}_{z,1}}{2} \cdot \begin{pmatrix} -\cos \phi_{\text{bng.}} \\ \sin \phi_{\text{bng.}} \end{pmatrix} & \text{for } p_{\text{bng.}} = p_{\text{rot.}} - 1 \\ \begin{pmatrix} 0 \\ 0 \end{pmatrix} & \text{for } p_{\text{bng.}} \neq p_{\text{rot.}} \pm 1, \end{cases} \quad (3.32)$$

so adjusting  $\hat{J}_{z,1}$  and  $\phi_{\text{bng.}}$  enables controlling the magnitude and direction of the force, respectively.

As mentioned before, the excitation of the coils generates a magnetic flux density inside

the stator iron  $\vec{B}_{st.}$ . This causes a reluctance force which acts upon the cylindrical inner surface, with direction  $-\vec{r}$ , of the stator iron of radius  $r_{st.,in}$  and height  $h_{st.}$ . Upon this surface, the magnetic flux density the rotor and stator are superimposed as  $\vec{B}_\delta = \vec{B}_{rot.} + \vec{B}_{st.}$ , so the reluctance force is estimated as

$$\begin{aligned}\vec{F}_{rel.} = -\vec{F}_{rel.,mag} &= \frac{1}{2\mu_0} \left( \int |\vec{B}_\delta|^2 \cdot (-\vec{r}) \cdot dA \right) \\ &= \frac{1}{2\mu_0} \left( \int |\vec{B}_\delta|^2 \cdot (-\vec{r}) \cdot (r \cdot h \cdot d\gamma) \right), \\ &= \frac{1}{2\mu_0} \left( \int |\vec{B}_\delta|^2 \cdot (-\vec{r}) \cdot d\gamma \right) \cdot (r_{st.,in} \cdot h_{st.}).\end{aligned}\quad (3.33)$$

The last line of Eq. (3.33) is then expanded as

$$\begin{aligned}\vec{F}_{rel.,rot.} &= \frac{(r_{st.,in} \cdot h_{st.})}{2\mu_0} \cdot \\ &\int \left\{ \hat{B}_r \cos(p_{rot.}\gamma - \psi_{el.}) + \hat{B}_{st.} \cos(p_{bng.}\gamma - \psi_{el.} - \phi_{bng.}) \right\}^2 \cdot \begin{pmatrix} \cos \gamma \\ \sin \gamma \end{pmatrix} \cdot d\gamma.\end{aligned}\quad (3.34)$$

The argument is then expanded, and the integral computed. It gives away a result similar to Eq. (3.32), that is,

$$\vec{F}_{rel.,mag} = \begin{cases} \frac{r_{st.,in} \cdot h_{st.}}{2\mu_0} \cdot (\pi \hat{B}_r \hat{B}_{st.}) \cdot \begin{pmatrix} \cos \phi_{bng.} \\ \sin \phi_{bng.} \end{pmatrix} & \text{for } p_{bng.} = p_{rot.} + 1 \\ \frac{r_{st.,in} \cdot h_{st.}}{2\mu_0} \cdot (\pi \hat{B}_r \hat{B}_{st.}) \cdot \begin{pmatrix} \cos \phi_{bng.} \\ -\sin \phi_{bng.} \end{pmatrix} & \text{for } p_{bng.} = p_{rot.} - 1 \\ \begin{pmatrix} 0 \\ 0 \end{pmatrix} & \text{for } p_{bng.} \neq p_{rot.} \pm 1 \end{cases}\quad (3.35)$$

Inspecting the direction of the forces from Eq. (3.32) and (3.35), it becomes apparent that, for interior rotor configurations, it is wise to choose a  $p_{bng.} = p_{rot.} + 1$  pole-pair number configuration. This choice results in a constructive addition of the Lorentz and reluctance forces upon the rotor. If a stator pole-pair number  $p_{bng.} = p_{rot.} - 1$  is chosen, both force types add up destructively fashion. Ultimately, this means higher currents (and thus, larger losses) for a given force.

Figure 3.8 depicts the build-up of Lorentz and reluctance forces for  $p_{rot.} = 4$  and  $p_{bng.} = 5$ . Along the perimeter of the rotor, the arrows represent the force direction, and their length is proportional to their magnitude. The arrows are integrated, i.e. summed up, and the net force is displayed in the center of the rotor.

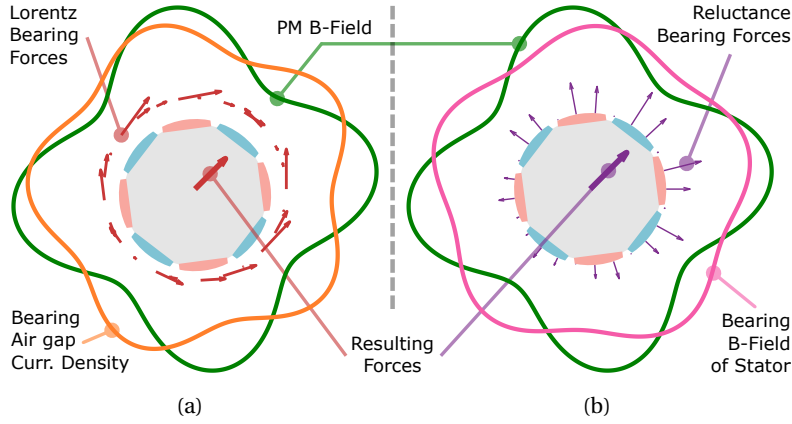


Figure 3.8: Electromagnetic force generation upon a slotless drive with  $p_{\text{rot.}} = 4$  and  $p_{\text{bng.}} = 5$ . (a) Lorentz forces build up tangentially around the rotor and result in a net radial force. (b) Reluctance forces, on the other hand, build up radially. The net force upon the rotor is the sum of both.

### Active Torque

As mentioned before, the torque generation is analyzed as if originating from Lorentz forces [89]. To this end, Eq. (3.19) is used with  $p_{\text{st.}} = p_{\text{drv.}}$ ,  $\phi_{\text{st.}} = \phi_{\text{drv.}}$ ,  $\vec{r} = \vec{r} \cdot \hat{e}_r$ , and evaluated as

$$\begin{aligned} \vec{T}_L &= \int \vec{r} \times (\vec{J} \times \vec{B}) dV = \int \vec{r} \times (\vec{J}_{\text{surf.}} \times \vec{B}) r dr d\gamma dh, \\ &= h_{\text{st.}} \cdot \int \vec{r} \times (\vec{J}_{\text{surf.}} \times \vec{B}) r dr d\gamma, \\ &= h_{\text{st.}} \cdot \int (\vec{r} \hat{e}_r) \times (\vec{J}_{\text{lin.}} \times \vec{B}) \vec{r} d\gamma, \end{aligned} \quad (3.36)$$

which leads to the calculation

$$\begin{aligned} \vec{T}_{L,\text{mag}} &= (\vec{r}^2 h_{\text{st.}}) \cdot (\hat{B}_r \hat{J}_{z,1}) \cdot \\ &\int_0^{2\pi} \sin(p_{\text{drv.}}\gamma - \psi - \phi_{\text{drv.}}) \cdot \cos(p_{\text{rot.}}\gamma - \psi) \cdot (-\hat{e}_z) d\gamma. \end{aligned} \quad (3.37)$$

Solving the integral leads once again to a case by case scenario in which

$$\vec{T}_{L,\text{mag}} = \begin{cases} \pi \vec{r}^2 h_{\text{st.}} \hat{B}_r \hat{J}_{z,1} \cdot \sin \phi_{\text{drv.}} \cdot \hat{e}_z & \text{for } p_{\text{drv.}} = p_{\text{rot.}} \\ \vec{0} & \text{for } p_{\text{bng.}} \neq p_{\text{rot.}} \end{cases} \quad (3.38)$$

The angle of drive excitation  $\phi_{\text{drv.}}$  may be chosen arbitrarily. In the case of PM drives, with negligible reluctant torque, it is usually fixed to  $\phi_{\text{drv.}} = \pi/2$  to maximize the torque per current and thus minimize copper losses for a given torque. This simplifies Eq. (3.37) into

$$T_z = k_T \cdot N_{\text{Turns}} \cdot i_{T,q} \quad (3.39)$$

with  $k_T$  the torque-current gain,  $N_{\text{Turns}}$  the number of turns of a coil, and  $i_{T,q}$  the quadrature-current of Field-Oriented Control (FOC).

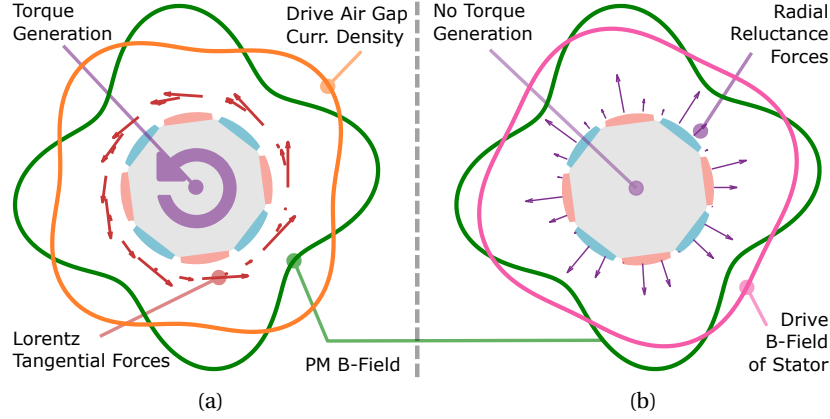


Figure 3.9: Electromagnetic torque generation upon a slotless drive with  $p_{\text{rot.}} = 4$  and  $p_{\text{drv.}} = 4$ . (a) Lorentz forces build up tangentially around the rotor and result in a net torque. (b) Reluctance forces, on the other hand, can only pull upon the rotor surface. They do not contribute to torque generation.

Figure 3.9 displays the role of Lorentz and reluctance forces upon torque generation. By choosing  $p_{\text{drv.}} = p_{\text{rot.}}$ , Lorentz forces pull tangentially upon the perimeter of the rotor. On the other hand, reluctance forces can only pull radially, and symmetrically, therefore producing no torque.

The magnitude of the forces and torques that can be generated is a function of the constructive and material parameters of the drive. With these parameters fixed, the magnitude and direction of the force and torque are determined by the magnitude of the current density inside the windings and its electric phase. With  $p_{\text{bng.}} = p_{\text{rot.}} + 1$ , the force generation is determined as

$$\vec{F}_{\text{rot.}} = \{k_{F,\text{rel.}} + k_{F,\text{Lor.}}\} \cdot \left( \frac{N_{\text{Turns}}}{\gamma_{\text{coil}} \bar{r}} \right) \hat{I}_1 \cdot \begin{pmatrix} \cos \phi_{\text{bng.}} \\ \sin \phi_{\text{bng.}} \end{pmatrix} = k_F \cdot N_{\text{Turns}} \cdot \begin{pmatrix} i_{Fx} \\ i_{Fy} \end{pmatrix}, \quad (3.40)$$

with  $\hat{I}_1$  the magnitude of the current of the bearing's fundamental harmonic,  $i_{Fx}$  and  $i_{Fy}$  its projections, and

$$\begin{aligned} k_{F,\text{rel.}} &= \left( \frac{\pi \hat{B}_r h_{\text{st.}}}{2} \right) \cdot \frac{r_{\text{st.,in}} k_{\text{J-B}}}{\mu_0}, \\ k_{F,\text{Lor.}} &= \left( \frac{\pi \hat{B}_r h_{\text{st.}}}{2} \right) \cdot \bar{r}. \end{aligned} \quad (3.41)$$

Indeed, the equations here presented enable determining the torque and force magnitude for a given magnetically-levitated drive. They offer insight into their parametric dependence, i.e. how active forces scale with  $r$  and torques with  $r^2$ , and how both fundamentally change with the axial length of the drive.

Nevertheless, these equations were obtained under the assumptions that stray fluxes do not contribute either to torque or force and that the coils are thin. Both of these *do not apply* to disc drives. They are deliberately conceived to have large quantities of stray fluxes for

the emergence of restoring effects, e.g. axial and tilting stiffnesses. Moreover, as shown in Chapter 4, the reduction of the stator's height —and its corresponding axial length— does not curb the torque and force generation linearly, indicating that stray fluxes *indeed* contribute to active forces. For these reasons, and to obtain accurate results, the force and torque generating capacity of the drives are promptly evaluated by 3D FE computational software.

#### 3.3.3 Spatial and Electric Distribution of Windings

For high-speed drives, it makes sense to reduce the number of pole pairs [20]. This in turn reduces the electric frequency of the drive, yielding smaller power losses for a given rotating mechanical speed. In this section, an exemplary motor with  $p_{\text{rot.}} = 1$ .

An electric drive with inner rotor and  $p_{\text{rot.}} = 1$  requires the simultaneous generation of  $p_{\text{drv.}} = 1$  and  $p_{\text{bng.}} = 2$  fields and excitations. These conditions can be met either with a *separate* set of coils, i.e. one set for the drive plus another for the bearing, or a set of combined windings [142], in which each coil contributes to torque and force. The first option simplifies control schemes, whereas the second reduces the number of coils and Joule losses. For the latter reasons, a combined coil system is preferred in this research.

Numerous phase and winding number combinations can propel disc drives towards high speeds [49, 112, 114, 151]. However, aiming to reduce construction complexity, a six-phase, six coil system is envisioned [140].

To achieve the number of electric poles  $p_{\text{bng.}} = 2$  required for the bearing with six coils, the currents must have a  $(4\pi \text{ radians})/(6 \text{ coils}) = 2\pi/3$  phase shift. The currents  $I_{\text{bng.,}k}$  must then have the form

$$I_{\text{bng.,}k} = \hat{I}_{\text{bng.}} \cos\left(\psi + \phi_{\text{bng.}} - \frac{2\pi}{3}(k-1) + \frac{\pi}{2}\right) \quad \text{with } k = 1, 2, \dots, 6, \quad (3.42)$$

with  $\hat{I}_{\text{bng.}}$  the bearing phase current. With the currents of a triphasic system of sub-index  $a, b, c$ , these currents  $I_{\text{bng.,}k}$  can be generated as

$$\begin{aligned} I_{\text{bng.,}a} &= I_{\text{bng.,}1} = I_{\text{bng.,}4} \\ I_{\text{bng.,}b} &= I_{\text{bng.,}2} = I_{\text{bng.,}5} \\ I_{\text{bng.,}c} &= I_{\text{bng.,}3} = I_{\text{bng.,}6} \end{aligned} \quad (3.43)$$

which means that the opposite coils can be connected in series and wired in the same direction.

Analogously, drive currents must have a  $\pi/3$  phase shift to complete the number of electric poles  $p_{\text{drv.}} = 1$  required for torque. Assuming  $\phi_{\text{drv.}} = \pi/2$ , currents  $I_{\text{drv.,}k}$  have the form

$$I_{\text{drv.,}k} = \hat{I}_{\text{drv.}} \cos\left(\psi + \pi - \frac{\pi}{3}(k-1)\right) \quad \text{with } k = 1, 2, \dots, 6, \quad (3.44)$$

with  $\hat{I}_{\text{drv.}}$  the drive phase current. Drive phase currents with subindexes  $r, s, t$  are obtained

from the three phases as

$$\begin{aligned} I_{\text{drv},r} &= I_{\text{drv},1} = -I_{\text{drv},4} \\ I_{\text{drv},s} &= I_{\text{drv},3} = -I_{\text{drv},6} \\ I_{\text{drv},t} &= I_{\text{drv},5} = -I_{\text{drv},2} \end{aligned} \quad (3.45)$$

so opposite coils are to be connected in series *but* wound in opposite direction.

Having defined the currents, it is noteworthy to point out that

$$\begin{aligned} I_{\text{bng},a} + I_{\text{bng},b} + I_{\text{bng},c} &= 0, \\ I_{\text{drv},r} + I_{\text{drv},s} + I_{\text{drv},t} &= 0, \end{aligned} \quad (3.46)$$

meaning that the current triads can compose three-phase systems with a star point. Notably, the drive and bearing currents can even be *superposed* and powered by two three-phase modules. These modules are commercially available and can be piloted with ready-for-use computational software packages. By taking advantage of the two three-phase modules, the torque and force control may be distributed upon the two, star-point three-phase systems as

$$\begin{aligned} I_1 &= I_{\text{bng},a} + I_{\text{drv},r} & I_4 &= I_{\text{bng},a} - I_{\text{drv},r} \\ I_3 &= I_{\text{bng},c} + I_{\text{drv},s} & I_6 &= I_{\text{bng},c} - I_{\text{drv},s} \\ I_5 &= I_{\text{bng},b} + I_{\text{drv},t} & I_2 &= I_{\text{bng},b} - I_{\text{drv},t} \end{aligned} \quad (3.47)$$

with currents  $I_{1,3,5}$  and  $I_{2,4,6}$  composing the different three-phase systems.

The output of the control laws is linked to the aforementioned phase currents by the *dq transform* [127]. This is addressed in Chapter 6.

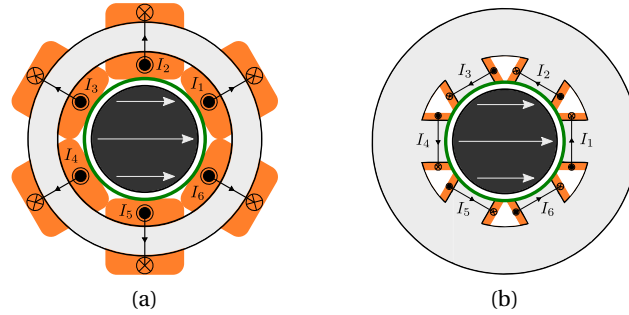


Figure 3.10: Coil distribution of the (a) slotless and (b) slotted motor. Force and torque commands can be superposed as in Eq. (3.47).

### 3.4 Power Losses

High-speed electric drives are usually small, so the surface that can dissipate heat is also limited [20]. The minimization of losses is thus a fundamental objective in electric motor design since it leads to better exploitation of energy and is therefore crucial if battery-powered applications are within scope. Lower operation temperatures—due to less losses—also leads

to predictable and long lifespans.

The sum of estimated power losses is defined as

$$P_{\text{losses}} = P_{\text{Joule}} + P_{\text{Cu,Ed.}} + P_{\text{Fe,Ed}} + P_{\text{Rot.,Ed.}} + P_{\text{Fe,H}}, \quad (3.48)$$

and its components are explained followingly.

### 3.4.1 Joule losses

Joule losses  $P_{\text{Joule}}$  arise in non-null resistivity conductors with a flowing current. For  $N_{\text{coils}}$  coils, these are calculated as

$$\begin{aligned} P_{\text{Joule}} &= N_{\text{coils}} \cdot R_{\text{coil}} \cdot I_{\text{RMS}}^2 \\ &= N_{\text{coils}} \cdot \left( \rho_{\text{Cu.}} \cdot \frac{\bar{l}_{\text{wdg.}}}{A_{\text{coil}} \cdot k_{\text{Cu.}}} \right) \cdot I_{\text{RMS}}^2, \end{aligned} \quad (3.49)$$

with  $\rho_{\text{Cu.}}$ ,  $\bar{l}_{\text{wdg.}}$ ,  $A_{\text{coil}}$ ,  $I_{\text{RMS}}$ ,  $k_{\text{Cu.}}$  the resistivity of the (copper) conductor at a given temperature (equal to 16.8 nΩ·m for copper at 20 °C) and the mean length and the cross-section of the coil in current flow direction, the RMS current and winding filling factor, respectively.

### 3.4.2 Eddy-current losses

Eddy-currents (ECs) are current loops that arise inside electric conductors when these are in the presence of a changing magnetic field. The currents within the conductor flow generating a magnetic field opposing the source as well as Joule losses. This phenomenon, caused by a rotating magnet is displayed in Fig. 3.11.

EC effects invariably emerge in electric drives. Components such as copper conductors, magnets as well as stator materials are inherent electric conductors, and are penetrated by

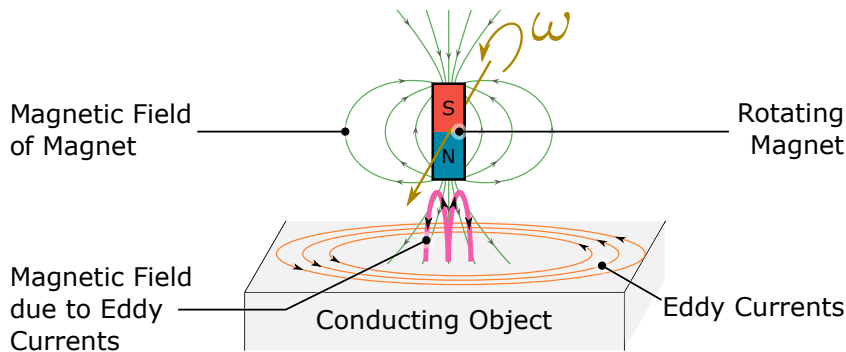


Figure 3.11: EC effect generated by a rotating magnet upon a conductive material. The currents on the latter give way to a magnetic field opposing that of the source.

magnetic fields. The EC losses are thus divided according to where they originate inside the drive.

### In the Windings

The conductive windings of both slotted and slotless stators are penetrated (to a different extent) by the rotating magnetic flux of the rotor. These generate EC losses in the windings  $P_{\text{Cu,Ed}}$ . [20, 69].

These losses are larger in the slotless case because the airgap field *fundamentally* pierces the windings to enter the high permeability stator as shown in Fig. 3.12a. In the slotted case, the flux is *mainly* funneled into the high-permeability iron slots. Still, given their straight-pole form, a non-neglectable portion passes by and pierces the windings, as it can be seen in Fig. 3.12b.

The general derivation [20] of EC losses in windings has been applied [72] and observed [69] in straight slot motors. For slotless motors,  $\hat{B}_{\text{RMS,slotless}}$  is calculated toroidally in the surface around the stator [164], as depicted in Fig. 3.12a; in the slotted,  $\hat{B}_{\text{RMS,slotted}}$  can be analogously calculated in the volume encompassing the slot, as shown in Fig. 3.12b. All in all, this is calculated as

$$\begin{aligned}\hat{B}_{\text{RMS,slotless}} &= \sqrt{\frac{1}{A_{\times \text{sec}}} \cdot \int_{A_{\times \text{sec}}} (B_x^2 + B_y^2 + B_z^2) dA} \\ \hat{B}_{\text{RMS,slotted}} &= \sqrt{\frac{1}{V_{\text{coil}}} \cdot \int_{V_{\text{coil}}} (B_x^2 + B_y^2 + B_z^2) dV}\end{aligned}\quad (3.50)$$

with  $B_i$  the  $i$  component of magnetic flux density,  $A_{\times \text{sec}}$  the cross-section of a toroidal winding of a slotless motor, and  $V_{\text{coil}}$  the volume of the concentric coil of the slotted motor. For the latter,  $\hat{B}_{\text{RMS,slotted}}$  is calculated when the rotor pole is directly facing the winding or tooth, see Fig. 3.12b.

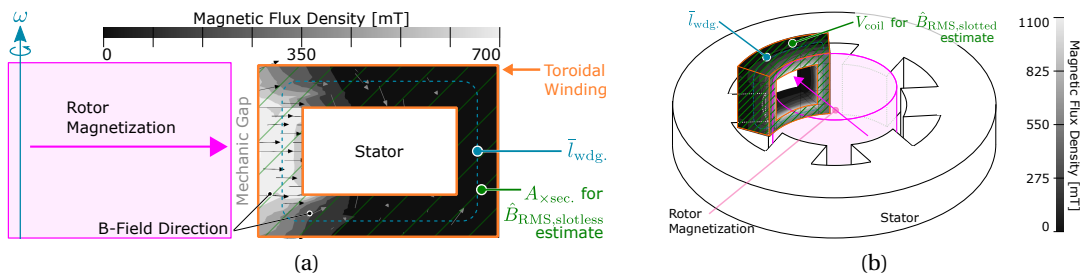


Figure 3.12: (a) The PM's magnetic field pierces the windings of slotless stator topologies directly, generating EC losses in them. (b) On the other hand, in the slotted topology, most of the magnetic field of the PM enters the slot directly. Yet, some leaks and first passes by the windings, also generating EC losses.



Aided by 3D FE simulations, Eq. (3.50) estimates that, given a motor size,  $\hat{B}_{\text{RMS}}$  values of the slotted motor are on average 2.5 times larger in comparison to slotless motors simulated in Chapter 4. Using these values, ECs losses in windings are calculated as in [164] as

$$P_{\text{Cu,Ed.}} = \frac{\pi^3}{32\rho_{\text{Cu}}} \cdot N_{\text{Turns}} N_{\text{coils}} d_{\text{wire}}^4 f_{\text{el}}^2 \bar{l}_{\text{wdg.}} \cdot (\hat{B}_{\text{RMS}})^2, \quad (3.51)$$

with  $d_{\text{wire}}$  the wire gauge,  $f_{\text{el}}$  the electric speed of the drive, and  $\bar{l}_{\text{wdg.}}$  the mean winding length of the coil as shown in Fig. 3.12.

Given this formula, the quadratic relation between electrical speed  $f_{\text{el}}$  and the magnitude of the losses  $P_{\text{Cu,Ed.}}$  can be seen. For high-speed drives, it is thus important to cap these losses by choosing a thin coil thickness  $d_{\text{wire}}$ , given its power of 4. To this end, litz wire, composed of multiple small strands to reduce  $d_{\text{wire}}$ , is usually used for high-speed drives, at the cost of higher Joule losses due to its reduced copper filling factor  $k_{\text{Cu.}}$

#### In the PM Rotor

The rare-earth material of the rotor of the drive is intrinsically conductive. As such, losses may develop due to magnetic fields generated by the coils or due to the changing reluctance of a slotted stator. Even though these losses are small, they might be critical, as they are not easy to dissipate to the environment [67]. This can be decisive for magnetically-levitated drives, as there are no heat conduction mechanisms to get rid of these losses, and because rare-earth materials and their magnetization are temperature sensitive.

In principle, the magnetic reluctance between the inner surface of the slotless stator and its centered rotor is constant. If a sinusoidal current excitation is employed, a spinning rotor sees a *static* magnetic field that precedes the rotatory motion, so these losses become negligible. The drives conceived in this thesis employ this excitation scheme, so only asynchronous bearing currents might be of concern.

If the current were to be block commuted, the magnetic field would rotate asynchronously

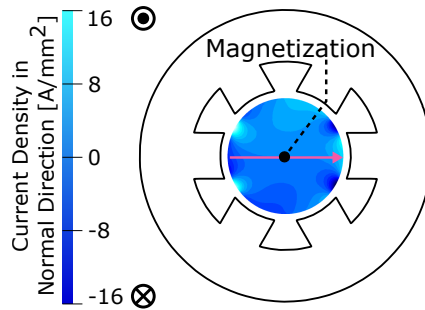


Figure 3.13: Simulated current density inside the rotating rotor of slotted drive, due to the EC effect. The rotor is conductive, so this effect leads to power losses in the drive. These losses are of considerable quantity in slotted drives.

with the rotor. Higher-order harmonics would then induce ECs in the surface of the rotor [13].

On the other hand, the stepwise high magnetic permeability of stator teeth generates high-order harmonics of magnetic flux inside the airgap [13]. They induce currents and therefore losses  $P_{\text{Rot.,Ed.}}$  in the PM rotor, as this is conductive.

Given the complexity of an analytical calculation, rotor losses are directly estimated by 2D FE transient simulations. The PM spins with no coil excitation until its losses converge in time.

Simulations estimate a current density inside the rotor; an example is displayed in Fig. 3.13. These can then be transformed into effective power losses, knowing the electric resistivity of rare-earth NdFeB  $\rho_{\text{PM}} = 1400 \text{ n}\Omega \cdot \text{m}$ . 2D simulations calculate losses for a default axial length of 1 mm height, so the estimated losses are multiplied by rotor height in mm.

### In the Stator Iron

Available high-permeability magnetic materials are also intrinsic electric conductors. A magnetic excitation generates ECs, leading to further losses  $P_{\text{Fe,Ed.}}$  inside them. The materials are produced in sheets to increase the electrical resistance of the material and constrain current circulation, as depicted in Fig. 3.14. The sheets are then stamped and glued together to form a solid material.

EC losses in the stator can be quantified [12] as

$$P_{\text{Fe,Ed}} = \int_{V_{\text{Fe}}} \rho_{\text{Fe}} c_{\text{Ed}} f_{\text{elec}}^2 \cdot \sum_i \left( i^2 \cdot \hat{B}_i^{\beta_{\text{Ed}}} \right) \cdot dV, \quad (3.52)$$

where  $\rho_{\text{Fe}}$ ,  $c_{\text{Ed}}$ ,  $\beta_{\text{Ed}}$ ,  $\hat{B}_i$ ,  $i$  are the volumetric density of the material, material parameters, and the magnetic flux density amplitude of the  $i$ -th harmonic, respectively. The magnetic flux density amplitude and its harmonic distribution in the stator are obtained by 3D FE simulations, as exemplarily shown in Fig. 3.15.

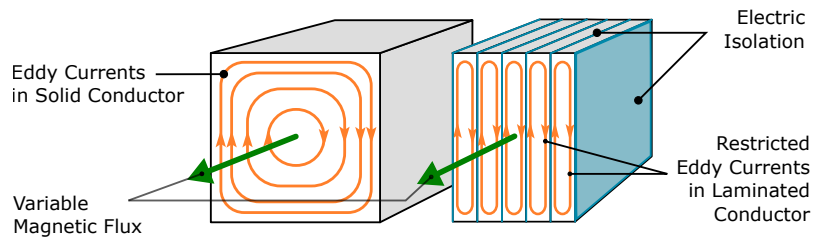


Figure 3.14: The ferromagnetic material of electric drives is usually laminated. In this way, the ECs, generated due to the changing magnetic fields, can be constrained; thus capping power losses.

### 3.4.3 Hysteresis losses

Hysteresis losses  $P_{\text{Fe,H}}$  arise in ferromagnetic materials because of the non-linear BH curve characteristics. They thus usually originate inside the stator of an electric drive and can be quantified as [88]

$$P_{\text{Fe,H}} = \int_{V_{\text{Fe}}} \rho_{\text{Fe}} c_{\text{Hy}} f_{\text{elec}} \hat{B}^{\beta_{\text{Hy}}} dV, \quad (3.53)$$

with  $c_{\text{Hy}}$ ,  $\beta_{\text{Hy}}$ ,  $\hat{B}$ , datasheet material parameters and the peak flux density, respectively.

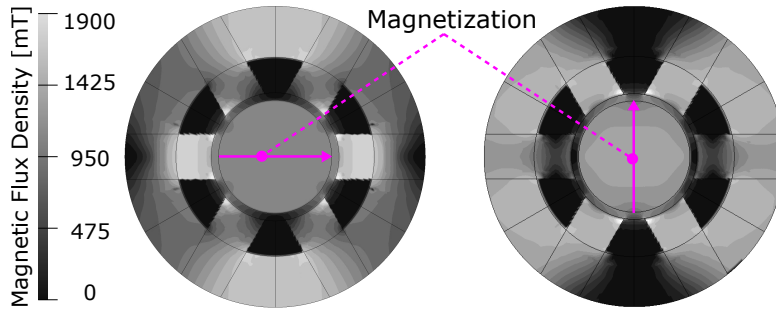


Figure 3.15: The magnetic flux density distribution in the drive mainly depends on the rotor angle. The changing field then causes hysteresis and EC losses in the stator.

The parameters for the eddy-current and hysteresis loss calculations within the amorphous iron material *Metglas* employed in this thesis are calculated in the Annex, Section A.

### 3.4.4 Current ripple losses

The presented drives are meant to be energized by voltage-source inverters (VSIs) with a Pulse Width Modulation (PWM) scheme for current control. Such a voltage modulation scheme intrinsically leads to current ripple upon the inductors. Their high-frequency flux ripple induces additional EC losses in the conductive rotor and stator, as this ripple is asynchronous to them. Skin and proximity-effect losses can also be measured in the windings.

The magnetic flux density of a drive's stator depicts a major hysteresis loop which is mainly determined by the position of the PM rotor and the fundamental harmonic of the current excitation. The high-frequency current-ripple of PWM switching frequency  $f_{\text{PWM}}$ —describing a minor loop- is superposed on this. Their superposition can be modelled as a DC bias of the former plus an AC component of the latter [34] since the current ripple is usually orders of magnitude faster than the rotor's electric frequency.

The losses inside the PWM-excited ferromagnetic material are proportional to the area of the minor loop at a determined DC-bias field. The current-ripple decreases linearly with  $f_{\text{PWM}}$ , so current-ripple losses decrease quadratically with  $f_{\text{PWM}}$  [185]. Within this regard, it has been experimentally verified that augmenting  $f_{\text{PWM}}$  makes the total stator losses increasingly resem-

ble those that can be estimated at low-frequency [34], i.e. considering no ripple. Increasing  $f_{\text{PWM}}$  ultimately *shifts* the losses from the actuator to the semiconductors.

Alternatively, the current ripple and its losses can be reduced by having low DC-link voltages  $U_{\text{DC}}$ . Since a portable, battery-powered ventilation system is foreseen (with  $U_{\text{DC}}$  in the  $10^0$  V range), this condition applies to the drives conceived in this thesis.

Nevertheless, for the sake of system flexibility, actuators are not always paired to specifically-designed power electronics. Thus, the switching capabilities of their semi-conductors and their admissible losses are *unknown* before the design phase. The current-ripple losses of a stator can nonetheless be diminished already at the design stage if the stator is sized to be biased *below* its knee region [34]. Such design choice reduces the area of the minor loops, along with its losses. The later chapter on the conceptualization of disc drives takes notice of this recommendation.

The conductive rotor is also affected by the high-frequency current ripple. As with the stator, higher  $f_{\text{PWM}}$  and lower  $U_{\text{DC}}$  values diminish the losses [185]. The bandaging of the rotor with conductive but non-ferromagnetic materials contributes to the increase in these losses given their deeper skin depths [13]. It is better to avoid bandaging if low rotor losses are important.

Otherwise, current-ripple-induced rotor losses have been commonly estimated via 3D transient FE simulations, which prove accurate compared to *a posteriori* experimental results if motor waveforms are available and fed into the FE simulation [192]. Such an approach requires once again the characterization of the drive's power electronics. Moreover, the time-consuming computational simulations are not suitable for a large parametrical study of motor variants, especially if these rotor losses are ultimately low for small drives [42].

The current-ripple effect also produces losses inside the windings, due to the skin and proximity-effect. As with other current-ripple-causes losses, lower  $U_{\text{DC}}$  and  $f_{\text{PWM}}$  values reduce these losses. Moreover, reducing the diameter of the conductors or using litz wire shows makes the AC resistance of the windings to converge its DC resistance [155].

All in all, the drive losses due to current-ripple are highly dependent on the interaction between the drive and its power electronics; the latter not being the focus of this thesis. The magnitude of these losses can be estimated with the aid of finely-meshed 3D FE simulations if precise information on the current waveform and experimental material characterization are available. The estimation of current-ripple losses is highly elaborated and time-expensive for the first design phase of an electric motor. Nonetheless, design guidelines proposed by the cited literature to decrease the influence of current-ripple losses are adopted. A summary of these can be found in Table 3.1.

Table 3.1: Approaches for the reduction of current-ripple losses.

Location	General Approach	Specific Approach
Stator	Reduction of $U_{DC}$ Increase of $f_{PWM}$	Bias below the knee of $B$ - $H$ curve
Rotor		No bandaging
Coils		Reduction of wire gauge, litz wire

## 3.5 Conclusion

In this chapter, the electromagnetic foundations that dictate the operation of magnetic levitation are presented. The principles that provoke the motion of magnets, coils, and ferromagnetic materials are overviewed. Moreover, the laws that determine how power losses are lost on the functioning of a rotatory drive are described.

The theories introduced here provide the basis to understand how the bearing and drive performance, as well as power losses, depend upon varied motor parameters. The geometry of a disc drive can be adapted to boost the performance of the drive or to match it to the specific requirements of an actuator system.

## 4 Conceptualization of Compact Disc Drives

### 4.1 Introduction

In this chapter, the performance of different topologies of bearingless drives is evaluated. Focusing on drives with small rotors, it is investigated how specific performance aspects can be adapted as a function of constructional parameters of the drive, and how its overall performance can be enhanced.

In this regard, the advantages and disadvantages of four different electric motor topologies are discussed in terms of their performance for small sizes and a given application. This assessment revolves around their performance as rotatory drives and the stability and feasibility of their contactless magnetic bearings. Moreover, practical aspects such as their miniaturization potential and their corresponding challenges are addressed. The most suitable electric drive types are narrowed down based on these considerations.

Nevertheless, the exact electromechanical requirements of a system are often incomplete. Therefore, it might not be possible to ponder the exact dimensions of the rotor, and if there are hard constraints to be met.

This thesis provides a framework to tackle this uncertainty. In this regard, a *parametric study* of the performance of bearingless as a function of their geometry is undertaken. Such an approach provides an overview of the performance that can be obtained for a given range of motor dimensions, defined inside a *design space*.

This investigation focuses on electromechanical torque, bearing load capabilities, and power losses, with the aid of computational 3D FE simulations. The single effects of the design parameters are analyzed. At the same time, it is emphasized how desired drive and bearing performances trade off.

The complete characterization of the drive variants within the design space offers a synoptic view of the attainable performances. If additional requirements on the system become available, constraints can be imposed upon the resulting drives, to further reduce the number of

candidates. Ultimately, a weighted pondering of the performance indicators within the design space then provides the *optimal* motors for different rotor dimensions and stator topologies. The advantages and disadvantages of different drive dimensions to meet a scenario constrained by inequalities are discussed.

## 4.2 Comparison of Drives with Interior and Exterior Rotor

### 4.2.1 Implementation of Axial Ventilator

The ventilators needed for the cooling of the suit of Fig. 2.9 can be drive in various ways. In principle, two design considerations must be pondered: if the motor drives the *propeller* at its

- hub or
- rim,

and if the *rotor* radially lies

- inside or
- outside

of the stator. For a *given diameter* of the axial impeller, these design choices impact the diameter of the rotor and stator. They are displayed and compared in Fig. 4.1.

For a given axial ventilator diameter, the hub rotors of Fig. 4.1a and Fig. 4.1b are smaller than their rim counterparts of Fig. 4.1c-4.1d. The reduced drive volume leads to lower material

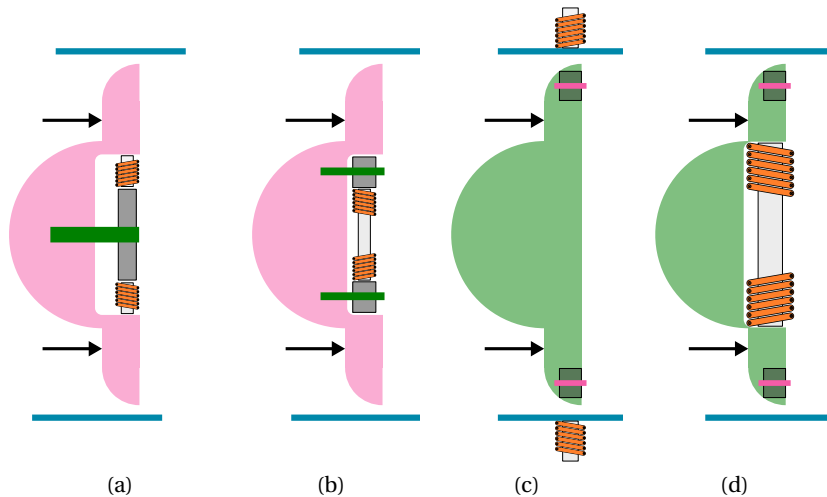


Figure 4.1: The bearingless disc drives may be coupled in different fashions with the impeller of the axial ventilator. The impeller may be driven at its hub—at a diameter in which blades no blades are present—by an (a) interior and (b) exterior rotor construction. Analogously, the impeller may be driven at its rim—or outer radius—by an (c) interior and (d) exterior rotor construction.

## 4.2 Comparison of Drives with Interior and Exterior Rotor

costs, and their smaller diameter is suited for higher speeds [203]. Yet smaller diameter render their manufacturing tolerances and assembly—inside a limited volume—increasingly challenging [19]. Furthermore, a decreasing drive radius—which reduces torque generation capacity—rapidly curtails the load capability of the bearing [165], as expressed in Table 4.1.

The outer rotor drives of Fig. 4.1b and Fig. 4.1d naturally comply with the construction of an axial ventilator. The stator of the drive is completely integrated into the hub of the impeller, whereas the rotor grasps either the hub or the impeller. The hub drive with the external rotor of Fig. 4.1b requires fewer materials due to its reduced radius, but more precise manufacturing, whereas its rim drive counterpart of Fig. 4.1d exploits the available space *inside* an axial impeller more naturally and compactly.

The inner rotor drives of Fig. 4.1a and Fig. 4.1c offer opposing degrees of compactness. The stator of the rim drive of Fig. 4.1c must be placed *outside* the conducting duct. This variant needs the largest stator, which sits *outside* the ventilation duct. This may be beneficial since *only* a ring rotor has to be fitted at the rim of the impeller, and no stator has to be fitted and energized *inside* the hub of the impeller. Such a configuration makes the system integration easier, as the duct naturally separates the stator from the rotor, and the latter must be built into the impeller. On the other hand, the radial compactness of the inner rotor hub drive of Fig. 4.1a translates into a reduction of achievable torque [20] and bearing stability [152], as seen in Table 4.1.

For a given hub or rim-propelled ventilator, exterior and interior rotor constructions provide different performances in terms of drive and bearing capabilities. Exterior rotor configurations must be multipolar for a good drive and bearing controllability [146], so their higher electric speeds yield higher power losses. Nonetheless, one pole-pair rotor configurations yield weak passive stiffnesses in directions perpendicular to their magnetic poles, i.e. anisotropic stiffnesses. These hinder the stability of motor operation. Within the scope of bearing stability,

Table 4.1: Scaling of drive and bearing performance [20, 165] for magnetically-levitated disc drives as a function of rotor radius  $r$ .

Rating	Symbol	Units	Proportionality
<i>Active Properties</i>			
Force gain	$k_F$	$[\text{N} \cdot \text{A}^{-1}]$	$r$
Torque gain	$k_T$	$[\text{Nm} \cdot \text{A}^{-1}]$	$r^2$
Mech. Power	$P_{\text{mech.}}$	$[\text{W}]$	$r^3$
<i>Passive Properties</i>			
Linear stiffnesses	$k_x, k_y, k_z$	$[\text{N} \cdot \text{m}^{-1}]$	$r$
Angular stiffnesses	$k_\alpha, k_\beta$	$[\text{Nm} \cdot \text{deg}^{-1}]$	$r^3$
<i>Power Losses</i>			
Losses in Windings	$P_{\text{Joule}}, P_{\text{Cu,Ed.}}$	$[\text{W}]$	$r^3$
Stator Losses	$P_{\text{Fe,Ed}}, P_{\text{Fe,H}}$		



## Chapter 4. Conceptualization of Compact Disc Drives

multipolar exterior rotors are desired, as they allow for smoother passive stiffnesses without weak directions [110]. Yet, their larger power losses at a given mechanical frequency limit their miniaturization potential due to possible temperature surges.

Table 4.2 summarizes the comparison of the discussed advantages and disadvantages of the drive-impeller coupling and exterior and interior rotor selection. For the foreseen ventilator dimensions of  $d_{\text{imp.}} = 20$  mm, the hub rotors are deemed as infeasible. They provide small torques and feeble bearing load capacity. The latter reason would be particularly critical, as either the radial active bearing or axial passive force must sustain the weight of the impeller when the ventilator is oriented horizontally or vertically, respectively.

This being said, the drives with *rim-mounted rotors* of Figs. 4.1c-4.1d are analyzed as possible candidates for the implementation of the high-speed magnetically-levitated drive in the following sections. Their performance as bearingless drive is quantified, and the easiness of construction and potential for low-cost manufacturing are debated.

Table 4.2: Qualitative comparison of motor-ventilator assembly possibilities of Fig. 4.1, with (+) is a good performance, (✓) an average performance, and (-) a rather weak performance.

Impeller-Rotor coupling Rotor Construction	Hub		Rim	
	Inner	Exterior	Inner	Exterior
Compactness	+	+	-	✓
Flexibility of assembly	-	-	+	✓
Bearing load capability	-	✓	✓	+
High-speed capability	✓	-	+	-
Overall	-	✓	+	+

### 4.2.2 Solution Portfolio

The implementation of the ventilator variants of Figs. 4.1c-4.1d —with an interior and exterior rotor, respectively— impose different constraints upon the distribution of PM, copper, and iron material in the available space.

The realization of the ventilator with an interior rotor configuration provides more design freedom, as only the rotor has to be integrated into an impeller. Provided there is no physical constraint *outside* of the ventilation duct, the geometry of the stator, such as air gap length  $\delta_{\text{air gap}}$  and copper thickness  $\delta_{\text{Cu}}$ , may be chosen freely.

On the other hand, the outlining of the ventilator with an exterior rotor proves more challenging. For a given impeller diameter  $d_{\text{imp}}$ , the stator of the drive must lay *inside* of the impeller hub, thus limiting the volume of stator iron and copper to be used. The volume of the stator iron is determined so that there is no saturation in the magnetic circuit of the drive, and the remaining volume can be filled with copper.

The considered drive variants may be implemented with a slotted or slotless stator. For slotted prototypes, conventional radial concentric coils are considered, whereas the slotless prototypes have toroidal coils, which are wound *around* the stator yoke. Such winding shape leads to shorter wires for low pole-pair rotor numbers —that require a large angular pitch between coils— and thin stator yokes than the classical air gap winding [110].

For the considered small motors, the available cross-section for copper is thus limited. For a fixed current density, this means that the reduced copper-cross sections of the exterior rotor drive admits feeble magnetomotive forces in terms of Ampere-Turns than those of the interior rotor drive. This adversely affects the active force and torque generation of the exterior rotor configuration for the proposed sizes.

3D FE simulations are performed to quantify and compare the passive and active characteristics that the four variants of Fig. 4.2 can offer. Their radial stiffnesses parallel and perpendicular to their magnetization directions,  $k_x$ , and  $k_y$ , respectively, as well as their tilting around these directions  $k_\alpha$  and  $k_\beta$  are evaluated, along their axial stiffness  $k_z$ . From the active point of view, the peak force  $F_{\text{act}}$  and torque  $T_z$  at a given current density is evaluated.

To make the comparison equivalent in terms of ventilator realization, the outer radii of the rotors are fixed at  $d_{\text{rot}}^* = 20$  mm, as well as the height of the rotor and stator as  $h_{\text{rot}}^* = h_{\text{st}}^* = 4$  mm. To render the comparison fair, the volume of PM  $V_{\text{PM}}^*$  is practically the same for all topologies.

This preliminary investigation *does not* intend to maximize the performance of every single drive. Its objective is to provide an overview of the comparative advantages and disadvantages of the considered topologies —in terms of drive and bearing ratings— that are obtained for fixed rotor diameter  $d_{\text{rot}}^*$  and PM volume  $V_{\text{PM}}^*$ .

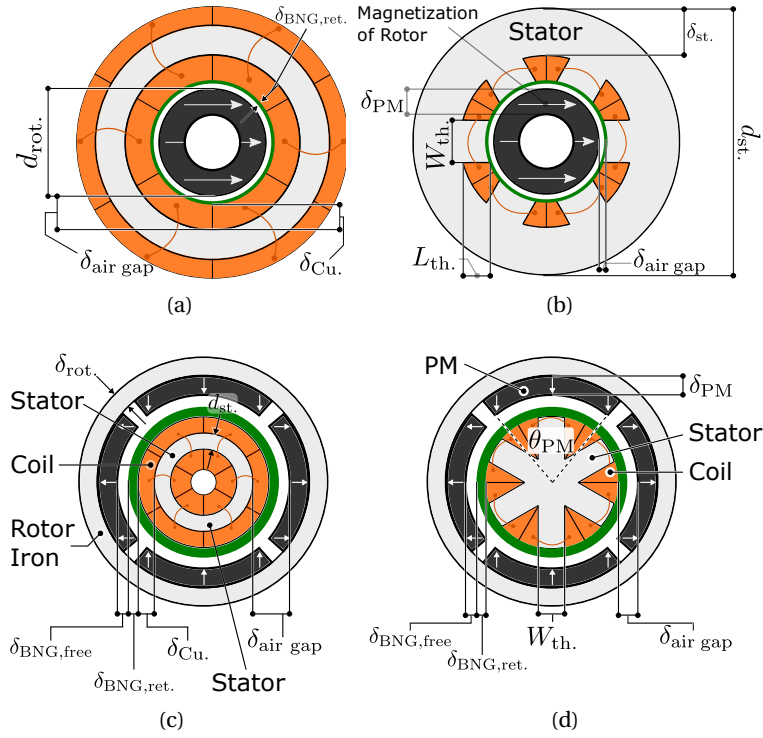


Figure 4.2: The rim-propelled axial fan of Fig. 4.1c can be driven by an interior rotor configuration with (a) slotless or (b) slotted stator. Analogously, the ventilator of Fig. 4.1d can be drive by an exterior rotor configuration with (c) slotless and (d) slotted stator. Not to scale.

Table 4.3: Geometric parameters and materials of the motors of Fig. 4.2. The dimensions have been chosen by fixing  $d_{rot.}$  for the ventilation system, fixing a comparable  $V_{PM}^*$  and then dimensioning the iron yokes to avoid saturation. All dimensions in [mm] unless otherwise noted.

Motor Part (Material)	Definition	Symbol	Interior		Exterior	
			Slotless	Slotted	Slotless	Slotted
Rotor (PM : NdFeB42H [46]) (Iron: M235-35A [39])	Outer diameter	$d_{rot.}$			20	
	Height	$h_{rot.}$			2	
	PM thickness	$\delta_{PM}$	1		1.5	
	PM volume	$V_{PM}^*$ [mm <sup>3</sup> ]	239		240	
	Iron yoke thickness	$\delta_{rot.}$	—		2.5	
	PM angle [deg]	$\theta_{PM}$	—		85	
Air gap	Magnetic air gap	$\delta_{air\ gap}$			2	
	Mech. clearance	$\delta_{bng,free}$			0.5	
	Bearing retainer	$\delta_{bng,ret.}$			0.5	
Copper	Thickness	$\delta_{Cu.}$	1	—	1	—
	Filling factor [ ]	$k_{Cu.}$			0.4	
	Cross section [mm <sup>2</sup> ]	$A_{coil} \cdot k_{Cu.}$	4.8	4.9	1.9	2.4
Stator (Metglas [106])	Height	$h_{st.}$			2	
	Outer diameter	$d_{st.}$	29	30.2	8	8
	Yoke thickness	$\delta_{st.}$	2.5	2	2	—
	Tooth width	$W_{th.}$	—	2	—	1.75
	Tooth length	$L_{th.}$	—	1.1	—	2.25

### 4.2.3 Electromagnetic Performance Analysis for Same Impeller Diameter

The performance of the drives of Fig. 4.3 is rated in terms of destabilizing stiffnesses, stabilizing stiffnesses, and active properties. These are depicted in Figs. 4.4, 4.5, and Fig. 4.6, respectively. The simulated magnetic flux densities displayed in Fig. 4.3 give insight into the performance of the different motors.

Figure 4.4 shows the radial stiffnesses of the configurations, which must be overcome by the active bearing control. Given the same rotor configuration and same air gap length  $\delta_{\text{air gap}}$ , slotted drives yield lower radial forces—for  $k_x$  and  $k_y$  axes—which is desired from the controllability point of view. The stiffnesses as a function of  $\delta_{\text{air gap}}$  is more thoroughly revised in Subsection 4.4.

On the other hand, exterior rotor configurations provide stronger radial stiffnesses. This is due to their larger air gap magnetic flux density, which can be traced back to the iron yoke of the rotor. This ferromagnetic ring helps to keep the four-magnet rotor together and helps in reducing the magnetic reluctance between these and the stator. By doing so, it intensifies the magnitude of the magnetic flux density in the air gap, thus leading to a stronger radial pull. Stark radial stiffness is unwanted as it requires for high-current start-up procedures.

Figure 4.5 shows the passive restoring characteristics—with their corresponding negative sign— of the electric drives. The higher magnetic flux density of the exterior rotors of

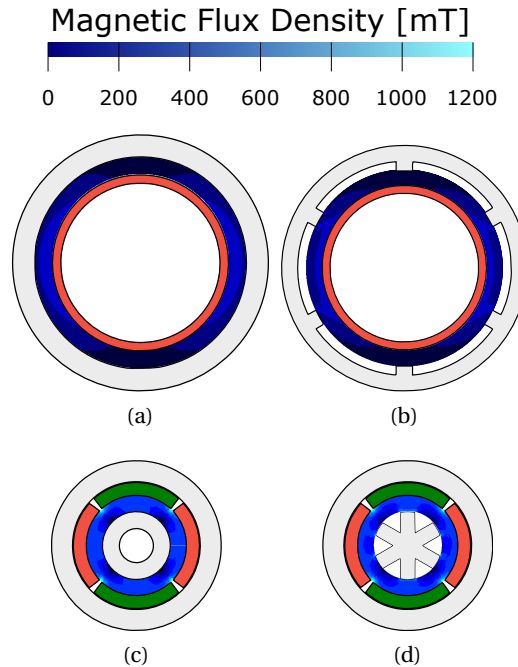


Figure 4.3: Magnetic flux density in the air gap of the interior rotor and (a) slotless and (b) slotted stator, and with exterior rotor and (c) slotless and (d) slotted stator. Geometric proportions are maintained.

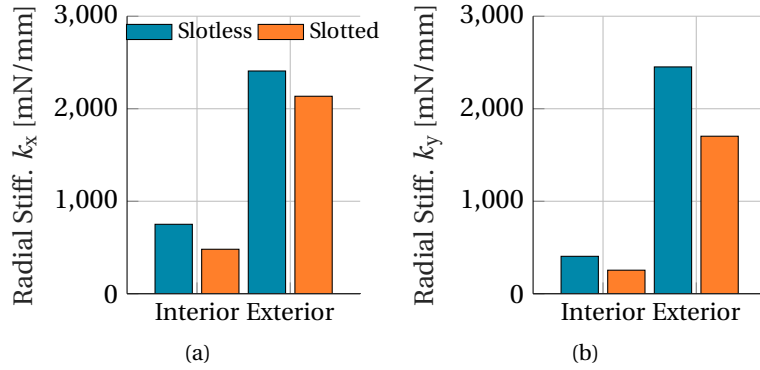


Figure 4.4: Destabilizing radial stiffnesses of the drive of the solution portfolio (a) parallel and (b) perpendicular to the magnetization direction of the rotor.

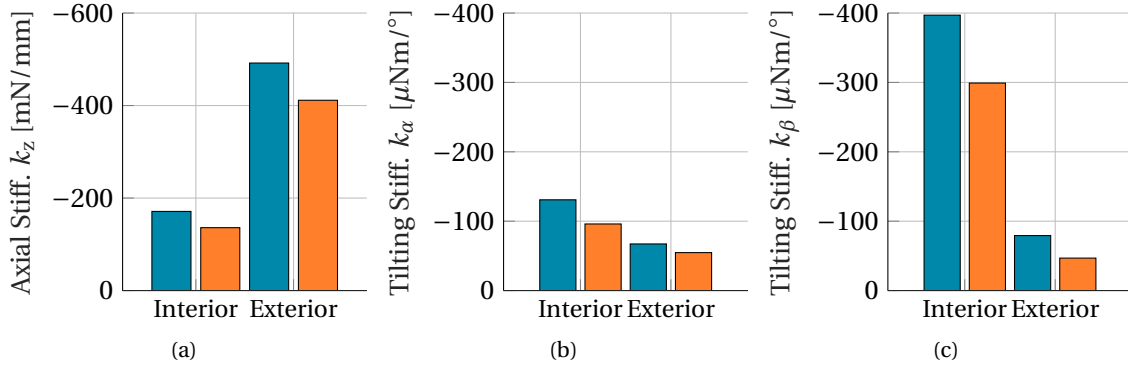


Figure 4.5: Stabilizing (a) axial stiffness and tilting stiffnesses around the (b) parallel and (c) perpendicular magnetization direction of the rotor.

Figs. 4.3c-4.3d results in the stronger restoring axial pull of Fig. 4.5a, which is preferable. Yet, the stronger magnetic flux density does not translate into an advantage for the tilting stiffnesses, as can be seen in Figs. 4.5b-4.5c.

The weaker tilting stiffnesses of the exterior rotor drives is due to their reduced overall size, as indicated by Table 4.1. This restoring torque is a product of the reluctant axial forces at the outer edge of the stator, its lever, and the displacement at the edge of the rotor. The last two quantities are larger for the interior rotor drives, so they outperform their outer rotor counterparts, despite their weaker restoring axial force and air gap magnetic flux density.

Nevertheless, the one pole-pair rotors render uneven tilting stiffnesses concerning the magnetization axis of the interior rotor configurations. The stiffness of the weak tilting axis of Fig. 4.5b is comparable for all motors. Therefore, it cannot be said that the interior rotor drives are superior with regards to tilting. The more-isotropic tilting stiffnesses of exterior rotor configurations is preferable.

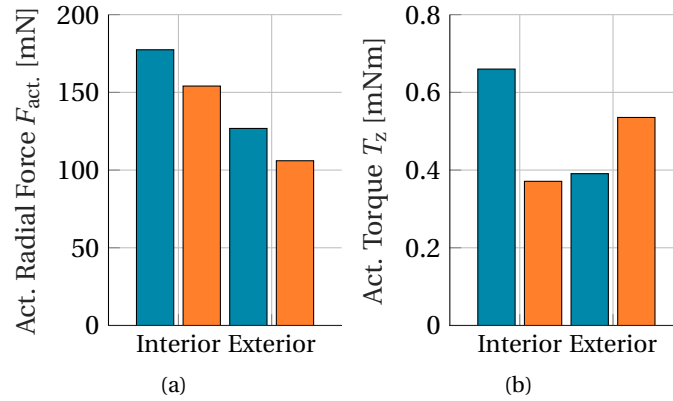


Figure 4.6: Actively generated (a) torque and (b) force at a current density of  $J = 4.2 \text{ A}_{\text{RMS}} \cdot \text{mm}^{-2}$ .

The active performance of the drives is similar in terms of magnitude, as shown in Fig. 4.6. In this context, the interior rotor slotless drives outperform their slotted counterparts. This observation holds no universal validity, as the active properties of the latter can be enhanced by adding more copper in the motor by increasing the teeth length  $L_{th.}$ , as seen hereafter.

The active radial forces of the exterior rotor drives are lower than those of the inner rotor drives, despite its stronger air gap flux densities. This is explained by their reduced available copper cross-section. The feebler active force of the investigated exterior rotor drives, along with their stronger radial pull of Figs. 4.4a-4.4b derive to substantially larger bearing start-up currents.

### 4.2.4 Practical Considerations of Drive Realization

The costs of a drive must be matched to its targeted requirements and final application. For the studied dimensions, exterior rotor drives require less material—and in principle cheaper in material costs—given their smaller overall radius. Still, the assembly of a drive has a considerable impact on the cost of a technological solution, especially for small geometries.

From the point of view of the stator assembly, the concentric coils of the slotted configurations can be externally wound and then slid onto the motor teeth. On the other hand, the toroidal coils of the slotless stators are wound around the stator yoke. This process can be regarded as more complex than the concentric coil insertion for slotted stators.

Alternatively, the coils can also be wounded externally, and then slid into the segmented slotless stator. This process might prove particularly challenging by the slotless stator of the exterior rotor drive, given its small dimensions.

On the other hand, the rotors of exterior and interior stator topology differ. The PM of the interior rotor configuration is just a ring, which can prove fragile given its rare-earth material

and limited thickness. The iron of the exterior rotor offers a distinctly higher shock resistance than the bare rare-earth magnet of the inner rotors. If glued magnets for exterior rotors are foreseen, incorrect placement could cause mass imbalances which are critical at high rotational speeds.

All in all, Table 4.4 qualitatively summarizes the considerations of this subsection and those of subsection 4.2.3. This assessment lays out an overview of the performance characteristics, advantages, and disadvantages, of interior and exterior rotor drives in a scenario in which rotor diameter  $d_{\text{rot}}$  and PM volume  $V_{\text{PM}}^*$  is fixed.

Based on these considerations, inner rotor topologies are further pursued in this work. Their lower radial stiffnesses—for almost the same active force—renders the start-up procedure considerably easier. Their larger available copper cross-sections lead to larger torques, thus facilitating the achievement of high rotational speeds. This being said, inner rotor drives are heavier and provide a weaker axial stiffness  $k_z$  which might prove critical for the operation of an axial ventilator.

With the choice of interior rotor drives as candidates for the axial ventilator, the improvement of its characteristics, based on geometric parameters, is further investigated in the next sections.

Table 4.4: Qualitative comparison of interior and exterior rotor configurations, deployed as rim-drive axial ventilators as seen in Figs. 4.1c-4.1d. (+) denotes a desired characteristic, (✓) average characteristic, and (-) unfavorable performance/characteristic.

Rotor Stator	Interior		Exterior	
	Slotless	Slotted	Slotless	Slotted
Passive stiffnesses				
Radial	+	+	-	-
Axial	✓	-	+	+
Tilting	+	+	✓	-
Active Characteristics				
Force	+	+	✓	-
Torque	+	✓	-	✓
Assembly				
Material Costs	-	-	+	+
Rotor Assembly	+	+	-	-
Stator-coil Assembly	-	+	-	+

## 4.3 Enhancing the Performance of Disc Drives

### 4.3.1 Motivation

The previous section assessed in an exploratory fashion which types of rotor can best drive an axial ventilator. The dimensions of Table 4.2 were chosen to offer comparability between the possible solutions. Yet the impact upon the geometric parameters upon the analyzed ratings was not analyzed.

In this section, the potential of inner rotor topologies —with slotless and slotted stators— is explored. The impact of manifold motor design parameters such as magnetic air gap, teeth geometry, rotor size, and rotor and stator height proportions upon active and passive characteristics is inspected in a parametric fashion. Additionally, power losses are estimated.

The relevance of the proposed parametric study lies in the notions that they help draw. Oftentimes are the exact requirements of an electromechanical actuator are incompletely described, so no *optimal* drive can be proposed. A parametric study aids to understand the range of performances that can be yield for a given parameter set, e.g. rotor size or axial length of the drive.

Such a parametric study helps to appreciate the effect of single parameters upon the performance of the drive, as well as how different performance ratings trade-off with each other. Moreover, a given set of design parameters yields a given set of realistic drive performances.

With an overview of the attainable ratings, further constraints might be imposed to discard subpar configurations. Ultimately, the relative performance of the variants and their relevance can be weighted to prioritize more critical aspects of the system, such as low-losses, bearing stability, etc.

### 4.3.2 Modelling of the Disc Drive

Literature has already covered the sizing of slotless and slotted drives with mechanical bearings for high-speed applications. For drives with long axial lengths, the consideration of 2D analytical models [14, 203] is sufficient, since stray fluxes barely affect relevant rotor characteristics. Analogously, for bearingless drives with large axial lengths and more DoFs to control, their active characteristics can be analytically estimated [52].

The cross-section modelling of electric drives commonly neglects stray fluxes, as they do not contribute to torque generation. In the case of disc drives, stray fluxes spawn the restoring stiffnesses in axial and tilting directions that are common —and even beneficial— to disc drives. The effect of an unequal rotor and stator height upon active force and torque generation has not yet been modelled by a cross-section in a precise manner.

In this thesis, a framework leading to the head-to-head study of magnetically-levitated disc



drives is presented. Due to the aforementioned considerations relevant to disc drives, the study is primarily aided by 3D magnetostatic FE.

The sizing process of single topologies of disc drives has been partially reviewed in the literature. The challenges of downscaling disc drives have been addressed [165] focussing upon bearing stiffness. The advantages and disadvantages of temple-topology slotted and slotless disc drives in the pump domain have been highlighted [139]. Yet, an exhaustive comparison between topologies with a given rotor size which also considers power losses is not available.

A generalized design procedure for disc drives is provided. Within this context, disc rotors, i.e. with no holes or  $\delta_{st.} = d_{rot.}/2$ , are considered, as this enhances the generality of the conclusions of this study and ensures a fairer comparison between rotor sizes. The suggested analysis may be also applied for the design of disc drives with thinner rotors in the context of ventilators. This is ultimately equivalent to choosing a PM disc rotor of a lower magnetic remanence.

### 4.3.3 Material Selection and Mechanical Considerations

For a fair comparison between slotted and slotless drives, their materials are chosen to be the same. This makes them equivalent in magnetic terms as well as in costs.

Aiming at compact actuators, high-energy-density NdFeB magnets [46] with 42UH grades are chosen as rotors. Their strong bias in the magnetic air gap allows—for a given ventilator electromechanical torque—for smaller currents, c.f. Eq. (3.38) and thus less heating.

An iron-based ferromagnetic amorphous metal material—marketed as *Metglas* [106]—is chosen for the stator, due to its power-loss properties. For a given rotational speed, this material produces fewer losses—and thus less heating—than traditional laminated steels. In return, it saturates at lower magnetic flux density values.

The bearing retainer needs a minimal thickness, as manufacturing technologies do not allow for increasingly thin structures. On the other hand, larger rotors do not imperatively need progressively thicker bearing retainers. To this end, a single thickness for the bearing retainer is determined for all sizes.

Similarly, a mechanical clearance in which the rotor levitates must be established. On the one hand, it cannot be set too low, to leave room for imperfections of the levitation control and wobbling of the rotor at high rotational speeds. Conversely, it should not become unnecessarily larger with increasing drive size, as this would hinder the bearing start-up procedure, i.e. require high bearing currents, and bring no further advantages to levitation.

The determined values of the discussed subjects are shown in Table 4.5.

Table 4.5: Magnetic and mechanical constants for the forthcoming comparison of slotless and slotted drives.

Choice	Symbol	Value
<b>Magnetic</b>		
NdFeB42 Rotor's Remanence	$B_{\text{rem.}}$	1.31 T [46]
Max. B-Field in <i>Metglas</i> Stator	$B_{\text{max.}}$	1.1 T
<b>Mechanic</b>		
Mech. Clearance of Rotor	$\delta_{\text{bng,free}}$	1 mm
Thickness of Bearing Retainer	$\delta_{\text{bng,ret.}}$	1 mm

#### 4.3.4 Parametric Study

The parameters to be varied, and how much they are varied, must be defined to frame the investigation. The combination of the varied parameters thus defined a *design space* that spawns a variety of drives to be considered and rated.

Initially, parameters that are *common* to slotless and slotted stators are defined. They relate to the height of the stator and rotor, as well as the diameter of the rotor. These are shown in Table 4.6. It must be noted that *flatter* (or more slender) drives are those with *smaller*  $\xi$  values.

Regarding the rotor diameter, it is assumed that an integrated system is being newly conceived, so that multiple rotor diameters, e.g. impeller sizes, can fulfill the specifications of the actuator and what it needs to drive. This situation corresponds to the ventilation requirements of the suit, so in principle, the rotor radius can be freely chosen, provided it can resist speeds in the  $10^1$  krpm range [91]. This design freedom might not be possible if a disc drive is to be integrated into an existing system.

On top of these considerations, parameters which modify the copper cross-section in both drives are varied. With the radial copper thickness of the slotless defined as

$$\delta_{\text{Cu.}} = \delta_{\text{air gap}} - \delta_{\text{bng,free}} - \delta_{\text{bng,ret}} \quad (4.1)$$

and constant  $\delta_{\text{bng,free}}$  and  $\delta_{\text{bng,ret.}}$  values, the copper radial width  $\delta_{\text{Cu.}}$  is augmented with an increase of its magnetic air gap  $\delta_{\text{air gap}}$ .

A larger air gap  $\delta_{\text{air gap}}$  also has an impact upon the rotor-stator reluctance and hence upon its passive bearing characteristics. For the slotted motor, a larger copper cross-section might be obtained simply by conceiving larger tooth values  $L_{\text{th.}}$ . This does not impact the overall magnetic air gap as in the slotless.

Table 4.6: Variation of parameters common to slotted and slotless motors.

Definition	Symbol	Range	Multiplier
Rotor Diameter [mm]	$d_{\text{rot.}}$	15, 20, 25	$3 \times$
Slenderness	$\xi = \frac{h_{\text{rot.}}}{d_{\text{mot.}}}$	0.1, 0.2, 0.3	$3 \times$
Rotor / Stator Height Ratio	$\lambda = \frac{h_{\text{rot.}}}{h_{\text{st.}}}$	1, 1.2, ... 2	$6 \times$
			$54 \times$

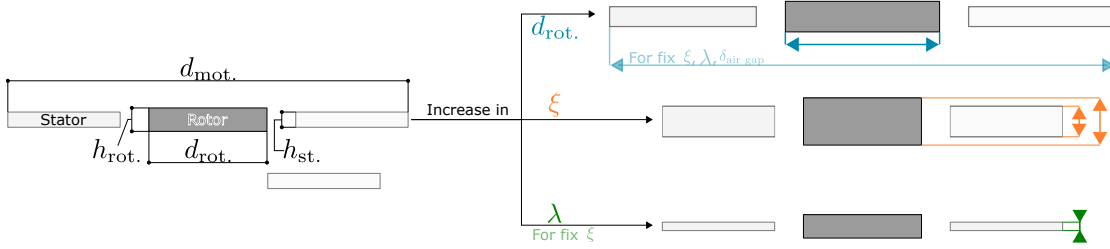


Figure 4.7: Effects of increasing the parameters of Table 4.6 upon drive geometry.

To further expand the design space based on a similar parameter, the magnetic air gap  $\delta_{\text{air gap}}$  of the slotless drive and the stator tooth length  $L_{\text{th.}}$  of the slotted drive are varied to modify the copper cross-section. The objective is to find variants that —for a given  $d_{\text{rot.}}$ ,  $\lambda$  and  $\xi$ — produce the same active torque  $T_z^{\text{slotless}} = T_z^{\text{slotted}}$  for a determined drive current density. Within this regard, the active torque grows by increasing  $\delta_{\text{air gap}}$  and  $L_{\text{th.}}$  in the slotless and slotted motor, respectively. This study is performed with the aid of 3D FE computational simulations.

With an equal mechanical torque  $T_z^{\text{slotless}}$  and  $T_z^{\text{slotted}}$ , the bias of the ferromagnetic material of the stator is corroborated. It must be verified that the complete volume is not overly saturated, i.e. the B-field surpasses  $B_{\text{max.}}$ , as this manifests itself as an increased magnetic reluctance in the magnetic circuit. Contrarily, it must be corroborated that the material is not underused, i.e. with B-fields below a certain percentage  $\alpha$  of  $B_{\text{max.}}$ . This would mean that the same drive performance could be attained with a less voluminous stator.

If the magnetic flux density inside the stator is to be diminished, the stator yoke thickness  $\delta_{\text{st.}}$  is augmented, and vice-versa. For the slotted stator, the teeth width  $W_{\text{th.}}$  is to be attuned accordingly, with the rotor pole facing it. The complete procedure is depicted in Fig. 4.8.

Once the canonical motors for each rotor size  $d_{\text{rot.}}$  are found, the newly validated parameters  $\delta_{\text{air gap}}^*$  and  $L_{\text{th.}}^*$  serve as a base for a further parametric exploration inside the design space: inside it, these values are varied *around*  $\delta_{\text{air gap}}^*$  and  $L_{\text{th.}}^*$  as in Table 4.7.

On the other hand, the values  $\delta_{\text{st.}}$ ,  $W_{\text{th.}}$  that permit an acceptable bias of the ferromagnetic

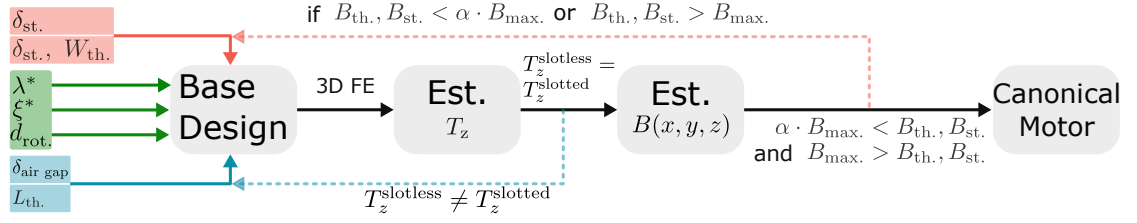


Figure 4.8: Flow diagram for determining the stator thickness  $\delta_{st}$  and air gap  $\delta_{air\ gap}$  of the slotless stator and the stator thickness  $\delta_{st}$  and teeth dimensions  $W_{th}$ ,  $L_{th}$  of the slotted stator. For each rotor diameter  $d_{rot}$ , slotless and slotted stators that provide the same torque are searched for. If they pass this criterion, their stators are spatially checked for the compliant utilization of their ferromagnetic material.

stator are retained and kept constant for the forthcoming exploration of the design space. They are marked with a  $\dagger$  superscript in Table 4.7.

The procedure of Fig. 4.8 is performed for  $d_{rot} = 15, 20$ , and  $25$  mm, with  $\lambda^* = 1.5$  and  $\xi^* = 0.2$ . The latter ratios are chosen because they yield a good trade-off between active and passive characteristics [165]. The result of this procedure is presented in Table 4.7. Its results contribute with a  $4 \times$  multiplier to the design space of Table 4.6. Thus, a total of 216 drive variants for each topology are simulated and confronted.

#### 4.3.5 Scenarios for the Characterization of Disc Drives

The design space framed by Tables 4.6 and 4.7 gives way to motor variants that must be characterized. Their performance needs to be studied separately, to avoid interaction between the rotor disturbances and coil-excitation effects. Single simulations are thus performed, and single motor characteristics are obtained from them.

Table 4.7: Results of stator dimensioning for  $\lambda^* = 1.5$  and  $\xi^* = 0.2$ . Slotless and slotted motors yield the same torque for  $\delta_{air\ gap}$  and  $L_{th}$  marked with a  $*$  superscript and serve as a reference for another free parameter in the design space. Their stator is correctly biased for  $\delta_{st}$  and  $W_{th}$  values with a  $\dagger$  superscript, whose values are fixed for the design space.

$d_{rot}$	Slotted				Slotless	
	$\delta_{air\ gap}$	$W_{th}^\dagger$	$\delta_{st}^\dagger$	$L_{th}$	$d_{st}^\dagger$	$\delta_{air\ gap}$
15		8	9	5.5, 6.5, 7.5*, 8.5	9	
20	2	12	15	7.5, 8.5, 9.5*, 10.5	13	3, 4, 5*, 6
25		14	16	8.5, 9.5, 10.5*, 11.5	18	

### Scenarios for the Study of Passive Characteristics

To calculate the *passive* motor characteristics, the simulations shown in Table 4.8 are proposed. The rotor is disturbed in the direction indicated by the scenario, and the stiffnesses are estimated by the FE output normalized by the magnitude of the displacement, see Eq. (3.24).

The disturbances are applied as shown in Fig. 3.4. Their magnitude is proportional to the  $d_{\text{rot.}}$ , as shown in Table 4.8 so that these are equally small relative to motor dimensions and are disturbed in their linear range. In the case of slotted motors, the scenarios proposed by Table 4.8 are performed twice: with the motor pole facing a teeth and between two of them. Ultimately, the stiffnesses are defined as the *mean* of these two slightly different values.

### Scenarios for the Study of Active Characteristics

Table 4.9 describes the simulation scenarios for determining the active characteristics of the drive. With a centered rotor, either a drive excitation *or* bearing excitation at the maximum admitted current density  $J_{\text{max.}}$  is applied. Maximum current density is fixed at  $J_{\text{max.}} = 8 \text{ A}_{\text{RMS}} \cdot \text{mm}^{-2}$ , which is a common value for PMSMs.

Before the rotatory operation, the rotor must be brought to levitation by applying a magnetic force. This procedure—the *bearing start-up*—defines the maximum bearing current that must be (very shortly) supplied to the windings.

To estimate the current density of a bearing start-up, the force-current density gain  $k_{F/J}$  is initially estimated at  $J_{\text{bng.}} = J_{\text{max.}}$ . The gain is thus calculated as

$$k_{F/J} = \frac{\sqrt{F_{\text{act.x}}^2 + F_{\text{act.y}}^2}}{J_{\text{bng.}}} = \frac{F_{\text{act.}}}{J_{\text{bng.}}}, \quad (4.2)$$

with  $k_{F/J}$  in  $\text{N} \cdot \text{A}_{\text{RMS}}^{-1} \cdot \text{mm}^2$  and  $F_{\text{act.x}}$ ,  $F_{\text{act.y}}$  the simulated active forces generated in  $(x, y)$  direction in N, respectively.

The passive force, which is determined by the largest estimate of the radial stiffnesses  $F_{\text{max,pass.}}$ ,

Table 4.8: Five FE simulation scenarios for the characterization of passive properties of the motor variants, along with the proportionality constants of the magnitude of the disturbances.

Parameters	Scenarios	FE Output	Evaluation	Constant	Definition	Value
$\lambda, \xi, d_{\text{rot.}}$ $\delta_{\text{air gap}}/L_{\text{th.}}$	$\Delta\alpha$	$T_x$ [Nm]	$k_\alpha$ [mNm/deg]	$\tau_{(\alpha / \beta)}$	$= \frac{\Delta(\alpha / \beta)}{d_{\text{rot.}}}$	1/20
	$\Delta\beta$	$T_y$ [Nm]	$k_\beta$ [mNm/deg]		$= \frac{\Delta(x / y)}{d_{\text{rot.}}}$	1/24
	$\Delta x$	$F_x$ [N]	$k_x$ [N/mm]		$= \frac{\Delta z}{d_{\text{rot.}}}$	1/10
	$\Delta y$	$F_y$ [N]	$k_y$ [N/mm]	$\tau_z$		
	$\Delta z$	$F_z$ [N]	$k_z$ [N/mm]			

Table 4.9: Two FE simulation scenarios for the characterization of active properties of the motor variants.

Parameters	Scenarios	Output	Evaluation
$\lambda, \xi, d_{\text{rot.}}$ $\delta_{\text{air gap}} / L_{\text{th.}}$	$J_{\text{DRV.}} = J_{\text{max.}}$	$T_{\text{max}}$	$P_{\text{mech.}}$
	$J_{\text{bng.}} = 0$	[mNm]	[W]
	$J_{\text{DRV.}} = 0$	$F_{\text{act.x}}, F_{\text{act.y}}$	$F_{\text{max.}}, J_{\text{bng.st.}}$
	$J_{\text{bng.}} = J_{\text{max.}}$	[N]	[N], $[A_{\text{RMS}} \cdot \text{mm}^{-2}]$

must be overcome by an active force  $F_{\text{max,act.}}$ . Assuming no magnetic iron saturation, the current density  $J_{\text{bng.st.}}$  required to *detach* the rotor from its retainer is estimated as

$$\begin{aligned}
 F_{\text{max,pass.}} &= \max(k_x, k_y) \cdot \delta_{\text{bng,free}}, \\
 F_{\text{max,act.}} &= k_{\text{F/J}} \cdot J_{\text{bng.st.}} \\
 &= -F_{\text{max,pass.}} \\
 J_{\text{bng.st.}} &= - \left( \frac{\max(k_x, k_y)}{k_{\text{F/J}}} \right) \cdot \delta_{\text{bng,free}}.
 \end{aligned} \tag{4.3}$$

This quantity is preferably minimized to reduce heating in the actuator and to ease the specifications of the semi-conductors, i.e. the maximum current they must supply.

With the rotor already levitating, the maximal mechanical power is evaluated with the information of the drive simulation as

$$P_{\text{mech.}} = T_{\text{max}} \cdot \omega_{\text{max.}} = T_{\text{max}} \cdot \frac{v_{\text{T}}}{d_{\text{rot.}}/2}, \tag{4.4}$$

with  $\omega_{\text{max.}}$  and  $v_{\text{T}}$  the maximal rotational and tangential speed of a rotor in  $\text{rad} \cdot \text{s}^{-1}$  and  $\text{m} \cdot \text{s}^{-1}$ , respectively. With a bare NdFeB disc magnet, maximum rotor tip speed is estimated to be  $v_{\text{T}} = 160 \text{ m} \cdot \text{s}^{-1}$  [46, 91]. The analyzed rotors can therefore spin at  $n_{\text{max}} = 203, 152$ , and  $122 \text{ krpm}$  for  $d_{\text{rot.}} = 15, 20$ , and  $25 \text{ mm}$ , respectively.

### Scenarios for the Study of Power Losses

Finally, the power losses in the drives are estimated as in Sec. 3.4.

For a disc drive, the magnetic flux density inside the coils is required to estimate  $P_{\text{Cu,Ed.}}$ , whereas the magnetic flux density inside the stator is needed to calculate both  $P_{\text{Fe,Ed}}$  and  $P_{\text{Fe,H.}}$ . To this end, a static 3D FE simulation for different rotor angles is needed.

On the other hand, the losses inside the rotor  $P_{\text{Rot.,Ed.}}$ —due to the slots of the stator—are approximated employing a 2D transient FE simulation, which is then scaled to fit the height of the rotor as in  $P_{\text{Rot.,Ed.}}^{\text{3D}} = h_{\text{rot.}} \cdot P_{\text{Rot.,Ed.}}^{\text{2D}}$ .

## Chapter 4. Conceptualization of Compact Disc Drives

Table 4.10: Two FE simulation scenarios for the characterization of power losses of the motor variants.

Parameters	Scenarios	Output	Evaluation
Static 3D FE $\lambda, \xi, d_{\text{rot.}}$ $\delta_{\text{air gap}}/L_{\text{th.}}$	$\theta = 0^\circ, 30^\circ,$ ..., $330^\circ$	$B(x, y, z, \theta)$ [T]	$P_{\text{Fe,H}}, P_{\text{Fe,Ed}}$ $P_{\text{Cu,Ed.}}, [\text{W}]$
Trans. 2D FE $d_{\text{rot.}}, L_{\text{th.}}$	$\theta = 0^\circ, 1^\circ,$ ..., $359^\circ$	$J_{z,\text{rot.}} [\text{A}_{\text{RMS}} \cdot \text{mm}^{-2}],$ $P_{\text{Rot.,Ed.}} [\text{W}]$	

The scenarios proposed in Table 4.10 aid to calculate the aforementioned losses. The high-speed rotatory magnetic fields inside the air gap of the slotless call for small wire diameters to cap EC losses  $P_{\text{Cu,Ed.}}$  in the windings, as demonstrated in Eq. (3.51). This is normally a less critical issue in slotted motors, as most of the magnetic flux passes directly into the teeth (and not through the coils). Yet, slotted disc drives still benefit from small wire diameters, as their flat geometry does lead to stray fluxes. This is especially the case in which the rotor is higher than the stator, e.g.  $\lambda > 1$ .

For high-speed, flat electric drives, it is, therefore, reasonable to foresee thin wire diameter, albeit smaller filling factor—and thus larger Joule losses—. To ensure comparability, a litz wire diameter with outer and  $(100 \times)$  strand diameters of  $d_{\text{wire}} = 1 \text{ mm}$  and  $d_{\text{strand}} = 71 \mu\text{m}$ , respectively, is chosen. A filling factor of  $k'_{\text{Cu}} = 0.35$  is considered for slotless and slotted motors.

Having approximated the power losses of a drive, its efficiency is calculated. A high-efficiency is desirable for battery-powered applications—that is, portable drive solutions—and is calculated as in

$$\begin{aligned}
 P_{\text{losses}} &= P_{\text{Joule}} + P_{\text{Fe,H}} + P_{\text{Fe,Ed}} + P_{\text{Cu,Ed.}} + P_{\text{Rot.,Ed.}}, \\
 \eta &= \frac{P_{\text{mech.}}}{P_{\text{mech.}} + P_{\text{losses}}}.
 \end{aligned} \tag{4.5}$$

Both quantities are estimated from rotational standstill  $n = 0 \text{ rpm}$  until maximal speed  $n_{\text{max}}$  and for fixed  $J_{\text{max.}}$ . Joule losses  $P_{\text{Joule}}$  are calculated knowing the geometry of the coils and thus need no simulations.

Having explained the simulations and how their output is processed, the results of the simulation in the design space are provided.

### 4.4 Comparison of Slotless and Slotted Topologies

The analysis of the performance of the drives inside the design space is divided into three sections. First off, the sensitivity of performance ratings to parameters inside the design space is analyzed. Then, a deeper analysis of how different performance ratings trade off with

one another is provided. Finally, an optimization case is presented, and the best contenders—according to an objective function—are picked out of the design space.

### 4.4.1 Effect of Drive Geometry upon Performance

The impact of the magnetic air gap  $\delta_{\text{air gap}}$  and rotor/stator height ratio  $\lambda$  is examined initially upon three crucial characteristics: electromagnetic torque (active), axial stiffness (passive), and the EC losses in the windings. The analysis is furnished for slotless and slotted motors in Fig. 4.9 and Fig. 4.10 respectively.

The tilting stiffnesses, which represents a critical parameter of the bearing's restoring capabilities, is analyzed as a function of the drive's slenderness. The needed current density to start-up the bearing—which defines the feasibility of magnetic levitation—is also studied.

#### Parametric Sensitivity of Slotless Drive

Figure 4.9 depicts the performance of the slotless motor as a function of the magnetic air gap  $\delta_{\text{air gap}}$  and height ratio  $\lambda$ . Figure 4.9a shows that increasing the parameter  $\delta_{\text{air gap}}$  increases the max magnetic torque  $T_z$ . The losses in the windings  $P_{\text{Cu,Ed}}$ , as seen in Fig. 4.9c, are modestly increased—in absolute terms—by increasing  $\delta_{\text{air gap}}$ .

By increasing  $\delta_{\text{air gap}}$ —for a fixed  $\delta_{\text{bng,free}}$  and  $\delta_{\text{bng,ret.}}$ —the copper cross-section is also enlarged utilizing a larger  $\delta_{\text{Cu}}$ , which in turn increases the admissible magnetomotive force for a given  $J_{\text{max}}$ . Despite augmenting the reluctance of the air gap—thus reducing its overall magnetic flux density—the extra copper leads to a larger torque. At the same time, as the coils become more massive, more magnetic flux passes through conducting material, which increases the losses. Both these quantities augment in a quasi-linear fashion with  $\delta_{\text{air gap}}$ .

Enlarging  $\delta_{\text{air gap}}$  decreases the axial stiffness, as evident in Fig. 4.9b. The increased air gap reluctance rapidly curbs the stray fields that yield the restoring pull in the axial direction between stator and rotor. To this end, a drive with  $\delta_{\text{air gap}} = 3 \text{ mm}$  is practically three times stiffer than a drive with  $\delta_{\text{air gap}} = 6 \text{ mm}$ .

Rendering the stator flatter, i.e. increasing  $\lambda$ , enhances the  $k_z$ , as it increases the proportion of rotor flux straying vertically upon the stator. Nevertheless, the yield in terms of  $k_z$  decreases for high  $\lambda$  values, i.e. for  $\lambda > 8/5$ .

In turn, high  $\lambda$  values decrease  $T_z$  mildly, as seen in Fig. 4.9a, since it shortens the active length of copper in the air gap, where the rotor's magnetic flux is the strongest. Yet, the narrower  $\delta_{\text{air gap}}$ , the smaller is the effect. This indicates that stray fluxes—along the wire strands above and below the stator—*do contribute* to torque generation: otherwise, drives with  $\lambda = 2$  would provide half the torque of those with  $\lambda = 1$ .

On the other hand, Figs. 4.9d-4.9f shows the change of tilting stiffnesses and of bearing start-up



currents as a function of slenderness  $\xi$  and magnetic air gap  $\delta_{\text{air gap}}$ .

The restoring tilting torque  $T_\beta$  of Fig. 4.9e is always negative and provides a restoring function. It can be boosted by increasing parameter  $\xi$  from 1/10 to 2/10. Going further as in  $\xi = 3/10$  shows no appreciable boost in tilting. As in Fig. 4.9b, enlarging  $\delta_{\text{air gap}}$  curbs the strength of the restoring stiffnesses as it leads to larger reluctance paths between rotor and stator.

The restoring torque on the weak axis  $T_\alpha$  of Fig. 4.9d is smaller than  $T_\beta$  and rapidly becomes destabilizing, i.e. positive for  $\xi > 2/10$ . This characteristic *limits* the employment of one pole-pair drives as disc drives, as these must be *very* flat, or at least flatter than its multi-polar disc drives which portray no weak tilting axis. For a fixed radius, multi-polar bearingless drives are still stable for larger  $\xi$  values. An increase in  $\xi$ —which boosts the drive's active length—is desirable in torque-demanding applications. On another note, enlarging  $\delta_{\text{air gap}}$  also diminishes the restoring torque  $T_\alpha$ , as with  $T_\beta$ .

The bearing start-up current density, i.e. the bearing start-up effort, can be considerably reduced by increasing the air gap  $\delta_{\text{air gap}}$ , as seen in Fig. 4.9f. By enlarging  $\delta_{\text{air gap}}$ , the magnetic flux density at the interior of the stator—where reluctance forces are calculated—is reduced. This curtails the radial stiffnesses  $k_x$  and  $k_y$ . Force gain  $k_{F/J}$  also increases with  $\delta_{\text{air gap}}$ —as the torque did in Fig. 4.9a—. Both the decrease in radial stiffnesses and increase in active force gain yielded by a larger  $\delta_{\text{air gap}}$  facilitate start-up. This approach can be always pursued in the interest of easier bearing start-ups.

The start-up bearing current density is nonetheless practically independent of slenderness  $\xi$ , as changing this value increases the axial length of the coils and inner stator surface linearly, thus scaling both  $k_{F/J}$  and  $k_x$ ,  $k_y$  in a linear fashion, respectively.

#### 4.4 Comparison of Slotless and Slotted Topologies

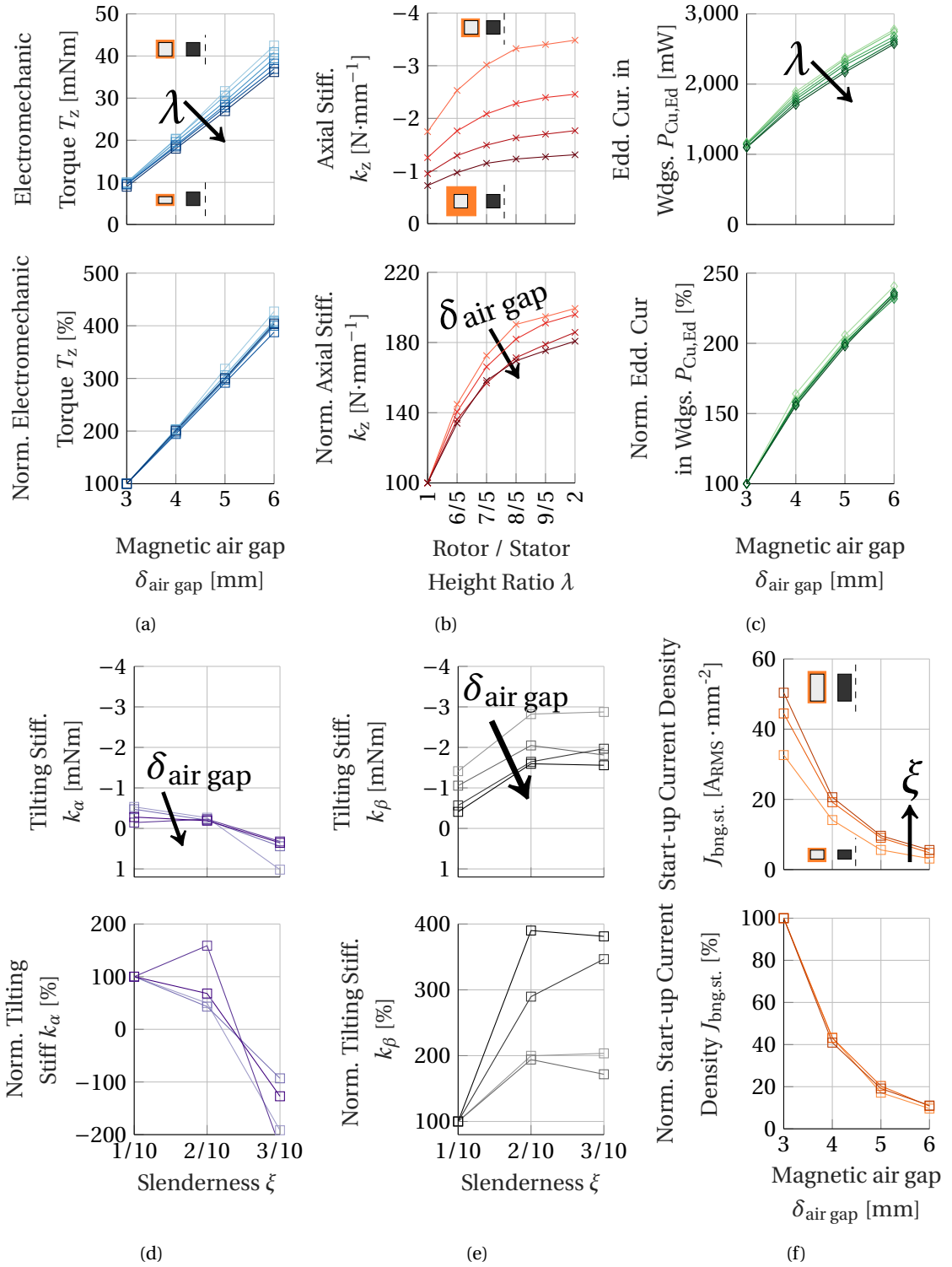


Figure 4.9: Effects of the parameters in the  $x$ -axis and upon the different curves (increasing in value as indicated by the arrows) upon active, passive, and loss characteristics of a *slotless* disc drive. The change of motor geometry upon the rotor and stator of the different plot lines is schematically depicted. Plotted for slotless variants of  $d_{\text{rot.}}=15$  mm (a)-(c) with  $\xi=0.3$  and (d)-(f) with  $\lambda=8/5$ .

### Parametric Sensitivity of Slotted Drive

Similarly, Fig. 4.10 displays the dependencies of active, passive, and power loss characteristics for the slotted motor. Analogous to the increase in  $\delta_{\text{air gap}}$  of the slotless motor, an increase in  $L_{\text{th}}$  enhances the  $T_z$  of the slotted motor, as shown by Fig. 4.10a. This boost is less marked than that of the slotless, as —within the design space— it only sees an increase of 150% this capacity, instead of 300%. Enlarging  $L_{\text{th}}$  has a modest impact upon increasing the copper cross-section, as the stator teeth occupy a large surface between their tips and the stator yoke. On another note, an increase in  $\lambda$  curtails  $T_z$  more strongly than by the slotless motor. This was expected, as the active length is reduced, and slotted topologies have fewer stray fluxes that could still contribute to the torque by making the stator thinner, as with the slotless.

Due to fewer stray fluxes passing through the copper, the losses  $P_{\text{Cu,Ed}}$  of Fig. 4.10c in the slotted drive are smaller than those in the slotless. Increasing  $L_{\text{th}}$  raises the losses in the windings  $P_{\text{Cu,Ed}}$ , but in a very limited manner. On the one hand, increasing teeth length  $L_{\text{th}}$  does not change the air gap reluctance, so the stray fluxes —which are stronger at the tooth's tip— do not change in magnitude. Nevertheless, the additional copper due to longer teeth is *still* penetrated by stray fluxes, thus lightly incrementing  $P_{\text{Cu,Ed}}$  losses. This increase —by approximately 30%— is more modest than the 150% increase of losses with the  $\delta_{\text{air gap}}$  of the slotless, in which copper was added directly inside the air gap.

On the other hand, ratio  $\lambda$  plays a bigger role upon  $P_{\text{Cu,Ed}}$ . Contrarily to the case of the slotless, increasing  $\lambda$  from  $\lambda=1$  to  $\lambda=2$  increments the losses for a slotted stator by up to 300%. For  $\lambda=1$ , most of the PM's flux radially pierces into the stator through the teeth —especially given the narrow  $\delta_{\text{air gap}}$ — thus keeping stray fluxes low. An increase in  $\lambda$ , i.e. reduction of stator height, diverts the magnetic flux to pass into the stator —from below and above— by first passing through the coils, hence increasing losses.

Figure 4.10b displays how parameter  $\lambda$  enhances the axial stiffness  $k_z$  of the variants, as with the slotless drive. Yet, the boost upon  $k_z$  is limited until  $\lambda=8/5$ . Contrarily to the slotless, modifying teeth length  $L_{\text{th}}$  has fundamentally no effect upon the stiffnesses because the extra teeth length is not involved in the generation of reluctance forces.

Both tilting stiffnesses  $T_\alpha$  and  $T_\beta$  of Figs. 4.10d-4.10e can rapidly become positive, i.e. destabilizing, if the overall slenderness  $\xi$  of the drive is augmented. Large  $\xi = 0.3$  values even render destabilizing  $T_\beta$  values, which was not the case by the slotless drive. This makes the sizing of slotted drives —at the studied dimensions— more restrictive than that of the slotless. As with the axial stiffnesses, tooth length  $L_{\text{th}}$  has a limited influence, with longer teeth offering a slightly larger surface to spawn the tilting forces.

The start-up current densities  $J_{\text{bng.st.}}$  depicted in Fig. 4.10f are substantially lower than those of the slotless drive. Force build-up in slotted drives is based upon reluctance forces, which —all other factors held equal— lead to a higher  $k_{\text{F/J}}$  [68]. For a fixed current density,  $J_{\text{bng.st.}}$  increases with tooth length  $L_{\text{th.}}$ , thus rendering  $J_{\text{bng.st.}}$  even lower.

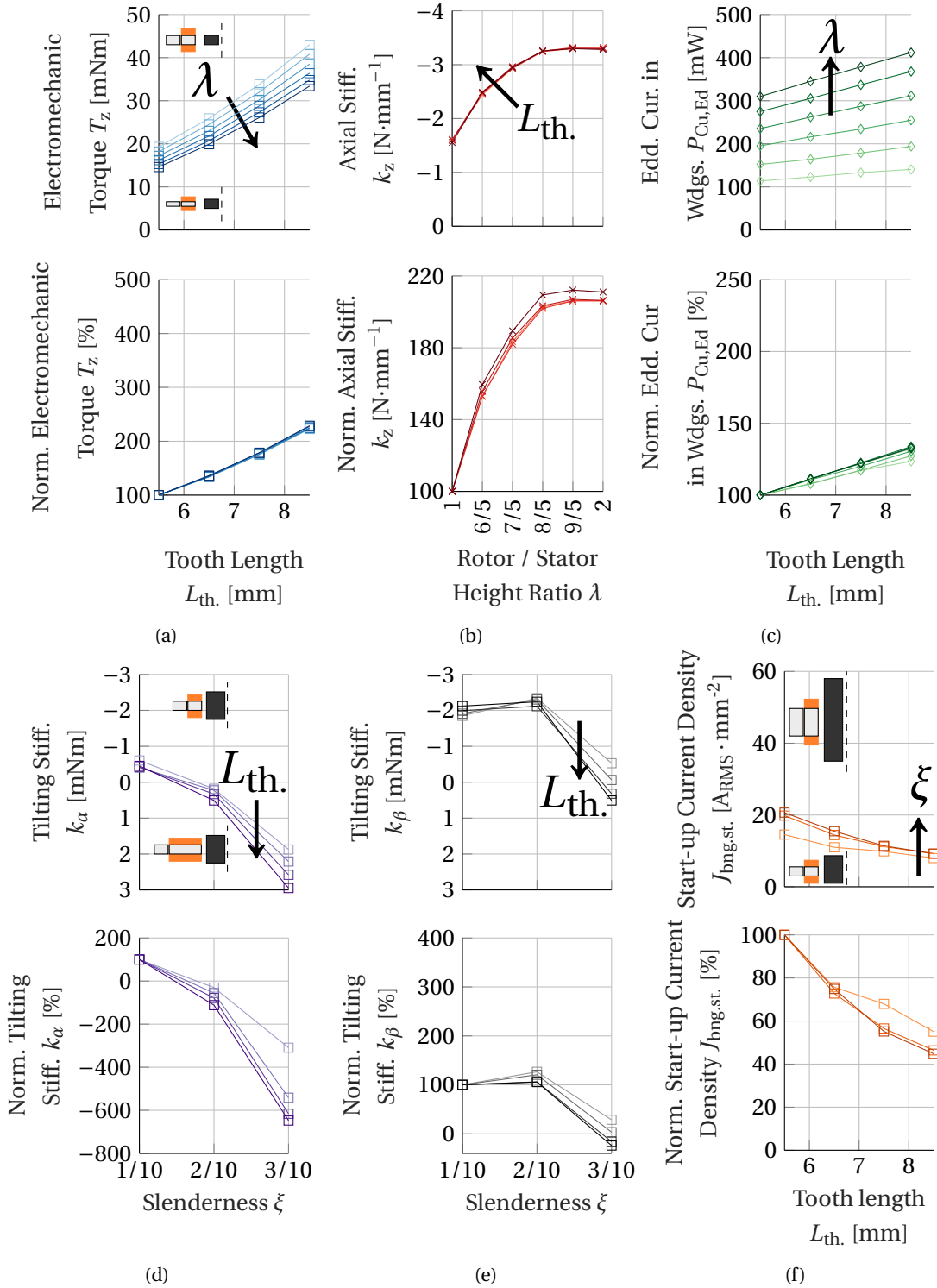


Figure 4.10: Effects of the parameters in the  $x$ -axis and upon the different curves (increasing in value as indicated by the arrows) upon active, passive, and loss characteristics of a *slotted* disc drive. The change of motor geometry upon the rotor and stator of the different plot lines is schematically depicted. Plotted for slotted variants of  $d_{rot.}=15$  mm (a)-(c) with  $\xi=0.3$  and (d)-(f) with  $\lambda=8/5$ .

### 4.4.2 Trade-offs in Slice Drives

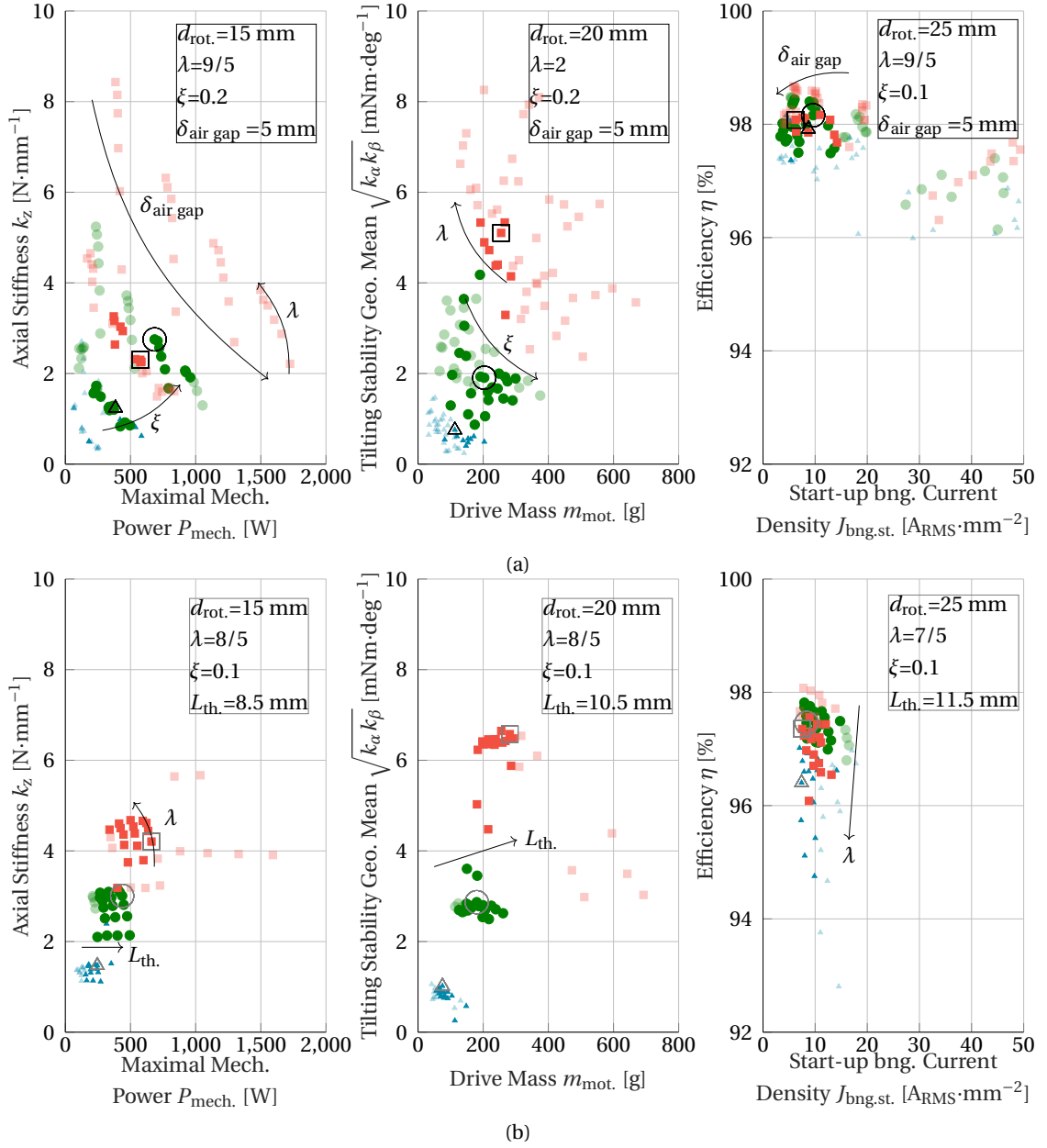
After having analyzed how *single* geometric parameters affect single performance parameters, it is also analyzed how performance parameters trade-off from each other. This analysis offers a clearer picture as to which performances can be attained with disc drives of different sizes  $d_{\text{rot.}}$ , and how certain ratings can be enhanced for the sake of others.

Figure 4.11a and Figure 4.11b depict the *compliant* design space. The impact upon the performance of increasing the value of single parameters is depicted with arrows. Drives with non-restoring tilting stiffnesses, i.e.  $T_\alpha$  or  $T_\beta > 0$  are not plotted as they are deemed infeasible. 79 slotted stator and 136 slotless stator drives comply with these conditions and are thus plotted.

The arrows of Fig. 4.11 indicate how design parameters can be modified to bias the characteristics of the motors within the design space. Higher rotors, i.e. enlarging  $\lambda$ , for slotless drives in Fig. 4.11a, boosts the axial stiffness  $k_z$  and tilting stiffnesses  $\sqrt{k_\alpha k_\beta}$ , and renders them lighter with  $m_{\text{mot.}}$ , at the cost of mechanical power  $P_{\text{mech.}}$ . For slotted motors, in Fig. 4.11b, a larger  $\lambda$  also boosts  $k_z$  and cuts down  $P_{\text{mech.}}$ , but it additionally decreases the efficiency  $\eta$  of the drive, as it enlarges the proportion of stray fluxes which cause ECs in the windings  $P_{\text{Cu.,Ed.}}$ .

Increasing the  $\xi$  parameter to 2/10 still renders feasible slotless drive variants for Fig. 4.11a. This rapidly increases mechanical power  $P_{\text{mech.}}$ , and boosts—to a lesser extent—the axial stiffness  $k_z$  at the cost of a higher  $m_{\text{mot.}}$  and reduced tilting stiffnesses  $\sqrt{k_\alpha k_\beta}$ . The decrease in the latter  $\sqrt{k_\alpha k_\beta}$  is such that elevating  $\xi$  for the slotted motors of Fig. 4.11b usually renders them unstable: hence the reduced number of drives with restoring tilting stiffnesses. This attribute restricts the versatility of slotted drives for the studied dimensions.

Increasing the teeth length  $L_{\text{th}}$  of the slotted drives of Fig. 4.11b boosts mechanical power  $P_{\text{mech.}}$  and tilting stiffnesses  $\sqrt{k_\alpha k_\beta}$  at no cost in axial stiffness  $k_z$ , yet it renders the drive heavier. The air gap  $\delta_{\text{air gap}}$  of the slotless drives in Fig. 4.11a has a more prominent impact upon motor performance: larger  $\delta_{\text{air gap}}$  values improve  $P_{\text{mech.}}$  at the cost of weaker  $k_z$  and  $\sqrt{k_\alpha k_\beta}$ , as well as heavier  $m_{\text{mot.}}$ . Positively enough, they cut down start-up currents  $J_{\text{bng.st.}}$ . The latter fact makes large air gaps  $\delta_{\text{air gap}}$  preferable for the levitation of slotless disc drives of the studied dimensions.



#### 4.4.3 Inequality Constraints upon Design Space

All the feasible drives are juxtaposed in an application scenario so that an overall rating of their performance—all performance markers included—can be determined. Contrasted to a real need, contenders of both topologies may be compared head-to-head. For this scenario, the following constraints are to be met

$$\begin{aligned}\Delta z^{\max} &< 2 \text{ mm at } F_z = 1 \text{ N}, \\ J_{\text{bng.st.}}^{\max} &< 15 \text{ A}_{\text{RMS}} \cdot \text{mm}^{-2}, \\ m_{\text{mot.}}^{\max} &< 300 \text{ g}, \\ P_{\text{mech.}}^{\min} &> 150 \text{ W}.\end{aligned}\tag{4.6}$$

42 out of the 136 slotless variants pass these conditions, whereas 51 of 79 slotted do. Slotless variants *usually* do not comply due to high start-up current densities, and the slotted because of weight. The passing variants are displayed with opaque colors in Figs. 4.11a - 4.11b, and those that do not are faded out.

Having sorted out the configurations that meet the conditions of Eq. (4.6), the performance ratings of each variant are numerically rated according to an adimensional criterion  $\mu$ .

The definition of merit criterion  $\mu_i$  is different if maximization  $\mu_{i,\uparrow}$  or minimization  $\mu_{i,\downarrow}$  is preferable. For each compliant drive, these are estimated as

$$\begin{aligned}\mu_{i,\uparrow} &= \frac{\kappa_i - \min(\kappa_i)}{\max(\kappa_i) - \min(\kappa_i)}, \quad \forall \kappa_i = k_z, \sqrt{k_\alpha k_\beta}, P_{\text{mech.}}, \eta \\ \mu_{i,\downarrow} &= \frac{\kappa_i - \max(\kappa_i)}{\min(\kappa_i) - \max(\kappa_i)}, \quad \forall \kappa_i = m_{\text{mot.}}, J_{\text{bng.st.}},\end{aligned}\tag{4.7}$$

considering *separate*  $\kappa_i$  values for slotted and slotless drives and their different rotor diameters. By definition,  $\mu_{i,\uparrow}, \mu_{i,\downarrow}$  lay between 0 and 1, with increasing performance order.

Thereafter, *overall* motor performance is represented by another indicator  $\Psi$ , that condenses  $\mu$  values for each  $d_{\text{rot.}}$  and topology. The overall merit  $\Psi$  is defined as

$$\Psi = \sqrt[6]{\prod_i \mu_i},\tag{4.8}$$

so a higher  $\Psi$  implies a better performing motor. Drives with the highest  $\Psi$ —for each rotor size  $d_{\text{rot.}}$  and topology—are picked out, resulting in a total of six optimal drives (three rotor diameters for the slotless and slotted) whose performance is depicted in Fig. 4.12.

#### 4.4.4 Head-to-head Comparison

The ratings of the drives with the largest  $\Psi$  values for each topology and rotor size are marked upon Fig. 4.11. Their design parameters are correspondingly indicated on each subplot, and

#### 4.4 Comparison of Slotless and Slotted Topologies

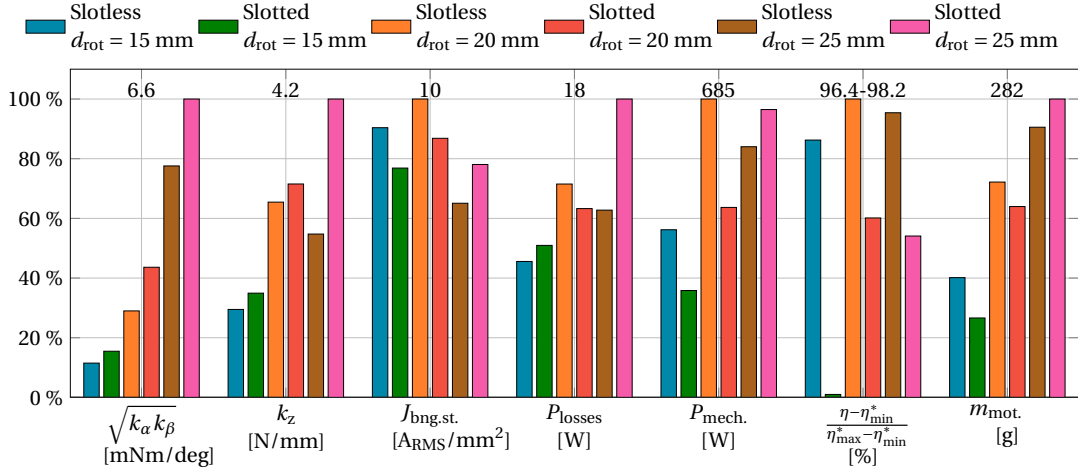


Figure 4.12: Slotless and slotted variants, for all rotor sizes, that perform best according to indicator  $\Psi$ . A 100% rating corresponds to the value above the bars, except for the efficiency (0% and 100% on its y-axis correspond to  $\eta=96.4\%$  and  $98.2\%$  of Eq. (4.5), respectively).

their actual dimensions are specified in Table 4.11.

To make the comparison more clear, these performance values are plotted head-to-head in Fig. 4.12. As it can be seen, drives of *all* the proposed rotor diameters  $d_{rot.}$  comply with the conditions of Eq. (4.6).

In terms of axial stiffness  $k_z$ , slotted drives always yield stronger restoring pulls. This is a natural consequence of their narrower air gap  $\delta_{air\ gap}$ . The same can be said for the tilting stiffnesses  $\sqrt{k_\alpha k_\beta}$ .

The  $\Psi$  rating picked out drives whose start-up current densities relate as in  $1/2 \cdot J_{bng.st.}^{max} < J_{bng.st.} < 2/3 \cdot J_{bng.st.}^{max}$ . Despite bestowing larger  $k_{F/J}$  values, all proposed slotted variants need start-up currents comparable to their slotless counterparts. This is due to the wider  $\delta_{air\ gap}$  values of the slotless drives that yielded better  $\Psi$  ratings, which simultaneously lead to weaker  $k_x$  and  $k_y$  radial stiffnesses. In this regard, most narrow-air gap slotless possibilities had already been discarded by the  $J_{bng.st.}^{max}$  condition of Eq. (4.6).

Slotless motors provide, for all sizes except  $d_{rot.}=25$  mm, larger mechanical power  $P_{mech.}$ . This is because of the optimal slotless drives for  $d_{rot.}=15$  mm and  $d_{rot.}=20$  mm all have higher  $h_{st.}$  and  $h_{rot.}$  values than their slotted counterparts; that is, a  $\xi = 0.2$  proportion. Such slenderness is not feasible for slotted drives as it renders them unstable in tilting, see Fig. 4.10d-4.10e.

The optimization procedure leads, for the rotor diameter  $d_{rot.}=25$  mm, in value  $\xi = 0.1$  for both slotless and slotted drives. In this case, the slotless variant is slightly less powerful than its slotted counterpart, despite the slotless' PM having 62% of the volume of the slotted's.. This case accounts for the recognized superiority of the slotless drives, in terms of mechanical power, for small overall diameters.



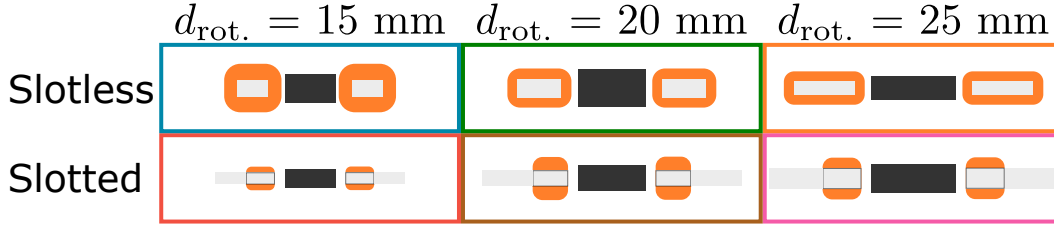


Figure 4.13: To-scale cross-sections of the optimized slotless and stator drives of Fig. 4.12, with dimensions of Table 4.11.

Table 4.11: Geometric parameters in [mm] of optimal variants of slotted and slotless motors.

$d_{rot.}$	Slotted					Slotless			
	$h_{rot.}$	$h_{st.}$	$W_{th.}$	$L_{th.}$	$d_{st.}$	$h_{rot.}$	$h_{st.}$	$\delta_{air\ gap}$	$d_{st.}$
15	5.6	3.5	8	8.5	9	8.6	4.8	5	9
20	7.7	4.8	12	10.5	15	11.2	5.6	5	13
25	8.6	6.2	14	11.5	16	7.1	3.9	5	18

An analogous panorama is offered by the power losses  $P_{losses}$ . The optimal slotless drives, with  $\xi = 0.2$  (for rotor diameters  $d_{rot.}=15$  mm and  $d_{rot.}=20$  mm) have comparable losses to its slotted counterparts, in spite of their longer stators and rotors. Conversely, for the optimal  $\xi = 0.1$  value of both  $d_{rot.}=25$  mm motors, the slotless drive generates only 60% of the losses of the slotted.

Observations on the motor losses  $P_{losses}$  and  $P_{mech.}$  make the optimal slotless motors more efficient than their optimal slotted partners. This assertion is true for all the simulated variants of the design space, as seen on the right side of Fig. 4.11.

The  $\xi = 0.2$  slotless variants are naturally heavier than their slotted counterparts, due to their overall larger axial length. Nevertheless, for the  $\xi = 0.1$  variants with  $d_{rot.}=25$  mm, the slotless one is lighter. For a given stator and rotor height, this can be explained by the smaller motor diameters  $d_{mot.}$  of slotless drives.

Ultimately, how the different ratings are weighted depends on the usage of the drive being considered and its particular constraints. Exemplary reasons for prioritizing some of the presented performance ratings are presented in Table 4.12. In any case, a design space may be alternatively searched for optima if other weighting schemes such as  $\Psi = \sum \alpha_i \cdot \mu_i$  are chosen, with normalized weights  $\alpha_i$  in the fashion  $\sum \alpha_i = 1$ .

The next sections of the thesis focus on the compact integration of a slotted *and* a slotless disc drive. To verify the potential of these drives, they are sized to comply with a rotor of dimensions  $d_{rot.}=20$  mm and  $\delta_{PM}=6$  mm and  $h_{rot.}=8$  mm. The lessons of this section related to the correct stator yoke dimensioning, as well as design trade-offs are considered for their sizing. The same drives are then tested with a rotor of similar dimensions but of thickness  $\delta_{PM}=1$  mm, which naturally suits the realization of an axial ventilator.

Table 4.12: Exemplary reasons for prioritizing particular ratings of magnetically-levitated disc drives.

Parameter	Demand
$\sqrt{k_\alpha k_\beta}, k_z$	Low vibration requirement, large axial loads
$J_{\text{bng.st.}}$	Low current for power stages
$P_{\text{losses}}$	System within low thermal-conduction encapsulation
$P_{\text{mech.}}$	High-power density, overall volume minimization
$\eta$	Battery-powered applications
$m_{\text{mot.}}$	System-weight minimization

## 4.5 Conclusion

In this chapter, a finite set of miniature motor variants is conceived, and their performance is evaluated. A framework for the evaluation of this performance, as a function of geometric parameters, is proposed.

To start, four possible electric motor topologies —with the same rare-earth volume— are gauged in terms of electromechanical, i.e. bearing and drive, performance. Moreover, quantitative aspects of the drive —such as its compactness and material distribution inside a given volume— are taken into account. Such a preliminary assessment helps to find out which motor topologies best match the deployment of an electric drive.

The matching drive variants can then be analyzed more deeply. In this thesis, a parametrical study for magnetically-levitated drives is then suggested as a framework. Without exact information about the drive, bearing and power ratings needed by the application, such an approach yields an overview of the achievable performances, if —for example— the rotor size is roughly known.

The parametric study enables visualizing the effect of design parameters upon single motor ratings, and at the same time, how the performance aspects trade-off. The parametric study also brings forth the performances that can be attained for a given set of parameters. Based on the capabilities of the considered motor configurations, a finer analysis might be undertaken if further insight upon the required performance is at hand.

With a more constrained variety of options, the characteristics of the drives can be prioritized differently. To do so, the indicators of the performance of the motor are mathematically weighted, ultimately yielding the best motors for different rotor dimensions and stator topologies. Their performance can be then gauged head-to-head, to understand the potential, advantages, and disadvantages of these best contenders.

# 5 Contactless Sensor Systems for Rotor Position Estimation

## 5.1 Introduction

Magnetic levitation fundamentally requires more sensors than its mechanical bearing counterparts, as rotor position has to be closely surveilled for proper levitation. This information must be rapidly sampled with high resolution since incorrect or slow bearing operation leads to rotor shocks. Rotor crashes lead to shortened lifetime and thus undermine one of the most noticeable virtues of magnetic levitation.

The surveillance of the radial position of the rotor is of paramount importance to know the operating state of the drive and bring the rotor into contactless levitation. Rotor position information enables the control of the bearing forces during operation. In practice, it enables the control system to distinguish between a landed or levitating rotor, to correct position drifts during operation, and to compensate against mechanical disturbances.

Within the scope of bearing operation, the angular position of the rotor is also needed. Its knowledge helps so that the reference, i.e. desired bearing forces *coincide* with the real forces applied to the system. In particular, it allows for the correct estimation of  $\phi_{\text{bng.}}$  of the bearing forces and thus to excite the coils with the correct phase shift concerning the rotor.

With magnetic levitation ensured, angular position information is further utilized to implement torque generation schemes (as MTPA) and to estimate the rotation speed of the rotor. The latter can be exploited to control the operating point relevant to the drive.

The advantages of magnetic levitation over conventional drives become apparent only when the rotor is mechanically separated from the rest of the drive. This implies that the measurement technology must also be *contactless* and that traditional measurements using encoders for angle measurement or wire position measurement are better avoided. Contactless rotor position estimation has allowed magnetic levitation to deliver its full potential [4] in numerous applications [115, 118, 122, 126], often by "seeing through" other materials and encapsulations.

In this chapter, a brief overview of the performance ratings of sensor technologies is given. Five

different sensor principles used within the scope of magnetic levitation are then presented. Their deployment, as well as their advantages and disadvantages within the scope of magnetic levitation, are discussed. Within these five concepts, two are sorted out as ideal for the scope of this thesis and are presented in a more detailed manner. These two sensor types are finally tested further down in the thesis in Chapter 7.

## 5.2 Contactless Sensor Technology

### 5.2.1 Performance of Sensor Systems

Depending on the exploited physical principle, contactless sensor systems may be characterized according to the following principles [156]:

- *Noise Immunity*: sensors are installed close to other sensors, switched amplifiers, and digital interfaces. It is desirable that this integration does not alter sensor specifications, nor adds noise.
- *Environmental Immunity*: measurement must be constant despite the accumulation of dust, chemicals, or mechanical shocks.
- *Compactness*: small sensor probes and amplifiers enable the sizing of easy to assemble, compact actuators.

For a chosen contactless measurement principle, their performance can be further rated quantified according to their

- *Measuring Range*: measurement range in which a change in the output signal still correlates to changes to a physical effect. Usually expressed as a maximum and minimum value (in the case of a current sensor, Ampere) that a sensor can measure.
- *Sensitivity*: indicates the ratio between output signal over the measured physical quantity; usually defined as a gain (or slope). A magnetic flux sensor that drives a voltage as output has a sensitivity defined as in  $\text{mV} \cdot \text{mT}^{-1}$  (analog) or  $\text{counts} \cdot \text{mT}^{-1}$  (digital).
- *Resolution*: smallest change in the output signal which can be distinguished with certainty; that is, considering noise. For a position measurement sensor, it can be expressed as an absolute value in  $\mu\text{m}$ .

### 5.2.2 Physical Principles

In this section, a total of five physical principles that enable contactless position measurement are discussed. They belong to the most recognized and researched within the domain of magnetic levitation [38, 156, 201].

### Capacitive Displacement Sensor

In capacitive position measurement, an alternating current is injected into a sensor probe, namely an electrode. This electrode then forms a capacitance with a mechanically isolated, conductive target, i.e. the rotor in the case of a bearingless motor, as seen in Fig. 5.1.

The target-sensor distance is obtained by indirectly measuring the value of the capacitance. This measurement is done by off-board electronics which must not lay close to the sensor probe. Magnetic levitation has been documented with the aid of this measurement principle [78, 84, 125, 154].

Capacitive measurement offers extremely high resolutions and wide bandwidth. Nevertheless, any change in the dielectric constant between the sensor electrode and the rotor, due to the presence of dust or liquids, perturbs position measurement. Moreover, electrostatic effects might build up a voltage in the insulated rotor and then disturb the measurement circuit. Capacitive position measurement remains a good solution if it can be ensured that the bearingless drive operates in highly pure environments. This *cannot* be ensured for a ventilator, for example.

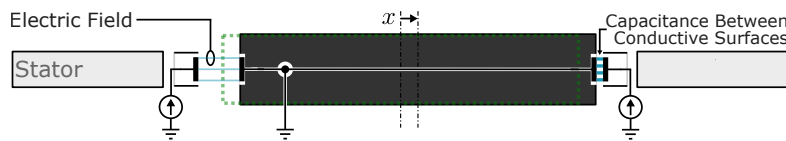


Figure 5.1: Capacitive position measurement principle. The rotor-sensor pair form a capacitance, whose value is continually determined by an amplifying circuit. Excellent measurement resolution is achieved, but it is susceptible to dust.

### Optical Displacement Sensor

The optical measurement of the distance to a target is possible by shining light upon the target and measuring its projected shadow, or light intensity, on the opposite side with a sensor as in Fig. 5.2. The light sensor can be a Charge-Coupled Device (CCD) or an array of photodiodes and it has been employed for bearingless motors [7, 119, 152].

The optic measurement principle allows for extremely high bandwidths as well as immunity against electromagnetic noise, which is abundant close to the air gap of the drive. Their electronics are more straightforward, as they do not require modulation techniques, and can be easily found as Integrated Circuits (IC) on the market.

The measurement range of optical sensors is limited by diffraction effects on the shadows of its target. If the application calls for encapsulation, this must warrant no interference from exterior light. Finally, the light source and sensor can be covered by dust or fluids, thus rendering the position measurement inexact.

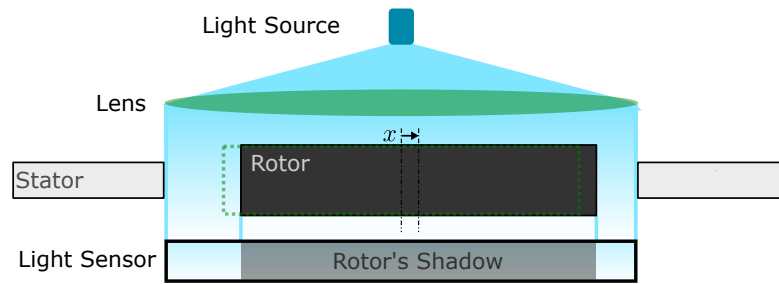


Figure 5.2: Optical position measurement principle. The target is illuminated from one side, and its projected shadow is measured. They offer extremely high bandwidths, but limited applicability due to the sensibility of the light source and sensor to dirt.

### Hall-Effect Based Displacement Sensor

The displacement and angular position of a PM rotor influence the magnetic flux density distribution in the air gap, along with its stray fields. The magnetic flux density can be measured, using the Hall-effect [63], to estimate the position of the rotor. This effect is traditionally used to estimate the angular position of rotors of electric drives. In this thesis, it is further shown how Hall-effect sensors (HESs) can help in the estimation of the radial position of the rotor in the air gap.

The advantage of exploiting the Hall-effect is that magnetic fields are present in measurable quantities even outside the air gap. In this way, off-the-shelf ICs can be easily positioned, in places where they do not interfere with drive construction or rotor encapsulation. These ICs also come with integrated electronics so their setup is relatively straightforward.

On the other hand, HESs not only pick up the magnetic flux of the rotor but also the field of the coils of the rotor, along its high-frequency Pulse Width Modulation (PWM) or other electromagnetic devices close to it. Therefore, electromagnetic noise must be heavily filtered out and fields from motor coils should be compensated for.

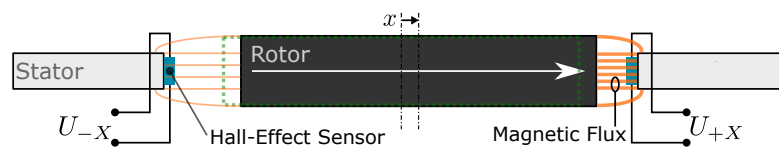


Figure 5.3: Hall-effect position measurement principle. HESs are installed around the air gap, to measure the magnetic flux density coming from the rotor. They are compact, and do not need complicate electronics, but can easily pick up electromagnetic noise.

### Inductive Displacement Sensor

Analogous to the capacitive position measurement, the position of the rotor can also be determined by using an inductor. In this case, a coil (which may or may not have a ferromagnetic core) is excited by an alternating voltage by an off-board circuit, thus generating magnetic flux. If a ferromagnetic object approaches the coil, magnetic flux through the coil increases. This phenomenon appears as an increase in coil inductance, as seen on Fig. 5.4a.

Inductive displacement sensors are naturally suited to measure ferromagnetic targets, e.g. iron, as proved in [137, 148]. As a consequence, this principle is naturally unfit for directly measuring rare-earth PM targets, such as the ones proposed for this thesis. These are barely ferromagnetic, with a  $\mu_{r,\text{NdFeB}} = 1.06$ , and are usually deployed as rotors in the bearingless domain.

### Eddy-Current Based Displacement Sensor

The hardware necessary for the implementation of an inductive displacement sensor can be adjusted to excite a (usually air-core) coil at high frequency. If the target is conductive, ECs are induced, generating losses inside the conductor. These power losses are then regarded as increased resistance at the terminals of the sensing coil.

These spawned ECs in the conductor also produce a magnetic flux against the coil, thus decreasing the total flux and its inductance. Ultimately, both the resistance and inductance of the sensing coil contain information, which is correspondingly exploited, about the distance to the target. The exploitation of this principle has rendered magnetic levitation possible for drives with [11, 112] and without PMs in their rotors [59, 61].

Among the advantages of EC position sensors, they have high bandwidth and are rather immune against dust or fluids. Moreover, the sensing coils might be fabricated onto Printed

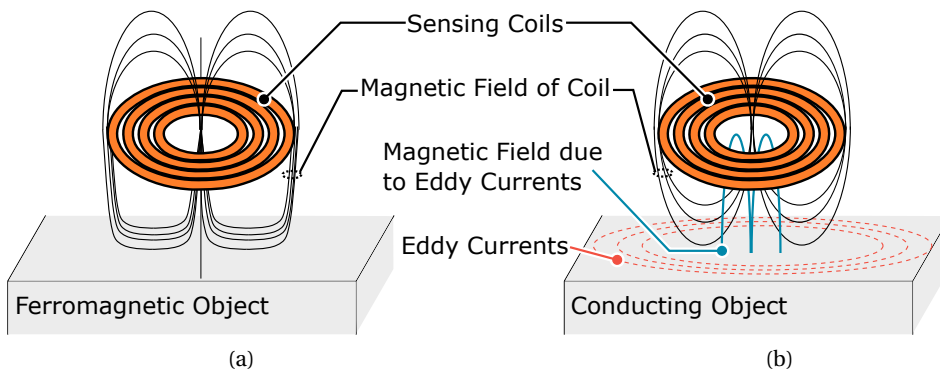


Figure 5.4: Contactless position measurement techniques that use sensing coils, exploiting (a) inductance changes due to ferromagnetic targets and the (b) EC effect due to conductive targets.

Circuit Boards (PCBs), so they can be fabricated with a reduced footprint.

On the other hand, they usually require electromagnetic shielding of one of the sensor sides, as they might measure motion on the coil plane opposite to the target, e.g. vibrations of the stator or coils. Also, they require complex excitation and demodulation electronics [77, 116, 128, 168, 200]. Different sensor probes of an array might interfere with one another, so their signal modulation must be tuned.

### Qualitative Overview

All in all, Table 5.1 summarizes the qualities of the aforementioned sensor types in a qualitative fashion. This table must be considered and suited to the application of the bearingless drive.

Foreign particles inside the rotor encapsulation must be considered for drives that are deployed in harsh environments. Dust would cover luminous devices and alter the dielectric constant in the air gap. Due to these reasons, sensors that exploit capacitive and optical principles are ruled out.

The conceived drive must also strive to high power density, despite its size. To this end, it is equipped with a PM rotor. This choice makes inductive sensors unsuitable for rotor position measurement.

As a consequence, EC and Hall-effect principles are usually regarded as the most robust and compelling. Both effects are looked upon in more detail in the next subsections.

Table 5.1: Qualitative comparison of position sensor technology. (+) indicates is a good performance, (✓) an average performance, and (-) a rather weak performance.

	Optic	Hall-effect	Capacitive	Inductive	Eddy-current
Meas. Range	+	✓	-	✓	✓
Linearity	+	✓	+	✓	✓
Resolution	+	-	+	✓	+
Noise Imm.	+	-	✓	✓	✓
Env. Imm.	-	✓	-	+	+
Compactness	-	+	✓	+	+



### 5.3 Eddy-Current Based Estimation of Rotor Radial Position

As mentioned, the EC position sensor relies upon an inductor that generates an AC magnetic field in its surroundings. In this section, the frequency and target-distance effects upon ECs, as well as sensing coil placement in bearingless drives, are discussed.

#### 5.3.1 Modelling

The impedance of the coil is a function of its geometry, but also of its nearby objects. This can be modeled [197] by the equivalent circuit of Fig. 5.5. If an electrically conductive target approaches, the power losses induced in this body can be regarded as an increase of the *resistance* viewed by an AC voltage source. The induced currents generate a field opposing to that of the coil, hence reducing its magnetic flux. Once again, this can be considered as a decrease in the *inductance* at the source.

The circuit of Fig. 5.5 can be modelled as *equivalent* impedance  $Z_{eq.}$  [56] with real and imaginary parts

$$\begin{aligned} \text{Re}\{Z_{eq.}\} &= R_{eq.} = R_{coil} + k^2 \cdot \left\{ \frac{(L_{coil}L_{targ.})\omega^2}{R_{coil}^2 + (L_{targ.}\omega)^2} \right\} \cdot R_{targ.}, \\ \text{Im}\{Z_{eq.}\} &= L_{eq.} = L_{coil} - k^2 \cdot \left\{ \frac{(L_{coil}L_{targ.})\omega^2}{R_{coil}^2 + (L_{targ.}\omega)^2} \right\} \cdot L_{targ.}, \end{aligned} \quad (5.1)$$

with  $0 < k < 1$  the inductance coupling coefficient as in  $k = M_{t/c} \cdot (L_{targ.} \cdot L_{coil})^{-1/2}$ ,  $M_{t/c}$  the mutual inductance between coil and target (as a function of distance  $x$ ) and  $\omega$  the fundamental excitation frequency of  $V_{HF}$ . If coupling coefficient  $k$  decreases for increasing coil-target distance  $x$ , the real and imaginary parts of  $Z_{eq.}$  follow the trends shown in Fig. 5.6. In this context, the equivalent inductance, i.e.  $\text{Im}\{Z_{eq.}\}$  can change by a factor of five depending on  $x$  and the material of the target [82].

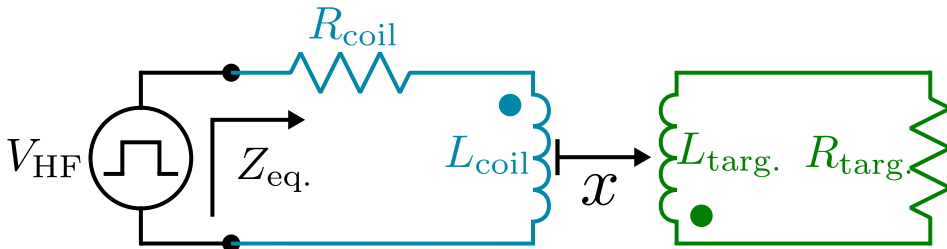


Figure 5.5: The EC sensing coil is modelled as a real inductance, coupled to another real inductance that corresponds to the conductive target. For a given target, the impedance at the source  $Z_{eq.}$  is a function of the target distance  $x$  and excitation frequency  $\omega$ .

### 5.3 Eddy-Current Based Estimation of Rotor Radial Position

The build-up of the EC effect is alternatively depicted by the FE simulation done in femm [105], shown in Fig. 5.7. At low frequencies, there is no induced current in the target, so the magnetic field of the sensing coil can penetrate it without opposition. Increasing the excitation frequency of the coil induces larger currents in the target, which then create the opposing magnetic flux. As a result, the magnetic flux distribution is compressed outwards and no longer passes through the target, leading to thinner conductive skin depth.

For a high frequency voltage excitation, the influence of a conductive target upon a nearby coil is depicted in Fig. 5.8. Intuitively, large target distances lead to practically no induced currents and little magnetic flux distortion. Analogously, closer targets have larger induced currents and increasingly compress the magnetic flux exiting the coil.

In reality, the drive geometry is 3D and more complex than that of Figs. 5.7-5.8. Moreover, different possible targets, such as copper and ferromagnetic material, lay close to the sensing coil and the desired NdFeB rotor target. The calibration of an EC setup is thus best performed empirically.

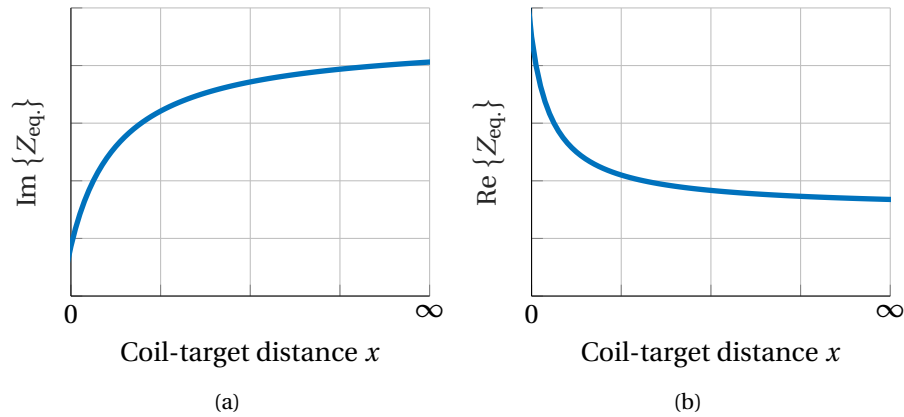


Figure 5.6: Typical trends for (a) imaginary and (b) real part—for a fixed excitation frequency  $\omega$ —of the equivalent impedance  $Z_{eq.}$  of the EC sensing coil.

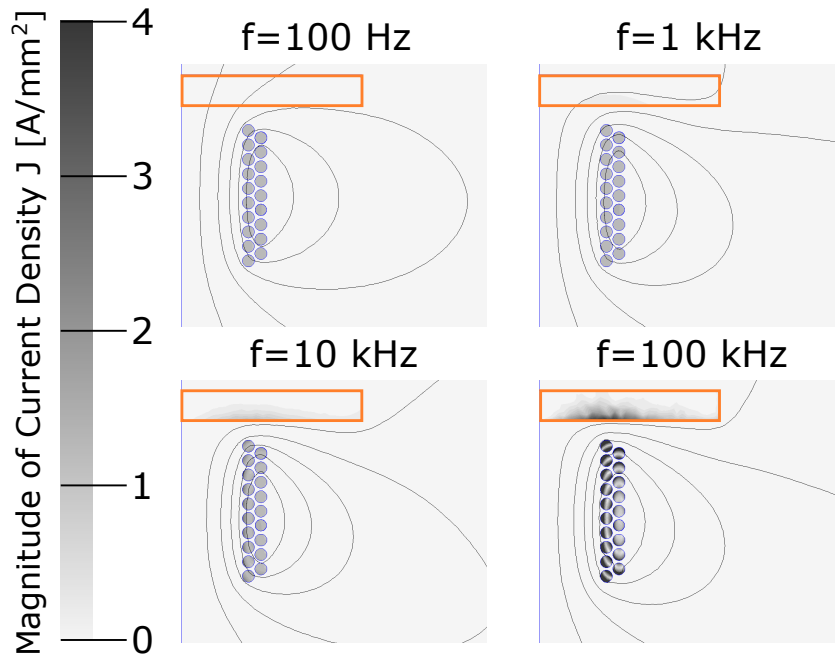


Figure 5.7: Exemplary 2D FE simulation, with angular symmetry, of the EC effect. A coil excites the conductive target out of copper, marked in orange. The simulation is performed for increasing excitation frequency. The magnetic flux density is defined by isolines and the current density in greyscale.

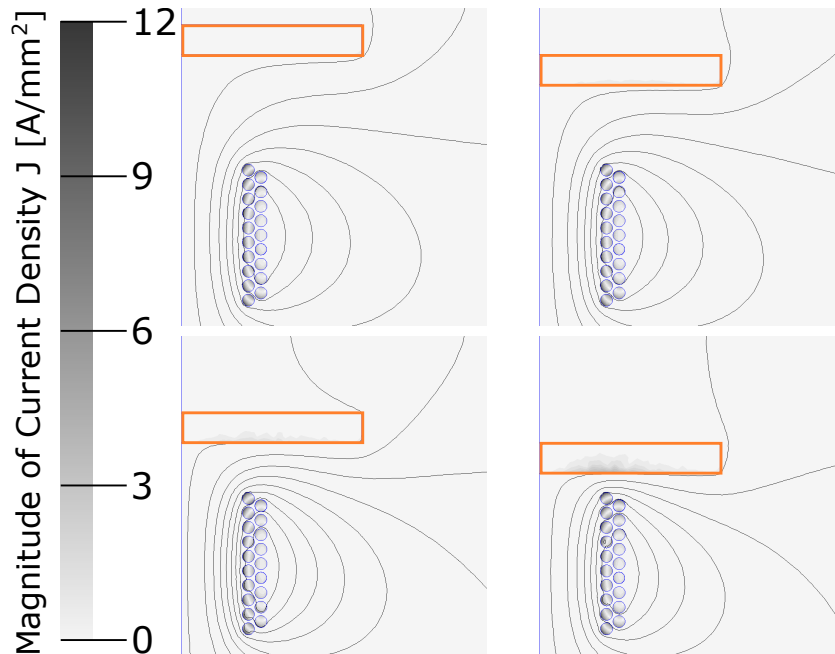


Figure 5.8: Same simulation as in Fig. 5.7, but now with fixed excitation frequency  $f = 10$  kHz and an approaching target.

### 5.3.2 Placement of Sensor

With the desired PM-iron configuration, the radial position of the rotor must be controlled. Therefore, the natural choice is to place the sensing coils radially, as depicted in Fig. 5.9. This has the advantage, that it directly measures the desired direction. Furthermore, if the rotor is larger in  $z$ -direction than the coils (which is usually the case), the sensing system becomes less sensitive to axial displacements and tilting movements of the rotor. It is also suitable if an axial ventilator, with a bore in its conduct, is envisaged.

Nonetheless, the problem of this installation is that the sensors lay inside the air gap, so they are close to the ferromagnetic (and electrically-conductive) stator, the coils, and their associated electromagnetic noise. Moreover, the room here is limited.

A cleaner approach would be to axially place the sensors so that the coils excite the exterior or interior edges of the rotor. In this fashion, the sensing coils can be removed from the proximity of noisy motor coils and other conductors that might vibrate. Nevertheless, when detecting the conductive edges of the rotor, the positioning system *cannot* distinguish between tilting and radial motions. Axial rotor displacement might also bring the excitation electronics of the system out of their operation range. Moreover, this installation possibility is less compatible with an axial blower —as it would lay in the ventilation bore—. For this application and topology, the axial sensor orientation is thus dismissed.

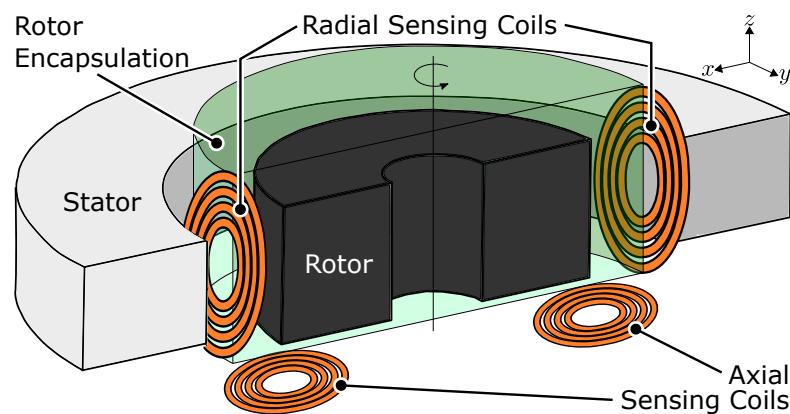


Figure 5.9: Sensing coils exploit the EC effect to measure the radial position (here the  $x$  axis) of its electrically conductive rotor. The coils can be either placed radially, to measure the cylindrical surface of the rotor, or axially, to measure its edges.

### 5.4 Hall-Effect Sensor Estimation of Rotor Angular and Radial Position

The magnetic flux coming from the PM rotor enters the stator by passing through the air gap. By employing HESs, this magnetic flux is measured to estimate the angular and radial position of the rotor, and to control the current of the bearingless motor accordingly.

In this section, an overview of how rotor flux information is utilized to evaluate the radial position of the rotor.

#### 5.4.1 Placement of Sensor

Figure 5.10 depicts in an exemplary fashion the flux paths in a disc drive. Most of the flux, depicted in red, closes radially into and out of the stator. This portion of the flux contributes to the classic torque generation in electric drives, but also to the force generation and radial stiffness in the foreseen bearingless drive configuration.

Nevertheless, given the flat design of the intended drives, a sizable part of the magnetic flux corresponds to stray fluxes, depicted in blue in Fig. 5.10. By definition, they scarcely contribute to torque generation and do not flow directly through the magnetic air gap. This apparent disadvantage, amplified by the geometry of the conceived drives, can be exploited for sensor placement.

A sensor array that lays *outside* the magnetic air gap enables an easy assembly of electric drives, as no extra space or constructive measures must be conceived during the development process. Moreover, it opens the way towards *simple* encapsulation concepts, which further reinforce the upside of bearingless drives. Conveniently enough, stray fields outside the airgap show low intensities, compatible with most off-the-shelf HESs. Hence, in this thesis, sensor placements that measure radial and axial stray fields are researched.

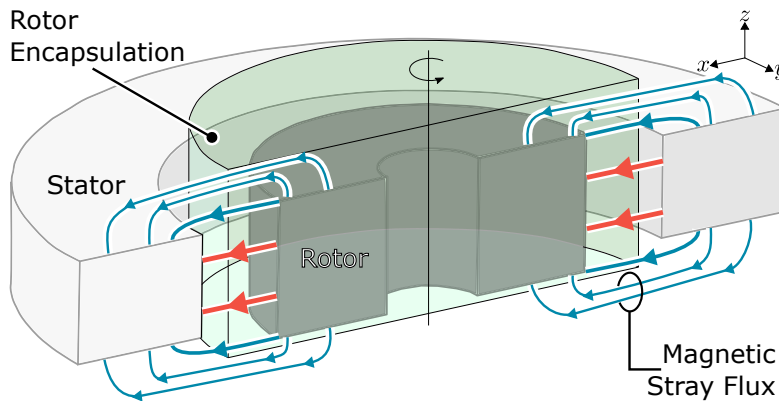


Figure 5.10: Magnetic flux coming from the PM rotor into the stator. HESs are installed so that they are axially or radially pierced by stray fields, drawn in blue.

An array of four opposing hall-sensors would lead to an intuitive radial rotor position estimation in  $x - y$  coordinates, but would not fit symmetrically onto a six-coil drive. A six HES array is thus initially proposed. This array may be placed on the top or bottom side of the stator of Fig. 5.10.

### 5.4.2 Modelling of Rotor Fields

Fine control of the bearing force demands an accurate knowledge of the rotor angular position [38]. To comply with this stipulation, ratiometric-output HESs, whose output is linear to the measured magnetic flux density, are employed.

An array of ratiometric HESs thus enables the estimation of rotor angular position with high resolution. These fields contain information about the radial position of the rotor in the air gap that usually goes unexploited. Indeed, bearingless motors with a slotted stator have already been commissioned only by measuring the magnetic flux density of the HESs [189], but its specifics are not disclosed.

The mathematical derivation of angle and position estimation is general for any diametrically-magnetized one pole-pair levitated drives  $p_{\text{rot.}} = 1$ , starting from Fig. 5.11.

The drive's magnetic flux density is now studied by an array of six HESs  $H_k$  with  $k=1,2,\dots,6$ . They are symmetrically distributed on the interior of the stator, with separation  $\gamma_{\text{hs}} = \pi/3$  and angular position  $\theta_k = (k-1) \cdot \gamma_{\text{hs}}$  as in Fig. 5.11.

For the diametrically-magnetized rotor, the magnetic flux density in the air gap is simplified

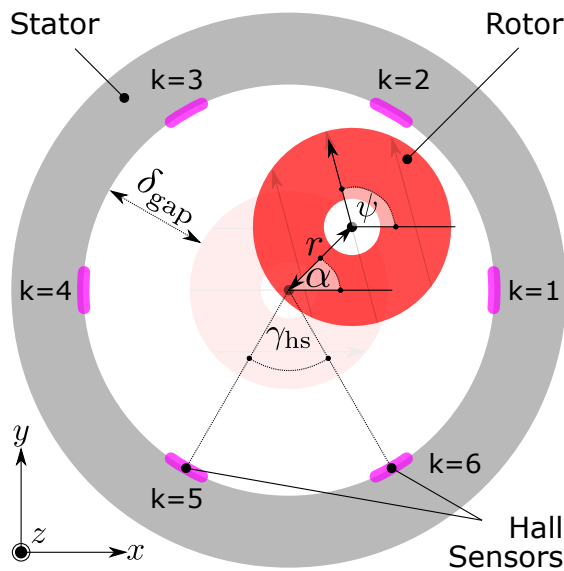


Figure 5.11: Cross-section of a slotless drive with an exaggeratedly uncentered rotor and the symmetrical positioning of six HESs on the stator.

and only a fundamental harmonic is considered. In the case of multi-polar rotors or large teeth numbers, this is an oversimplification, which may produce an error between the real and estimated rotor position.

On the whole, each sensor  $k$  then measures a phase-shifted magnetic flux density  $B_k$  as in

$$B(\psi, r, \alpha, k) = \hat{B}(r, \alpha, k) \cdot \cos(\theta_k - \psi - \tau_k), \quad (5.2)$$

with  $k = 1, 2, \dots, 6$ ,

with  $\tau_k$  the rotor displacement projected onto the tangential axis of the coordinate system of the  $k$ th-sensor —denominated  $r_{\tau,k}$ —, and  $s_\tau$  the phase-shift to displacement sensitivity as in  $\tau_k = s_\tau \cdot r_{\tau,k}$ . This proportional phase-shift only distorts the magnetic flux density at large rotor deflections —according to FE simulations—, so it is hereafter *disregarded*.

For feeble rotor displacements  $r$  in direction  $\alpha$ , the peak magnetic flux density  $\hat{B}(r, \alpha, k)$  of Eq. (5.2) varies as in [95]

$$\begin{aligned} \hat{B}(r, \alpha, k) &= \hat{B}_0 \cdot \frac{1}{1 - \frac{r}{\delta_{\text{gap}}} \cdot \cos(\alpha - \theta_k)} \approx \hat{B}_0 \cdot \left[ 1 + \frac{r}{\delta_{\text{gap}}} \cdot \cos(\alpha - \theta_k) \right], \\ &= \hat{B}_0 \cdot [1 + r \cdot s_r \cdot \cos(\alpha - \theta_k)], \end{aligned} \quad (5.3)$$

using the Taylor series approximation of  $1/(1-x) \approx (1+x)$ , for  $|x| < 1$  and  $\hat{B}_0$  the peak-flux density of the centered rotor.

The normal flux path is initially assumed to be determined by  $\delta_{\text{gap}}$ , which appears as a gain  $1/\delta_{\text{gap}}$  of radial displacement  $r$ . Yet, this flux path is not always straight nor evident, especially in disc drives. Therefore, the equation is further generalized with a radial displacement gain  $s_r$ , in  $\text{mm}^{-1}$ , that depends on *where* the sensor is placed.

HESs also sense the axial displacements ( $z$ -direction) of the rotor. If they are *not* placed at the same axial plane as the rotor, they can sense if it approaches or moves away. This might prove useful in applications where axial vibrations need to be suppressed [169]. Provided a small displacement, the change in peak magnetic flux density  $\hat{B}$  can also have a linear dependency upon the axial position  $z$ , as  $r$  has in Eq. (5.3).

Considering Eqs. (5.2) - (5.3) and the possibility of axial displacement, the magnetic flux density that the  $k$ -th HES measures is

$$B^\pm(\psi, r, \alpha, k, z) = \hat{B}_0 \underbrace{[1 + r \cdot s_r \cdot \cos(\alpha - \theta_k)]}_{\text{polar rotor displacement}} \underbrace{(1 \pm z \cdot s_z)}_{\text{axial rotor displacement}} \underbrace{\cos(\theta_k - \psi)}_{\text{rotor rotation}}, \quad (5.4)$$

with the  $+$  or  $-$  sign for axial rotor displacement if the HES lies on above or below the rotor still stand position, respectively.

Measuring the flux of the rotor from above *and* below, for a total of 6 top and 6 bottom HESs, helps to estimate the axial position of the rotor with high accuracy and without bias.

### 5.4.3 Estimation of Angular Rotor Position

The objective of rotor angle  $\psi$  estimation is to generate a signal pair  $(\cos \psi, \sin \psi)$  out of the Hall-effect sensor measurements. For this, the effects of radial and axial displacement contained in each HES measurement in Eq. (5.4),  $r$ , and  $z$ , respectively, must be eliminated.

To eliminate the axial position dependency of the HESs, the top and bottom sensors are added, generating the pair

$$\begin{aligned} B^{\text{sum}}(\psi, r, \alpha, k) &= B^+(\psi, r, \alpha, k, z) + B^-(\psi, r, \alpha, k, z) \\ &= 2 \cdot \hat{B}_0 \cdot [1 + r \cdot s_r \cdot \cos(\alpha - \theta_k)] \cdot \cos(\theta_k - \psi). \end{aligned} \quad (5.5)$$

To cancel the effect of the displaced rotor in  $(r \cdot s_r)$ , all opposing Hall-sensor pairs signals  $B_k^{\text{sum}}$  for  $k = 0, 1, 2$  are subtracted, resulting in

$$\begin{aligned} & B^{\text{sum}}(\psi, r, \alpha, k) - B^{\text{sum}}(\psi, r, \alpha, k+3) \\ = & 2 \cdot \hat{B}_0 \cdot [1 + r \cdot s_r \cdot \cos(\alpha - \theta_k)] \cdot \cos(\theta_k - \psi) \\ & - 2 \cdot \hat{B}_0 \cdot [1 - r \cdot s_r \cdot \cos(\alpha - \theta_k)] \cdot -\cos(\theta_k - \psi) \\ = & 4 \cdot \hat{B}_0 \cdot \cos(\theta_k - \psi), \quad \text{for } k = 1, 2, 3. \end{aligned} \quad (5.6)$$

since  $\theta_{k+3} = \theta_k + \pi$ . Hereafter,  $(\cos \psi, \sin \psi)$  are calculated by combining the signals as

$$\begin{aligned} S_{\cos} &= \begin{aligned} & \{B^{\text{sum}}(\psi, r, \alpha, 1) - B^{\text{sum}}(\psi, r, \alpha, 4)\} \\ & + \frac{1}{2} \{B^{\text{sum}}(\psi, r, \alpha, 2) - B^{\text{sum}}(\psi, r, \alpha, 5)\} \\ & - \frac{1}{2} \{B^{\text{sum}}(\psi, r, \alpha, 3) - B^{\text{sum}}(\psi, r, \alpha, 6)\} \end{aligned} \\ &= 6 \cdot \hat{B}_0 \cdot \cos \psi, \\ S_{\sin} &= \begin{aligned} & \frac{\sqrt{3}}{2} \{B^{\text{sum}}(\psi, r, \alpha, 2) - B^{\text{sum}}(\psi, r, \alpha, 5)\} \\ & + \frac{\sqrt{3}}{2} \{B^{\text{sum}}(\psi, r, \alpha, 3) - B^{\text{sum}}(\psi, r, \alpha, 6)\} \end{aligned} \\ &= 6 \cdot \hat{B}_0 \cdot \sin \psi. \end{aligned} \quad (5.7)$$

These signals are traditionally utilized only for drive control purposes, such as field-oriented control, but are also needed to demodulate the radial rotor position, as it is seen next.

### 5.4.4 Estimation of Radial Rotor Position

The estimation of the radial rotor position aims towards obtaining a signal pair  $(x, y)$  on the fixed stator coordinate system of Fig. 5.10. In practice, this means obtaining the polar displacement  $r$  and the polar angle  $\alpha$ .

For a centered, one-pole pair rotor, opposing sensors measure the same flux but with opposing



signs, thus rendering a null signal sum. Yet, any radial rotor eccentricity would become apparent in this sum. This intuition is seen in the mathematical model as

$$\begin{aligned}
 & B^{\text{sum}}(\psi, r, \alpha, k) + B^{\text{sum}}(\psi, r, \alpha, k+3) \\
 = & 2 \cdot \hat{B}_0 \cdot [1 + r \cdot s_r \cdot \cos(\alpha - \theta_k)] \cdot \cos(\theta_k - \psi) \\
 & + 2 \cdot \hat{B}_0 \cdot [1 - r \cdot s_r \cdot \cos(\alpha - \theta_k)] \cdot -\cos(\theta_k - \psi) \\
 = & 4 \cdot \hat{B}_0 \cdot [r \cdot s_r \cdot \cos(\alpha - \theta_k)] \cdot \cos(\theta_k - \psi), \quad \text{for } k = 1, 2, 3.
 \end{aligned} \tag{5.8}$$

Hereafter, the position of the rotor on its coordinate system is calculated by computing

$$\begin{aligned}
 S_{x_{\text{rot}}} &= \{B^{\text{sum}}(\psi, r, \alpha, 1) + B^{\text{sum}}(\psi, r, \alpha, 4)\} \\
 &\quad - \frac{1}{2} \{B^{\text{sum}}(\psi, r, \alpha, 2) + B^{\text{sum}}(\psi, r, \alpha, 5)\} \\
 &\quad - \frac{1}{2} \{B^{\text{sum}}(\psi, r, \alpha, 3) + B^{\text{sum}}(\psi, r, \alpha, 6)\} \\
 &= 3 \cdot \hat{B}_0 \cdot (r \cdot s_r) \cdot \cos(\psi + \alpha), \\
 S_{y_{\text{rot}}} &= \frac{\sqrt{3}}{2} \{B^{\text{sum}}(\psi, r, \alpha, 2) + B^{\text{sum}}(\psi, r, \alpha, 5)\} \\
 &\quad - \frac{\sqrt{3}}{2} \{B^{\text{sum}}(\psi, r, \alpha, 3) + B^{\text{sum}}(\psi, r, \alpha, 6)\} \\
 &= 3 \cdot \hat{B}_0 \cdot (r \cdot s_r) \cdot \sin(\psi + \alpha).
 \end{aligned} \tag{5.9}$$

The position control, reviewed in a Chapter 6, is done on the *stator* coordinate system. Therefore, the results of Eq. (5.9) must be demodulated and its dependency on  $\psi$  removed as

$$\begin{bmatrix} S_{x_{\text{st}}} \\ S_{y_{\text{st}}} \end{bmatrix} = \frac{2}{S_{\cos}^2 + S_{\sin}^2} \cdot \begin{bmatrix} S_{\cos} & S_{\sin} \\ -S_{\sin} & S_{\cos} \end{bmatrix} \cdot \begin{bmatrix} S_{x_{\text{rot}}} \\ S_{y_{\text{rot}}} \end{bmatrix} = (r \cdot s_r) \cdot \begin{bmatrix} \cos \alpha \\ \sin \alpha \end{bmatrix}, \tag{5.10}$$

It is noteworthy to mention, that for *even* rotor pole-pair numbers, opposing Hall-sensor pairs see the same magnitude and sign of magnetic flux density. In this case, performing the operations of Eq. (5.7) would render the radial rotor position result of Eq. (5.9), and vice-versa. The calculations can be thus performed similarly.

### 5.4.5 Estimation of Axial Rotor Position

As indicated, the HESs are sensible to axial rotor displacements. Depending on the application, it might be desirable to eliminate vibrations in this direction [48, 113, 169].

To obtain a signal proportional to the axial displacement, i.e an unbiased signal, the sinusoids of Eq. (5.7) are calculated with the upper and lower sensors separately. Their difference is

subsequently calculated, and these signals demodulated, as in

$$\begin{aligned}
 S_{\cos}^{\pm} &= \begin{aligned} &\{B^{\pm}(\psi, r, \alpha, 1) - B^{\pm}(\psi, r, \alpha, 4)\} \\ &+ \frac{1}{2} \{B^{\pm}(\psi, r, \alpha, 2) - B^{\pm}(\psi, r, \alpha, 5)\} \\ &- \frac{1}{2} \{B^{\pm}(\psi, r, \alpha, 3) - B^{\pm}(\psi, r, \alpha, 6)\} \end{aligned} \\
 &= 3 \cdot \hat{B}_0 \cdot \cos(\psi) \cdot (1 \pm z \cdot s_z), \\
 \rightarrow S_{\cos}^+ - S_{\cos}^- &= 6 \cdot \hat{B}_0 \cdot (z \cdot s_z) \cdot \cos \psi \\
 S_{\sin}^{\pm} &= \begin{aligned} &\frac{\sqrt{3}}{2} \{B^{\pm}(\psi, r, \alpha, 2) - B^{\pm}(\psi, r, \alpha, 5)\} \\ &+ \frac{\sqrt{3}}{2} \{B^{\pm}(\psi, r, \alpha, 3) - B^{\pm}(\psi, r, \alpha, 6)\} \end{aligned} \\
 &= 3 \cdot \hat{B}_0 \cdot \sin(\psi) \cdot (1 \pm z \cdot s_z), \\
 \rightarrow S_{\sin}^+ - S_{\sin}^- &= 6 \cdot \hat{B}_0 \cdot (z \cdot s_z) \cdot \sin \psi.
 \end{aligned} \tag{5.11}$$

So the axial displacement signal is

$$S_z = \frac{S_{\cos} \cdot (S_{\cos}^+ - S_{\cos}^-) + S_{\sin} \cdot (S_{\sin}^+ - S_{\sin}^-)}{S_{\cos}^2 + S_{\sin}^2} = z \cdot s_z. \tag{5.12}$$

### 5.4.6 Compensation of Coil Currents

To measure the radial and angular rotor position with precision, the HESs must ideally measure *only* the magnetic flux density of the rotor. Nevertheless, the actuation of the drive requires that this field is superposed to that of the motor coils, that control the levitation and turning motion of the rotor.

The magnetic flux density of the rotor is superposed to that of the motor coils, and the magnetic flux density of the latter is modelled as a linear function of the coil current. Since the current is anyways measured for current control purposes, this allows for a straightforward compensation of the coil excitation for a more precise estimation of the magnetic flux density of the rotor.

The magnetic flux density at the location of sensor  $H_i$  is

$$B_{H_i} = B^{\pm}(\psi, r, \alpha, i, z) + \sum_{k=1}^6 d_{i,k} \cdot I_k \tag{5.13}$$

with  $I_k$  and  $d_{i,k}$  the current in the  $k$ -th coil and a proportionality constant of the magnetic flux density at sensor  $i$  due the current of the  $k$ -th coil in  $\text{T} \cdot \text{A}^{-1}$ , respectively. Correspondingly, the farther away coil  $k$  is from the sensor  $H_i$  the smaller the value of  $d_{i,k}$ .

To further typify the compensation, the currents are separated into drive and bearing components. Given the relationship between the currents of opposing coils of Eq. (3.43)-(3.45), the

compensation then results in

$$\begin{aligned}
 B_{H_i} &= B^\pm(\psi, r, \alpha, i, z) + \sum_{k=1}^6 d_{i,k} \cdot I_{\text{drv},k} + \sum_{k=1}^6 d_{i,k} \cdot I_{\text{bng},k} \\
 &= B^\pm(\psi, r, \alpha, i, z) \\
 &\quad + \{d_{i,1} I_{\text{drv},1} + d_{i,2}(-I_{\text{drv},3}) + d_{i,3} I_{\text{drv},2} + d_{i,4}(-I_{\text{drv},1}) + d_{i,5} I_{\text{drv},3} + d_{i,6}(-I_{\text{drv},2})\} \\
 &\quad + \{d_{i,1} I_{\text{bng},1} + d_{i,2} I_{\text{bng},2} + d_{i,3} I_{\text{bng},3} + d_{i,4}(I_{\text{bng},1}) + d_{i,5}(I_{\text{bng},2}) + d_{i,6}(I_{\text{bng},3})\}.
 \end{aligned} \tag{5.14}$$

The currents are regrouped and the sum of a star point system of Eqs. (3.46)-(3.47) is utilized to further simplify Eq. (5.14) into

$$\begin{aligned}
 B_{H_i} &= B^\pm(\psi, r, \alpha, i, z) \\
 &\quad + \{(d_{i,1} + d_{i,2} - d_{i,4} - d_{i,5}) I_{\text{drv},1} + (d_{i,2} + d_{i,3} - d_{i,5} - d_{i,6}) I_{\text{drv},2}\} \\
 &\quad + \{(d_{i,1} - d_{i,3} + d_{i,4} - d_{i,6}) I_{\text{bng},1} + (d_{i,2} - d_{i,3} + d_{i,5} - d_{i,6}) I_{\text{bng},2}\}.
 \end{aligned} \tag{5.15}$$

The currents flowing in its upper and lower half of Fig. 5.12 affect the magnetic flux density upon sensor  $H_i$  in opposing fashion, so that

$$-d_{i,6} = d_{i,1} \quad -d_{i,5} = d_{i,2} \quad -d_{i,4} = d_{i,3}. \tag{5.16}$$

This renders

$$\begin{aligned}
 B_{H_i} &= B^\pm(\psi, r, \alpha, i, z) \\
 &\quad + \{(d_{i,1} + 2d_{i,2} + d_{i,3}) I_{\text{drv},1} + (d_{i,1} + 2d_{i,2} + d_{i,3}) I_{\text{drv},2}\} \\
 &\quad + \{2 \cdot (d_{i,1} - d_{i,3}) I_{\text{bng},1} + (d_{i,1} - d_{i,3}) I_{\text{bng},2}\},
 \end{aligned} \tag{5.17}$$

so only parameters  $d_{i,1}$ ,  $d_{i,2}$ , and  $d_{i,3}$  must be obtained.

All in all, Eq. (5.14) can be represented in its matrix form, for all  $H_i$  sensors, with  $i = 1, 2, \dots, 6$ , as

$$(B_{H_1}, B_{H_2}, B_{H_3}, B_{H_4}, B_{H_5}, B_{H_6})^T = \vec{B}_H = \vec{B}_{\text{rot.}} + k_{\text{HES,drv.}} \cdot \vec{I}_{\text{drv.}} + k_{\text{HES,bng.}} \cdot \vec{I}_{\text{bng.}}, \tag{5.18}$$

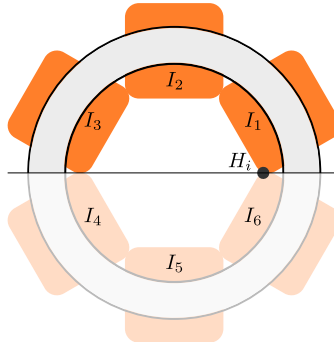


Figure 5.12: The symmetric sensor and coil array, highlighted by the line, simplifies the compensation scheme of the motor current upon the HESs by providing Eq. (5.16).

with  $k_{\text{HES,drv.}}$ ,  $k_{\text{HES,bng.}}$  the drive and bearing compensation matrixes and  $\vec{I}_{\text{drv.}} = [I_{\text{drv.,1}}, I_{\text{drv.,2}}]^T$  and  $\vec{I}_{\text{bng.}} = [I_{\text{bng.,1}}, I_{\text{bng.,2}}]^T$ . Doing the previous development for all sensors simplifies Eq. (5.18) to

$$\vec{B}_H = \vec{B}_{\text{rot.}} + d_{\text{drv.}} \begin{pmatrix} 1 & 1 \\ 0 & 1 \\ -1 & 0 \\ -1 & -1 \\ 0 & -1 \\ 1 & 0 \end{pmatrix} \begin{bmatrix} I_{\text{drv.,1}} \\ I_{\text{drv.,2}} \end{bmatrix} + d_{\text{bng.}} \begin{pmatrix} 2 & 1 \\ -1 & 1 \\ -1 & -2 \\ 2 & 1 \\ -1 & 1 \\ -1 & -2 \end{pmatrix} \begin{bmatrix} I_{\text{bng.,1}} \\ I_{\text{bng.,2}} \end{bmatrix}, \quad (5.19)$$

$$\vec{B}_H = \vec{B}_{\text{rot.}} + \{d_{\text{drv.}} M_{I,\text{drv.}}\} \cdot \vec{I}_{\text{drv.}} + \{d_{\text{bng.}} M_{I,\text{bng.}}\} \cdot \vec{I}_{\text{bng.}}$$

which means that, in theory, only *two* parameters  $d_{\text{drv.}} = d_{i,1} + 2d_{i,2} + d_{i,3}$  and  $d_{\text{bng.}} = d_{i,1} - d_{i,3}$  have to be determined.

In practice, Eq. (5.19) does not compensate for the influence of motor coils completely, due to mounting imperfections and sensor-gain dispersion. The singular elements of matrixes  $k_{\text{HES,drv.}}$  and  $k_{\text{HES,bng.}}$  of Eq. (5.18) must be determined for high-precision current compensation.

## 5.5 Conclusion

In this chapter, the physics behind various contactless sensor types exploited in the domain of magnetic levitation is reviewed. Their advantages and disadvantages are exposed and matched to the possible operating conditions of the drives presented in this thesis.

The motivation and demands of the disc-drives considered in this thesis best match the EC-based position estimation to measure the *radial position* of the rotor inside its mechanical clearance.

On the other hand, linear HESs are deemed fit to estimate the *angular position* of the rotor. Detailed modelling of the magnetic flux density imposed by the rotor inside the air gap reveals that this flux *also* contains information about the radial position of the rotor. By combining the signals of the sensors, the radial position of the rotor can be theoretically estimated. For the sake of the estimation accuracy using HESs—in terms of angular and radial position—a compensation scheme of the coil currents is also proposed.

Considering the advantages and disadvantages of both sensor technology candidates, both EC and HESs are installed and rated in Chapter 7.

## **6 Control and Compact System Integration in Magnetically-levitated Drives**

### **6.1 Introduction**

In this chapter, the integration of the hardware for two bearingless disc drives prototypes is presented. The control and sensor schemes of the drive are also explained.

The control schemes that regulate magnetic levitation and rotatory speed control of the drives are introduced. The interaction of these mechanic phenomena is explained along the faster control needed to regulate the current and the power electronics that energize the drives.

The realization of the highly-compact sensor system and electronics are presented, along with their flexibility for adaptation to other systems. This is fundamental for the compactness of the prototypes of the next chapters.

### **6.2 Motor Control**

The control of ball-bearing rotatory electric drives focuses on the precise regulation of either the angular position *or* speed of the motor. Failure to comply can lead to position or speed errors, unnecessary vibrations, and sub-par drive energetic efficiency.

In the domain of magnetic levitation, the additional task of stable, contactless levitation is due. Failure to control rotor position surely leads to excess vibrations and drive damage in the case of a mechanical shock. Therefore, rotor position control represents one of the biggest challenges in this domain.

In this section, the automatic control schemes needed to regulate proper drive functioning are detailed in a general and particular fashion. The software, as well as the hardware required for these tasks, are presented.

### 6.2.1 Control Schemes

Figure 6.1 displays the control system, the transducers, and the electric and mechanical model of the actuator. The control system—which is programmed in a microcontroller—gathers information about the states of the actuator through the transducers.

The *main* objective of the control schemes is to control the radial position of the rotor, and—with this task under control—regulate the rotatory speed of the rotor. The modulation of the current is subordinate and serves to precisely and timely impose the current references yielded by the aforementioned tasks in the coils of the drive.

### 6.2.2 Rotor Position Control

The proposed magnetic configuration of the drive leads to an unstable radial position of the rotor. This radial position, which lays on the  $x$  and  $y$  direction, must be controlled for contactless levitation. The position control model is studied initially for one axis and is valid for both axes due to their similarity [110].

#### Radial Instability

The model for radial position control for a *single* axis can be derived from the balance of forces of the mechanical system in Fig. 6.1 as

$$\Sigma F = m_{\text{rot.}} \cdot \ddot{x} = F_{\text{load}} + F_{\text{act.}} + F_{\text{r.}}, \quad (6.1)$$

with  $x$  the position of the rotor in the air gap,  $F_{\text{act.}}$  the active force on the rotor due to coil energization,  $F_{\text{r.}}$  the passive force upon the rotor due to reluctance forces, and  $F_{\text{load}}$  a disturbance force. The passive and active forces are modelled as

$$\begin{aligned} F_{\text{r.}} &= k_x \cdot x, \\ F_{\text{act.}} &= k_F \cdot i_{\text{bng.}}, \end{aligned} \quad (6.2)$$

with  $i_{\text{bng.}}$  the bearing current on the controlled axis. Thus, for a perfectly controlled current, the bearings model's transfer function results in

$$P_{\text{bng.}}(s) = \frac{X(s)}{I_{\text{bng.}}(s)} = \frac{k_F}{m_{\text{rot.}} \cdot s^2 - k_x}, \quad (6.3)$$

which composes an intrinsically unstable system for  $k_x > 0$ . For the studied drive dimensions, bearing time constants lay in the order of  $\tau_{\text{bng.}} = \sqrt{m_{\text{rot.}}/k_x} \sim 10^0$  ms, so its control must follow more rapidly.

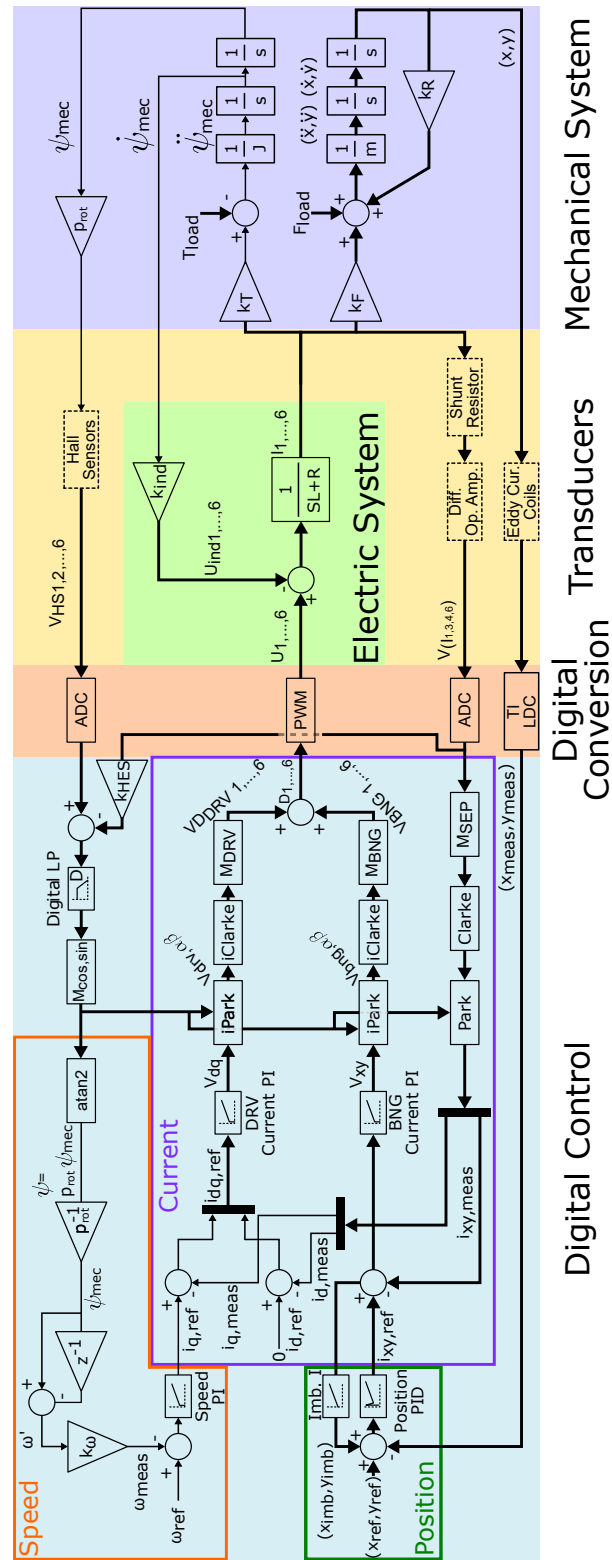


Figure 6.1: Diagram of the digital control, analogical conversion, transducers, and electric and mechanical model of a magnetically-levitated system. The digital control schemes and their implementation are explained in this section, as well as the digital conversion of their required signals.

### Disturbance Rejection

Within this context, the control aims to bring the rotor to a (usually) fixed position  $x_{\text{ref}} = 0$ . To this end, the destabilizing action of the passive stiffness must be counteracted *and* enough damping must be provided so that the position of the rotor is immune to disturbance  $F_{\text{load}}$  [156]. For an ideal, non-delayed current generation of  $i_{\text{bng}}$ , and sensor transfer-function, an ideal *PD* controller in the form

$$C_{PD}(s) = K_P + K_D \cdot s, \quad (6.4)$$

with  $K_P$ ,  $K_D$  tunable gains, can displace the poles of the model of Eq. (6.3) to the left-side plane, rendering levitation possible.

Yet, for a stable levitating system, this form of *PD* control *does not* correct permanent disturbances in the form of  $F_{\text{load}}(s) = F_{\text{load}} \cdot u(s)$ , as it can be corroborated with the end value theorem [57]. To correct this, a *PID* controller in the form

$$C_{PID}(s) = K_P + \frac{K_I}{s} + K_D \cdot s, \quad (6.5)$$

is preferred [38], and employed in the digital position control of Fig. 6.1. The bearing's closed loop function becomes

$$L_{PID}(s) = \frac{X(s)}{F_{\text{load}}(s)} = \frac{s}{m_{\text{rot}} \cdot s^3 + (K_D \cdot k_F) \cdot s^2 + (K_P \cdot k_F - k_x) \cdot s + K_I \cdot k_F}, \quad (6.6)$$

so that a constant-valued disturbance  $F_{\text{load}}$  can be corrected to null as in

$$\lim_{t \rightarrow \infty} x(t) = \lim_{s \rightarrow 0} s \cdot X(s) = \lim_{s \rightarrow 0} s \cdot (L_{PID}(s) \cdot F_{\text{load}} u(s)) = 0. \quad (6.7)$$

### PID Controller Implementation

In reality, the controller  $C_{PID}(s)$  is implemented discretely, using the  $z$ -transform, as

$$C_{PID}(z) = K_P + \left( K_I \cdot T_s \cdot \frac{1}{z-1} \right) + \left( K_D \cdot \frac{1}{T_s} \cdot \frac{z-1}{z} \right) \cdot W_{\text{IIR}}(z), \quad (6.8)$$

with

$$W_{\text{IIR}}(z) = \frac{u_{\text{LP}}(z)}{u(z)} = \frac{\alpha}{1 + (\alpha - 1)z^{-1}}$$

with  $K_i$  values gains,  $T_s$  the sampling period of the position,  $u(z)$  and  $u_{\text{LP}}(z)$  the input and the low pass-filtered input of the controller, and  $\alpha$  the filtering weight of the latter. This implementation intrinsically introduces a delay in the control, yet it enables stable levitation and eliminates steady-state disturbances as in Eq. (6.7).

For the rotor position control in the two radial directions, an indirect position control scheme



is employed [38]. This means that the position of the rotor is controlled on the *stator* fixed  $x$  and  $y$  axes. Therefore, constant forces, such as the rotor's weight, are controlled as such (and not as rotatory). These are mapped onto phase currents by using linear transformations analog to those used for the field-oriented control [96] for rotatory motion described later in this chapter.

The position control is executed at the EC position sensor's  $f_{\text{bng.}} = 1/T_s = 3.7$  kHz sampling frequency. This corresponds to the fastest sampling frequency of the position sensors.

### Minimization of Bearing Currents

In an ideal case, the center position measured by the sensors  $\hat{x}$  coincides with the magnetic center  $x_{\text{rot.}}$  of the stator-rotor configuration. In this case, a position controller reference  $x_{\text{ref}} = 0$  mm effectively brings the rotor to a position where  $F_r = k_x \cdot x_{\text{rot.}} = 0$  N, rendering  $i_{\text{bng.}} \approx 0$  A.

Nevertheless, assembly imperfections often lead to sensor installations whose center differs from the magnetic, as in  $\hat{x} = x_{\text{rot.}} + \delta_x$ . Provided  $\delta_x$  is small, a stable *PID* position controller with reference  $x_{\text{ref}} = 0$  mm then holds the rotor at position  $\delta_x$  thanks to an

$$i_{\text{imb.}} = \frac{k_x \cdot \delta_x}{k_F} \quad (6.9)$$

imbalance current, which can produce considerable Joules losses in the windings.

To eliminate these currents, the output of the *PID* position controller is integrated *and* fed back as a position reference, as seen in Fig. 6.1. The reference of the position controller is thus deliberately displaced to hold the rotor at the sensore-estimated  $\delta_x$ .

This approach also removes bearing currents that arise due to the weight of the rotor, e.g. when the actuator is positioned vertically. In such a case, the rotor is exemplarily displaced to  $x_{\text{vert.}}$  so that rotor weight is compensated by the passive stiffness as in

$$x_{\text{vert.}} = m_{\text{rot.}} \cdot g / k_x. \quad (6.10)$$

### 6.2.3 Rotational Speed Control

Many electric drive applications—for example ventilators—are dimensioned to work at fixed rotational speeds  $\omega_{\text{ref.}} = \dot{\psi}_{\text{mech.}}^{\text{ref}}$ , to attain a fixed operating point in terms of pressure and flow. In this regard, the mechanical model relevant to the rotatory speed is

$$P_{\text{drv.}}(s) = \frac{\omega(s)}{I_{\text{q,drv.}}(s)} = \frac{k_T}{J \cdot s}, \quad (6.11)$$

with  $J$  the rotor's moment of inertia in the  $z$ -axis and  $I_{T,q}(s)$  the Laplace transform of the quadrature current  $i_{T,q}$ . A discrete  $PI$  controller as in Eq. (6.8) with  $K_D = 0$  s is deployed. This controller outputs a reference current  $i_{T,q}^{\text{ref}}$  to reach the speed.

This type of controller can eliminate steady-state errors due to braking torque  $T_{\text{load}}$ . For a given impeller, this torque can be modelled as [25]

$$T_{\text{imp}} = T_{\text{load}} = c_{\text{imp}} \cdot \omega^2, \quad (6.12)$$

with  $c_{\text{imp}}$  a constant for the impeller in  $\text{Nm} \cdot \text{s}^2 \cdot \text{rad}^{-2}$ .

The rotational speed is estimated with the aid of the HES signals. Combined as in Eq. (5.7), angle  $\psi$  is obtained and its difference to its previous value is computed. This result is low-pass filtered and multiplied by a gain to deliver rotational speed  $\omega_{\text{meas}}$ .

On another note, the drive's direct current  $i_{T,q}$  is controlled to zero as no deflux nor axial dampening [169] is intended. As with the bearing currents, drive currents are transformed to phase currents by the current control.

The rotational speed varies significantly slower than the radial position of the rotor and the current in the coils, so the rotational speed  $\omega_{\text{ref}}$  is controlled at  $f_{\text{speed}} = 1$  kHz.

#### 6.2.4 Current Control

The coils of the actuators are energized differently if torque or force is to be produced, as explained in Subsection 3.3.3. This leads to dissimilar drive and bearing inductances  $L_{\text{drv}}$  and  $L_{\text{bng}}$ , respectively.

Due to the combined coil concept, the current circulating in each coil is composed of the sum

$$\begin{aligned} i_{\text{coil}} &= i_{\text{drv}} + i_{\text{bng}} \\ \text{where} \\ u_{\text{drv}} &= R_{\text{coil}} \cdot i_{\text{drv}} + L_{\text{drv}} \cdot \frac{di_{\text{drv}}}{dt} + u_{\text{ind}} \\ u_{\text{bng}} &= R_{\text{coil}} \cdot i_{\text{bng}} + L_{\text{bng}} \cdot \frac{di_{\text{bng}}}{dt}, \end{aligned} \quad (6.13)$$

in the time domain, with  $R_{\text{coil}}$  the resistance of the coil and  $u_{\text{ind}}$  the back EMF. In the Laplace domain, this results in

$$I_{\text{coil}}(s) = \underbrace{\left\{ \frac{1}{R_{\text{coil}}} \cdot \frac{1}{s \frac{L_{\text{drv}}}{R_{\text{coil}}} + 1} \cdot (U_{\text{drv}}(s) - U_{\text{ind}}(s)) \right\}}_{I_{\text{drv}}(s)} + \underbrace{\left\{ \frac{1}{R_{\text{coil}}} \cdot \frac{1}{s \frac{L_{\text{bng}}}{R_{\text{coil}}} + 1} \cdot U_{\text{bng}}(s) \right\}}_{I_{\text{bng}}(s)}. \quad (6.14)$$

Given the coupling of the magnetomotive forces of the coils, it follows that  $L_{\text{drv.}} \gg L_{\text{bng.}}$  [166]. Therefore, the electric time constant  $\tau_i = L_i / R_i$  of the  $LR$ -circuits differs as in  $\tau_{\text{drv.}} > \tau_{\text{bng.}}$ . The different time constants, plus the disturbance due to the induced voltage, require a different regulation of the drive and bearing currents.

The current control schemes *and* PWM-switching frequency are executed with a  $f_{\text{PWM}} = 44$  kHz frequency. This allows for low current-ripple losses as seen in Section 3.4 and more than 10 current control cycles per position control cycle. The latter ensures a good decoupling between the dynamics of the bearing and the current control.

Phase currents  $I_1$ ,  $I_3$ ,  $I_4$ , and  $I_6$  are measured by shunt resistors. They are output as a voltage and finally measured at an Analog-to-Digital (ADC) converter of the microcontroller. To separate its bearing and drive components, the measured currents are combined as

$$\begin{pmatrix} I_{\text{drv.,r}} \\ I_{\text{drv.,s}} \\ I_{\text{bng.,a}} \\ I_{\text{bng.,b}} \end{pmatrix} = \frac{1}{2} \underbrace{\begin{pmatrix} 1 & 0 & -1 & 0 \\ 0 & 1 & 0 & -1 \\ 1 & 0 & 1 & 0 \\ -1 & -1 & -1 & -1 \end{pmatrix}}_{M_{\text{SEP}}} \cdot \begin{pmatrix} I_1 \\ I_3 \\ I_4 \\ I_6 \end{pmatrix}, \quad (6.15)$$

and then correspondingly rotated to the coordinate system of their current controllers using the Clarke and Park Transform [124].

### Drive Currents

The control of the torque current  $i_{T,q}$  is performed on the rotor's  $dq$  coordinate system [127]. A  $PI$  controller is responsible for generating voltage references  $(v_d, v_q)$  from  $(i_{T,d}^{\text{ref}}, i_{T,q}^{\text{ref}})$ .

The reference voltages  $(v_d, v_q)$  on the  $dq$  axes are transformed into rotatory  $(v_{\text{drv } \alpha}, v_{\text{drv } \beta})$  components with the inverse Park transform, to its three phase equivalent with the inverse Clark transformation [96], and ultimately mapped onto the voltages of the six coils  $i = 1, 2, \dots, 6$  as in

$$\vec{v}_{\text{drv}} = \begin{pmatrix} v_{\text{drv } 1} \\ v_{\text{drv } 2} \\ v_{\text{drv } 3} \\ v_{\text{drv } 4} \\ v_{\text{drv } 5} \\ v_{\text{drv } 6} \end{pmatrix} = \underbrace{\begin{pmatrix} 1 & 0 & 0 \\ 0 & 0 & -1 \\ 0 & 1 & 0 \\ -1 & 0 & 0 \\ 0 & 0 & 1 \\ 0 & -1 & 0 \end{pmatrix}}_{M_{\text{DRV}}} \cdot \underbrace{\begin{pmatrix} 1 & 0 \\ -\frac{1}{2} & \frac{\sqrt{3}}{2} \\ -\frac{1}{2} & -\frac{\sqrt{3}}{2} \end{pmatrix}}_{\text{inv. Clarke}} \cdot \underbrace{\begin{pmatrix} \cos \psi & -\sin \psi \\ \sin \psi & \cos \psi \end{pmatrix}}_{\text{inv. Park}} \cdot \begin{pmatrix} v_d \\ v_q \end{pmatrix}, \quad (6.16)$$

to comply with the phase currents of Eq. (3.45).

### Bearing Currents

As mentioned, the position control and its corresponding current generation are implemented in indirect form. The current references  $(i_{F,x}^{\text{ref}}, i_{F,y}^{\text{ref}})$  of the position *PID* controller are also controlled with a *PI* controller that generates voltage references  $(v_x, v_y)$ .

The *PI* controller of the bearing current is different from that of the drive, given the feeble  $L_{\text{bng}}$ , which leads to a different time constant, as seen in Eq. (6.14).

As with the drive, the inverse Park transform is applied to voltages  $(v_x, v_y)$  to obtain its bi-phase equivalent rotatory  $(v_{\text{bng } \alpha}, v_{\text{bng } \beta})$  and with the inverse Clarke to its three phase representation. This is transformed onto the six coils  $i = 1, 2, \dots, 6$  as

$$\vec{v}_{\text{bng}} = \begin{pmatrix} v_{\text{bng } 1} \\ v_{\text{bng } 2} \\ v_{\text{bng } 3} \\ v_{\text{bng } 4} \\ v_{\text{bng } 5} \\ v_{\text{bng } 6} \end{pmatrix} = \underbrace{\begin{pmatrix} 1 & 0 & 0 \\ 0 & 1 & 0 \\ 0 & 0 & 1 \\ 1 & 0 & 0 \\ 0 & 1 & 0 \\ 0 & 0 & 1 \end{pmatrix}}_{M_{\text{BNG}}} \cdot \underbrace{\begin{pmatrix} 1 & 0 \\ -\frac{1}{2} & \frac{\sqrt{3}}{2} \\ -\frac{1}{2} & -\frac{\sqrt{3}}{2} \end{pmatrix}}_{\text{inv. Clarke}} \cdot \underbrace{\begin{pmatrix} \cos \psi & -\sin \psi \\ \sin \psi & \cos \psi \end{pmatrix}}_{\text{inv. Park}} \cdot \begin{pmatrix} v_x \\ v_y \end{pmatrix}, \quad (6.17)$$

to comply with Eq. (3.43).

Ultimately, the drive and bearing voltages are linearly combined as in  $\vec{v} = \vec{v}_{\text{drv}} + \vec{v}_{\text{bng}}$  and fed to a PWM-modulator. Subsets  $(v_1, v_3, v_5)$  and  $(v_2, v_4, v_6)$  compose the two separate three-phase power stages like the one shown in Fig. 3.43. They energize the coils in the combined manner expressed in Eq. (3.47).

### 6.2.5 Microcontrollers

A *Texas Instruments (TI)* LaunchXL-F28379D Development Kit [175] shown in Fig. 6.2 is used to implement the digital control of Fig. 6.1.

The Launchpad's microcontroller has two processing cores. One core runs at  $f_{\text{PWM}}$  and is *solely* dedicated to current control and the generation of PWM signals. The other core executes position and rotational speed control, samples and computes HES information at the ADCs, and receives the rotor position estimation from another microcontroller, as seen later in subsection 6.3.1.

It must be noted that not all the processing modules of the Development Kit are used, so more production-aimed applications may use a slimmed-down deployment of the processing core and its other interfaces.

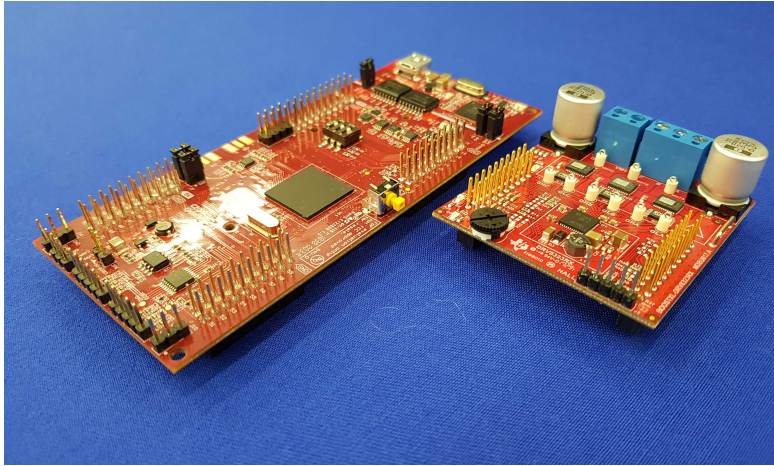


Figure 6.2: The digital drive control is implemented on the Delfino Launchpad (left) Development Kit. This microcontroller drives *two* Boost-XL three-phase power stages like the ones shown (right), which control the currents of the drive's coils with a PWM scheme for desired levitation and rotatory operation.

### 6.2.6 Power Converter

Two independent TI BoostXL-DRV8323RS evaluation modules [174] shown in Fig. 6.2 are employed for the PWM current control scheme. This power stage is chosen for its lower operating voltage range, i.e.  $U_{DC} > 6$  V, which makes it suitable for coupling it with battery, and its high maximum phase current of  $i_{max} = 20$  A that can handle bearing start-ups of large mechanical clearances.

## 6.3 Sensor Electronics

In this section, the sensor electronics devised and its components for the estimation of the rotor's radial and angular position are presented. For the former information, EC-based position sensors are ultimately employed; for the latter, HESs are deployed.

The overall size of the designed ventilator system calls for a slim footprint of the sensor systems. To this end, the aforementioned sensor systems are based on PCB technology. This technology offers reduced mechanical volumes and thin structures, has good manufacturing repeatability, and enables the precise positioning of the sensors inside the drive. Moreover, the sensor PCBs are compatible with both constructed prototypes.

Sleek sensor systems do not require special constructive measures that interfere with the electromagnetic design of the actuator or render it unnecessarily larger. Thus, the precise positioning of the sensors and their mounting way is crucial for bearingless drives and consists in one of the novelties of this work.

### 6.3.1 Eddy-Current Sensing Excitation

As explained in Section 5.3, the EC effect arises from a coil excited at high-frequency, as in Fig. 5.5. To recover information relative to coil-target distance, the voltage amplitude or frequency of the resonance must be exploited [201].

EC-based position systems can be developed in various ways. Tunable, off-the-shelf options are available [3, 98]. Yet they are costly and they require standardized probes, so electric drive designs must be conceived to incorporate and leave space for them.

Compact solutions can be implemented, but are highly system-specific. Analogical [92, 116, 168, 200] and digital [77, 128] approaches have enabled the levitation of bearingless drives.

Within this context, a rotor position estimation system is proposed in this work. Off-the-shelf ICs are employed to excite arbitrary coils, which in this work are fabricated on PCBs. This composition is a low-cost solution and enhances the adaptability of the position estimation system to bearingless motors of different sizes and configurations.

#### Excitation of Sensing Coil employing an LCR Resonant Tank

For a flexible and robust measurement system, the magnetically-levitated ventilator relies on market-ready technology. A *TI* Inductance to Digital Converter LDC1314 IC [180] is employed. To estimate the value of inductance, e.g. that of Fig. 5.5, the sensing coil is connected to form an LCR resonant tank.

This IC is capable of driving *and* tracking the resonant frequency  $f_{\text{res}}(x)$  of the LCR resonant tank of Fig. 6.3, which depends on the inductance's value. The latter depends, on its turn, on the distance  $x$  between coil and target. Frequency  $f_{\text{res}}(x)$  is thus worth

$$f_{\text{res}}(x) \approx \frac{1}{2\pi} \frac{1}{\sqrt{L_{\text{eq.}}(x) \cdot C_{\text{tank}}}}, \quad (6.18)$$

with  $L_{\text{eq.}}(x)$  the apparent inductance of the sensing coil as a function of its distance  $x$  to the target and  $C_{\text{tank}}$  the installed resonant capacitor, with  $R_{\text{eq.}}^2(x) \ll L_{\text{eq.}}(x)/C_{\text{tank}}$  [201] defined in Eq. (5.1).

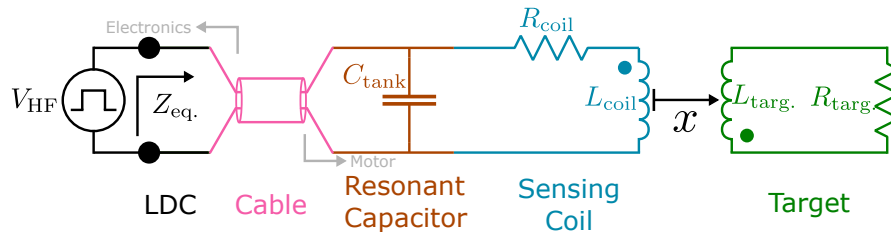


Figure 6.3: The EC rotor position system consists of an LCR resonant tank. The circuit's equivalent inductance  $L_{\text{eq.}}$  and resistance  $R_{\text{eq.}}$  are a function of coil-target distance.

For a fixed  $C_{\text{tank}}$ , the LDC1314 counts the oscillations within a time frame and transforms this number onto a 12-bit value. This 12-bit value is an indirect estimate of the sensing coil's inductance and of its distance  $x$  to the target .

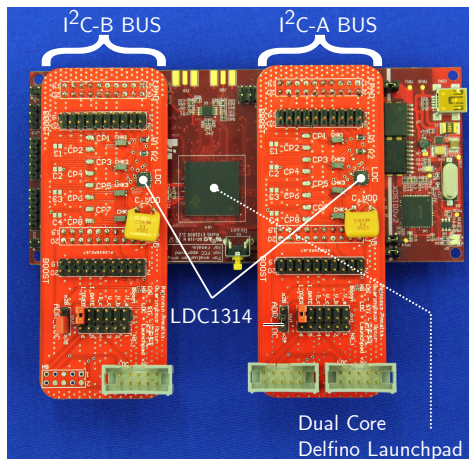
Large  $C_{\text{tank}}$  values lead to low  $f_{\text{res}}$ , so that the IC measures the inductance around the sensing coil, e.g. inductive position sensor. Conversely, low  $C_{\text{tank}}$  values result in high  $f_{\text{res}}$  values, so that the sensing coil generates ECs and the IC operates as an EC position sensor. The latter operative fashion is preferable for the conductive, non-ferromagnetic PM rotors of the conceived drives.

### Hardware

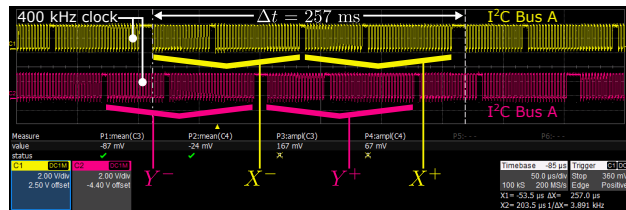
The I<sup>2</sup>C clock is configured to its fastest clock frequency of 400 kHz [180]. The transmission of *each* I<sup>2</sup>C message takes approximately  $\Delta t = 121 \mu\text{s}$ , so the four sensors can be sampled with a  $f_{\text{samp.}} \approx 2 \text{ kHz}$  frequency. The I<sup>2</sup>C message's length is the *bottleneck* of the sampling rate of position estimation, despite the LDC being capable of sampling a sensing coil faster.

Due to the short  $\tau_{\text{bng.}}$  of the prototypes, higher sampling rates are preferable. To this end, two LDC1314s and the Delfino microcontroller are set up together to compose a *stand-alone position-estimation system*, as seen in Fig. 6.4a. The independent I<sup>2</sup>C-A and I<sup>2</sup>C-B buses of the microcontroller manage the two LDC1314 ICs for  $x$  and  $y$  position estimation, respectively.

With the proposed arrangement, it is possible to send the conversion output of the two sensing coils of a differential axis —through an I<sup>2</sup>C bus— in a total of  $\Delta t = 257 \mu\text{s}$ . The I<sup>2</sup>C-A and I<sup>2</sup>C-B buses of the Delfino Launchpad communicate with the LDC1314 ICs of the  $x$  and  $y$  position estimation, respectively. The time window is marked with the cursors of Fig. 6.4b and



(a)



(b)

Figure 6.4: A total of four LCR resonant tanks are driven by (a) two LDC1314 IC's, coupled to a Launchpad Development kit. Axes  $x$  and  $y$  are treated by separate LDC1314s and (b) their sampling information is sent through independent I<sup>2</sup>C buses of the microcontroller.

corresponds to a  $f_{\text{samp.}} = 3.89$  kHz frequency.

With any set of coils, correctly tuned with the help of  $C_{\text{tank}}$ , such a configuration may be added onto existing prototypes, with its integration potential being determined by how coils are integrated into the drive. It must be noted that slimmer electronic configurations, without a microcontroller, can manage the same system. I<sup>2</sup>C-dedicated ICs could connect to the LDCs to then communicate their results via other protocols, e.g. CAN, DAC, SPI, etc. In this case, the differential calculation is sent to the control microcontroller through the CAN communication protocol.

### Sampling Time Requirements

The sampling time of the positioning system is compared to the dynamics of the radial bearing at *standstill*, to analyze if they can at least enable levitation at null speed. Within this context, the drives provide a radial natural frequency defined by

$$f_{\text{rad.bng.}} = \frac{1}{2\pi} \sqrt{\frac{k_r}{m}}, \quad (6.19)$$

with  $k_r$  and  $m$  the radial stiffness and rotor mass, respectively. Equation (6.19) results in  $f_{\text{rad.bng.}}^{\text{slotless}} = 60$  Hz and  $f_{\text{rad.bng.}}^{\text{slotted}} = 115$  Hz, so  $f_{\text{samp.}}$  is 30 and 60 times faster than the time constant of the bearing of the slotted and slotless drive, respectively.

Yet the issue is different for spinning operation. Rotor mass imbalance must be controlled and appears at its rotational speed, so the higher the aimed rotational speed, the faster sensor sampling rate is required. If ten position measurements per rotation [200] are needed to maintain levitation and spinning, the attained  $f_{\text{samp.}}$  limits the rotatory speed to

$$n = 60 \text{ sec/min} \cdot (f_{\text{samp.}}/10) = 23340 \text{ rpm.} \quad (6.20)$$

### 6.3.2 Integration of Eddy-Current Sensing Coils and their Shielding

In this subsection, the integration into the motor air gap of the EC sensing coils along with its shielding is reviewed. These components must have a small footprint, so that they do not require special constructive measures.

#### Eddy-current sensing coils

The EC sensing coils must lay in the magnetic air gap of the rotor, as shown in Fig. 6.5. These probes have ideally a minimal thickness, so that there is

- enough cross-section to be filled with copper of the motor coils,
- sufficient encapsulation thickness to separate and hold rotor shocks,
- and that there is still enough mechanical clearance for the rotor to levitate,



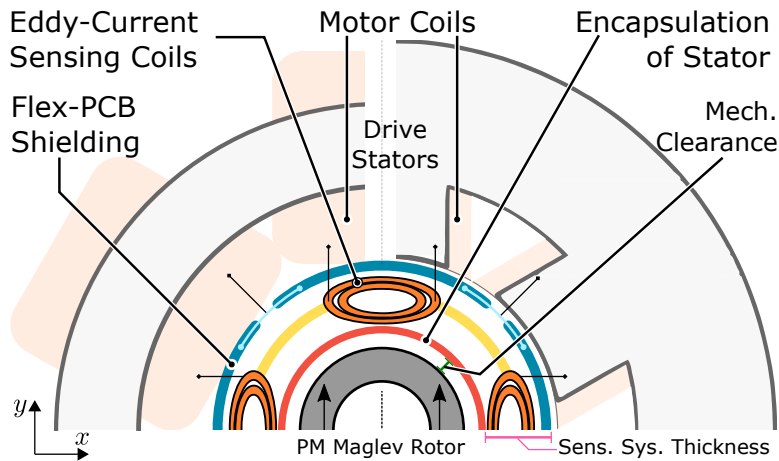


Figure 6.5: The radial EC sensing coils are axially slid into the air gaps of drives. The shielding that dampens their sensitivity towards the stator and the motor coils is wrapped around these. They amount to the indicated Sensor System Thickness, depicted in pink, which is to be minimized.

with the corresponding structures indicated in Fig. 6.5.

Minimizing the thickness of the sensing probes and their shielding—depicted in pink in Fig. 6.5—allows for more freedom in the choice of the itemized quantities from above. Therefore, thin coils—whose integration potential in a bearingless drive is feasible—are investigated in terms of position sensitivity in Chapter 7.

### Shielding of Sensing Coil

The sensor coils are introduced in the air gap as shown in Fig. 6.5. At this location, it is desirable that the sensing coils *only* measure a change of inductance due to the rotor position, and not of eventual vibrations of other conductive components in their proximity, such as the drive's stator and coils. Moreover, the latter are energized by switched PWM-voltages that radiate magnetic waves, e.g. electromagnetic noise, in the proximity of the sensor coils.

The shielding Flex-PCB from Fig. 6.6 is conceived and fabricated. Their  $150\text{-}\mu\text{m}$  thickness makes it ideal for wrapping it *around* the sensor coils, as in Fig. 6.5. This shielding diminishes their sensitivity to structures other than the rotor and dampens electromagnetic interference from the coils.

For its functioning, the high-frequency magnetic field of the sensing coils generates ECs in the copper tracks of the shielding. Nevertheless, the open-path, grid-like pattern of Fig. 6.6a is chosen to *partially* dampen the magnetic field of the sensing coils [178, 190]. A solid copper surface would completely dampen the magnetic field and render the sensing coils insensitive to the desired target. The shielding tracks of the Flex-PCB are internally connected and connected to the ground of the electronics.

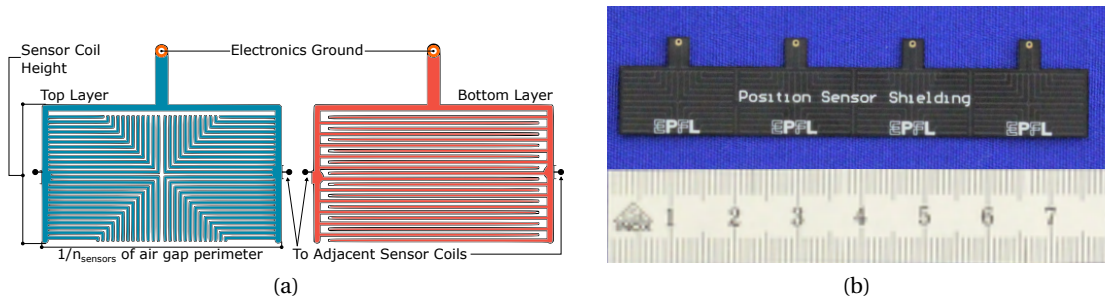


Figure 6.6: A shielding Flex-PCB is designed to minimize the influence of stator and coil vibrations upon the rotor position sensing system. (a) Each shield is made of two layers, one on top of the other. The two layers cover a sensing coil, so a (b) complete shielding Flex PCB—for a total of four of these connected sections—is rolled around the air gap connected to signal ground.

### 6.3.3 Hall-Effect Sensor PCB

The estimation of the angular position of the rotor  $\psi$  is performed by linearly combining the magnetic flux density measured by six HESs as in Eq. (5.7). For accurate angle estimation, the exact spatial placement of the sensors is essential.

To measure the magnetic flux density, six linear *Texas Instruments* DRV5055 HESs [71] with analog output are deployed, close to their corresponding supply capacitor. To ensure that the sensors are symmetrically distributed in the air gap, they are placed onto the PCB of Fig. 6.7. This PCB can admit either radial *or* axially mounted HES ICs with its through-holes or soldering pads, respectively.

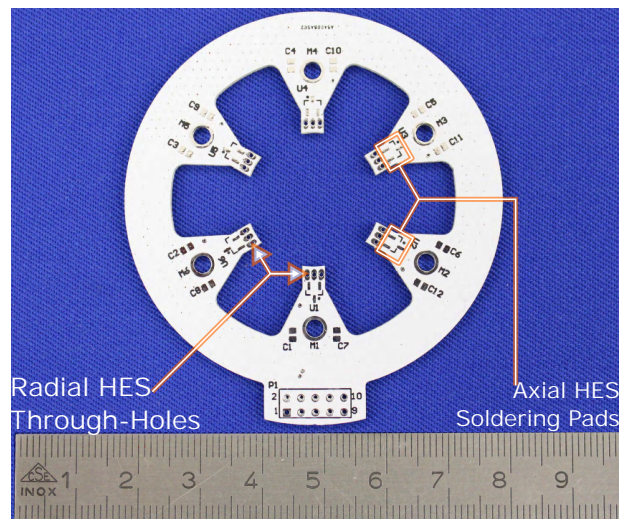


Figure 6.7: A dedicated PCB is conceived for the symmetric placement of the HESs along the perimeter of the stator.

The PCB can be placed above or below the drive. To provide electromagnetic immunity to the HES signals against the PWM excitation of the coils, the sensor PCB is made of four layers. The upper and lower layer consists of ground plates, and the middle layers having output signals and the supply voltages of the sensors.

The HESs are positioned to lie outside the encapsulation of the drives. This way, they do not interfere with the hermetic sealing between rotor and stator. The ICs are also installed between the motor coils, so that they pick up as little magnetic field of the coil as possible.

### 6.4 Conclusion

In this chapter, the mechanical laws that determine the dynamics of the magnetic bearing and its rotatory operation are described with its required hardware. The corresponding control schemes required to control these two tasks are described, as well as how their reference output currents are imposed in the drive.

The measurement of the information needed for the operation of the bearingless drive — namely rotor radial and angular position— is based on mechanically precise, low-footprint PCB technology. Therefore, the slim sensors do not interfere with the electromagnetic conceptualization of the actuator. Additionally, the PCBs provide mechanical stability at a reduced volume, thus leading to an overall reduced actuator volume.

Within the context of sensors, a generic rotor-position estimation system that uses market-ready technology is proposed. This system can be set-up to operate independently from other microcontrollers, i.e. as stand-alone, but it can be adapted to work on available I<sup>2</sup>C protocols of a microcontroller. The core of the system sensing can drive arbitrary sensing coils, which can be adapted to the necessities of specific systems. In this case, thin Flex-PCB coils are successfully integrated in the electric drives.

In the next chapter, the experimental characterization of the sensor systems and the actuator —as drive *and* ventilator— is undertaken.

# 7 Disc Drive Prototypes

## 7.1 Introduction

In this chapter, the characteristics and operation of two working bearingless disc drive *prototypes* are described.

To start, the modular integration of the prototypes is portrayed. This allows the motor prototypes to share various constructive elements, and to be assembled in an easy and precise manner supported by PCB technology.

Part of this assembly must contain sensor probes, which serve to estimate the radial position of the rotor exploiting the EC principle. In this context, a differential sensor array provides a sensor signal which linearly relates to the radial position of the rotor.

The coils of the EC-based positioning systems are tuned to resonate at various frequencies with the aid of different capacitors. The performance of this type of position measurement is evaluated with the aid of a test bench. Exciting the sensor coils at high frequencies provide superior sensitivities to rotor displacement that can ultimately render better resolutions if properly filtered. The noise picked up by the sensor probes —due to bearing and drive electromagnetic excitation— is also quantified.

On the same line, the rotor position estimation capabilities of HES arrays are investigated. For two different sensor orientations, two PCB-mounted arrays provide precise rotor angle and rotor axial position estimation. Moreover, a simple model is implemented to cancel out the influence of the excitation of motor coils upon the HESs. This current compensation enables a preciser estimate of the position information of the rotor, by removing the influence of the needed actuation of the drives.

Slotted and slotless stator prototypes are fabricated. The validity of the FE simulations is verified by measuring their passive and active forces on a test bench. Their quantification lead to an indicator of the effort needed to levitate a rotor.

The experiments show that FE simulations yield results that can differ up to  $\sim 10\%$ , and that those simulations can misrepresent the rotor-angle dependency of motor characteristics. Nonetheless, such mismatches can be deemed acceptable for design purposes.

The levitation and rotational operation of a slotted *and* slotless prototype are enabled by the estimation of the angular and radial rotor position, provided by the Hall-effect and EC sensors, respectively. Both drives are mounted onto a plexiglass test bench, where a microcontroller for motor control purposes and another dedicated to the EC sensors are fastened.

The bearing start-up procedures are documented, as well as the harmonic content of the rotor positions during rotational operation. Moreover, it is validated that the axial-flux variant of the HESs yields acceptable results in terms of the estimation of the radial position of the rotor. This is tested by comparing HES-based position signals to those of the EC sensors in terms of mathematical cross-correlation and frequency content.

Finally, a prototype is made to drive a real-world application. Different axial impellers are integrated into a thin PM rotor so that the bearingless slotless disc drive can be deployed as an axial ventilator. A test rig is conceived to measure the achievable pressure and airflow at different rotational speeds and working points. Impeller designs intended for larger pressures or flows are highlighted.

### 7.2 Compact PCB-based Axial Assembly of the System

The drives are conceived to be axially assembled with their sensor systems and corresponding PCBs, as in Fig. 7.1.

The PCB-based assembly provides power and sensor signal routing, as well as high mechanical precision and additional mechanic stability. Mechanical pieces, such as the bearing retainer or the mounts to screw the stator are fabricated using 3D Print technology or high-precision laser cutting.

The base of this construction is the *Power PCB*, which enables the tidy connection of the motor coils to the power electronics through Phoenix Connectors. It has a bore in its middle to permit the airflow of an axial ventilator, and has  $5\text{ mm} \times 200\text{ }\mu\text{m}$  copper tracks to allow for large currents.

A zoom-in of the fabricated drives, with and without sensor systems, is shown in Fig. 7.2. Only the sandwiched mechanical pieces, e.g. stator mount and bearing retainer are different for the prototypes.

The electric drives are optimized for an off-the-shelf NdFeB rotor, e.g. rotor #1, leading to stator dimensions of Table 7.1. Such rotor configuration can accommodate radial impellers for pump applications [121]. This stator can also drive rotor #2, whose ample bore suits the mounting of an axial impeller.

The slotless prototype uses litz wire for its windings, to diminish the EC losses inside them at high-speeds, whereas the slotted uses enameled wire as these losses are less critical in slotted drives. The slotted stator is also constructed out of three stator segments, which enabled better utilization of the raw, amorphous *Metglas* [106] U-cores before cutting. The segmented construction also makes the sliding of the concentric coils onto the teeth easier.

As mentioned before, the active and passive ratings of both drives are computationally and experimentally characterized in this chapter. The testing of sensor systems is mostly done on stators, paired with their PM, and no motor coils.

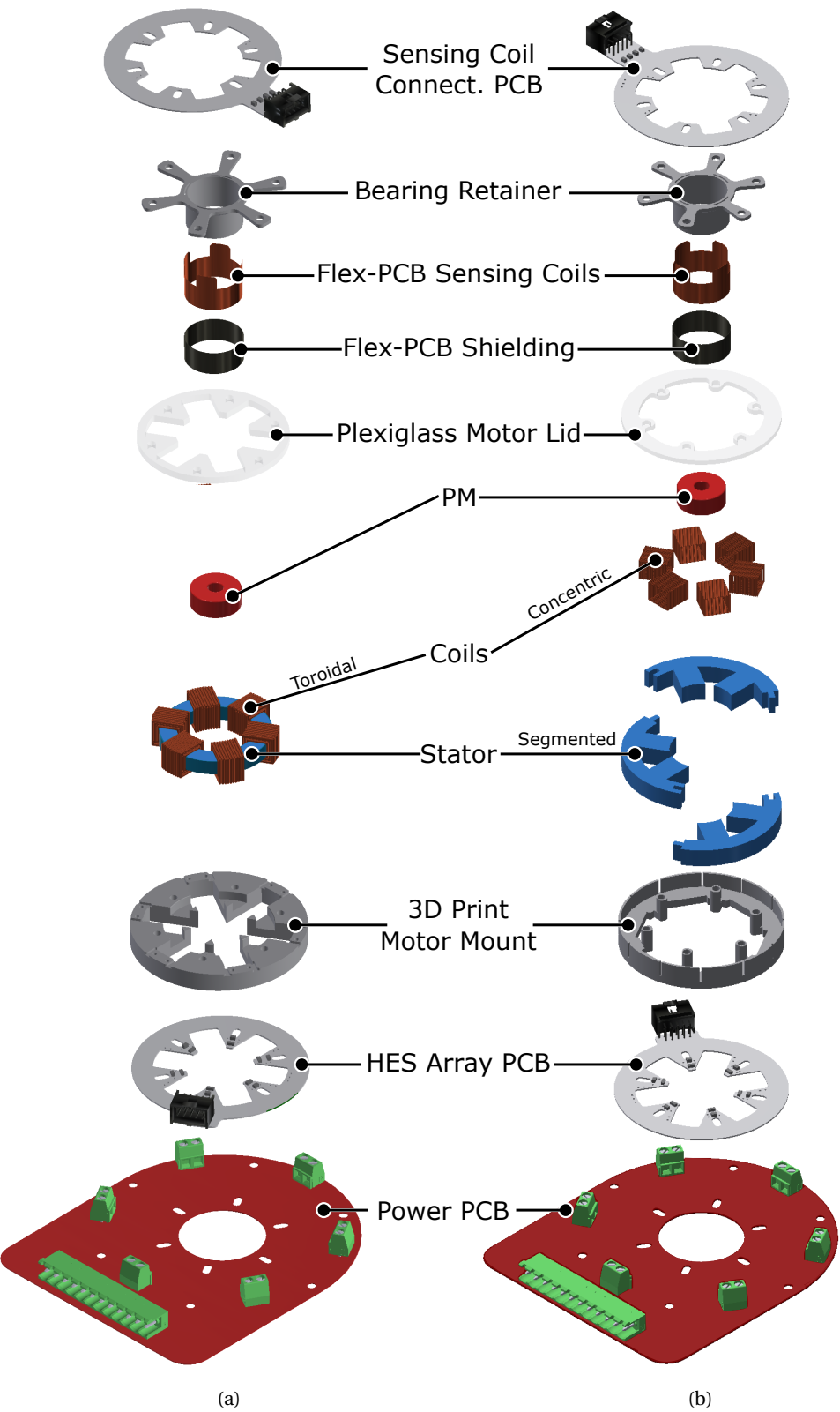


Figure 7.1: Axial mounting concept of the sensor, mechanical, and drive pieces for the slotless and slotted drive.

## 7.2 Compact PCB-based Axial Assembly of the System

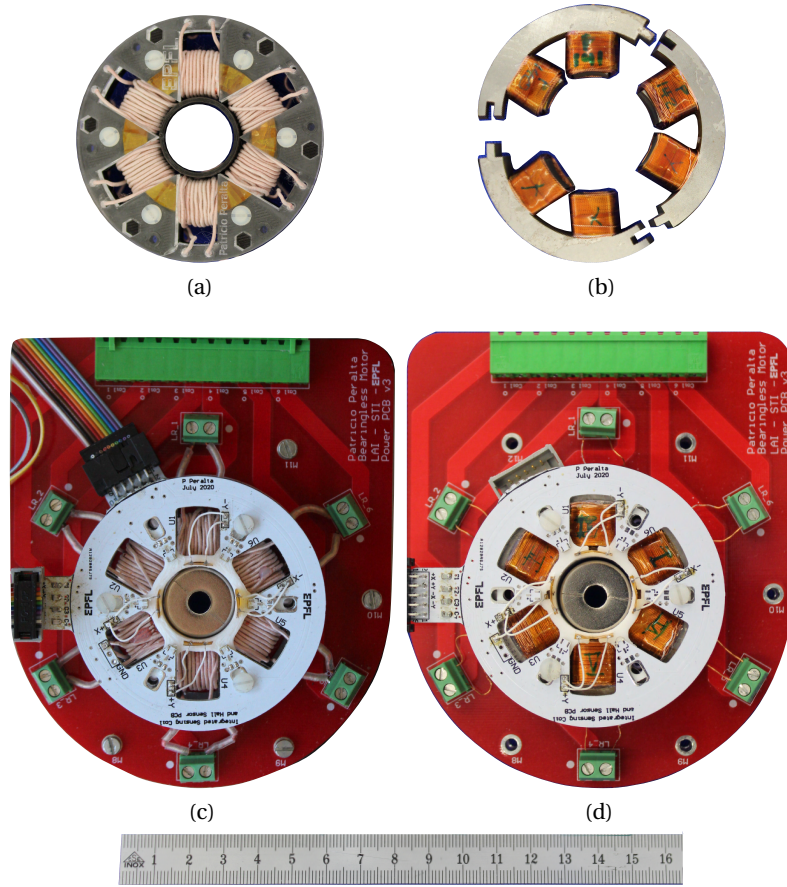


Figure 7.2: (a) Slotless motor and (b) slotted motor, mounted with their respective (c)-(d) sensors system PCBs onto the power PCBs. Shown with rotor #1.

Table 7.1: Geometric dimensions, in mm, and materials of the drives of Fig. 7.2.

Stator Mat.	<i>Metglas</i> 2605SA1 [106]		Rotor Mat.	NdFeB42H [46]	
	Slotless	Slotted		Rotor #1	Rotor #2
$d_{\text{stator,out}}$	45	65	$d_{\text{rotor,out}}$	20	
$d_{\text{stator,in}}$	30	51	$\delta_{\text{PM}}$	7	1
$\delta_{\text{airgap}}$	5	3	$h_{\text{rotor}}$	8	
$h_{\text{stator}}$	6	7.75			
$W_{\text{th.}}$	—	10			
$L_{\text{th.}}$	—	13			
$N_{\text{Turns}}$ [Turns]	140	33			
$R_{\text{coil}}$ [m $\Omega$ ]	1410	150			
$d_{\text{wire}}$ [ $\mu\text{m}$ ]	300	1000*			

\* total  $\varnothing$  of litz wire



## 7.3 Experimental Validation of the Eddy-Current-Based Estimation of Rotor Position

### 7.3.1 Testing of Sensor Coils

#### Sensing Coils

Three sensing coils, pictured in Fig. 7.3a, are assessed for position measurement purposes. They are similar in dimensions, so their measuring range is also analogous [179].

The 400  $\mu\text{m}$  thin TDK coil [173] is conceived for wireless energy-transfer applications. Its sensing performance is juxtaposed to that of a 150  $\mu\text{m}$  thin, two-layer Flex PCB 10 mm  $\times$  10 mm coil, designed in [176]. The Flex PCB coil is tried out in single and series (double) configuration, to see the effects of the increased inductance upon its performance as a probe.

Figure 7.3b shows the obtained series inductance and resistive characteristics of the trial coils. The TDK coils and double Flex PCB Coil have a comparable inductance, but the double Flex PCB Coil is more resistive at DC. The lower Q-factor makes the PCB coils less preferable from the sensing point of view [177]. On the other hand, Flex PCB coils are thinner, so they can be more easily built into a bearingless drive.

The Self-Resonant Frequency (SRF)  $f_{\text{SRF}}$ —at which the inductance of the coil resonates with its parasitic capacitance—is also marked, as the inequality  $f_{\text{res}} < 0.8 \cdot f_{\text{SRF}}$  ([180]) must be kept to ensure the stability of the resonance.

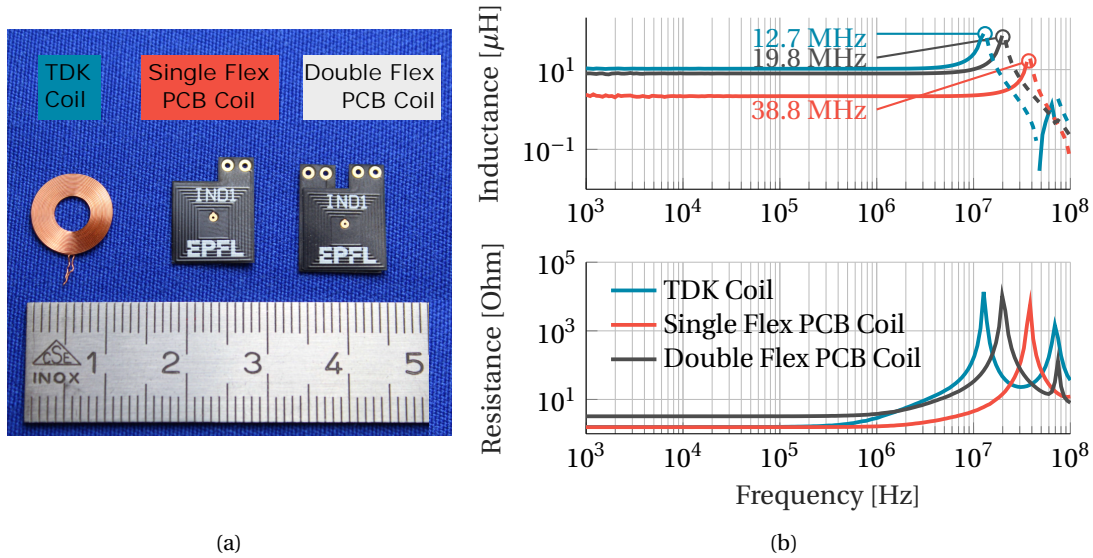


Figure 7.3: (a) Sensing coil probes for EC position measurement and (b) series inductance and resistance of the sensing coils (as in (a)). Obtained with Agilent 4294A impedance analyzer.

### 7.3 Experimental Validation of the Eddy-Current-Based Estimation of Rotor Position

#### Test Bench

A test bench is conceived to determine the position estimation capabilities of the EC sensor system. Figure 7.4a shows the setup used to characterize the sensing coils. Mounted on the XYZ linear stage, the stator of Table 7.1 is displaced relative to the fixed rotor #1 with the aid of a DC motor

The sensing coils  $X^+$  and  $X^-$  are installed radially in the magnetic air gap, as indicated in Fig. 7.4b. The LDC1314 Evaluation Module and its GUI are utilized for a swifter configuration of the IC, as different sensing coils and capacitor values are tested. The LDC sensor data is recorded and matched with the position information estimated by a Keyence LK-G82 laser sensor and its Keyence LK-GD500 readout device.

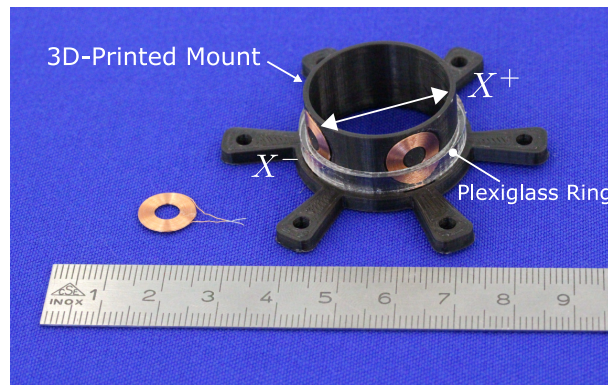
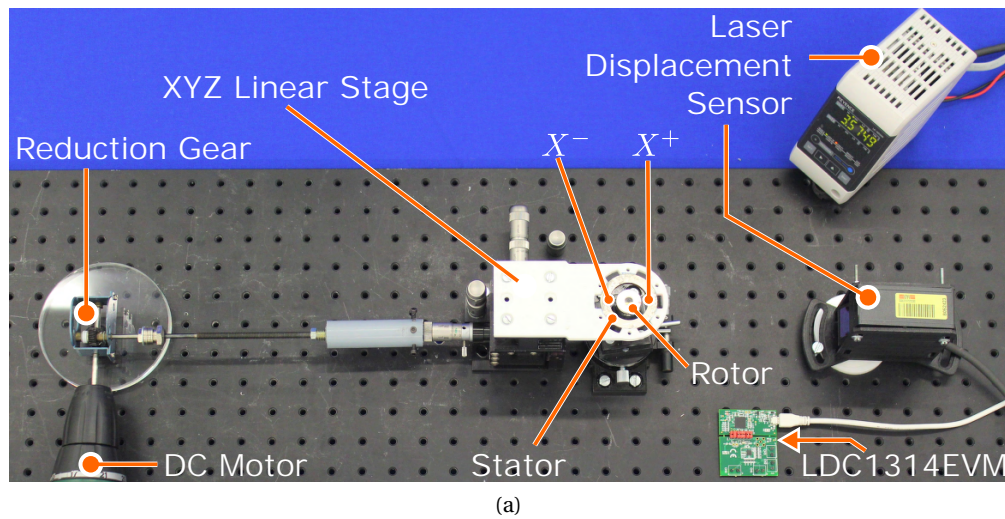


Figure 7.4: (a) Test bench setup. A linear XYZ table moves the stator relative to the rotor. Its  $x$ -axis is displaced at a fixed speed thanks to a DC motor and a reduction gear. The test bench's position is measured with a laser displacement sensor, and the digital inductance values of the coils are logged by the LDC1314 EVM. (b) A 3D-printed tool with slots for the TDK coils is slid into the stator's air gap. For the Flex PCB coils, the same structure but with slits is used.

### Sensor Characterization

The sensor is designed for an  $x = -2250 : 2250 \mu\text{m}$  range, despite that the configuration is conceived to levitate inside a  $\pm 1000 \mu\text{m}$  clearance. On top, these radial displacements are tested each for axial displacements in the range of  $z = 0 : 500 : 3500 \mu\text{m}$ .

The  $z$ -direction is measured to test the robustness of the position estimation against vibrations in the  $z$  direction. The  $z$  position of the rotor should affect the sensitivity of the sensor system in the  $x$ -direction as little as possible, as this can unsettle bearing levitation.

### Configuration of LCR Resonant Tank

The shown position-estimation system excites the electric conductivity of a body. Yet, in magnetic levitation, the *geometric position* of a target must be regulated, and an estimate of the conductivity of the target may not correspond to its geometric proximity. Discontinuities in electric conductivity—but not in geometry—might therefore be recognized as target position deviations.

Estimating *how deep* the excitation magnetic fields of the sensing coils pass into the target thus becomes relevant. In this context, it is helpful to choose a  $f_{\text{res}}$  that renders robust and sensitive position estimation. This is done by calculating the skin depth of the target.

The target is a nickel-plated NdFeB PM. The conductive coating—with an estimated  $\delta_{\text{Ni}} = 12 \mu\text{m}$  thickness—has a  $\rho_{\text{Ni}} = 30 - 110 \mu\Omega \cdot \text{cm}$  resistivity [70] and a  $\mu_{\text{r,Ni}} = 100$  [79] magnetic permeability. A 10 MHz magnetic field thus penetrates skin depths in the order of

$$\delta_{\text{sk.depth}} = \sqrt{\frac{\rho}{\pi \mu_0 \mu_r f}} \quad (7.1)$$

$$8 \mu\text{m} < \delta_{\text{sk.depth}} < 17 \mu\text{m}.$$

The calculated skin depth  $\delta_{\text{sk.depth}}$  is in the order of magnitude of  $\delta_{\text{Ni}}$ . This is advantageous, as it makes the fields less sensitive towards shallow imperfections in conductivity. The  $f_{\text{res}} \approx 10 \text{ MHz}$  value serves as a reference for the EC displacement-estimation of nickel-coated targets, such as many rare-earth magnets.

The excitation frequencies  $f_{\text{res}}$  of the LC tank are thus selected based on skin depth  $\delta_{\text{Ni}}$ , to analyze how this impacts the sensitivity and resolution of the position estimation. A wide range of  $f_{\text{res}}$  is chosen so that the skin depth lays in the range of

$$0.6 \cdot \delta_{\text{Ni}} < \delta_{\text{sk.depth}} < 2 \cdot \delta_{\text{Ni}}, \quad (7.2)$$

with the given  $\rho_{\text{Ni}}$  and  $\mu_{\text{r,Ni}}$  values. Resonant frequencies  $f_{\text{res}}$  are chosen to achieve the

### 7.3 Experimental Validation of the Eddy-Current-Based Estimation of Rotor Position

conditions of Eq. 7.2. This provides the configurations shown in Table 7.2.

Table 7.2: Each sensing coil is matched with four different capacitors  $C_{\text{tank}}$  (in pF) to modify the LCR tank's resonant frequency  $f_{\text{res}}^*$  (in MHz). This modifies the target's excited skin depth.

TDK Coil	$C_{\text{tank}}$	1	3.9	5.9	4.1
	$f_{\text{res}}^*$	7.3	7.1	5.9	4.1
Single Flex	$C_{\text{tank}}$	2.2	8.2	56	220
PCB Coil	$f_{\text{res}}^*$	16	14.9	11.2	6.6
Double Flex	$C_{\text{tank}}$	1.2	3.9	30	115
PCB Coil	$f_{\text{res}}^*$	9.5	9.2	6.8	4.6

#### 7.3.2 Single and Differential Sensor Characteristic

The sensing coil pair is fit in the stator and its data is logged as a function of the rotor position  $x$  (which is varied). The data is plotted as a function of the position values provided by the laser displacement sensor as shown, for example, in Fig. 7.5. The data from a single sensor is a non-linear of the position.

The differential data of the two opposing sensors render a different picture. It describes a cubic function if a wide clearance must be measured, so a third-order polynomial could be fit.

For narrower ranges of  $x$ , the differential measurement portrays a more linear picture. In this case, it becomes more reasonable to characterize the measurement around  $x = 0$  mm, i.e. for a rotor levitating at the center of the clearance. To do so, a weighted least-square regression is performed, weighted with a Gaussian distribution with  $\sigma = 1.2$  mm around  $\mu = 0$  mm.

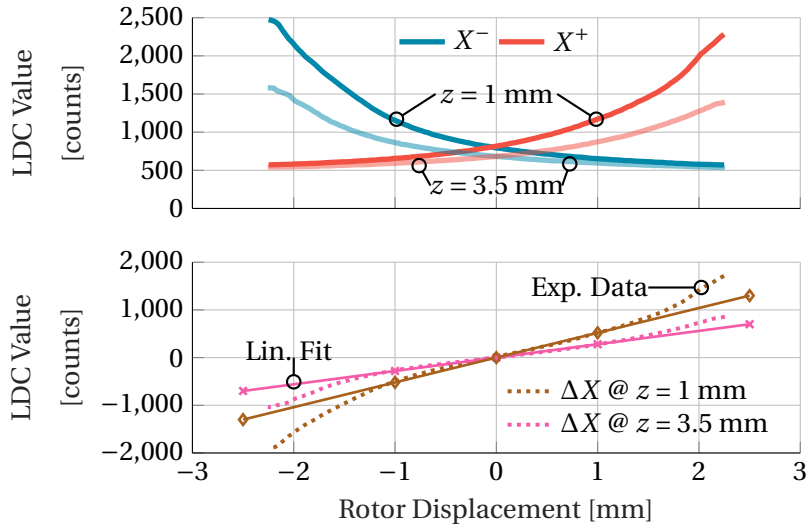


Figure 7.5: Sensor data obtained by using a Double Flex PCB Coil with  $f_{\text{res}} = 6.6$  MHz at two different  $z$  heights. The data of single sensors holds a non-linear characteristic with position; yet the differential calculation  $X_{\text{POS}} = X^- - X^+$  relates more linearly to the position.

### 7.3.3 Sensor Resolution Characteristic

The sensor configurations suggested in Table 7.2 are evaluated in terms of sensitivity  $s_{\text{pos}}$  in count/ $\mu\text{m}$ . Sensitivity corresponds to the slope of the linear regression of the differential sensor data of Fig. 7.5. A larger sensitivity renders a larger difference in signal amplitude for a given rotor displacement, i.e. mechanical clearance, and is thus —all other factors held constant— preferable.

Figure 7.6a portrays the sensitivity of the different probes excited at central resonant frequency  $f_{\text{res}}^*$ . The different bars represent the sensitivity at different  $z$  axial displacements.

Figure 7.6a shows how the higher the resonant frequency  $f_{\text{res}}^*$ , the higher the sensitivity. The largest obtained sensitivity is 1.15 [count/ $\mu\text{m}$ ], which means 1 count would change for an 850 nm displacement. On another subject, if the rotor is axially moved, the sensitivity deteriorates rapidly and can be eventually halved.

To fairly evaluate the sensor configurations, the noise of the sensor configurations and their relationship with resonant frequency  $f_{\text{res}}^*$  is also recorded. For this experiment, the rotor of Fig. 7.4a is held in the center of its clearance, and the differential data of the sensors are logged and plotted as a histogram. This provides bell-shaped curves, with data values that span with a standard deviation  $\hat{\sigma}_{\text{counts}}$  around a mean position. The estimated  $\hat{\sigma}_{\text{counts}}$  values thus correlate to the noise in the signal. Configurations with low sensitivities result in low standard deviations.

The position resolution  $rs$  is characterized as the smallest displacement that can be *precisely* detected for a given level of signal noise. This rating relates  $s_{\text{pos}}$  and  $\hat{\sigma}_{\text{counts}}$  as in

$$rs = \frac{\hat{\sigma}_{\text{counts}}}{s_{\text{pos}}}, \quad (7.3)$$

in units of length, where *small* resolutions —or being *certain* about a small displacement— are desirable.

Resolution  $rs$  is plotted in Fig. 7.6c, condensing Figs. 7.6a-7.6b. This gauge shows that configurations with higher sensitivities, e.g. also with  $f_{\text{res}}$ , do not necessarily outperform their less sensitive counterparts. The unfiltered signals with high  $f_{\text{res}}$  are noisier, thus adding uncertainty to the estimated position. With these data, resolutions between 2  $\mu\text{m}$  and 6  $\mu\text{m}$  for targets with  $z = 0$  mm are feasible. On another topic, axial displacement reduces sensitivity  $s$  without changing the noise  $\sigma_{\text{counts}}$ , so it worsens resolution.

The signal used for control purposes is filtered so as to increase resolution (at the cost of bandwidth). Sensor probes are ultimately integrated into the prototypes and are energized around 10 MHz. This is done with the Single Flex PCB coils, because they are thinner and their low inductance allows for larger capacitances to reach high frequencies. For better mechanical stability, corresponding to the Single Flex PCB Coil are fabricated in one strip, as in Fig. 7.7,

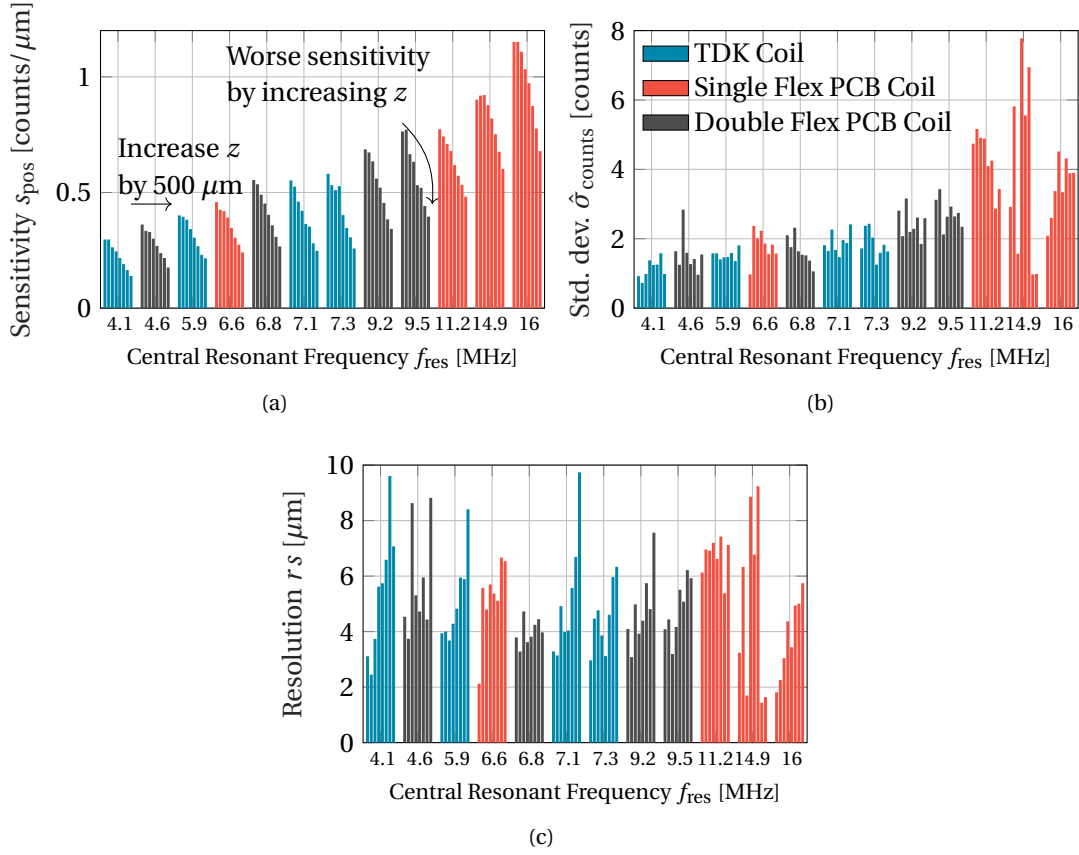


Figure 7.6: (a) Sensitivity and (b) standard deviation (representing the noise) in position and count units for the LC tanks of Table 7.2. The sensitivity is assessed by displacing the rotor; the noise by keeping it static. The measurements lead to the estimation of the sensor's (c) resolution.

and are slid into the air gaps of the slotless and slotted drives. The shielding Flex PCB of Fig. 6.6 is wrapped around the sensing coils and its ground is connected to electronic's ground.

#### 7.3.4 Sensor Noise Characteristic

The sensing probes reside in the air gaps of the prototypes, which are additionally excited with magnetic fields for the functioning of the drive and bearing. It is thus relevant to research if these excitations disturb the sensing system.

In the case of the slotless drive, the backside of the Flex PCB shielding and the sensing coils are close to the motor coils, made out of copper litz wire. As such, they are an inherent target for the EC sensing system, especially as they can vibrate due to the force build-up (as in Lorentz Forces) of slotless drives [156]. They also radiate large  $dE/dt$  gradients due to their PWM excitation.



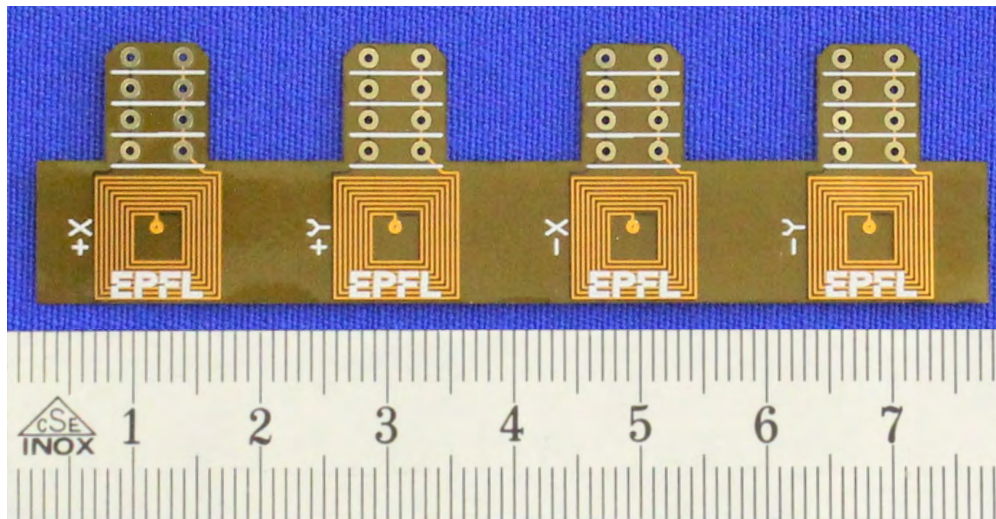


Figure 7.7: Complete Flex PCB strip with four Single Flex PCB of Fig. 7.3a for differential measurement. The strip is rolled and inserted into the air gap of the drives.

In the slotted motor, the sensing coils of the  $y$ -axis lay in front of a motor tooth (top coil in Fig. 6.5). The sensor coils are pierced by the magnetic field of the stator tooth, which is regulated by the PWM-switched motor currents and bear their associated ripple. By contrast, the sensing coils of the  $x$ -axis are exposed to two materials: a drive coil and a stator tooth.

The reason for this section is to investigate how the sensor systems permit the levitation of two drives with different constructions; their sensing coils being exposed to different environments beyond the rotor target.

For this test, the drives from Figs. 7.2c-7.2d are utilized, and the rotors are fixed in the center of their clearances with the XYZ stage. Currents rotating at 10 Hz are then set in the coils, using a 37 kHz switching-frequency PWM, and the position signals are logged at 5 kHz.

Bearing and drive fields are imposed separately and with different amplitudes to better document their different impact upon the signals of the sensors. Coil excitations go from 0 to 264 A·Turns, with 33 A·Turns steps and 0 to 203 A·Turns with 29 A·Turns steps for the slotless and slotted prototypes, respectively.

The influence of a magnetic bearing field upon the  $x - y$  position signals is shown in Fig. 7.8. Figure 7.8b, which belongs to measurements of the slotted prototype, represents the noisiest recorded measurement with peak-to-peak values that represent less than 4% of the sensor signal inside the clearance. For the slotless prototype, the disturbance amounts to less than 3%. As it can be seen, the noisiest axes are the  $x$  and  $y$  for the slotless and the slotted, respectively.

A frequency analysis of the disturbances, for each axis, excitation type (and intensity), and prototype is performed. To this end, a Fast Fourier Transform (FFT) is applied on the different signal portions (or colors) of the positions signals disturbed by the bearing excitation, c.f.

### 7.3 Experimental Validation of the Eddy-Current-Based Estimation of Rotor Position

Fig. 7.8, and by the drive excitation (not plotted).

The amplitude distribution resulting from the FFT is integrated upon the frequency to render the Cumulative Amplitude Spectrum (CAS). The CAS portrays more cleanly how single frequencies contribute to total noise than the FFT.

Figure 7.9 displays the frequency CAS of the  $x$  and  $y$ -axes, for both drives and both excitation types. At a general level, stronger excitations in terms of A·Turns induce more cumulated noise.

The step-like trend of the curves hints that the 10 Hz excitation frequency used in the tests causes most of the noise in *all* cases. Furthermore, in both drives, the magnitude of the noise picked up by the bearing excitation considerably changes with the sensor axis.

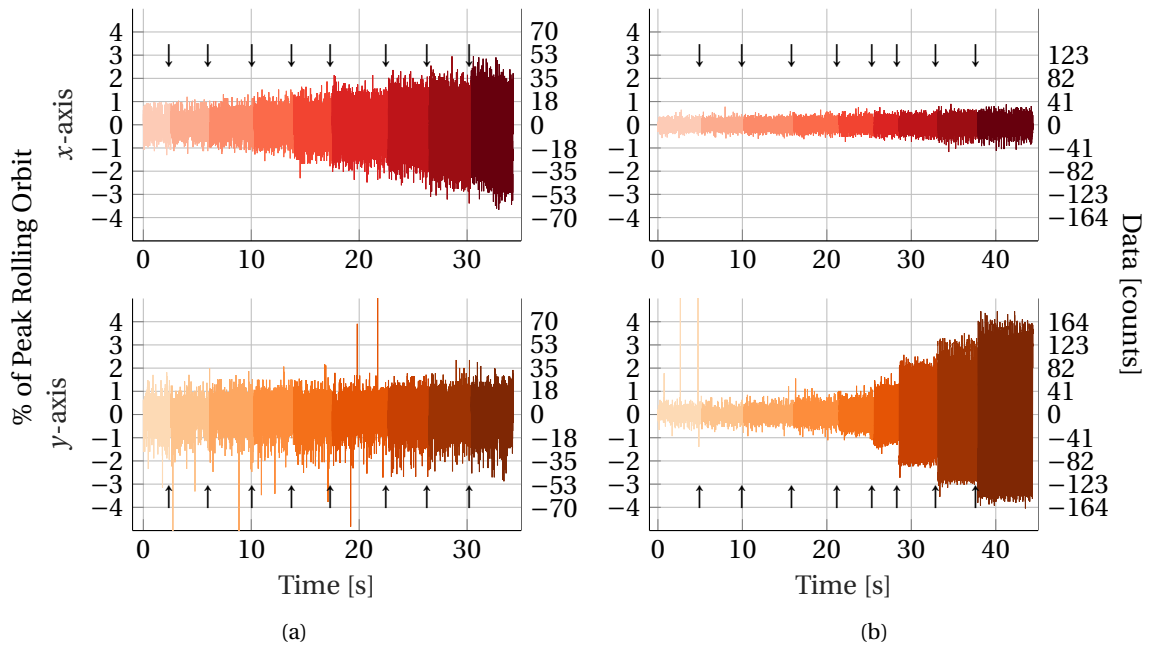


Figure 7.8: Position signals of the (a) slotless and (b) slotted prototypes being disturbed by 10 Hz bearing currents with increasing amplitudes —marked by darkening colors— with a center-fixed rotor.



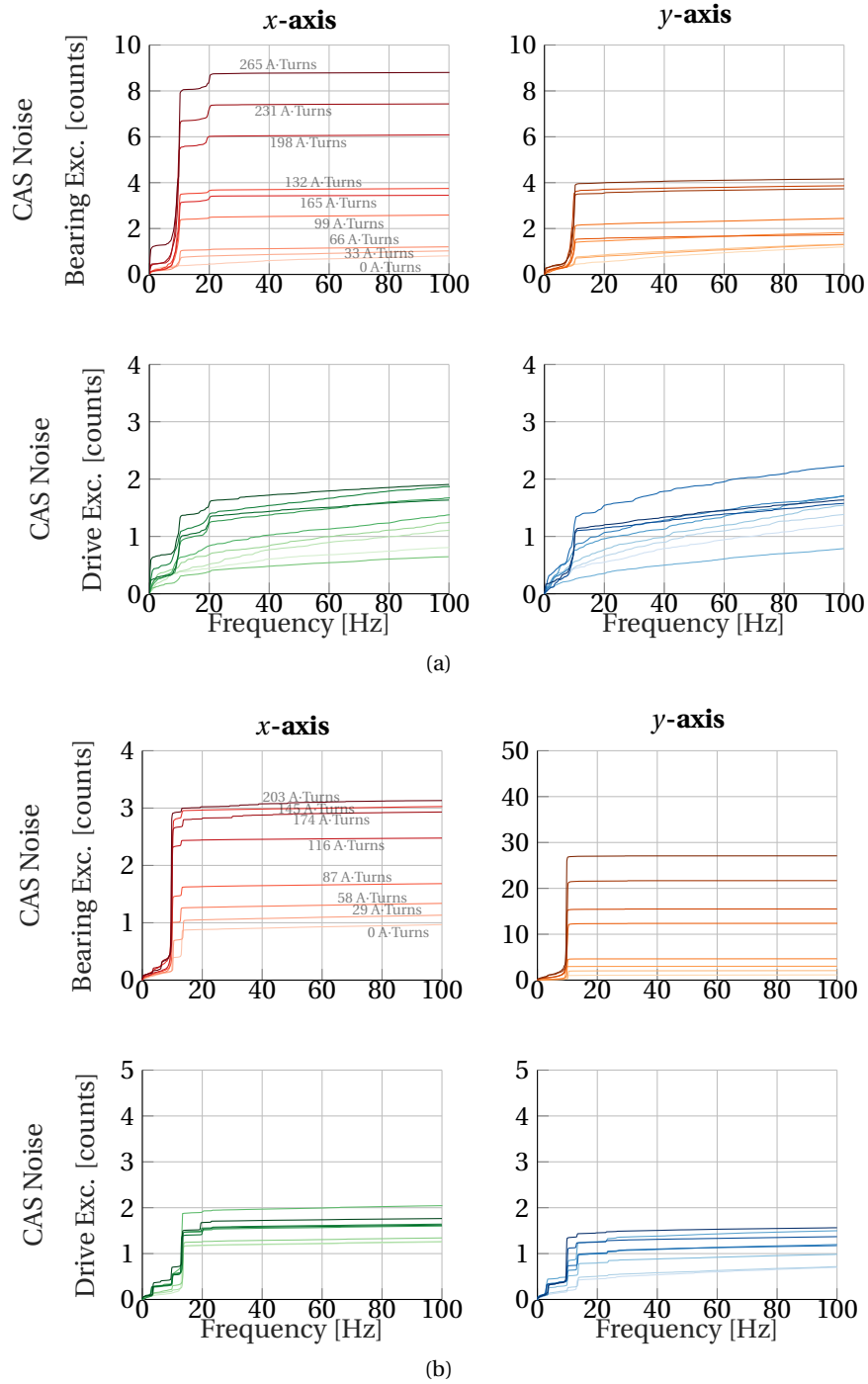


Figure 7.9: CAS induced by bearing and drive currents of increasing amplitude (indicated on the lines, plotted in darkening colors), turning at 10 Hz, for the (a) slotless and (b) slotted motor. The noise considerably increases at the 10 Hz excitation frequency for all axis and motors.

### 7.3 Experimental Validation of the Eddy-Current-Based Estimation of Rotor Position

The different amounts of noise being picked on the  $x$  and  $y$  sensors can be explained by the sensor positioning, along with the bearing's and PM's magnetic fields, shown in Fig. 7.10.

The probes on the  $y$  axis of the slotted prototype are installed in front of the stator teeth, as in Fig. 7.10b. In this motor, force is built up by *reducing* the magnetic flux of the PM at one side of the stator and *augmenting* it on the opposite. The opposing magnetic biases at the teeth on the  $y$  axis (due to the PM's magnetization) alter the magnetic permeability of the iron in the vicinity of the sensing coils, thus changing their probes' inductance.

The case of the slotless motor's  $x$ -axis is similar and is shown in Fig. 7.10a. For bearing excitation, an electric phase difference of  $120^\circ$  is needed between adjacent coils. For currents with opposing signs, magnetic fluxes leak from between the coils, out of the stator yoke, and into the air gap. These leakage fluxes generate noise in the measurement probes. Concerning the axes, more flux penetrates the sensing coils of the  $x$ -axis than those of the  $y$ -axis, as the latter are not installed *between* two coils.

On the other hand, drive fields cause disturbances that are one order of magnitude smaller than those of the bearing excitation. For the slotless motor, adjacent coils carry currents with an electric  $60^\circ$  phase shift for torque generation, so lesser magnetic flux leaks. This causes a lesser disturbance of the position signal.

In the slotted drive, drive excitations bias the opposite stator teeth to the same magnitude of magnetic flux density. This either increases *or* decreases the inductance of both opposing sensing coils. Nonetheless, this alteration in inductance of the sensing coils of the same axis is canceled out by the differential position calculation, resulting in less noise.

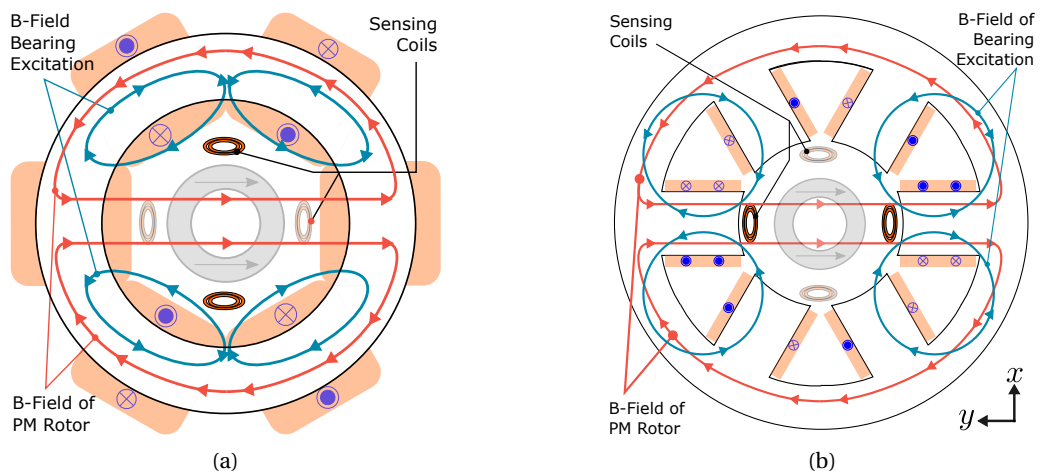


Figure 7.10: Fluxes of the bearing excitation and PM rotor for the (a) slotless and (b) slotted motor. Bearing fluxes pass through the sensing coils of the  $x$ -axis and  $y$ -axis of the slotless and slotted motor, respectively. This modifies the magnetic permeability of the iron close to the opposing sensors and it is ultimately picked up as noise. The noisier orientations of the sensing coils are depicted in opaque, and the less noisy directions are faded out.

## 7.4 Experimental Validation of the Hall-Effect-Based Estimation of Rotor Position

As introduced in Chapter 5, the magnetic flux density in the air gap of the drives contain information on the axial, radial, and angular positions of the rotor. To characterize the fields and their sensitivity to displacements of the rotor, the slotless stator from Table 7.1 is mounted onto an XYZ precision table. This time, rotor #1 can be rotated thanks to a rotatory stage. This is shown in Fig. 7.11a.

Two PCBs are mounted onto the stator: one below and one above, for a total of 12 HESs. The HESs can be mounted to pick up either axial or radial fields, and are referred to according to the *orientation* of the magnetic flux picked up by them.

Testing both sensor orientations allows comparing which configuration is more sensitive to rotor movements. The mounting and position of these sensors are depicted in Fig. 7.11b.

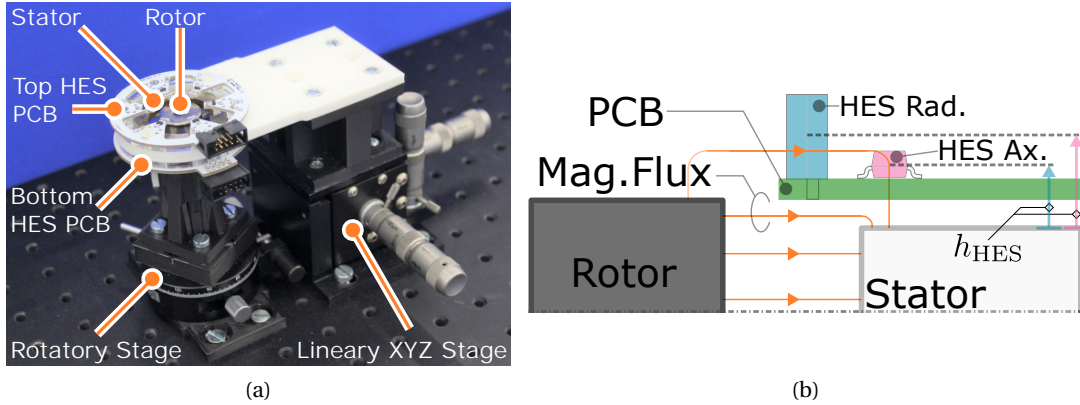


Figure 7.11: (a) The stator of the slotless drive is mounted onto an XYZ optical table for linear translation, and the PM is mounted onto a rotatory stage. (b) PCBs above and below the former to position its HES at  $(r, h)=(13, 8.3)$  and  $(16, 7.3)$  mm.

The outputs of the 12 HES are logged by 12-bit ADCs. To test the models developed in Section 5.4, a displacement is manually imposed onto the screws of the linear or rotational stage, and the data is logged.

### 7.4.1 Rotor Angle Estimation

As a first test, the angle estimation capabilities of the HES array are trialled. The rotor is centered in its mechanical clearance, and turned with  $5^\circ$  steps. The output of each HES, as well as the resulting  $(\cos \psi, \sin \psi)$  are plotted in Fig. 7.12.

Figure 7.12 displays that axial sensors measure larger magnetic flux amplitudes. This enhances the signal-to-noise ratio, making axial orientation preferable to the radial for angle estimation.

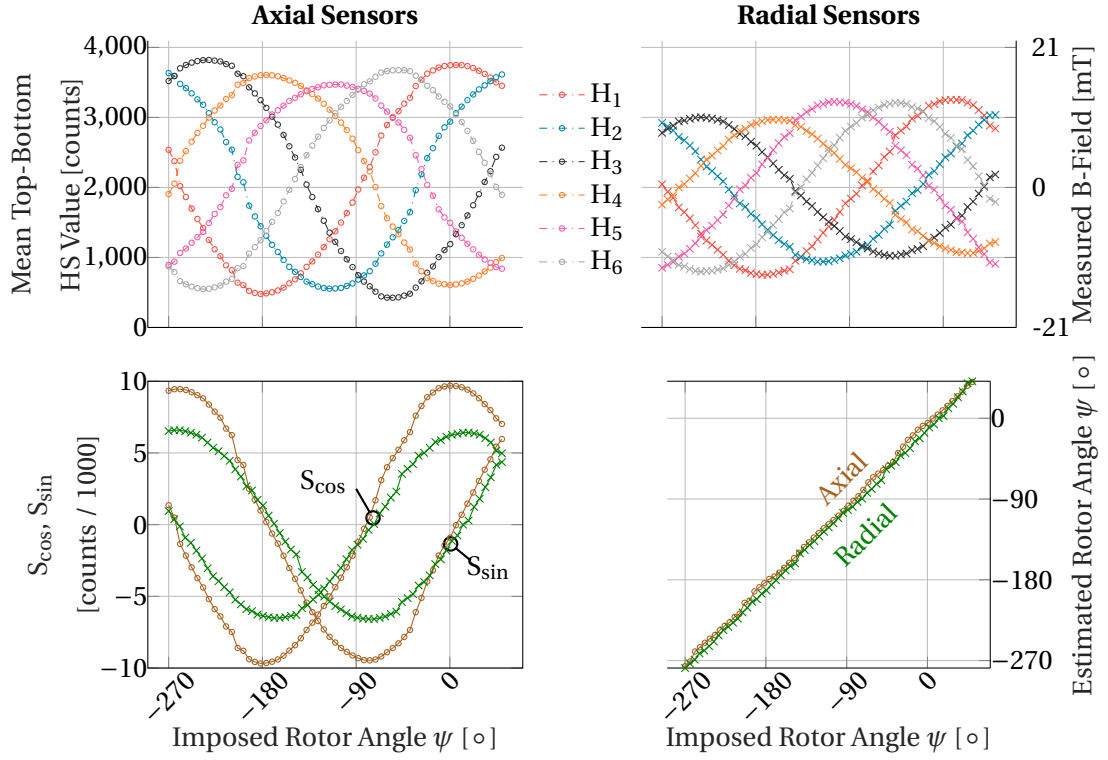


Figure 7.12: The rotor is rotated in  $+\psi$  direction.

Nonetheless, both HES orientations suffice to estimate rotor angle with precision, as they both draw a linear relationship with the angle imposed on the test bench.

### 7.4.2 Radial Rotor Position Estimation

The capability of the HES to estimate the radial position of the rotor is then tested. Figure 7.13 displays how the mean of the bottom and top HES changes when the rotor with  $\psi = 270^\circ$  (the north pole of the rotor between  $H_5$  and  $H_6$ ) is displaced in  $+x$ -direction (from  $H_4$  and  $H_1$ ).

Two different progressions along with the displacement are logged. The magnetic fluxes measured by the radial sensors  $H_1$  and  $H_4$  —perpendicular to the rotor poles— change with rotor displacement, although this is not forecasted by the model. These field gradients —perpendiculars to the magnet poles— are as large as those next to the rotor poles, so that all HES measure the same slope. Thus, parameter  $\tau_k$  from Eq. (5.2) *may not* be neglected, so the proposed model can estimate rotor position with lower accuracy for such HES readings.

On the other hand, a quasi-null gradient is present for the axial HES  $H_1$  and  $H_4$ , so  $\tau_k$  can be neglected and the assumed model holds valid. If the radial position of the rotor is to be estimated with the presented model, axial sensors should render a more precise rotor position evaluation.

With  $\psi = 270^\circ$  (rotor north pole between  $H_5$  and  $H_6$ ), the position of the rotor is displaced in  $x$ ,

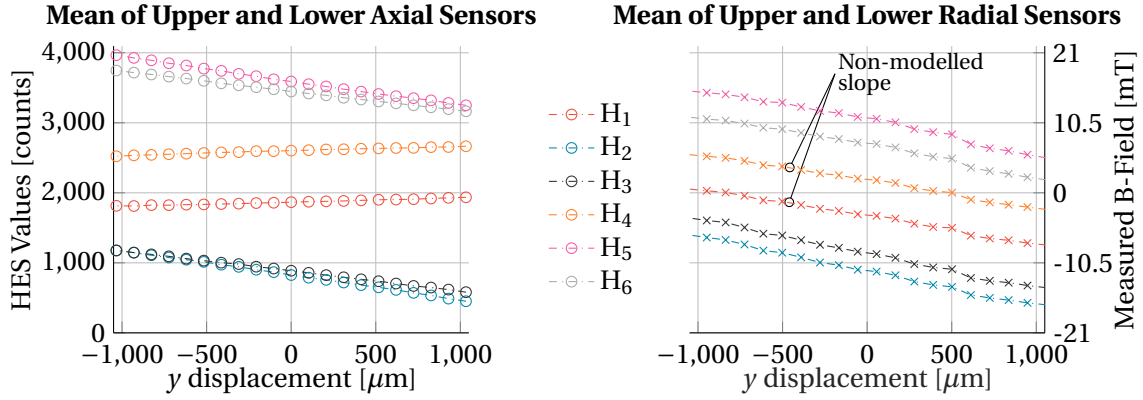


Figure 7.13: The rotor is displaced in +y direction —towards  $H_2$  and  $H_3$ — with  $\psi = 270^\circ$ .

y, and  $x - y$  direction for radial and axial HES. The HES outputs are recorded and the position on stator coordinates ( $S_{x_{st}}, S_{y_{st}}$ ) is determined and shown in Fig. 7.14.

Figure 7.14a depicts the estimated position ( $S_{x_{st}}, S_{y_{st}}$ ) calculated utilizing the axial sensors. Their displacements in  $x$  and  $y$  directions are rather (but not perfectly) perpendicular. This may be due to the rotor drifting in the  $x$ -direction, i.e. the direction of magnetization of the rotor *during* the test, owing to the stark radial stiffnesses of the drive configuration.

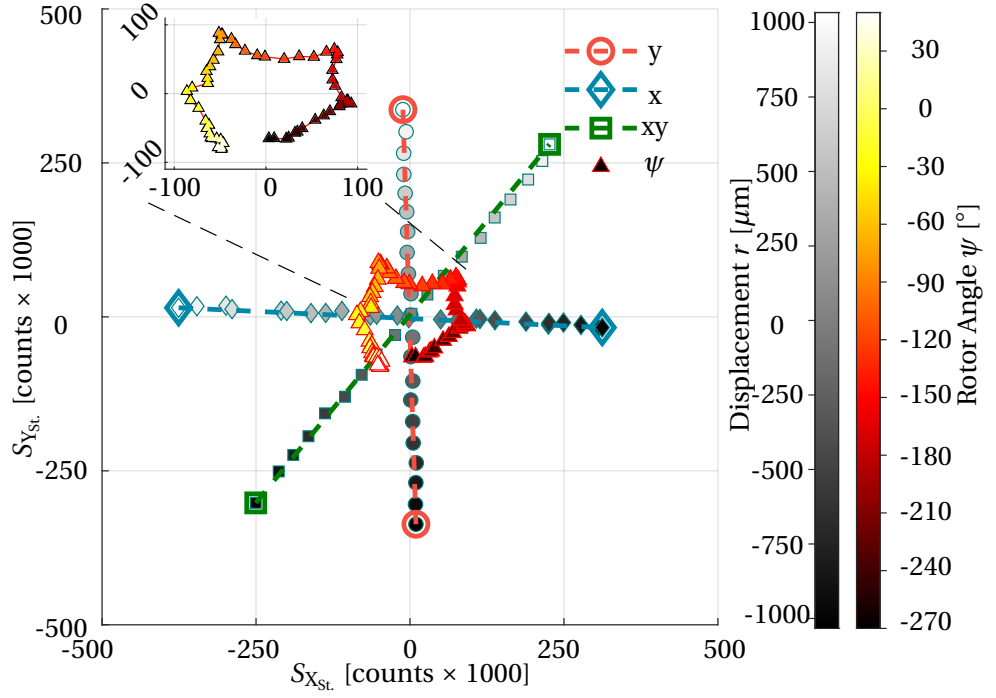
The estimated position of the rotating (but centered) PM that leads to the signals in Fig. 7.12 is also depicted. As mentioned, the rotor is spun for  $270^\circ$  and it can be supposed that it *slightly* buds out of its center. The test bench is not infinitely stiff and may slightly arch under the radial stiffnesses of the drive configuration; yet the amplitude of the position estimation is comparable to the tests upon the  $x$ ,  $y$ , and  $x - y$  axes. This position estimation exhibits ripple which does not completely account to rotor translation.

The experience is recreated employing the radial sensors. The estimated positions of Fig. 7.14b on the  $x$  and  $y$  are once again almost perpendicular, but the amplitude of the signal is considerably lower than that of the previous axial sensors.

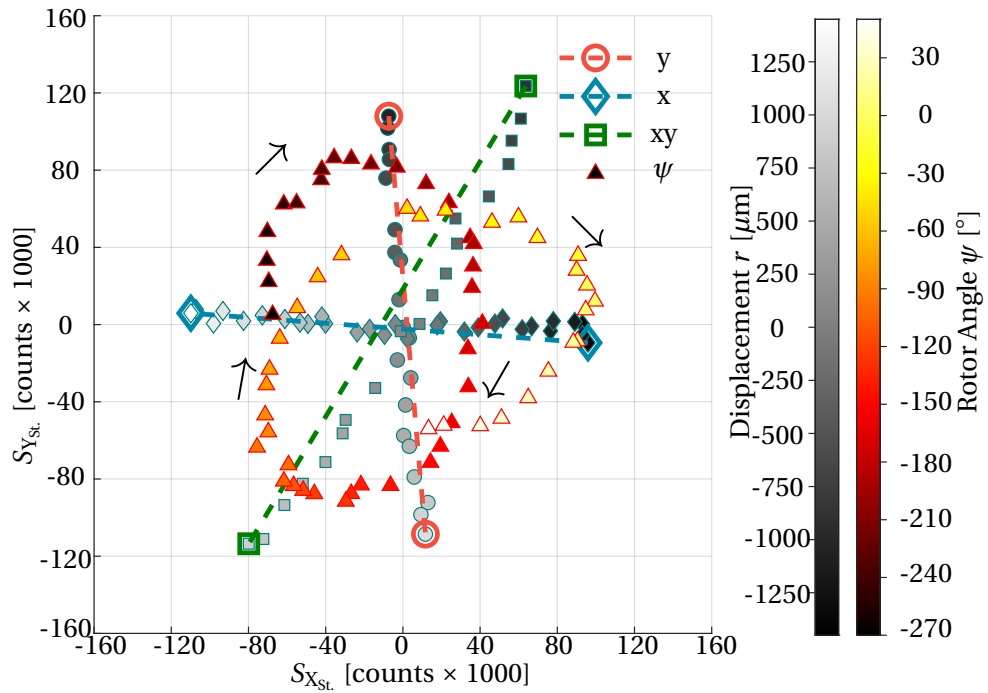
When the rotor is just turned in the middle of the air gap, a second harmonic arises in the estimated position of Fig. 7.14b. The amplitude of this ripple is similar to the amplitudes of the displacements around 1 mm, rendering the estimation with this sensor placement not suitable for exact position estimation. The eccentricity of the rotor affects the air gap flux distribution, and axial fields —or its position— are less sensitive to this effect.

The signal amplitude  $r \cdot s_r$  of Eq. (5.10) and its linearized sensitivity  $s_r$  are displayed in Fig. 7.15 for the axial and radial HES. The different sensitivities of the axial HES  $s_r$  in the  $x$ ,  $y$  and  $x - y$  directions could be caused by the PCBs not being perfectly centered, the DRV5055s being imperfectly placed, or by the test bench slightly bending more towards some magnetization directions than towards others. Nonetheless, the first two reasons may be corrected via software, after capturing the signals.

## 7.4 Experimental Validation of the Hall-Effect-Based Estimation of Rotor Position



(a)



(b)

Figure 7.14: Estimated rotor position  $(S_{X_{st}}, S_{Y_{st}})$  for a displacement (marked on the gray color bar) on the  $x$ ,  $y$ ,  $x - y$ , axes and  $270^\circ$  of a centered rotor. The estimated position of the turning rotor (see Fig. 7.12) is marked with a  $\Delta$ , and the rotor angle is displayed on the red color bar. The position cloud is depicted for (a) axial and (b) radial HES.

On the other hand, the sensitivity of the radially-placed HES is circa 3 times lower than that of the axial sensors. Besides, it varies considerably with the direction in which the rotor moves. These issues render the radial configuration along with its sensor locus inappropriate for rotor position estimation purposes. The validity of the estimation of the rotor's radial position employing one PCB with axial HES is further analyzed in this chapter by comparing its signals to that of the EC *during* motor operation.

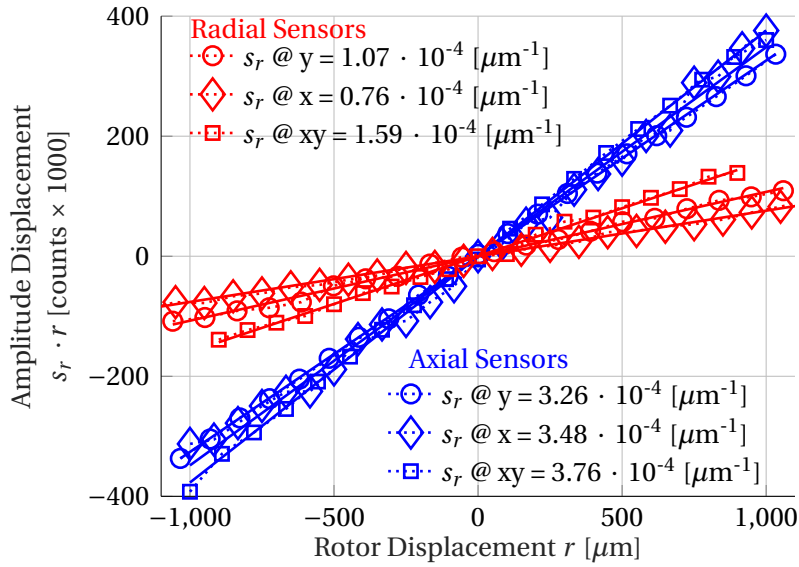


Figure 7.15: Calculated radial rotor position sensitivities  $s_r$  for axial and radial HESs.

### 7.4.3 Axial Rotor Position Estimation

The trend of the single HES signals as a function of axial rotor displacement is documented in Fig. 7.16. When pulling the rotor upwards, the amplitude of the bottom sensors reduces, while that from the top sensors increases. The axial sensors respond more linearly to the  $z$  displacement than the radially-placed, as the latter tend to be more parabolic towards  $-2000 \mu\text{m}$  and  $2000 \mu\text{m}$ .

Signal  $S_z$  and its corresponding sensitivity  $s_z$  of Eq. (5.12) are linear and constant all through the tested  $z$  range, respectively. Coincidentally, both sensor placements result in extremely similar  $S_z$  trends and sensitivities  $s_z$ .

## 7.4 Experimental Validation of the Hall-Effect-Based Estimation of Rotor Position

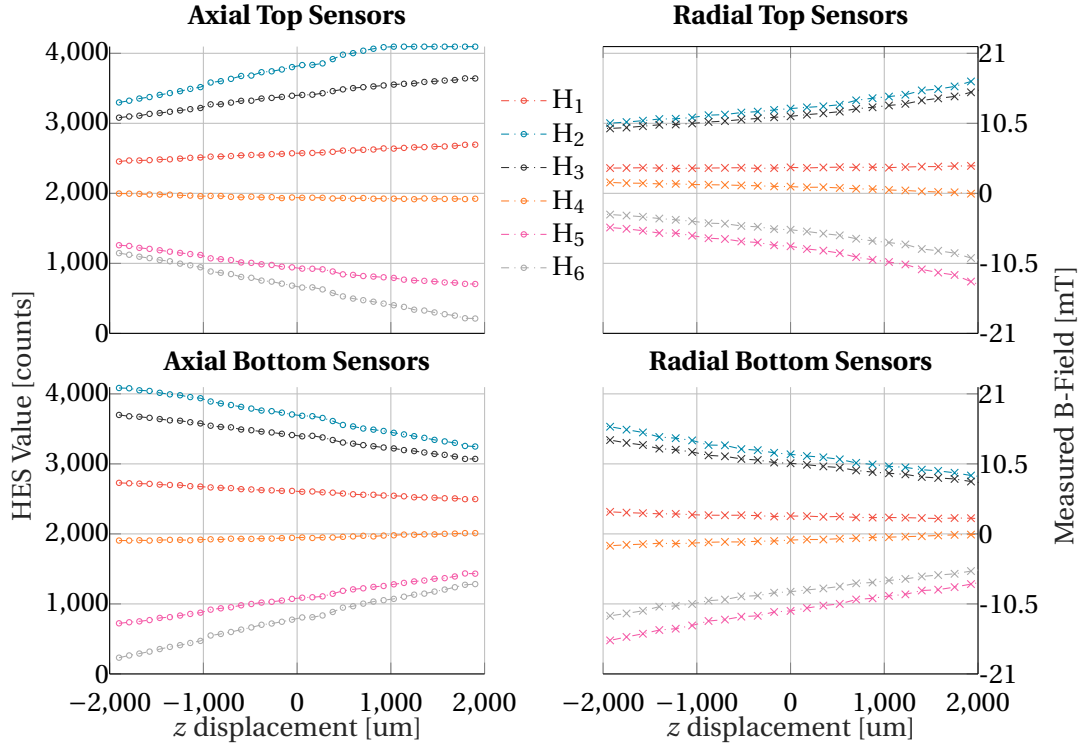


Figure 7.16: The rotor is displaced in the +z direction. The values of the HESs are read at the ADC of the microcontroller.

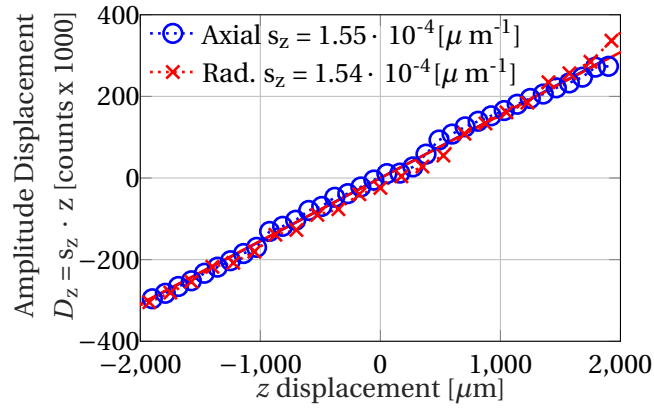


Figure 7.17: Axial displacement signal, using axial and radial HES.



#### 7.4.4 Current Compensation for Hall-Effect Sensors

With the previous results, the axial HES are deemed better suited for the integration in the prototypes. They offer a larger signal amplitude and —if needed— a better accuracy of radial position estimation.

After having characterized their response to rotor movement, their response to coil excitation is investigated. To this end, a coil is wound between  $H_1$  and  $H_6$  as shown in Fig. 7.18a. This coil is energized by a current-controlled source. Without a rotor in the air gap, the change in signal of all the HES is measured as a function of the current.

The results of the experiment are plotted in Fig. 7.18b. *All* currents hold a linear dependency with the tested current, and the slopes of this relationship are indicated. There are fundamentally three slope values, which determine the relationship between the measured magnetic flux density and the current, with a positive or negative sign if the HES lays left or right from the coil, respectively. This supports the assumption of the mirror influence of currents upon HES shown in Fig. 5.12.

The rest of the coils of the drive are wound. To remove the influence of the currents upon the HES, their signals are first calibrated, i.e. their offset is removed. Then, with the experimental data from Fig. 7.18b, the magnetic field of the motor currents is compensated—for all sensors—

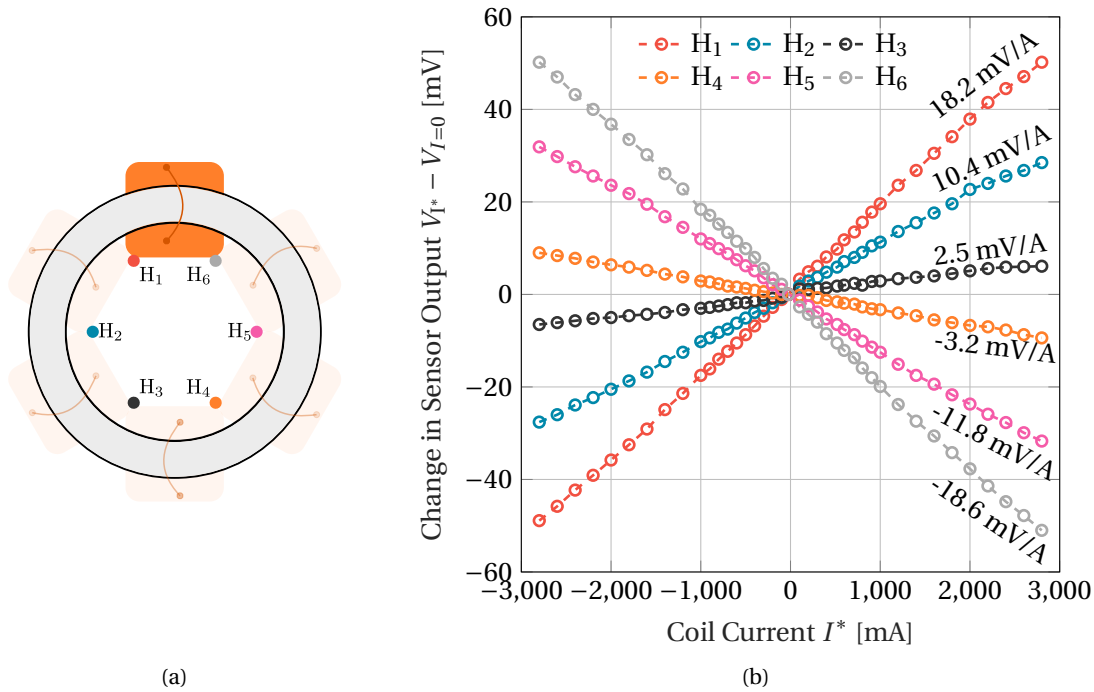


Figure 7.18: (a) The opaque coil is energized with currents between  $\pm 3$  A, and (b) the measured outputs of the HES  $H_{1,\dots,6}$  are measured, rendering a linear relationship with the current.

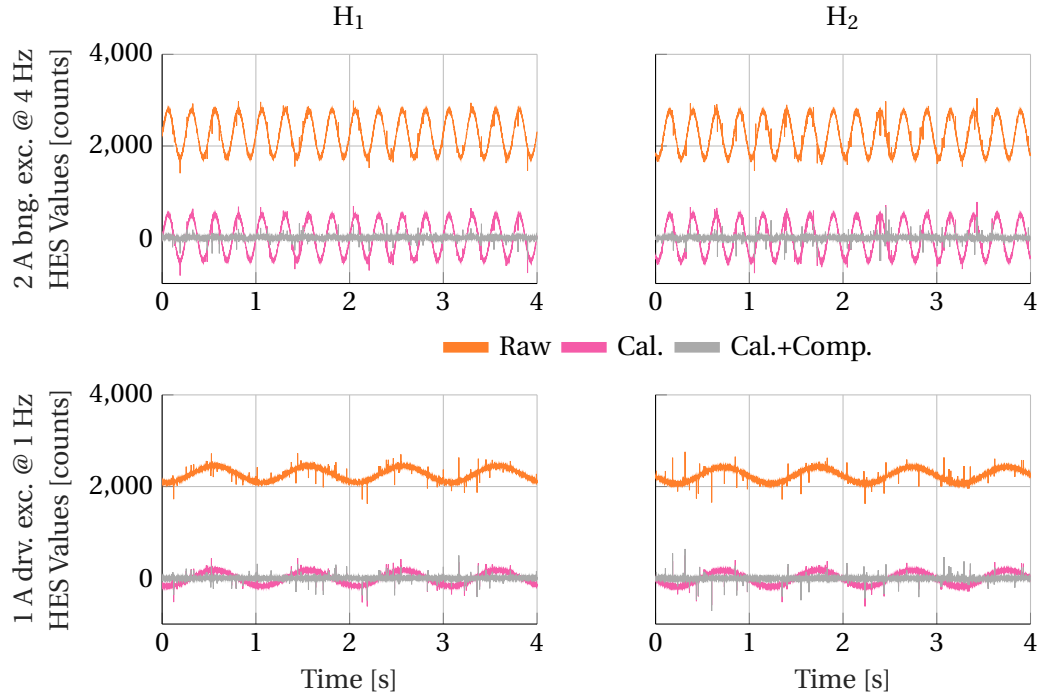


Figure 7.19: Bearing (top) or drive (bottom) excitations are imposed into the coils of the drive, and the outputs of  $H_1$  and  $H_2$  are logged. The characterization of Fig. 7.18b enables compensating the signals to remove the disturbance created by the coils to *only* see the magnetic flux of the PM.

via software as proposed in Eq. (5.19). The effect of the calibration and compensation is shown for sensors  $H_1$  and  $H_2$ , for bearing and drive currents of different frequencies. It can be seen that the calibrated, compensated HES values stay practically unmoved despite the current excitations.

The same compensation scheme is implemented for the slotted drive. Instead of rerunning the experiment of Fig. 7.18b with this prototype, a linear least-squares compensation scheme is implemented on the microcontroller. This enables the online calculation of the compensation parameters and eliminates the current disturbance with the same success shown in Fig. 7.19.

### 7.5 Measurement of Forces of the Prototypes

In this section, the electromechanical characterization of two stators topologies and two PM rotors is performed. Their passive and active forces and torques are measured on a test bench. Merit ratings that evaluate the magnetic levitation effort and the torque generation in terms of Joule losses are proposed. The measurable advantages and disadvantages of each motor topology are remarked.

The mentioned evaluations are juxtaposed to the results coming from FE simulations. This comparison aids to validate the FE simulations as a valuable asset for the modelling of the electromechanical attributes of bearingless drives.

#### 7.5.1 Test Bench

The characterization of the prototypes is aided by a force-torque transducer and a linear XYZ stage that helps determine the position of the rotor using a non-ferromagnetic pin. The pin is long enough to keep the rotor and stator away from the XYZ stage. This guarantees that there is no magnetic coupling between the stage and the drive. The complete test bench is pictured in Fig. 7.20.

To test the active force and torque, the interconnections of the coils are redone at a connector level. This way, only *one* three-phase power stage [174] is needed for the test and assures that either force *or* torque are built up on the rotor. Current generation and force and torque control are regulated by the *TI* microcontroller [175]. This hardware is shown in Fig. 6.2.

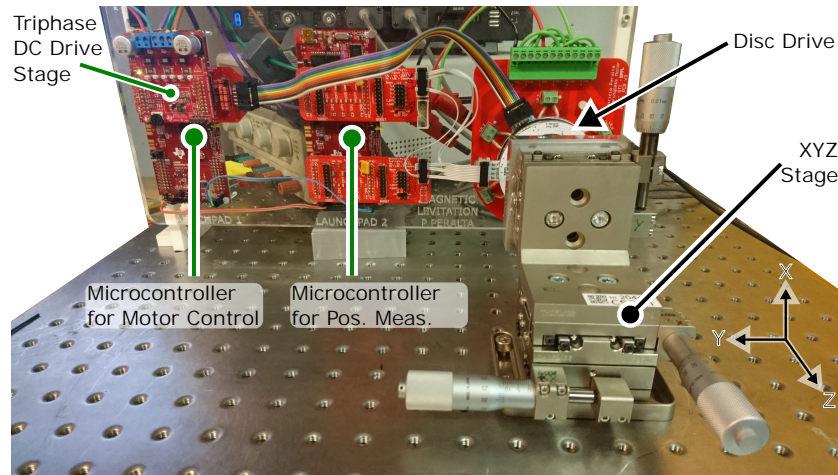
#### 7.5.2 Passive Forces

##### Radial Forces

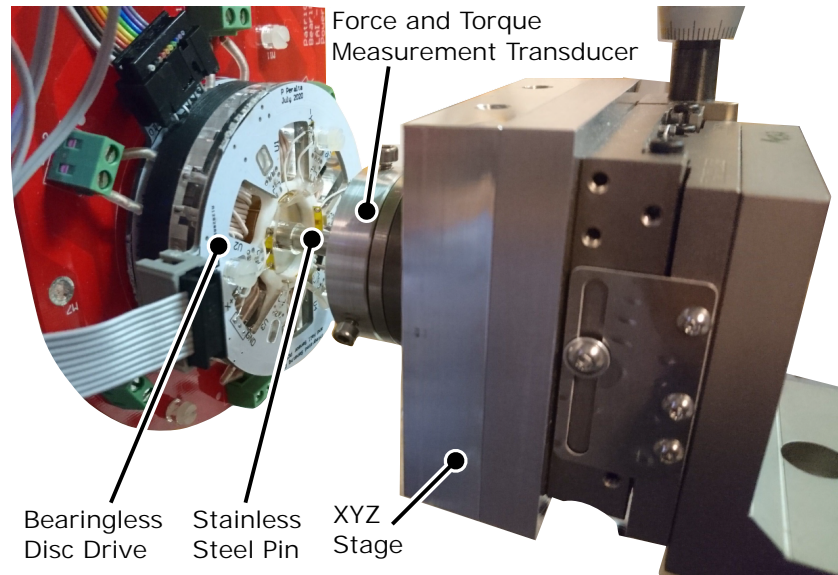
The rotor is moved within the mechanical clearance, in the  $x$  or  $y$ -directions as shown in Fig. 7.20c. The rotor is displaced parallel and perpendicular to the magnetization direction ( $x$  and  $y$  respectively) of the rotor for the slotless drive. On the slotted motor, this is done with the rotor at angles  $\psi = 0^\circ$  and  $\psi = 90^\circ$ : with a rotor pole in front of a tooth, or between two of them, respectively. In this manner, a notion of how the radial stiffnesses vary with rotor angular position is provided.

The measured radial forces are displayed in Fig. 7.21. They are rather linear with the radial displacement of the rotor within the tested displacements [156].

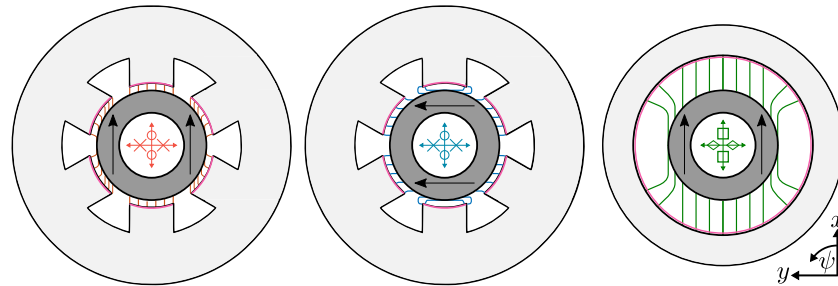
To calculate the stiffnesses of the radial forces, a linear function is fit to each of the curves of Fig. 7.21. Their slopes correspond to the radial stiffnesses, which are plotted in Fig. 7.22. The measured stiffnesses are juxtaposed to the FE-estimated stiffnesses, which are depicted in gray.



(a)



(b)



(c)

Figure 7.20: (a) The electric motors, and microcontroller are screwed onto a plexiglass table, which is fixed onto an optic table, along with the force-torque sensors. (b) This sensor is mounted onto an XYZ linear stage that positions the PM rotor inside the mechanical clearance by employing a non-ferromagnetic stainless steel pin. The radial forces of the prototypes are tested in the directions depicted in (c) which correspond to those depicted in Fig. 7.21.

As expected, the magnitude of the stiffness depends on the orientation of the magnet poles regarding the stator teeth (for the slotted motor) and the direction of displacement concerning PM magnetization.

The slotless drive provides weak radial stiffnesses because of its larger magnetic air gap. This is favorable if the system operation must meet low vibration requirements [21].

In the slotted drive, the stiffness is a function of the rotor's magnetization orientation and its angular position regarding stator teeth. It has a less intuitive progression. In any case, it

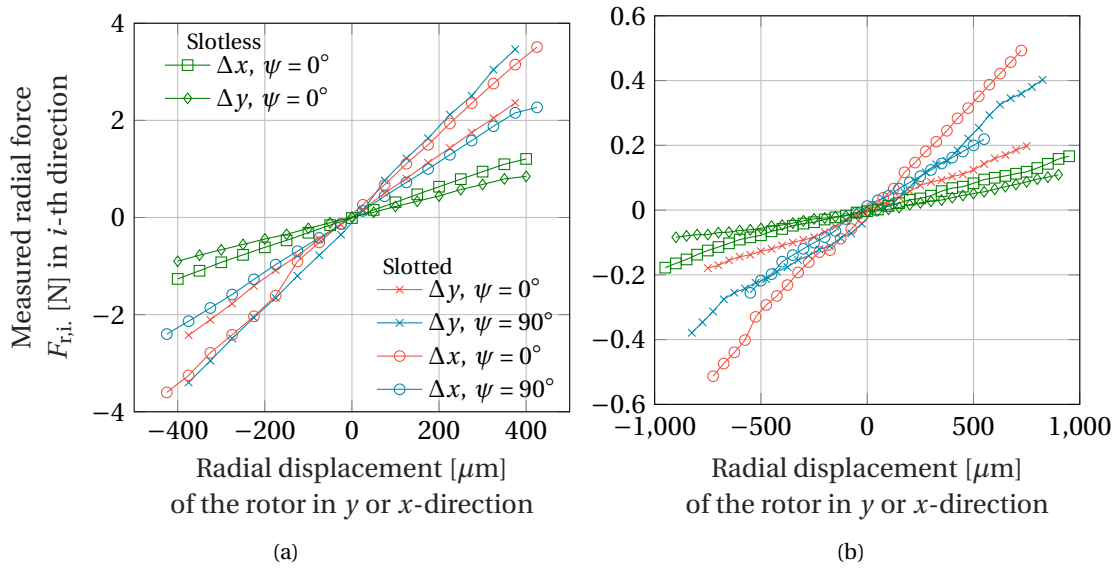


Figure 7.21: Measured radial forces  $F_{r,i}$  for the (a) rotor #1 and (b) rotor #2.

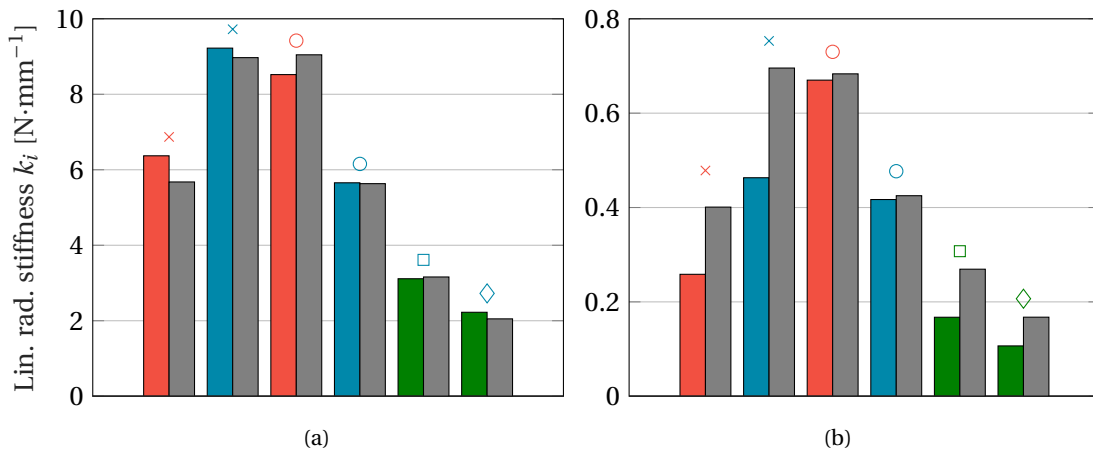


Figure 7.22: Estimated radial stiffness  $k_i$  for the (a) rotor #1 and (b) rotor #2. Same legend as in Fig. 7.21.

renders stronger stiffnesses than those of the slotless rotor, fundamentally because it has a narrower air gap.

Rotor #1 supplies the strongest stiffness. Among these, i.e.  $\Delta y, \psi = 90^\circ$  vs.  $\Delta x, \psi = 0^\circ$ , the former is stronger. In the case of  $\Delta y, \psi = 90^\circ$ , the surface generating the reluctance pull is determined by two poles, thus reducing the reluctance of the air gap in comparison to  $\Delta x, \psi = 0^\circ$ .

In contrast, the force is relatively feeble at  $\Delta x, \psi = 90^\circ$ . In this case, the stator tooth covers the perimeter of the magnet that is perpendicular to the pole. With this alignment, the magnetic flux barely penetrates the stator. In contrast, with  $\Delta x, \psi = 90^\circ$ , a larger portion of the pole, parallel to the magnetization, is enclosed by the teeth, so more magnetic flux passes into the stator and builds up force.

The FE estimations of Fig. 7.21a lay within 10 % of the experimental values for the slotless prototypes. On the other hand, they practically dismiss the influence of the rotor orientation, only portraying if the rotor is displaced parallel or perpendicular to its magnetization. According to the computational simulation, the first and fourth grey columns of Fig. 7.21a result in practically the same value. This is also the case for the second and third columns.

The test results deviate from these values. The measured forces are different according to the orientation of the rotor so that the aforementioned *colored* columns (1<sup>st</sup> red with 4<sup>th</sup> blue, and 2<sup>nd</sup> blue with 3<sup>rd</sup> red) do show a difference. They can be either stronger or weaker than the FE estimations. If high precision is required, FE simulations are thus unreliable to portray the subtleties of the radial force as a function of rotor orientation.

The stiffnesses of rotor #2 behave differently. The largest radial stiffnesses are naturally on the magnetization directions  $\Delta y, \psi = 90^\circ$   $\Delta x, \psi = 0^\circ$ ; but the strongest is that with the rotor pole towards the stator tooth.

The agreement of the FE-provided forces with the measured ones is poorer for rotor #2. As with rotor #1, it does not completely account for differences in rotor orientation. On top of these, the computational simulations systematically overestimated the radial stiffnesses. This is more apparent when moving the rotor towards two stator teeth, e.g. the first two columns.

The computational results for the slotless drive with rotor #2 also overestimate the radial stiffness. From the results of rotor #2, it can be concluded that if weak magnetic fluxes inside air gaps are simulated, the results of the simulations might be unprecise or need special care, e.g. finer meshing, etc.

### Axial Forces

The rotors are pulled in the  $+z$  direction, producing a reaction force  $F_z$  in the  $-z$  direction. This force augments almost linearly, plateaus, and then rapidly falls.

The axial pull of rotor #1 is approximately one order of magnitude stronger than that of rotor #2, due to its stronger air gap  $B$  field. Likewise, the wider air gap of the slotless drive leads to feeble pulls. In the case of both rotors, the pull amounts to about half of those of the slotted drive.

Concerning the slotted motor, it can be seen that the initial slope of Fig. 7.23, i.e. the axial stiffness, is almost identical rotor orientations  $\psi = 0^\circ$  and  $\psi = 90^\circ$ . Nonetheless, if the rotor is axially pulled too far away, the axial reactions follow different paths. The slotted drive with  $\psi = 0^\circ$  provides a stronger restoring force.

The trend of the axial forces, as well as the linearized axial stiffness, are also estimated with the aid of FE simulations. They are plotted in grey in Fig. 7.23.

The course of the axial forces along with displacement  $z$  is practically the same for rotor angles  $\phi = 0^\circ$  and  $\phi = 90^\circ$ , thus resulting in the same values of maximal axial force  $F_z^*$ . The mean of their (practically) identical trends is depicted on the right plots of Fig. 7.23. The FE-simulated

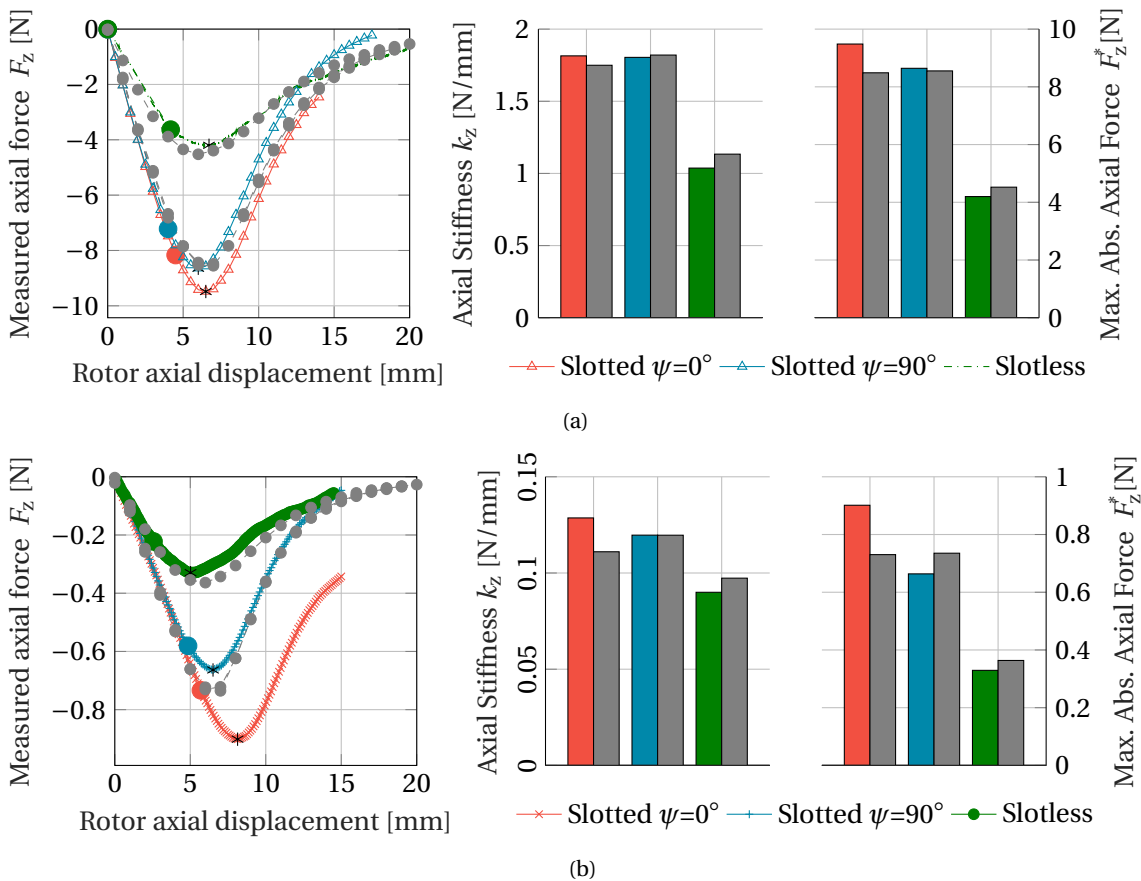


Figure 7.23: Measured axial forces for the (a) rotor #1 and (b) rotor #2. The linearized stiffnesses and maximum axial pull are estimated at the colored dots and black asterisks, respectively, and are also plotted in the bar graphs.

$F_z^*$  value is in all cases closer to the one measured for the  $\phi = 90^\circ$  of the slotted motor, and thus underestimates the max force which was obtained with  $\phi = 0^\circ$ . The max axial force of the slotless drive is also overestimated by the FE simulations.

The axial stiffness is calculated employing the resulting axial pull at a rotor displacement of  $z = -1$  mm. For the slotted stator, this resulted in minor differences among axial stiffness for rotor orientations  $\phi = 0^\circ$  and  $\phi = 90^\circ$ , with the latter providing larger values. The experimental results render the opposing picture: rotor orientations of  $\phi = 0^\circ$  gave way to larger axial stiffnesses. For the slotless stator, the FE simulations overestimated the axial stiffnesses for both rotors.

All in all, the FE simulations provide axial characteristics which can deviate up to 12 % from measured values; either below or above these. In this regard, finer meshes at the stator teeth could better represent the axial stiffness and its angle dependency. Moreover, percentual errors are larger for feebler magnetizations, e.g. rotor #2.

Depending on the application, such percentual error might not be tolerated. As with the radial stiffness, the simulations are more accurate stronger magnetic flux densities in the air gap, e.g. rotor #1. Therefore, special attention must be given to very wide air gaps or weak rare-earth magnetic materials. Again, the simulation does not portray the differences in axial stiffness due to rotor orientation.

### 7.5.3 Active Forces and Torque

The motor coils must be excited to control the destabilizing radial pull and enable magnetic levitation. The active forces can be independently generated in  $\pm x$  and  $y$ -direction as in Eqs. (3.32)-(3.35).

Incrementing  $i_{F,x/y}$  currents are set for forces in  $\pm x$  and  $y$ -directions, and the resulting active forces are logged. Since the slotted motor has more  $N_{\text{Turns}}$  than the slotless, c.f. Table 7.1, it is expected that the former spawns a stronger force for the same current  $i_{F,x/y}$ . This stronger force generation capacity is preferable for the slotted drive as it generates larger radial passive forces.

The forces do not lay *exactly* on top of the axes, especially those of Fig. 7.24a. This becomes evident for large currents. For the slotted rotor, the direction of the deviation changes if the direction of the rotor is  $\psi = 0^\circ$  or  $\psi = 90^\circ$ .

Nonetheless, the deviation of the forces from the  $y$  or  $x$ -axes remains constant, and they are not dependent on the current magnitude, which is beneficial for control [76]. This suggests that the deviations are not rooted in motor design, but that they are caused by some issues at the estimation of rotor angle.

In any case, the deviation of the radial forces from the desired direction accounts for less than



4°. This is considered acceptable for magnetic levitation [38], and can be naturally corrected by the PID position controller.

The built-up forces are compared more fairly by regarding  $N_{\text{Turns}}$ . The result is displayed on the right side of Fig. 7.24, where the absolute value of the slopes corresponds to  $k_{F_x}$  and  $k_{F_y}$ . For a given motor, these force-current gains barely vary from one another. They can be characterized by a single  $k_F$ , which is desirable.

In terms of magnitude, the right side of Fig. 7.24 portrays that  $k_{F,\text{slotted}} \approx 3 \cdot k_{F,\text{slotless}}$  for each ring thickness. This agrees with literature on magnetic levitation, which states that slotted drives can generate stronger forces than their slotless counterparts [68], for similar drive dimensions.

Again, the measured forces are compared to FE-simulated results. These results are depicted in grey and black in the right plots of Fig. 7.24. The FE simulations match the measured active forces of the *slotless* within a 9 % for both rotors.

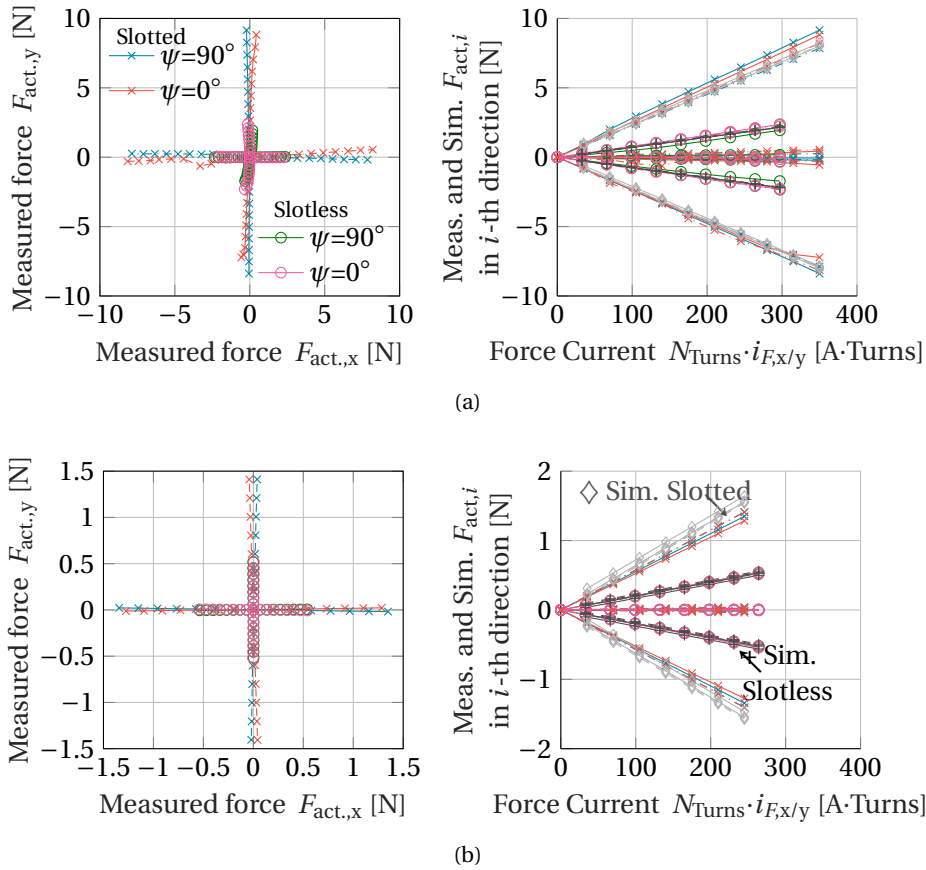


Figure 7.24: Measured  $F_{\text{act},x}$  and  $F_{\text{act},y}$  (with continuous and dashed lines, respectively) for (a) rotor #1 and (b) rotor #2. The slotless motor is excited with  $i_{F,x/y} = 0 : 1 : 8/9$  A and the slotted with  $i_{F,x/y} = 0 : 250 : 1750/2500$  mA (max current limit for rotors #1/#2, respectively).

For the *slotted* drive, the simulation slightly underestimates the forces for rotor #1 by  $\sim 12\%$ . This coincides with the simulation's slight underestimation of axial forces for rotor #1. Yet, they can also overestimate the axial force of rotor #2 by  $14\%$ . The FE simulations are a useful tool to roughly predict the active forces, but it might over or underestimate the real values.

As with ball-bearing motors, the force generation capacity is assessed by how much Joule losses, i.e. heating, they produce. The efficacy of the active bearing can be defined as

$$k_{M,F} = \frac{|\vec{F}_{\text{act.}}|}{\sqrt{P_{\text{Joule}}}} = \frac{|\vec{F}_{\text{act.}}|}{\sqrt{6 \cdot R_{\text{coil}} \cdot |\vec{I}_F|^2}}, \quad (7.4)$$

with  $\vec{I}_F = (i_{F,x}, i_{F,y})^T$ .

Factor  $k_{M,F}$  is evaluated for both stators and rotors and for  $\psi = 0^\circ$  and  $\psi = 90^\circ$ . The results are presented in Fig. 7.25a. The values shown in this plot scale with  $k_F$ , since

$$k_{M,F} = \frac{|\vec{F}_{\text{act.}}|}{\sqrt{6 \cdot R_{\text{coil}} \cdot |\vec{I}_F|^2}} \sim \frac{k_F \cdot N_{\text{Turns}} \cdot |\vec{I}_F|}{N_{\text{Turns}} \cdot |\vec{I}_F|} = k_F \quad (7.5)$$

As previously remarked, motor configurations with larger active forces also provide stronger radial forces. To this end, a magnetic levitation bearing *effort* factor that relates passive to active forces is defined as

$$\chi_{\text{bng.}} = \frac{\max(k_x, k_y)}{k_{M,F}}, \quad (7.6)$$

which is desired to be minimized, i.e. minimize the levitation effort, and is plotted in Fig. 7.25b.

Figure 7.25b offers a fairer outline of the levitation efforts needed by the tested stator and rotor types. Despite the stronger radial stiffness of the slotted drive, its larger active force compensates for it, so that according to rating  $\chi_{\text{bng.}}$ , slotted drives of the tested geometric scale require *less* levitation effort.

Although the slotted drive can produce stronger active forces for the same Joule losses, c.f. Fig. 7.25a, it also renders a stronger radial passive stiffness than the slotless drive, c.f. Fig. 7.22.

For a given rotor, the Joule losses needed to control the radial displacements and its corresponding forces are comparable, with factor  $\chi_{\text{bng.}}$  being slightly lower, i.e. better, for the slotted drive. Nevertheless, this indicator does not account for issues regarding the angle-variability of  $k_r$ .

Moreover, for a given stator, factor  $\chi_{\text{bng.}}$  is lower for rotor #2, meaning that their levitation requires a lower effort. This is expected as passive forces scale with air gap field as in  $\sim B^2$ , and active forces scale with  $\sim B^1$  in PM motors [165]. Therefore, a feebler PM renders the ratio

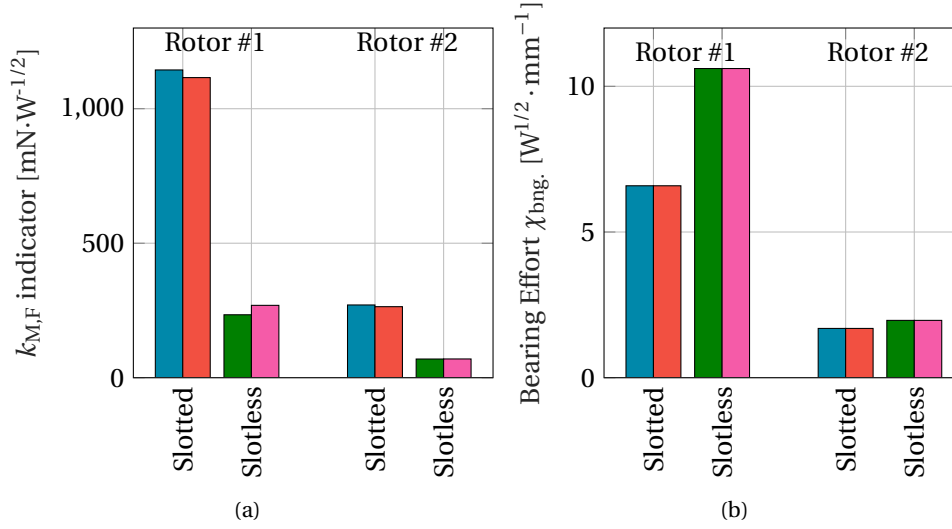


Figure 7.25: (a) Efficacy of the active bearing  $k_{M,F}$  of Eq. (7.4), and (b) bearing performance factor  $\chi_{Bng.}$  of Eq. (7.6).

$\chi_{Bng.}$  smaller and levitation easier.

#### 7.5.4 Active Torque

The active torque that leverages rotatory operation is also tested. It is depicted as a function of  $N_{\text{Turns}} \cdot i_{T,q}$  in Fig. 7.26a.

Figure 7.26a portrays a straight slope for  $k_T$ , without evidencing iron saturation at high currents. Moreover, the torque produced on rotor #2 displays no difference for orientations  $\psi = 0^\circ$  and  $\psi = 90^\circ$ .

For the slotted drive with rotor #1, the torque at  $\psi = 0^\circ$  is 16% larger than that at  $\psi = 90^\circ$ . On the other hand, the torque difference produced by the slotless drive with different orientations of rotor #1 accounts for only 1%.

The FE simulations are also undertaken to predict the torque of the motor variants. The simulations can precisely forecast the torques of the slotted drive with rotor #2 and of the slotless drive with rotor #1. The measured torques of the two other variants—slotted stator with rotor #1 and slotless stator with rotor #2—are over and underestimated by the simulation, respectively.

As for the magnetic bearing in Eq. (7.4), the motor constant is defined as

$$k_{M,T} = \frac{T_z}{\sqrt{P_{\text{Joule}}}} = \frac{T_z}{\sqrt{6 \cdot R_{\text{coil}} \cdot i_{T,q}^2}}, \quad (7.7)$$

and is displayed in Fig. 7.26b. As with  $k_{M,F}$ , slotted variants provide a larger torque per Joule loss by less than a factor of 2. For  $k_{M,F}$ , this was in the range of a factor of 3.

Nonetheless, it must be reckoned that comparing motor torque *solely* to Joule losses offers an incomplete overview of the rotatory performance of the drive. Joule losses  $P_{\text{Joule}}$  account for a small part of the total losses, particularly in high-speed motors, as losses in the windings and stator iron rashly increase with rotatory speed [20].

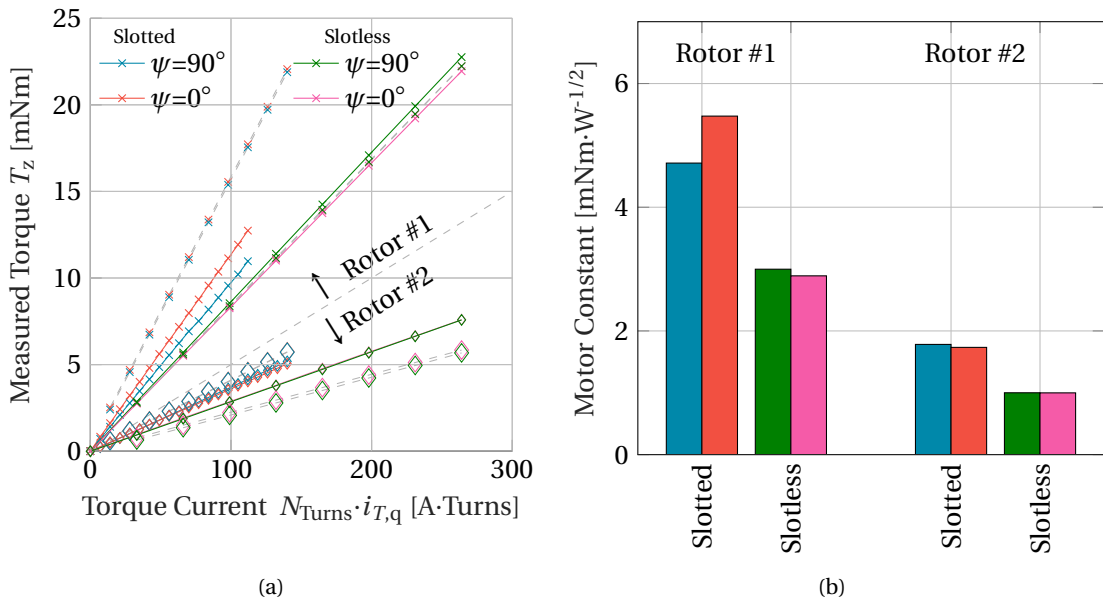


Figure 7.26: (a) Measured active torque  $T_z$  and (b) motor constant  $k_{M,T}$  as of Eq. (7.7).

## 7.6 Commissioning

### 7.6.1 Drive and Ventilator Test Bench

The drives of Figs. 7.2c-7.2d are screwed upon a plexiglass plate, where the microcontrollers for drive control and rotor position estimation—with their corresponding PCBs—are also fastened in place. The plexiglass plate is perforated below the drive's mechanical clearance to permit airflow and thus the testing of the drive as an axial ventilator. The construction is depicted in Fig. 7.27.

With the running control, sensor, and power electronics systems, the slotted and slotless drives can be successfully brought to levitation and thereafter to rotatory operation. The levitating slotless drive with an impeller mounted on rotor #2 is pictured in Fig. 7.28.

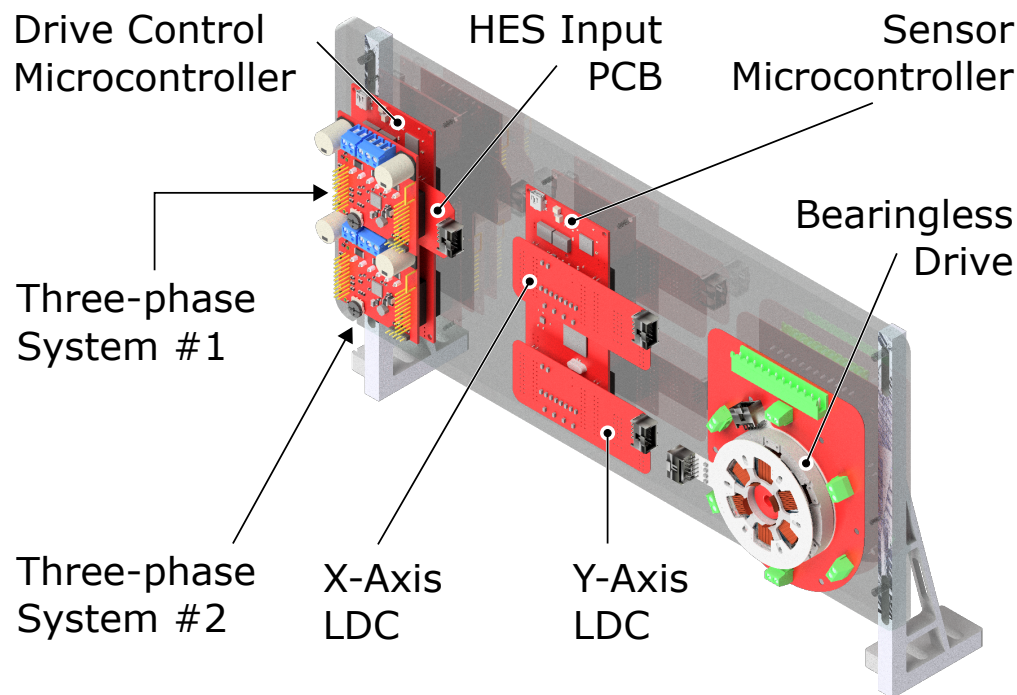


Figure 7.27: Test bench of the bearingless disc drives. Two microcontrollers and the drive are mounted on a plexiglass plate by screws.

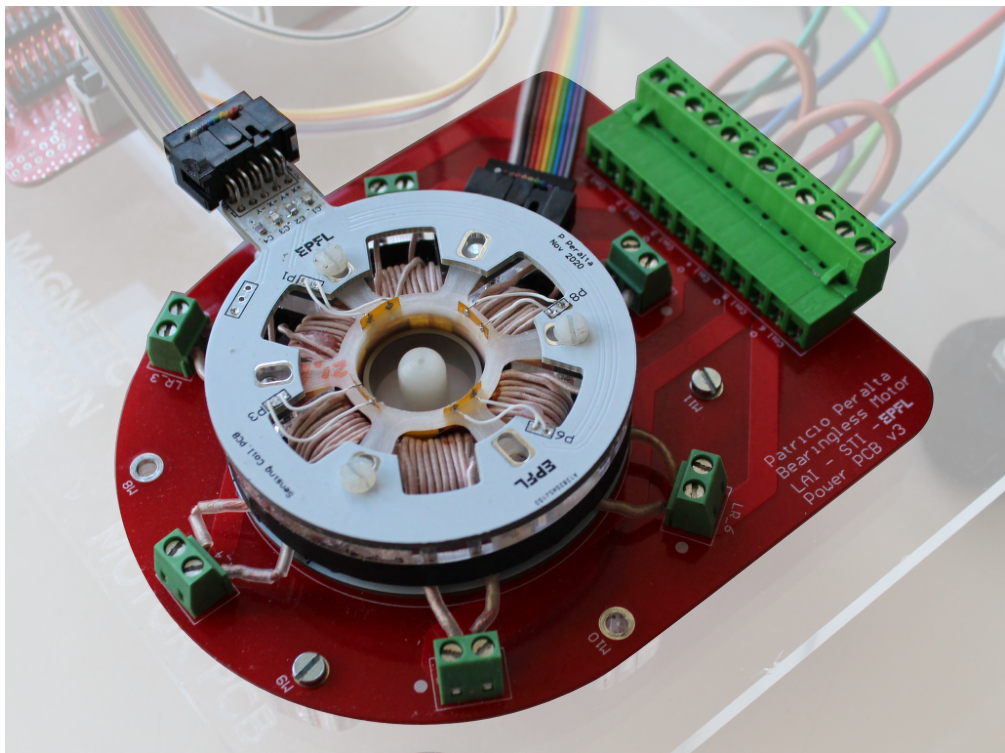


Figure 7.28: Levitating and spinning slotless drive on its test bench.

### 7.6.2 Bearing Start-Up

The first documented operation of the drives is their bearing start-up. This is the detachment of the rotor from the bearing retainer and its active positioning in the middle of the air gap.

The reference position of the bearing is *soft-started* from the initial rotor position to  $(x, y) = (0, 0)$ , employing of a low-pass filter. The rotor position and the reference currents of the bearing PID controller are shown for the slotted and slotless drives, with rotor #1, in Fig. 7.29.

The reference PID currents exponentially increase until the rotor detaches from the bearing retainer, which is indicated by vibrations in the position signals. After detachment, the rotor draws closer to its magnetic center, so the currents begin to diminish along the excentricity of the rotor. Different constants of the low pass filter of the soft start-up result in different start-up times, so the slotted drive in Fig. 7.29a comes to levitate in half of the time of that of the slotless drive in Fig. 7.29b.

The magnitude of the start-up currents of the slotless drive is approximately 4 times larger than that of the slotted. Despite its feeblar radial pull, this is foreseeable, as the slotless prototype has a smaller force-current gain  $k_F$  and fewer turns  $N_{\text{Turns}}$ .

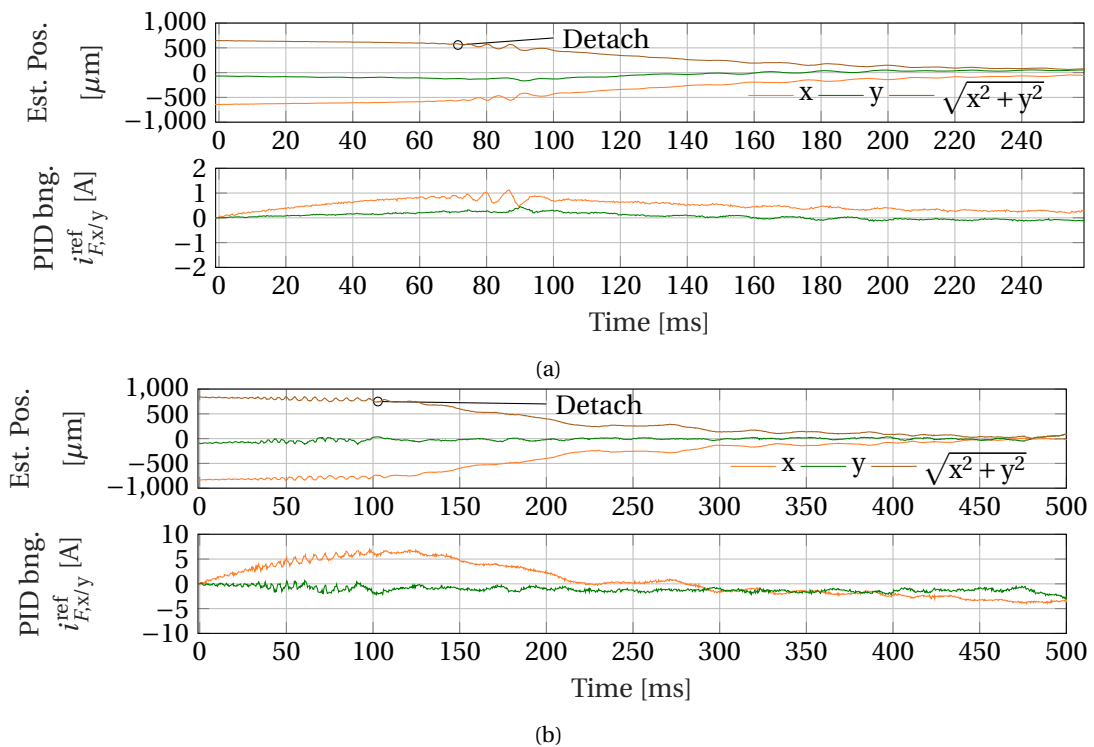


Figure 7.29: Soft start-up procedure of the bearing for the (a) slotted and (b) slotless drives with rotor #1.

### 7.6.3 Rotation

With levitation ensured, torque is generated up the rotors to start spinning operation. The position signals, their corresponding bearing currents, and the estimated rotational speed for the commissioned prototypes and rotors are displayed in Figs. 7.30a-7.30c.

The DC-values of the position signals are removed, and a frequency analysis is performed. A one-sided FFT is performed on an 8-sec time window, resulting in Fig. 7.30d.

The depicted bearing currents have the same fundamental frequency as the rotor's vibrations. To counter these, the bearing currents must build a  $\sim 180^\circ$  phase shift to the position signals. The bearing currents of the slotless drive are larger due to the differences in force-current gain  $k_F$  and  $N_{\text{Turns}}$ , as said before.

The turning rotor of the slotted drive has two frequency peaks: the first one at  $f = 70$  Hz for both axes; that is, above the rotational frequency of  $f_n = 2500 \text{ rpm}/60 \text{ min} = 41.6$  Hz.

A double and triple harmonic, e.g. at 140 Hz and 210 Hz, then appear in the  $x$  and  $y$ -axes, respectively. The difference in the frequency content of the axes might be due to the anisotropic radial stiffnesses of one pole-pair rotors—which is different towards the placement of the  $x$  and  $y$  sensor probes—, as well as to their considerably different noise-immunity, shown in Fig. 7.9. For these reasons, the harmonic content of the rotor position of the slotted drive is larger than those of the slotless.

The rotor positions of the slotless drives only have one peak. In the case of rotor #1, the harmonic content peaks at its rotational frequency, indicating that rotor vibrations probably arise from rotor imbalance.

The position of rotor #2 is —on the other hand— prone to vibrations *below* the rotational frequency at 56 Hz. These sub-harmonics can be spawned by the PID position controller and its transfer function, as rotordynamical effects are milder due to the lighter weight and feebler radial pull of the rotor.

All in all, the rotor of the slotted drive vibrates with larger amplitudes and with frequencies above its rotational speed. This renders this drive less preferable for high-speed operation with the current set-up.

For the rest of this chapter, the slotless drive with rotor #2 is tested. It enables reaching higher speeds, with less and slower vibrations, and its rotor geometry enables the mounting of an impeller.

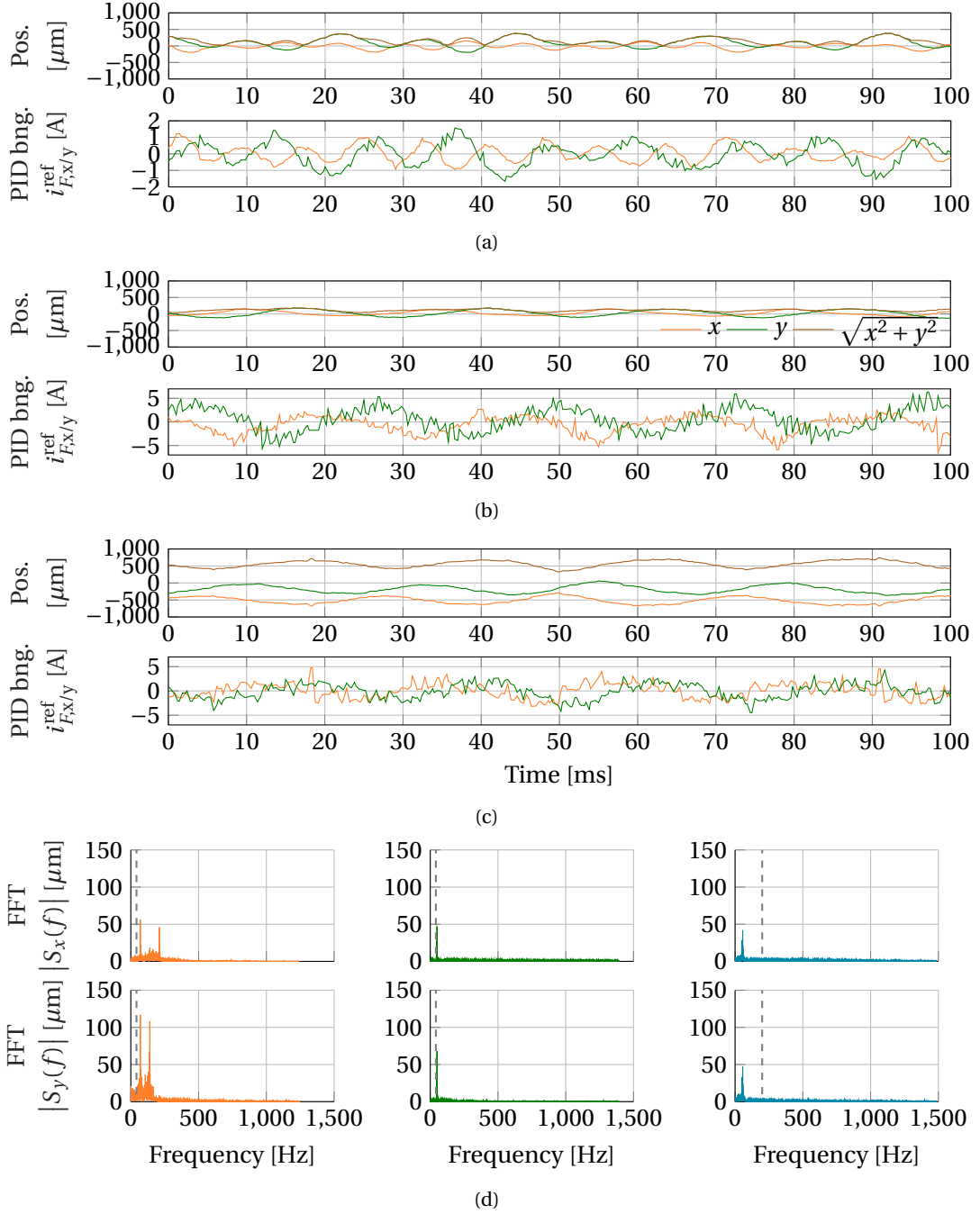


Figure 7.30: Measured rotor position, and bearing currents of the (a) slotted prototype with rotor #1 running at 2500 rpm and the slotless with (b) rotor #1 running at 2500 rpm and (c) rotor #2 running at 12000 rpm. The (d) FFT is calculated for the rotor positions, and the rotatory speed is indicated by the dashed grey lines. Frequencies with high power content are indicated.



#### 7.6.4 Hall-Effect vs. Eddy-Current-Based Position Estimation

The slotless drive with the thin rotor #2 is brought to levitation, using the EC position sensors to estimate the *radial* position of the rotor and six HESs —mounted on a single PCB below the stator— to estimate its *angular* position. The HES-based position estimation is calculated with and without the current compensation of Fig. 7.19, to appreciate if such an approach improves the precision of the estimation.

For this study, the motor is operated at different speeds, and the results of the position estimated by the EC and HES are both recorded and correspondingly compared, to analyze their compliance.

The compliance between the two position-estimation approaches is initially tested without levitation. A force reference rotating at  $f_{\text{mech.}} = 240$  Hz and amplitude  $\hat{I}_{\text{bng.}} = 4$  A is imposed, so that the rotor rolls *and* turns inside the mechanical clearance.

For such a test, the position-estimation results are shown for half a rotor turn in Fig. 7.31. The position trends depicted by the EC sensors and the HES fundamentally coincide, with the HES estimation having more high-frequency components.

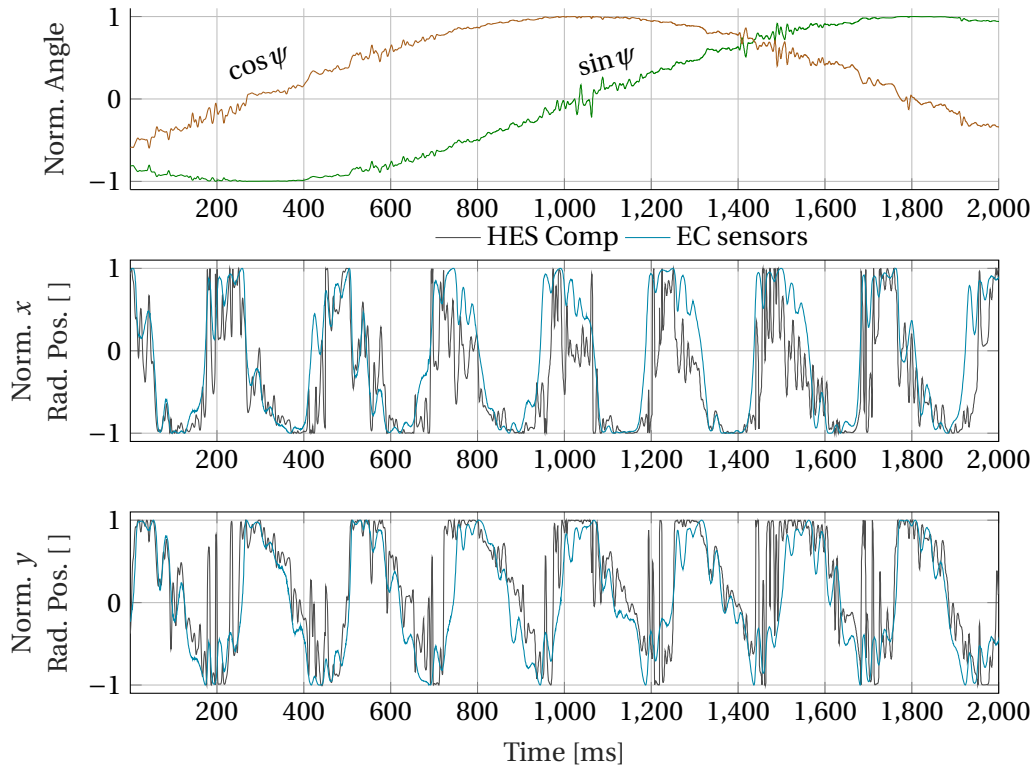


Figure 7.31: Comparison of the radial rotor position estimation performed by the EC sensors and HESs for a rotor rolling inside its mechanical clearance. The angles are estimated with the HESs.

For a more thorough analysis, the motor is operated at different frequencies, and the CAS of the position —estimated by the EC sensors, the HES, and the current-compensated HES— is assessed.

The plots on the left of Fig. 7.32 correspond to the position signals of the  $x$  and  $y$ -axes. As in Fig. 7.31, the position estimated by the EC sensors and HES follow the same trend regarding their fundamental harmonic —with its period indicated upon the graph— and its corresponding phase.

The match between the signals is quantified by their cross-correlation ( $\times$ -correlation); that is, between the EC estimated position and the HES estimated positions. Maximal correlations at feeble lag values represent similar signals, which are desired. Such ratings are depicted in Fig. 7.32.

For the rotatory speed of 2000 rpm of Fig. 7.32a, the cross-correlation values for the HES, with and without compensation, are maximal at lag  $\iota = 0$  samples. The position estimated by the current-compensated and uncompensated HES schemes is very similar due to the feeble currents needed to operate the drive at low speeds, so the single HES signal values match closely. There is therefore no lag difference at the maxima of the HES and compensated-HES predicted positions.

For the 6000 rpm rotatory operation of Fig. 7.32b, the cross-correlation of the position calculated by the current-compensated HES renders is maximal at  $\iota = 0$  samples for both the  $x$  and  $y$ -axes. The position estimated by the uncompensated HES correlates to that of the EC sensors with a lag, indicating a slightly worse estimation of rotor position.

At 10000 rpm in Fig. 7.32c, the positions estimated by the HES match those estimated by the EC sensors less than at lower speeds. Observing the position signals, it is not clear that the sole HES could enable levitation, despite their cross-correlation values being maximal for lag  $\iota = 0$  samples.

The amplitude of the different frequency components is studied, to compare the content of the signals and what these pick up from rotor movement. The CAS of the different signals is normalized on the  $y$ -axis by its 100 % value, and it is shown on the right of Fig. 7.32. The rotational frequency  $n$  of the rotor is evidenced, in Hz, and the frequencies with a large harmonic content are indicated with arrows.

For a 2000 rpm rotational speed, all position estimation approaches effectively recognize the first harmonic at  $n = 33.3$  Hz, excited by the rotational frequency of the rotor. Approximately 25 % of the total amplitude spectrum is accumulated until this frequency by the EC sensor. This means that most of the amplitude of the position signals are concentrated until this frequency, which is could be expected. The EC sensors also detect an increase in harmonic content at  $f = 70$  Hz, which is a second harmonic from the rotational speed.

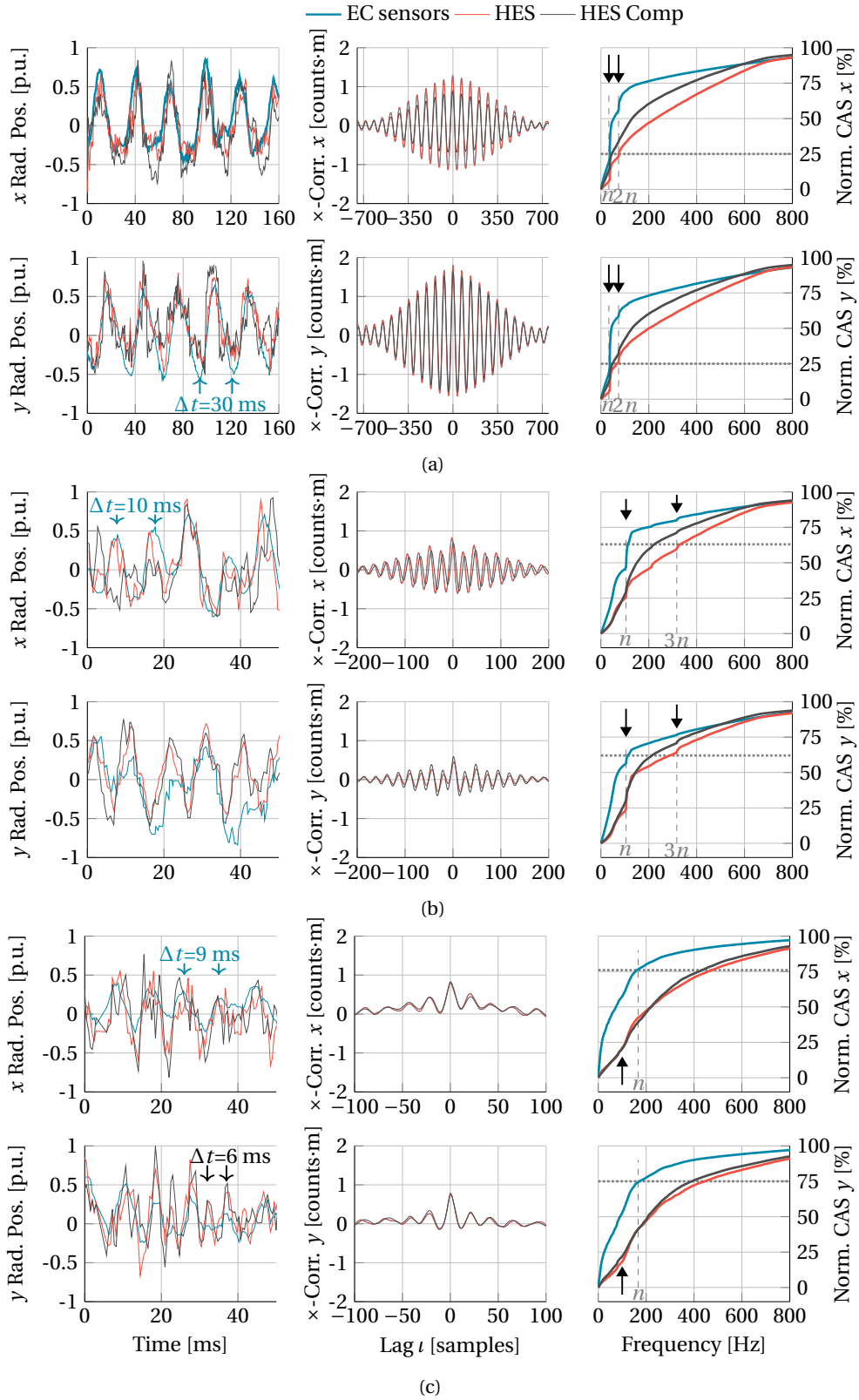


Figure 7.32: Position of the rotor estimated by the EC sensors (used in the bearing position controller) and the HESs, with their CAS and cross-correlation, for the slotless drive with rotor #2 rotating at (a) 2000 rpm, (b) 6000 rpm, and (c) 10000 rpm.

The HES-estimated positions accumulate only 25 % of the signal's amplitudes until  $n$ . Starting at  $n$ , the harmonic content at 70 Hz in the EC sensors is mostly overlooked. The position estimated by the uncompensated HES *does* pick up the harmonic content at 70 Hz, yet it cumulates at the most 30 % of the amplitudes until this frequency.

For the HES-estimated positions, there is therefore a considerable amount, e.g. 60 %, of high-frequency components in the signal correspond to frequencies above 70 Hz. This might correspond to high-frequency magnetic fields coming from the motor coils. According to the EC sensors, this does not correspond to actual rotor displacements, as only ~35 % of the power of the position signals is found above 70 Hz.

The harmonic content between the current-compensated and uncompensated HES schemes is also different. The compensated HES have an overall larger CAS value for the displayed frequencies below 800 Hz. This means that they are relatively richer in lower frequencies than the uncompensated HES position values. Given the low rotational frequency of the rotor, i.e. 2000 rpm or 33.3 Hz, rotor vibrations above its third harmonic (>100 Hz) would rarely arise and are probably amplified by the rotor position control. In this sense, the CAS of the position resulting from the compensated HES is closer to that of the eddy current sensors, so it has fewer high-frequency harmonics, and as such, it can be deemed as a more reliable representation of the rotor position than its uncompensated counterpart.

The case at 6000 rpm is similar to that of the 2000 rpm. All position-estimation approaches have their energy concentrated at  $n = 100$  Hz, which corresponds to the first harmonic. This amounts to a cumulated value of close to 65 % for the  $x$  and  $y$ -axes of the EC sensors, whereas this amounts to ~40 % for the HES-based approaches. Above  $n$ , the cumulated value of the amplitude of the position of the current-compensated HES-estimated increases more rapidly than its uncompensated counterpart, especially for the  $x$ -axis.

A third harmonic —instead of a second harmonic— at  $f = 310$  Hz is captured on the positions by all estimation approaches. As with the previous case of 2000 rpm, approximately 75 % of the frequency amplitudes are cumulated by the EC sensors until this frequency.

Between the first and third harmonic, e.g. 100 Hz and 310 Hz, the CAS of the HES-based position estimation rapidly increases; increase which is not detected by the EC sensors. This points out that this harmonic content might not represent real rotor displacements but noise or magnetic fields from the motor coils. As with the rotor at 2000 rpm, the spectrum of the current-compensated HES position signal resembles that of the ECs more closely, so it can be once again regarded as preciser.

The frequency distribution for the rotor turning at 10000 rpm (= 166.7 Hz) is slightly different. All position signals concentrate harmonic content at  $f = 100$  Hz, indicated by the arrow. This frequency already accumulates 55 % of the amplitude spectrum for the EC sensors. At the rotational frequency  $n$ , the position estimated by these sensors has already accumulated 75 %, and there are no measured higher-order oscillations. Therefore, the position estimation with

the EC sensors measures a feeble quantity of harmonics above this frequency.

The HES-based position estimation effectively recognizes the most important frequency amplitudes at  $f = 100$  Hz. This component accumulates however a smaller part of the total amplitude: around 25 % vs. 55 % of the EC position estimation. Above the rotational frequency of  $n = 10000$  rpm = 166.7 Hz, the HES approaches accumulate 40 % of the CAS, with the EC sensors already having accumulated 75 % of the CAS. The HES, therefore, measure a high harmonic content above the rotational frequency, which is less measurable to the ECs.

All in all, the HES-based position estimation can correlate to the EC-based measured position, and at the same time, detect relevant rotor translations that arise from the spinning of the rotor. Nevertheless, the position signals of the HES contain rich, high-frequency content which is not detected by the EC sensors that enabled robust levitation.

The additional harmonic content of the HES-based position estimation can be ascribed to bearing currents that originate from the derivative of the PID position controller, and not necessarily from real rotor displacements. The rotor position is estimated by bottom-placed HESs, whose estimation is sensitive to axial vibrations of the spinning rotor that can be interpreted as radial displacements. The PID's derivative amplifies noise content in the position signals, which ultimately leaks into the bearing current references, which are measured by the HES. These sensors, on their part, cannot be perfectly compensated. The compensation nevertheless aided the accuracy of the position estimation, as its harmonic content better resembled that of the EC-based position.

### 7.7 Experimental Validation of an Axial Ventilator

The operating slotless drive coupled with the ring-like rotor #2 is tested as an *axial* ventilator. Such a deployment serves as a robustness trial upon the systems, which must be stable despite vibrations —due to the interaction of the impeller with air— and axial forces —due to air pressure on the impeller—.

The characteristics of the ventilator are measured with the running motor for various operating points and different impellers.

#### 7.7.1 Measurement Rig

The axial clearance of the test bench of Fig. 7.27 is extended to assimilate the cross-section depicted in Fig. 7.33a. The objective is to measure the airflow *through* the duct and the static air pressure before *and* after the impeller, to estimate the pressure difference generated by the spinning impeller.

The flow is estimated by attaching a flow element. This is a tube that straightens out and stabilizes the flow in the conduit with a fine grid, at a low loss of hydraulic charge. The flow

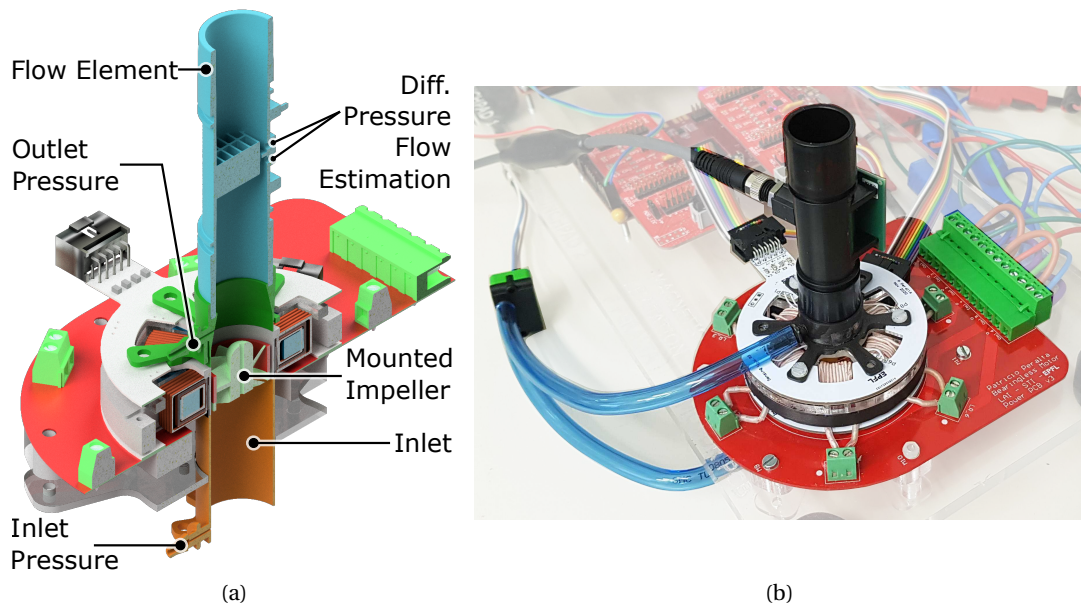


Figure 7.33: Test bench adaptations for the measurement of pressure and flow of the axial fan.

element is normed so a differential *pressure* measured at the grid's level is indirectly related to a given flow in  $\text{l}\cdot\text{min}^{-1}$ . A Sensirion EK - P4 evaluation kit [158] estimates and logs the flow.

The differential pressure of the rotating impeller is measured more simply. Small perforations at the inlet and outlet are fabricated, and these are connected via hydraulic hoses to a differential pressure sensor. The latter digital sensor—a Sensirion EK - P5 evaluation kit [157]—logs the pressure in a computer.

The mentioned sensors are mounted on the test bench as in Fig. 7.33b.

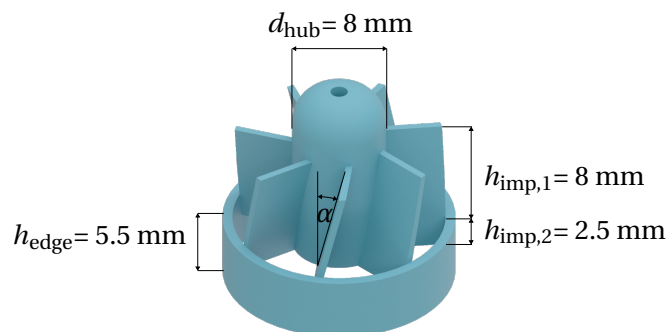


Figure 7.34: Example of an  $\alpha=13^\circ$ , 7-bladed impeller.

### 7.7.2 Results

For the ventilation tests, various impellers are mounted onto rotor #2 and tested at different rotatory speeds. The number of blades, as well as their angles, are varied, generating a total of 12 impeller variants that are assessed.

An exemplary rotor is depicted in Fig. 7.34. A lower border is added to the construction as it adds weight to the bottom of the impeller, thus increasing the angular inertia of the rotor and stabilizing tilting vibrations.

For the tests, the rotor is levitated with an impeller and spun. The airflow  $Q$  and differential pressure  $\Delta P$  are measured for different rates of flow element *obstruction*—ranging from completely open to complete closed—which determines the operating point of the ventilator. This procedure is conducted for each impeller turning at 7 krpm, 8 krpm, 9 krpm, and 10 krpm.

The results of the described tests are described in Fig. 7.35. For all impellers, increasing the speed augments both the pressure and the flow. This is foreseeable, as these scale with  $n^2$  and  $n$ , respectively [103].

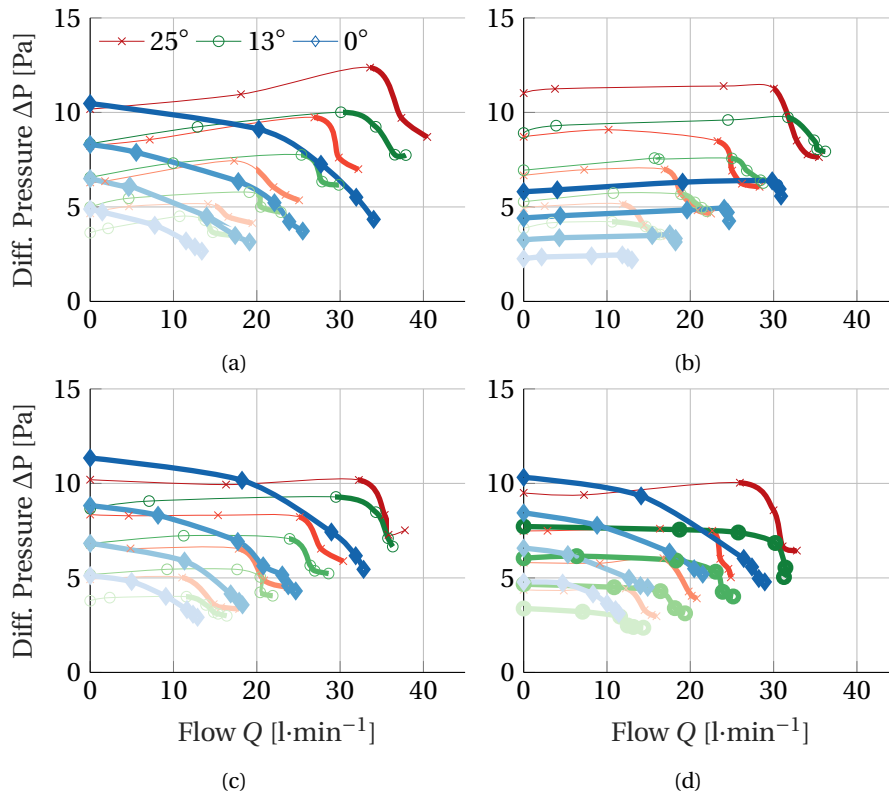


Figure 7.35: Measured airflow and pressure difference, using the slotless drive with rotor #2, for impellers with (a) 5, (b) 7, (c) 9, and (d) 13 blades and different blade angles. Stable operating points are plotted in bold, and darkening colors represent speeds 7, 8, 9, and 10 krpm.

Stable operating points can be *identified* by a decreasing pressure for an increasing flow [181], in which the performance of the fan *does not* oscillate between two flow values. These operation segments are highlighted with a thicker line width in Fig. 7.35.

According to this definition, straight blades *always* supply stable operating points, whereas angled blades do this only for large flow values.

For stable operating points, impellers with angled blades, e.g.  $13^\circ$  and  $25^\circ$ , provide more differential pressure than their straight-bladed counterparts. Particularly, for high flows and at 10 krpm, straight impellers provide  $\sim 5$  Pa of pressure, with  $13^\circ$  providing between 8 Pa and 10 Pa, and blades with a  $25^\circ$  angle rendering between 8 Pa and 12 Pa. Angled blades can also reach slightly larger flows than their straight counterpart.

All in all, angled blades outperform the straight blades within the space of tested impellers, as they can simultaneously provide larger pressures and higher flows. Nevertheless, angled impellers are only stable for large airflows. If a wide stable operation range is desired, or if the operation point is unknown, straight blades are therefore preferable.

## 7.8 Conclusion

This section describes the commissioning of two functioning prototypes. The section starts by describing how the drives are modularly and axially mounted.

The modular mounting gives way to the precise mounting of the sensor systems needed for magnetic levitation. The sensitivity and noise characteristic of different tunings of the EC sensor systems is calculated, to analyze the precision with which they can detect rotor displacements. The disturbance caused by the excitation of the motor coils is documented, along with the sensor directions that pick up more noise.

Similarly, the performance of a *double* six-sensor array of HESs for the estimation of radial, angular and axial rotor position is experimentally assessed. These magnetic flux density sensors can correctly estimate the angle and axial position of a PM rotor, by measuring axial *and* radial fields.

Measuring axial magnetic flux density render a more acceptable estimation of the radial position of the rotor inside the mechanical clearance is obtained, with more consistent results, i.e. free of rotor-angle dependency. The position estimated by measuring radial fluxes, on the other hand, proves unreliable. The single HES values do not correspond to the supposed model, which ultimately means that different movement directions have different position gains and that turning, yet centered-fixed rotors appear to be moving.

Regarding motor excitation, the influence of the magnetic fields of the motor's coil is corrected upon the single HESs, so that these pick up *only* the magnetic flux density due to the PM rotor, in the interest of a more precise rotor position information.



Having characterized the sensor systems, the electromechanical properties of the prototypes are investigated. Deviations can be appreciated between the experimental and computational results, with the latter not correctly portraying the angular dependence of motor electromechanics. These discrepancies lay in the order of 10%. Depending on the application, they can be considered acceptable, to deem FE simulations helpful in the design of disc drive bearingless motors.

Thereafter, the prototypes are commissioned, so that they can levitate and rotate. Both of these operations are documented, and the position estimation based on EC and HESs is compared.

Finally, the slotless prototype is deployed as an axial ventilator, by mounting an impeller on a thin, ring-like PM rotor. The performance of various impellers is rated in terms of pressure and flow, with speeds of up to 10 krpm.

## 8 Conclusion and Outlook

### 8.1 Summary

This thesis addresses the modelling of magnetically-levitated disc drives along with sensor possibilities that enable their contactless magnetic levitation. The research of these aspects converges to the fabrication of two *working* electric machines; one of which is eventually operated as an axial blower at speeds of 10 krpm. To obtain these results, the thesis started with theoretical considerations and proceeded towards more practical endeavors.

To embark upon the subject, an investigation of electric machines and their research trends is performed. This frames the most innovative research trends within the need for smaller, compacter motors that are more directly coupled to faster mechanical loads. The challenges of reaching higher rotational speeds render magnetic bearings a very compelling alternative, since they enable frictionless and long lifetime operation, which are challenging for miniaturized ball bearings. Their inherent intricacy in terms of design, control, and hardware is also brought forward.

The state of the art is investigated, to know the actual stand of the techniques in the magnetic levitation of very compact drives. Different motor types, as well as different principles that facilitate magnetic levitation are presented. A PM-based, flat-drive topology deemed "disc drive" is further studied in this thesis, due to its compactness and more simple in actuation.

A bibliographical study then determines the performances that have been reached by other disc drives. Among the documented drives, the prototypes conceived in this thesis rank amongst the smallest disc drives that have driven an application. Such a study also highlights the spare potential that the actuators developed in this thesis still have.

Subsequently, the electromagnetic principles exploited for the generation of torque and force are explained. These are classified as either passive —between the PM and ferromagnetic material— or active —due to the energization of the coils— effects. The chapter then explains how force and torque can be spawned by leveraging standard semiconductors devices. The

power losses that arise due to motor operation are also described.

Then, a framework for their conceptualization and optimization is proposed. The framework starts by considering and matching various motor structures to an application, to then narrow the search to inner rotor drives for given rotor diameters. A deeper analysis of these is conducted, considering their passive and active ratings as well as their power loss characteristics. A parametric analysis of their performances and the arising trade-offs is provided, to finally determine the best contenders according to an objective function.

The contactless measurement of the angular and radial position of the rotor is a requirement for its contactless levitation. In this regard, sensor concepts based on the generation of ECs—inside a conductive target— or the measurement of the magnetic flux of the PM—by using the HESs— are proposed. The mathematical modelling of the magnetic flux density that allows for the estimation of the rotor's position employing the HESs is revealed.

The practical aspects for the implementation of the prototypes are then reviewed. The control schemes that regulate the magnetic levitation, spinning operation, and PWM-based energization of the coils are described. The microcontroller where the control schemes are programmed, the power electronics for the energization of the coils, and the electronics required for the sensors are displayed.

Two disc drive prototypes are fabricated, and the sensor systems are installed in them. The EC-based rotor position systems are tuned for increased sensitivity, and the disturbance of magnetic fields upon them is documented. On the other hand, the accuracy of the estimation of rotor position using the HESs is gauged for two sensor orientations.

The passive and active forces and torques of the prototypes are measured and compared to FE results, validating the accuracy of the latter for the design of compact disk drives. The two prototypes—one with a slotless stator and the other with a slotted one—are commissioned, and the start-up of their radial magnetic bearings, as well as their rotatory operation, are registered. The EC-based positioning system is ultimately used for the operation of the drives, and its signals are also compared to those resulting from the position estimation based on the signals of the HESs.

Finally, an axial blower is implemented. Different axial impellers are mounted onto a thin PM rotor, which is then driven by the slotless prototype. The performance of the various impellers is logged in terms of differential pressure and airflow. Such tests situate the drive conceived in this thesis amongst the smallest magnetically-levitated disc drives that have been tested with a mechanical load within the scope of an application.

The described course of the investigation thus started analyzing the latest advances in magnetic levitation and small drives. It then focussed upon the different electromagnetic ratings in terms of bearing, rotatory operation, and losses. Two different sensor system alternatives are analyzed, and the hardware needed for the implementation of the drives is chosen. Finally,

two prototypes are fabricated and operated, and their operation as well as sensor systems are analyzed. The proper operation of the prototypes thus finalizes with the slotless disc drive being commissioned at high speeds as an axial ventilator with different impeller types.

## 8.2 Original contributions

The scientific analysis undertaken within the scope of this thesis amounts to the following contributions:

- *Methodology to conceive magnetically-levitated disc drives*

A FE based framework is proposed to conceive magnetically-levitated disc drives. The overall performance of an actuator is analyzed and includes an assessment of passive, active, and power-loss characteristics and their trade-offs. Their relevance for particular design priorities can be mathematically weighted and adjusted if there are hard constraints to be met.

The accuracy of the FE method as a predictor of electromagnetic quantities such as torque and force, both active and passive, is corroborated by the experimental characterization of two prototypes.

- *Mathematical modelling of the magnetic flux density for radial rotor-position estimation*

The magnetic flux density inside the air gap of the rotor is evaluated as a function of its angular position but also its radial position. Algebraic manipulation thus enables to estimate these positions by measuring the magnetic flux density—with the aid of Hall-effect sensors—at different locations around the air gap. A scheme for the compensation of the magnetic fields generated by the motor coils and their excitation is proposed.

Two sensor loci are experimentally tested to estimate the radial, axial, and angular position of the rotor in the air gap, with one of the loci rendering better results in terms of accuracy and sensitivity.

The effectiveness of the estimation of the rotor's radial position is contrasted against the eddy-current-based position estimation that ultimately enables the operation of the prototypes. The implementation of a coil-current compensation scheme results in more precise estimates.

- *Stand-alone, eddy-current-based estimation system for the rotor's radial position*

In this thesis, off-the-shelf components are exploited and combined to propose a radial rotor-position estimation system. This system can be matched with generic sensor coils (which can be adapted to the requirements of multiple drives) for a low-cost and with a small footprint.

The positioning system is tested with 150  $\mu\text{m}$ -thin Flex PCB Coils as probes, and it is validated by enabling the levitation and spinning of two prototypes.

The position estimation system delivers sensitivities within the order of magnitude of its more complex, system-specific counterparts. Its noise characteristic—which depends on the position of the probes in a drive—is also studied.

- *Manufacturing and commissioning of two magnetically-levitated disc drives*  
A disc drive with a slotted stator and another with a slotless stator are fabricated. Both prototypes follow an axial mounting concept, leveraged by the sandwiching of PCBs conceived to route sensor electronics and the cabling of the drives' coils.  
The start-up characteristic of the drives is documented, as well as the rotor position and its vibrations at different rotational speeds.
- *Deployment of a slotless motor as an axial ventilator*  
Different axial impeller geometries are mounted onto a thin PM rotor, which is then levitated and spun by the slotless drive. The system constitutes an axial fan that can blow air. The pressure and flow generated by the various impeller variants are documented. To the knowledge of the authors, such an application corresponds to the smallest disc drive that has been tested with a mechanical load.

### 8.3 List of Publications

The lessons drawn from this work have derived into the following conference and journal contributions:

#### Journal Articles

- [135] Peralta, P., Thomas, S., and Perriard, Y. (2021b). Characterization and verification of eddy-current position sensing for magnetic levitation. *IEEE Transactions on Industry Applications*, 57(6):5796–5805
- [131] Peralta, P., Araujo, D. M., and Perriard, Y. (2020). Design of compact bearingless disc drive systems. *IEEE Transactions on Industry Applications*, 56(5):4870–4881

#### Conference Papers

- [132] Peralta, P., Borque-Gallego, G., Lapijover, Y., and Perriard, Y. (2021a). Experimental electromechanical characterization of slotted and slotless miniature bearingless drives. In *2021 IEEE International Electric Machines Drives Conference (IEMDC)*, pages 1–8
- [134] Peralta, P., Thomas, S., and Perriard, Y. (2020b). Integrated, eddy-current-based sensing of rotor position for magnetic levitation. In *2020 IEEE Energy Conversion Congress and Exposition (ECCE)*, pages 1749–1755
- [133] Peralta, P., Leo, J., and Perriard, Y. (2020a). Rotor position estimation with hall-effect sensors in bearingless drives. In *2020 22nd European Conference on Power Electronics and Applications (EPE'20 ECCE Europe)*, pages 1–10
- [130] Peralta, P., Araujo, D. M., and Perriard, Y. (2018). Speed and stability limits for high-speed bearingless disc drives. In *2018 IEEE Energy Conversion Congress and Exposition (ECCE)*, pages 2319–2326

- [129] Peralta, P., Araujo, D. M., and Perriard, Y. (2018). Passive, active and loss tradeoffs in high-speed bearingless motors. In *2018 21st International Conference on Electrical Machines and Systems (ICEMS)*, pages 162–168

### Student Works

- Gajo, Elias (June 2019), *High Stiffness Bearingless Motor*, Semester Project
- Leo, Jacopo (January 2019), *Test Bench Construction for the Validation of Rotor Position Measurement in Magnetic Bearings*, Semester Project
- Lapijover, Yoann (April 2020), *Alternative, Magnetically-Levitated Motor Topologies for High Speed*, Master Project

## 8.4 Outlook

The lessons drawn in this thesis open further research perspectives. These new research vectors call for *deeper* knowledge in research subjects, or towards *broadier* investigations upon the applicability of the knowledge and functioning systems generated in this work. Some of the open questions can be defined as follows:

- *Global optimization of the actuation system*  
The thesis tackled the sizing of a disc drive by balancing their active, passive, and power loss performances. A more global system overview would enable a finer characterization of even compacter systems.  
To this end, the power electronics and their specifications could be matched to the drives. Such consideration could assess how the power losses are distributed between semiconductors —considering current ratings, switching frequency, etc.— and the rotatory drive —considering the number of turns in coils and their wire diameter, etc.—. Additionally, a thermal model could be coupled to the design framework. This enables gauging the power losses in terms of the temperature rise that they provoke on the components. The temperature rise determines the stress upon the single components and thus provides an idea of the achievable lifetime of the complete system.
- *Optimization procedure using other objective functions and other algorithms*  
The conceptualization methodology in this thesis was undertaken by exploring a discretized design space and simulating the variants inside them. More advanced optimization schemes might permit a finer resolution in terms of drive parametrization. Such optimization strategies can be coupled to other objective functions —which require given torque at a certain speed or max tolerable temperature rise—. The sensitivity of the results of the optimization as a function of the objective function could also be analyzed.

Similarly, more precise data regarding the operating points of the ventilator —such as torque and axial forces— would prove valuable for the optimization procedure.

- *Improvement of eddy-current-based rotor-position estimation*

The proposed rotor-position estimation system based on ECs enabled the commissioning of two magnetically-levitated prototypes.

Nevertheless, hardware and software efforts could make the positioning system more immune to noise. The sensor probes could pick up less electromagnetic noise if they were placed differently at the perimeter of the air gap, or below their target.

On another subject, the sampling rates of the sensors —determined by the I<sup>2</sup>C protocol— do interfere with the attainable speeds of high-speed drives. Other hardware combinations could provide a faster data transfer from the LDCs to the microcontroller. This could be also enabled by other LDC variants that work over the digital SPI communication protocol.

Alternatively, a mixed approach could exploit the resonance of the LCR tank excited by the LDC. Analog circuitry could then more rapidly process the resonant signals of the LCR tank, directly perform the differential computation of the position, and be sampled by an ADC.

- *Improvement of rotor-position estimation using Hall-effect sensors*

The estimation of rotor position using HESs was —according to test bench results— not completely accurate. The axial-field HESs provided more accurate results than the radial-field variant; yet both observed a significant position variation for a rotating—but radially static— PM. Therefore, none enabled rotor position estimation for levitation.

A finer analytical model of the magnetic flux density in the air gap is needed to better understand the inaccuracy of these results. Alternatively, preciser FE models and meshing could indicate the best loci for the positioning of the HES, so that these do not have to be empirically determined.

- *More-advanced control schemes*

The magnetic bearing and the power electronics of the drive system were controlled by traditional PID schemes. Such an approach leaves the information about the radial bearing's stiffness and the phases' inductance and resistance unexploited.

Control and signal schemes that leverage the characterization of the system could improve its operation in terms of noise, power consumption, and overall easiness of commissioning. For example, Kalman filters could provide a cleaner estimate of the position of the rotor, and model predictive control could minimize the current ripple in the power electronics.

- *Test the robustness of the complete system*

The alleged advantages of magnetic levitation must still be tried out upon the fabricated prototypes. Stress tests must reveal if the prototypes provide longer lifetimes than similar drives with ball bearings. The resistance of various encapsulation concepts to aggressive environments and sterilization procedures must still be evaluated.

- *Push rotational speeds further*

The rotors employed in the prototypes can theoretically hold rotatory speeds of around 100 krpm. Nevertheless, instabilities arising in the magnetic bearing did not allow the slotless drive to push beyond 12 krpm, or the slotted beyond 2.5 krpm. Other levitation mediums, e.g. fluids, would provide dampening to the magnetic bearing, eventually muffling resonances and enabling higher speeds. Additionally, finer control schemes and the improvement of sensor signals should be investigated to scoop the complete potential—and mechanical power— out of the prototypes.

- *Other types of applications*

A prototype built for this work was deployed as an axial fan. This prototype can be also employed to treat fluids and function as an axial *pump*. Such an environment would provide more dampened dynamics, that would ease the requirements upon the control of the magnetic bearing but at the same time require more torque for a given rotational speed.

Alternatively, the prototypes could be used as radial pumps or ventilators. Such impeller type generates higher pressures and lower flows.

- *Other motor topologies*

Similarly, the application of a compact axial ventilator inspired the research and steered this work towards inner rotor topologies. Nevertheless, other actuator dimensions or applications can guide research towards external rotor topologies or axial-flux drives with magnetic bearings. The design framework, power electronics, and sensor systems proposed in this thesis can still be adopted for such endeavors.



# A Metglas Stator Material

For the implementation of the drives, the iron-based ferromagnetic amorphous metal material *Metglas* material is used. For an accurate modelling of its magnetization capabilities its  $BH$  characteristic, coming from [106] and plotted in Fig. A.1a, is used in the FE simulations. Its relative permeability  $\mu_r$  is also depicted for a small magnetic field strength.

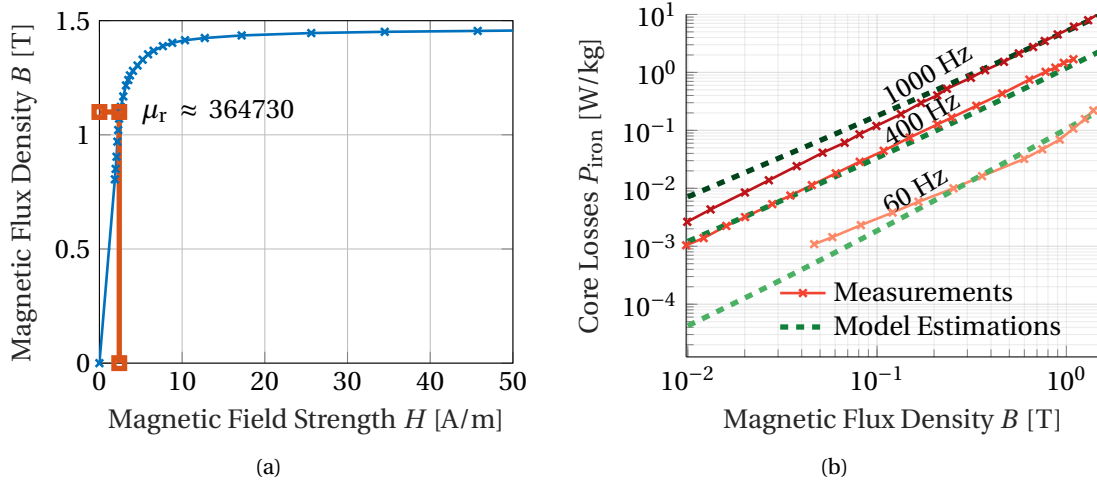


Figure A.1: (a)  $BH$  curve of *Metglas* and its (b) measured vs. modelled losses using Eq. (A.1).

During drive operation, hysteresis and eddy current losses arise in the *Metglas*. These may be amplified due to current-ripple losses. Thus for the given 1.3 T saturation of A.1a, a 1.1 T design values is determined for Chapter 4.

Loss measurements are extracted from the datasheet of the material. The datasheet losses are then modelled as a function of the magnetic flux density  $\hat{B}$  and the frequency of its excitation  $f$  as in Eq. (A.1). The parameters of Table A.1 are determined by numerical fitting and their

---

match to material measurements is displayed in Fig. A.1b.

$$\begin{aligned} p_{\text{Fe,H}} &= \rho_{\text{Fe}} c_{\text{Hy}} f \hat{B}^{\beta_{\text{Hy}}} \\ p_{\text{Fe,Ed}} &= \rho_{\text{Fe}} c_{\text{Ed}} f^2 \hat{B}^{\beta_{\text{Ed}}} \end{aligned} \quad (\text{A.1})$$

Table A.1: Loss parameters for ferromagnetic material *Metglas*. Calculated using [106].

$\beta_{\text{Hy}}$	$\beta_{\text{Ed}}$	$c_{\text{Hy}}$ [W·kg <sup>-1</sup> ·Hz <sup>-1</sup> ·T <sup>-1.86</sup> ]	$c_{\text{Ed}}$ [W·kg <sup>-1</sup> ·Hz <sup>-2</sup> ·T <sup>-1.54</sup> ]
1.86	1.36	$1.54 \times 10^{-3}$	$3.58 \times 10^{-6}$

# Bibliography

- [1] AG Electromag (2021). Electromag sa - moteurs pour outils chirurgicaux et orthopédiques moteurs ultra silencieux à haute vitesse. Available in <https://www.electromagmotor.com/realisations/moteurs-pour-outils-chirurgicaux/>.
- [2] Altair (2019). Electromagnetic, Electric and Thermal Analysis | Altair Flux.
- [3] Althen Sensors (2019). Eddy Current Sensors. Available at <https://www.althensensors.com/sensors/linear-position-sensors/eddy-current-sensors/>.
- [4] Amrhein, W., Gruber, W., Bauer, W., and Reisinger, M. (2016). Magnetic levitation systems for cost-sensitive applications—some design aspects. *IEEE Transactions on Industry Applications*, 52(5):3739–3752.
- [5] Asama, J. and Chiba, A. (2021). Performance evaluation of a homopolar bearingless motor for ultra-high-speed applications. *IEEE Transactions on Industry Applications*, Early Access.
- [6] Asama, J., Kanehara, D., Oiwa, T., and Chiba, A. (2014). Development of a compact centrifugal pump with a two-axis actively positioned consequent-pole bearingless motor. *IEEE Transactions on Industry Applications*, 50(1):288–295.
- [7] Asama, J., Oi, T., Oiwa, T., and Chiba, A. (2016). Simple driving method for a two-dof controlled bearingless motor using one three-phase inverter. In *2016 XXII International Conference on Electrical Machines (ICEM)*, pages 2615–2621.
- [8] Asama, J., Oi, T., Oiwa, T., and Chiba, A. (2017). Investigation of integrated winding configuration for a two-DOF controlled bearingless PM motor using one three-phase inverter. In *2017 IEEE International Electric Machines and Drives Conference (IEMDC)*, number 26289064, pages 1–6. IEEE.
- [9] Bartholet, M. T., Nussbaumer, T., Silber, S., and Kolar, J. W. (2009). Comparative evaluation of polyphase bearingless slice motors for fluid-handling applications. *IEEE Transactions on Industry Applications*, 45(5):1821–1830.
- [10] Bauer, W. and Amrhein, W. (2014). Electrical design considerations for a bearingless axial-force/torque motor. *IEEE Transactions on Industry Applications*, 50(4):2512–2522.

- [11] Baumgartner, T. and Kolar, J. W. (2015). Multivariable state feedback control of a 500 000-r/min self-bearing permanent-magnet motor. *IEEE/ASME Transactions on Mechatronics*, 20(3):1149–1159.
- [12] Bertotti, G., Boglietti, A., Chiampi, M., Chiarabaglio, D., Fiorillo, F., and Lazzari, M. (1991). An improved estimation of iron losses in rotating electrical machines. *IEEE Transactions on Magnetics*, 27(6):5007–5009.
- [13] Bianchi, N., Bolognani, S., and Luise, F. (2003). Potentials and limits of high speed PM motors. *38th IAS Annual Meeting on Conference Record of the Industry Applications Conference, 2003.*, 3(6):1570–1578.
- [14] Bianchi, N., Bolognani, S., and Luise, F. (2005). Analysis and design of a PM brushless motor for high-speed operations. *IEEE Transactions on Energy Conversion*, 20(3):629–637.
- [15] Binder, A. (2008). Potentials for energy saving with modern drive technology — a survey. In *2008 International Symposium on Power Electronics, Electrical Drives, Automation and Motion*, pages 90–95.
- [16] Binder, A. and Schneider, T. (2007). High-speed inverter-fed AC drives. In *2007 International Aegean Conference on Electrical Machines and Power Electronics*, pages 9–16. IEEE.
- [17] Binder, A., Schneider, T., and Klotz, M. (2006). Fixation of buried and surface-mounted magnets in high-speed permanent-magnet synchronous machines. *IEEE Transactions on Industry Applications*, 42(4):1031–1037.
- [18] Binder, A. and Energietechnische Gesellschaft Fachbereich Elektrische Maschinen und Antriebe (2001). *Monitoring und Diagnose elektrischer Maschinen und Antriebe: Stand der Forschung, Entwicklungstendenzen ; 28. Juni 2001, Frankfurt am Main, VDE-Haus*. ETG.
- [19] Bleuler, H., Kawakatsu, H., Tang, W., Hsieh, W., Miu, D. K., Tai, Y. C., Moesner, F., and Rohner, M. (1994). Micromachined Active Magnetic Bearings. *4th International Symposium on Magnetic Bearings*, pages 349–352.
- [20] Borisavljevic, A. (2013). *Limits, Modeling and Design of High-Speed Permanent Magnet Machines*. Springer theses. Springer Berlin Heidelberg, Berlin, Heidelberg.
- [21] Borque Gallego, G., Rossini, L., Onillon, E., Achtnich, T., Zwyssig, C., Seiler, R., Martins Araujo, D., and Perriard, Y. (2019). On-line micro-vibration measurement method for lorentz-type magnetic-bearing space actuators. *Mechatronics*, 64:102283.
- [22] Bosch, R. (1988). Development of a bearingless electric motor. In *1988 International Conference on Electrical Machines (ICEM)*, pages 373–375.
- [23] Bossmanns, B. and Tu, J. F. (2000). A Power Flow Model for High Speed Motorized Spindles—Heat Generation Characterization . *Journal of Manufacturing Science and Engineering*, 123(3):494–505.

- [24] Burdet, L. (2006). *Active magnetic bearing design and characterization for high temperature applications*. PhD thesis, EPFL.
- [25] Burnand, G., Araujo, D. M., Koechli, C., and Perriard, Y. (2017a). Validation by measurements of a windage losses model for very-high-speed machines. In *2017 20th International Conference on Electrical Machines and Systems (ICEMS)*, pages 1–4.
- [26] Burnand, G., Araujo, D. M., and Perriard, Y. (2017b). Very-high-speed permanent magnet motors: Mechanical rotor stresses analytical model. In *2017 IEEE International Electric Machines and Drives Conference (IEMDC)*, pages 1–7.
- [27] Burnand, G. and Perriard, Y. (2019). Very-high-speed miniaturized permanent magnet motors: Modeling and experimental validation. In *2019 IEEE Energy Conversion Congress and Exposition (ECCE)*, pages 5251–5257.
- [28] Burnand, G. P.-A. (2020). *Small scale very high speed slotless permanent magnet motors*. PhD thesis, Lausanne.
- [29] Cao, X., Zhou, J., Liu, C., and Deng, Z. (2017). Advanced control method for a single-winding bearingless switched reluctance motor to reduce torque ripple and radial displacement. *IEEE Transactions on Energy Conversion*, 32(4):1533–1543.
- [30] Celeroton (2021). Home Celeroton AG - Ultra-high-speed electrical drive systems. Available in <https://www.celeroton.com/>.
- [31] Celeroton, A. (2018). Optical switches based on high-speed magnetic bearing motors.
- [32] Centers for Disease Control and Prevention (2017a). Ebola outbreaks. Available at <https://www.cdc.gov/vhf/ebola/outbreaks/history/summaries.html>.
- [33] Centers for Disease Control and Prevention (2017b). Ebola outbreaks. Available at <http://www.cdc.gov/vhf/ebola/hcp/international/chlorine-solutions.html>.
- [34] Chang, L., Jahns, T. M., and Blissenbach, R. (2020). Characterization and modeling of soft magnetic materials for improved estimation of pwm-induced iron loss. *IEEE Transactions on Industry Applications*, 56(1):287–300.
- [35] Chen, J., Zhu, J., and Severson, E. L. (2020). Review of bearingless motor technology for significant power applications. *IEEE Transactions on Industry Applications*, 56(2):1377–1388.
- [36] Chiba, A., Deido, T., Fukao, T., and Rahman, M. (1994). An analysis of bearingless ac motors. *IEEE Transactions on Energy Conversion*, 9(1):61–68.
- [37] Chiba, A. and Fukao, T. (1998). Optimal design of rotor circuits in induction type bearingless motors. *IEEE Transactions on Magnetics*, 34(4):2108–2110.

- 
- [38] Chiba, A., Fukao, T., Ichikawa, O., Oshima, M., Takemoto, M., and Dorrell, D. G. (2005). *Magnetic Bearings and Bearingless Drives*. Elsevier.
  - [39] Cogent (2017). Electrical steel non oriented fully processed. Available at <https://perso.uclouvain.be/ernest.matagne/ELEC2311/T2006/NOFP.pdf>.
  - [40] Cui, C., Liu, G., and Wang, K. (2015). A novel drive method for high-speed brushless dc motor operating in a wide range. *IEEE Transactions on Power Electronics*, 30(9):4998–5008.
  - [41] Darlow, M. (1989). *Balancing of High-Speed Machinery*. Mechanical Engineering Series. Springer New York.
  - [42] Deng, F. and Nehl, T. (1998). Analytical modeling of eddy-current losses caused by pulse-width-modulation switching in permanent-magnet brushless direct-current motors. *IEEE Transactions on Magnetics*, 34(5):3728–3736.
  - [43] Diao, X., Zhu, H., Qin, Y., and Hua, Y. (2018). Torque ripple minimization for bearingless synchronous reluctance motor. *IEEE Transactions on Applied Superconductivity*, 28(3):1–5.
  - [44] e+a Elektromaschinen und Antriebe AG (2020). Produktdokumentationen. Available at <https://www.eunda.ch/produkte/produktdokumentationen/>.
  - [45] Eaton, D., Rama, J., and Singhal, S. (2010). Magnetic bearing applications and economics. In *2010 Record of Conference Papers Industry Applications Society 57th Annual Petroleum and Chemical Industry Conference (PCIC)*, pages 1–9.
  - [46] Eclipse Magnetics (2014). Rare Earth Neodymium NdFeB Magnets Datasheet. Available at [https://www.eclipsemagnetics.com/site/assets/files/2418/ndfeb\\_neodymium\\_iron\\_boron-standard\\_ndfeb\\_range\\_datasheet\\_rev1.pdf](https://www.eclipsemagnetics.com/site/assets/files/2418/ndfeb_neodymium_iron_boron-standard_ndfeb_range_datasheet_rev1.pdf).
  - [47] Epstein, A. H. (2004). Millimeter-Scale, Micro-Electro-Mechanical Systems Gas Turbine Engines. *Journal of Engineering for Gas Turbines and Power*, 126(2):205–226.
  - [48] Fang, J., Le, Y., Sun, J., and Wang, K. (2012). Analysis and design of passive magnetic bearing and damping system for high-speed compressor. *IEEE Transactions on Magnetics*, 48(9):2528–2537.
  - [49] Farhan, A., Johnson, M., Hanson, K., and Severson, E. L. (2020). Design of an ultra-high speed bearingless motor for significant rated power. In *2020 IEEE Energy Conversion Congress and Exposition (ECCE)*, pages 246–253.
  - [50] Faulhaber (2020). FAULHABER B-Micro. Available at <https://www.faulhaber.com/en/products/brushless-dc-motors/ Faulhaber-b-micro/>.
  - [51] Fuller, D. D. (1969). A Review of the State-of-the-Art for the Design of Self-Acting Gas-Lubricated Bearings. *Journal of Lubrication Technology*, 91(1):1–16.

## Bibliography

---

- [52] Gallego, G. B., Rossini, L., Achtnich, T., Zwyssig, C., Araujo, D. M., and Perriard, Y. (2018). Force analysis of a slotless lorentz-type active magnetic bearing actuator. In *2018 21st International Conference on Electrical Machines and Systems (ICEMS)*, pages 75–80.
- [53] Garg, A. (2012). *Classical Electromagnetism in a Nutshell*. Princeton University Press.
- [54] Genta, G. (2005). *Dynamics of Rotating Systems*. Mechanical Engineering Series. Springer New York.
- [55] Gerada, D., Mebarki, A., Brown, N. L., Gerada, C., Cavagnino, A., and Boglietti, A. (2014). High-speed electrical machines: Technologies, trends, and developments. *IEEE Transactions on Industrial Electronics*, 61(6):2946–2959.
- [56] Giuffrida, R. V., Mirić, S., Bortis, D., and Kolar, J. W. (2020). "Looking Through Walls" – Actuator Position Measurement Through a Conductive Wall. In *2020 23rd International Conference on Electrical Machines and Systems (ICEMS)*, pages 1649–1654.
- [57] Graf, U. (2004). *Applied Laplace Transforms and Z-Transforms for Scientists and Engineers: A Computational Approach Using a Mathematica Package*. Springer-Verlag New York Incorporated.
- [58] Group Maxon (2021). Precision drive systems by maxon | maxon group. Available in <https://www.maxongroup.com/maxon/view/content/sterilizable>.
- [59] Gruber, W., Radman, K., and Göbl, E. (2018). Novel bearingless flux-switching motor with exterior rotor. In *2018 IEEE Energy Conversion Congress and Exposition (ECCE)*, pages 2314–2318.
- [60] Gruber, W., Radman, K., and Schob, R. (2014). Design of a Bearingless Flux-Switching Slice Motor Wolfgang. *The 2014 International Power Electronics Conference Design*, (2):1691–1696.
- [61] Gruber, W., Rothbüch, M., and Schoeb, R. T. (2015). Design of a Novel Homopolar Bearingless Slice Motor With Reluctance Rotor. *IEEE Transactions on Industry Applications*, 51(2):1456–1464.
- [62] Gruber, W., Silber, S., Amrhein, W., and Nussbaumer, T. (2010). Design variants of the bearingless segment motor. *SPEEDAM 2010 - International Symposium on Power Electronics, Electrical Drives, Automation and Motion*, pages 1448–1453.
- [63] Hall, E. H. (1879). On a new action of the magnet on electric currents. *American Journal of Mathematics*, 2(3):287–292.
- [64] Holtz, J. (2006). Sensorless control of induction machines—with or without signal injection? *IEEE Transactions on Industrial Electronics*, 53(1):7–30.
- [65] Hou, E. and Liu, K. (2013). Tilting Characteristic of a 2-Axis Radial Hybrid Magnetic Bearing. *IEEE Transactions on Magnetics*, 49(8):4900–4910.

- [66] Howe, D. (2005). Advanced electrical machines and actuators for new and emerging applications. In *2005 International Conference on Electrical Machines and Systems*, volume 1, pages 18–23 Vol. 1.
- [67] Howey, D. A., Childs, P. R. N., and Holmes, A. S. (2012). Air-gap convection in rotating electrical machines. *IEEE Transactions on Industrial Electronics*, 59(3):1367–1375.
- [68] Imoberdorf, P. (2011). *Ultrakompakter Antrieb mit radial und axial kombiniertem Magnetlager*. PhD thesis, ETH Zürich.
- [69] Inderka, R., Carstensen, C., and Doncker, R. D. (2002). Eddy currents in medium power switched reluctance machines. *2002 IEEE 33rd Annual IEEE Power Electronics Specialists Conference. Proceedings (Cat. No.02CH37289)*, 2.
- [70] Indulkar, C. (2008). *An Introduction to Electrical Engineering Materials*. S.Chand Limited.
- [71] Instruments, T. (2019). DRV5055 High accuracy 3.3 V or 5 V ratiometric bipolar Hall effect sensor. Available at <http://www.ti.com/product/DRV5055>.
- [72] Iwasaki, S., Deodhar, R. P., Liu, Y., Pride, A., Zhu, Z. Q., and Bremner, J. J. (2009). Influence of PWM on the proximity loss in permanent-magnet brushless AC machines. *IEEE Transactions on Industry Applications*, 45(4):1359–1367.
- [73] J. Nerg, M. R. and Pyrhonen, J. (2008). Thermal Analysis of Radial-Flux Electrical Machines With a High Power Density. *IEEE Transactions on Industrial Electronics*, 55(10):3543–3554.
- [74] Jang, G., Kim, D., and Oh, J.-E. (1999). New frequency domain method of nonrepeatable runout measurement in a hard disk drive spindle motor. *IEEE Transactions on Magnetics*, 35(2):833–838.
- [75] Jang, J.-H., Sul, S.-K., Ha, J.-I., Ide, K., and Sawamura, M. (2003). Sensorless drive of surface-mounted permanent-magnet motor by high-frequency signal injection based on magnetic saliency. *IEEE Transactions on Industry Applications*, 39(4):1031–1039.
- [76] Jastrzebski, R. P., Jaatinen, P., Pyrhönen, O., and Chiba, A. (2017). Design of 6-slot inset pm bearingless motor for high-speed and higher than 100kw applications. In *2017 IEEE International Electric Machines and Drives Conference (IEMDC)*, pages 1–6.
- [77] Jastrzebski, R. P., Tolsa, K., and Iskanius, M. (2010). Customization of Digital Circuit for Material Independent Eddy Current Proximity Sensor for Active Magnetic Bearings. In *ISMB 12*, pages 376–382, Wuhan.
- [78] Jeon, S., Ahn, H.-J., Han, D.-C., and Chang, I.-B. (2001). New design of cylindrical capacitive sensor for on-line precision control of amb spindle. *IEEE Transactions on Instrumentation and Measurement*, 50(3):757–763.
- [79] Jiles, D. (1998). *Introduction to Magnetism and Magnetic Materials, Second Edition*. Taylor & Francis.



## Bibliography

---

- [80] Kang, S. (2001). *Fabrication of Functional Mesoscopic Ceramic Parts for Micro Gas Turbine Engines*. PhD thesis, Stanford.
- [81] Kemper, H. (1937). Overhead suspension railway with wheel-less vehicles employing magnetic suspension from iron rails. *Germ. Pat. Nos. 643316 (1937) and 644302 (1937)*.
- [82] Khazan, A. (1994). *Transducers and Their Elements: Design and Application*. PTR Prentice Hall.
- [83] Kim, H., Son, J., and Lee, J. (2011). A high-speed sliding-mode observer for the sensorless speed control of a pmsm. *IEEE Transactions on Industrial Electronics*, 58(9):4069–4077.
- [84] Kim, O.-S., Lee, S.-H., and Han, D.-C. (2003). Positioning performance and straightness error compensation of the magnetic levitation stage supported by the linear magnetic bearing. *IEEE Transactions on Industrial Electronics*, 50(2):374–378.
- [85] Kimman, M. H. (2010). *Design of a Micro Milling Setup with an Active Magnetic Bearing Spindle*. PhD thesis, TU Delft.
- [86] KOMMISSION DER EUROPÄISCHEN GEMEINSCHAFTEN (2006). Aktionsplan für Energieeffizienz: Das Potenzial ausschöpfen. Available at <https://eur-lex.europa.eu/LexUriServ/LexUriServ.do?uri=COM:2006:0545:FIN:DE:PDF>.
- [87] Kozuka, S., Tanabe, N., Asama, J., and Chiba, A. (2008). Basic characteristics of 150,000r/min switched reluctance motor drive. In *2008 IEEE Power and Energy Society General Meeting - Conversion and Delivery of Electrical Energy in the 21st Century*, pages 1–4.
- [88] Krings, A. and Soulard, J. (2010). Overview and Comparison of Iron Loss Models for Electrical Machines. *Journal of Electrical Engineering*, 10:162–169.
- [89] Küpfmüller, K., Mathis, W., and Reibiger, A. (2013). *Theoretische Elektrotechnik*. Springer-Lehrbuch. Springer Berlin Heidelberg, Berlin, Heidelberg, 19 edition.
- [90] Langhaar, H. (2016). *Energy Methods in Applied Mechanics*. Dover Publications.
- [91] Larssonneur, R. (1990). *Design and control of active magnetic bearing systems for high speed rotation*. PhD thesis, ETH Zürich.
- [92] Larssonneur, René and Bühler, Philipp (2004). New Radial Sensor For Active Magnetic Bearings. In *ISMB9*, pages 709–713, Kentucky.
- [93] Levitronix (2018). Products. Available at <https://www.levitronix.com/en/products.html>.
- [94] Li, C. (2007). *Development of Bearingless Motor with Rectifier Circuit*. PhD thesis, Kochi University of Technology.

- [95] Li, K., Cheng, G., Sun, X., Zhao, D., and Yang, Z. (2019). Direct Torque and Suspension Force Control for Bearingless Induction Motors Based on Active Disturbance Rejection Control Scheme. *IEEE Access*, 7:86989–87001.
- [96] Li, Q., Boesch, P., Haefliger, M., Kolar, J. W., and Xu, D. (2008). Basic characteristics of a 4kW permanent-magnet type bearingless slice motor for centrifugal pump system. In *2008 International Conference on Electrical Machines and Systems*, pages 3037–3042.
- [97] Li, Z., Zhao, C., Lu, Z., and Liu, F. (2019). Thermal performances prediction analysis of high speed feed shaft bearings under actual working condition. *IEEE Access*, 7:168011–168019.
- [98] Lion Precision (2019). Eddy-Current Displacement & Position Sensors. Available at <https://www.lionprecision.com/products/eddy-current-sensors/>.
- [99] Liu, G., Chen, B., Wang, K., and Song, X. (2019). Selective current harmonic suppression for high-speed pmsm based on high-precision harmonic detection method. *IEEE Transactions on Industrial Informatics*, 15(6):3457–3468.
- [100] Liu, P. and Cao, X. (2019). Control method for single-winding 12/4 bearingless switched reluctance motor. In *2019 14th IEEE Conference on Industrial Electronics and Applications (ICIEA)*, pages 2087–2091.
- [101] Looser, A. and Kolar, J. (2011). A hybrid bearing concept for high-speed applications employing aerodynamic gas-bearings and a self-sensing active magnetic damper. In *IECON 2011 - 37th Annual Conference of the IEEE Industrial Electronics Society*, pages 1686–1691.
- [102] maxon (2020). Top Performance Precision Brushed DC Motors by maxon. Available at <https://www.maxongroup.com/maxon/view/content/Overview-brushed-DC-motors>.
- [103] McKenzie, A. (1997). *Axial Flow Fans and Compressors: Aerodynamic Design and Performance*. Cranfield Series in Turbomachinery. Ashgate.
- [104] Médecins sans Frontieres (2014). Ebola 2014-2015 facts & figures. Available at [https://www.msf.org/sites/msf.org/files/ebola\\_accountability\\_report\\_low\\_res.pdf](https://www.msf.org/sites/msf.org/files/ebola_accountability_report_low_res.pdf).
- [105] Meeker, D. (2021). HomePage:Finite Element Method Magnetics. Available at <https://www.femm.info/wiki/HomePage>.
- [106] Metglas (2017). PowerLite C-Cores Technical Bulletin Alloy 2605SA1. Available at <https://metglas.com/wp-content/uploads/2016/12/Amorphous-Alloys-for-Transformer-Cores-.pdf>.
- [107] Millinger, J., Wallmark, O., and Soulard, J. (2018). High-frequency characterization of losses in fully assembled stators of slotless pm motors. *IEEE Transactions on Industry Applications*, 54(3):2265–2275.

- [108] Millinger, J., Wallmark, O., and Soulard, J. (2020). Investigation of harmonic losses in a two-pole slotless permanent-magnet motor due to wide bandgap inverter supply. *IEEE Transactions on Industrial Electronics*, 67(8):6280–6289.
- [109] Mitterhofer, H. and Amrhein, W. (2012). Motion control strategy and operational behaviour of a high speed bearingless disc drive. In *6th IET International Conference on Power Electronics, Machines and Drives (PEMD 2012)*, pages 1–6.
- [110] Mitterhofer, H., Amrhein, W., and Grabner, H. (2012). Comparison of two-and four-pole rotors for a high speed bearingless drive. In *ISMB 2012*, Wuhan.
- [111] Mitterhofer, H. and Gruber, W. (2017). Effizienzsteigerung durch die und in der magnet-lagertechnik. *e & i Elektrotechnik und Informationstechnik*, 134(2):191–196.
- [112] Mitterhofer, H., Gruber, W., and Amrhein, W. (2014). On the high speed capacity of bearingless drives. *IEEE Transactions on Industrial Electronics*, 61(6):3119–3126.
- [113] Mitterhofer, H., Jungmayr, G., Amrhein, W., and Davey, K. (2018). Coaxial tilt damping coil with additional active actuation capabilities. *IEEE Transactions on Industry Applications*, 54(6):5879–5887.
- [114] Mitterhofer, H., Mrak, B., and Gruber, W. (2015). Comparison of High-Speed Bearingless Drive Topologies With Combined Windings. *IEEE Transactions on Industry Applications*, 51(3):2116–2122.
- [115] Miyamoto, K., Takemoto, M., Ogasawara, S., and Hiragushi, M. (2014). Verification of a novel 5-axis active control type bearingless canned motor pump utilizing passive magnetic bearing function for high power. In *2014 IEEE Energy Conversion Congress and Exposition (ECCE)*, pages 2454–2461.
- [116] Moriyama, S.-i., Watanabe, K., and Haga, T. (1998). Inductive Sensing System for Active Magnetic Suspension Control. In *ISMB6*, pages 529–537.
- [117] Muetze, A. and Strangas, E. G. (2016). The useful life of inverter-based drive bearings: Methods and research directions from localized maintenance to prognosis. *IEEE Industry Applications Magazine*, 22(4):63–73.
- [118] Noh, M., Cho, S.-R., Kyung, J.-H., Ro, S.-K., and Park, J.-K. (2005). Design and implementation of a fault-tolerant magnetic bearing system for turbo-molecular vacuum pump. *IEEE/ASME Transactions on Mechatronics*, 10(6):626–631.
- [119] Noh, M., Gruber, W., and Trumper, D. L. (2017). Hysteresis bearingless slice motors with homopolar flux-biasing. *IEEE/ASME Transactions on Mechatronics*, 22(5):2308–2318.
- [120] Nussbaumer, T., Karutz, P., Zurcher, F., and Kolar, J. W. (2011). Magnetically Levitated Slice Motors - An Overview. *IEEE Transactions on Industry Applications*, 47(2):754–766.

- 
- [121] Nussbaumer, T., Raggl, K., Boesch, P., and Kolar, J. (2007). Trends in integration for magnetically levitated pump systems. In *2007 Power Conversion Conference - Nagoya*, pages 1551–1558.
- [122] Ooshima, M. and Takeuchi, C. (2011). Magnetic suspension performance of a bearingless brushless dc motor for small liquid pumps. *IEEE Transactions on Industry Applications*, 47(1):72–78.
- [123] Organization, W. H. (2015). Liste OMS des équipements de protection individuelle de prévention et de contrôle de l’infection orientée sur Ebola. Available at [https://www.who.int/medical\\_devices/ppe\\_list\\_31mar2015FR.pdf](https://www.who.int/medical_devices/ppe_list_31mar2015FR.pdf).
- [124] O’Rourke, C. J., Qasim, M. M., Overlin, M. R., and Kirtley, J. L. (2019). A geometric interpretation of reference frames and transformations: dq0, clarke, and park. *IEEE Transactions on Energy Conversion*, 34(4):2070–2083.
- [125] Ortiz Salazar, A., Dunford, W., Stephan, R., and Watanabe, E. (1990). A magnetic bearing system using capacitive sensors for position measurement. *IEEE Transactions on Magnetics*, 26(5):2541–2543.
- [126] Park, C. H., Kim, S., and Kim, K.-S. (2013). Vacuum chamber-free centrifuge with magnetic bearings. *Review of Scientific Instruments*, 84(9):095106.
- [127] Park, R. H. (1929). Two-reaction Theory of Synchronous Machines Generalized Method of analysis-part I. *Transactions of the American Institute of Electrical Engineers*, 48(3):716–727.
- [128] Passenbrunner, J., Silber, S., and Amrhein, W. (2015). Investigation of a digital eddy current sensor. In *2015 IEEE International Electric Machines Drives Conference (IEMDC)*, pages 728–734.
- [129] Peralta, P., Araujo, D. M., and Perriard, Y. (2018). Passive, active and loss tradeoffs in high-speed bearingless motors. In *2018 21st International Conference on Electrical Machines and Systems (ICEMS)*, pages 162–168.
- [130] Peralta, P., Araujo, D. M., and Perriard, Y. (2018). Speed and stability limits for high-speed bearingless disc drives. In *2018 IEEE Energy Conversion Congress and Exposition (ECCE)*, pages 2319–2326.
- [131] Peralta, P., Araujo, D. M., and Perriard, Y. (2020). Design of compact bearingless disc drive systems. *IEEE Transactions on Industry Applications*, 56(5):4870–4881.
- [132] Peralta, P., Borque-Gallego, G., Lapijover, Y., and Perriard, Y. (2021a). Experimental electromechanical characterization of slotted and slotless miniature bearingless drives. In *2021 IEEE International Electric Machines Drives Conference (IEMDC)*, pages 1–8.

## Bibliography

---

- [133] Peralta, P., Leo, J., and Perriard, Y. (2020a). Rotor position estimation with hall-effect sensors in bearingless drives. In *2020 22nd European Conference on Power Electronics and Applications (EPE'20 ECCE Europe)*, pages 1–10.
- [134] Peralta, P., Thomas, S., and Perriard, Y. (2020b). Integrated, eddy-current-based sensing of rotor position for magnetic levitation. In *2020 IEEE Energy Conversion Congress and Exposition (ECCE)*, pages 1749–1755.
- [135] Peralta, P., Thomas, S., and Perriard, Y. (2021b). Characterization and verification of eddy-current position sensing for magnetic levitation. *IEEE Transactions on Industry Applications*, 57(6):5796–5805.
- [136] Pfister, P.-D. (2010). *Very high-speed slotless permanent-magnet motors*. PhD thesis, STI, Lausanne.
- [137] Pilat, A. and Gliwa, J. (2020). Analysis of magnetic inductance, coil current and levitating sphere displacement recorded during stabilization experiments. In *2020 International Conference Mechatronic Systems and Materials (MSM)*, pages 1–6.
- [138] Portescap (2020). Brushless Motor - BLDC Motor | Portescap. Available at <https://www.portescap.com/en/products/brushless-dc-motors>.
- [139] Puentener, P. (2020). *Haemolysis in Bearingless Centrifugal Pumps*. PhD thesis, ETH Zürich.
- [140] Puentener, P., Schuck, M., Steinert, D., Nussbaumer, T., and Kolar, J. W. (2018). A 150 000-r/min Bearingless Slice Motor. *IEEE/ASME Transactions on Mechatronics*, 23(6):2963–2967.
- [141] Pyrhnen, J., Jokinen, T., and Hrabovcov, V. (2008). *Design of Rotating Electrical Machines*. John Wiley & Sons, Ltd, Chichester, UK.
- [142] Raggl, K., Kolar, J. W., and Nussbaumer, T. (2007). Comparison of winding concepts for bearingless pumps. In *2007 7th International Conference on Power Electronics*, pages 1013–1020. IEEE.
- [143] Rahman, M. A., Chiba, A., and Fukao, T. (2004). Super high speed electrical machines - summary. In *IEEE Power Engineering Society General Meeting, 2004.*, pages 1272–1275 Vol.2.
- [144] Reichert, T. (2012). *The Bearingless Mixer in Exterior Rotor Construction*. PhD thesis, ETH Zürich.
- [145] Reichert, T., Kolar, J. W., and Nussbaumer, T. (2013). Stator tooth design study for bearingless exterior rotor PMSM. *IEEE Transactions on Industry Applications*, 49(4):1515–1522.
- [146] Reichert, T., Nussbaumer, T., and Kolar, J. W. (2012). Investigation of exterior rotor bearingless motor topologies for high-quality mixing applications. *IEEE Transactions on Industry Applications*, 48(6):2206–2216.

- 
- [147] Ren, Y., Su, D., and Fang, J. (2013). Whirling modes stability criterion for a magnetically suspended flywheel rotor with significant gyroscopic effects and bending modes. *IEEE Transactions on Power Electronics*, 28(12):5890–5901.
- [148] Rui, C., Hongwei, L., and Jing, T. (2018). Structure design and simulation analysis of inductive displacement sensor. In *2018 13th IEEE Conference on Industrial Electronics and Applications (ICIEA)*, pages 1620–1626.
- [149] Savi, F., Barater, D., Nardo, M. D., Degano, M., Gerada, C., Wheeler, P., and Buticchi, G. (2020). High-speed electric drives: A step towards system design. *IEEE Open Journal of the Industrial Electronics Society*, 1:10–21.
- [150] Schneeberger, T., Nussbaumer, T., and Kolar, J. W. (2010). Magnetically levitated homopolar hollow-shaft motor. *IEEE/ASME Transactions on Mechatronics*, 15(1):97–107.
- [151] Schneider, T. and Binder, A. (2007). Design and Evaluation of a 60 000 rpm Permanent Magnet Bearingless High Speed Motor. In *2007 7th International Conference on Power Electronics and Drive Systems*, pages 1–8. IEEE.
- [152] Schuck, M., Fernandes, A. D. S., Steinert, D., and Kolar, J. W. (2017). A high speed millimeter-scale slotless bearingless slice motor. In *2017 IEEE International Electric Machines and Drives Conference (IEMDC)*, pages 1–7.
- [153] Schuck, M., Puentener, P., Holenstein, T., and Kolar, J. W. (2019). Skalierung und Auslegung von lagerlosen Miniatur-Scheibenläufermotoren für hohe Drehzahlen. In *"more drive 2019" Workshop*.
- [154] Schuhmann, T., Hofmann, W., and Werner, R. (2006). Sensor integration and state estimation on magnetically levitated rotors. In *International Symposium on Power Electronics, Electrical Drives, Automation and Motion, 2006. SPEEDAM 2006.*, pages 1172–1177.
- [155] Schwager, L., Tuysuz, A., Zwyssig, C., and Kolar, J. W. (2014). Modeling and comparison of machine and converter losses for PWM and PAM in high-speed drives. *IEEE Transactions on Industry Applications*, 50(2):995–1006.
- [156] Schweitzer, G., Bleuler, H., Maslen, E., Cole, M., Keogh, P., Larssonneur, R., Maslen, E., Nordmann, r., Okada, Y., Schweitzer, G., et al. (2009). *Magnetic Bearings: Theory, Design, and Application to Rotating Machinery*. Springer Berlin Heidelberg.
- [157] Sensirion (2016a). Differential Pressure - EK-P5 Evaluation Kit.
- [158] Sensirion (2016b). Flow Element - EK-P4 Evaluation Kit.
- [159] Severson, E., Nilssen, R., Undeland, T., and Mohan, N. (2015). Magnetic equivalent circuit modeling of the ac homopolar machine for flywheel energy storage. *IEEE Transactions on Energy Conversion*, 30(4):1670–1678.

## Bibliography

---

- [160] Shakibapour, F. (2018). 2D Analytical Model for Heteropolar Active Magnetic Bearings Considering Eccentricity. *IET Electric Power Applications*, 12:614–626(12).
- [161] Siemens (2015). ZVEI - German Electrical and Electronic Manufacturer's Association. Available at [https://www.zvei.org/fileadmin/user\\_upload/Presse\\_und\\_Medien/Publikationen/2015/mai/Energy\\_Efficiency\\_with\\_Electric\\_Drive\\_Systems/ZVEI-Brochure-Energy-Efficiency-with-Drive-Systems.pdf](https://www.zvei.org/fileadmin/user_upload/Presse_und_Medien/Publikationen/2015/mai/Energy_Efficiency_with_Electric_Drive_Systems/ZVEI-Brochure-Energy-Efficiency-with-Drive-Systems.pdf).
- [162] Siemens (2016). Retrofit for Integrated Drive Systems. Available at <https://assets.new.siemens.com/siemens/assets/api/uuid:f91c27ce-aeff-490c-8a31-e56985290295/df-cs-retrofit-integrated-drive-systems-en-lores.pdf>.
- [163] Siemens (2018). Integrated Drive Systems from Siemens for shorter time to market and accelerated time to profit. Available at <https://assets.new.siemens.com/siemens/assets/api/uuid:5c515d5f07d4faf49a38ae18b9699891346be152/ids-brochure-integration-at-its-best-pdcdg-b10007-00-7600.pdf>.
- [164] Steinert, D., Kovacevic-Badstubner, I., Nussbaumer, T., and Kolar, J. W. (2015). Loss investigation of slotless bearingless disk drives. volume 2, pages 4418–4424.
- [165] Steinert, D., Nussbaumer, T., and Kolar, J. W. (2013). Concept of a 150 krpm bearingless slotless disc drive with combined windings. *Proceedings of the 2013 IEEE International Electric Machines and Drives Conference, IEMDC 2013*, pages 311–318.
- [166] Steinert, D., Nussbaumer, T., and Kolar, J. W. (2014). Slotless bearingless disk drive for high-speed and high-purity applications. *IEEE Transactions on Industrial Electronics*, 61(11):5974–5986.
- [167] Steinert, D. K. (2015). *Der nutenlose lagerlose Scheibenläufermotor*. PhD thesis, ETH Zurich, Zürich.
- [168] Štusák, M. (2014). Eddy current sensors for magnetic bearings of the textile spinning machines. In *ISMB 2014*, pages 709–713, Linz.
- [169] Sugimoto, H., Miyoshi, M., and Chiba, A. (2018). Axial vibration suppression by field flux regulation in two-axis actively positioned permanent magnet bearingless motors with axial position estimation. *IEEE Transactions on Industry Applications*, 54(2):1264–1272.
- [170] Sugimoto, H., Srichiangsa, T., and Chiba, A. (2017). Design of a high-speed single-drive bearingless motor. In *2017 IEEE International Electric Machines and Drives Conference (IEMDC)*, pages 1–6. IEEE.
- [171] Sun, J., Wang, C., and Le, Y. (2016). Research on a novel high stiffness axial passive magnetic bearing for DGMSCMG. *Journal of Magnetism and Magnetic Materials*, 412:147–155.

- [172] Takahashi, I., Koganezawa, T., Su, G., and Ohyama, K. (1994). A super high speed pm motor drive system by a quasi-current source inverter. *IEEE Transactions on Industry Applications*, 30(3):683–690.
- [173] TDK Wireless Charging (2019). TDK Stacking Proposal for WR111180-36F5-B1. Available at [https://www.mouser.com/catalog/specsheets/tdk\\_WR111180-36F5-B1.pdf](https://www.mouser.com/catalog/specsheets/tdk_WR111180-36F5-B1.pdf).
- [174] Texas Instruments (2019a). BOOSTXL-DRV8323RS Evaluation board | TI.com. Available at <https://www.ti.com/tool/BOOSTXL-DRV8323RS>.
- [175] Texas Instruments (2019b). LAUNCHXL-F28379D C2000 Delfino MCU F28379D LaunchPad™ development kit | TI.com. Available at <http://www.ti.com/tool/LAUNCHXL-F28379D>.
- [176] Texas Instruments (2020). LDC Webench - Coil Designer. Available at <https://webench.ti.com/wb5/LDC/>.
- [177] Texas Instruments - Application Note (2019a). Configuring Inductive-to-Digital-Converters for Parallel Resistance (RP) (Rev. B). Available at <https://www.ti.com/lit/pdf/snaa221>.
- [178] Texas Instruments - Application Note (2019b). EMI Considerations for Inductive Sensing. Available at <https://www.ti.com/lit/pdf/snoa962>.
- [179] Texas Instruments - Application Note (2019c). LDC Sensor Design (Rev. B). Available at <https://www.ti.com/lit/pdf/snoa930>.
- [180] Texas Instruments - Data sheet (2019). LDC1314 4-channel, 12-bit Inductance-to-Digital Converter with I2C for Inductive Sensing. Available at <https://www.ti.com/lit/gpn/ldc1314>.
- [181] Theodorsen, T. (1948). *Theory of Propellers*. McGraw-Hill publications in aeronautical science. McGraw-Hill Book Company.
- [182] Tsao, P., Senesky, M., and Sanders, S. (2003). An integrated flywheel energy storage system with homopolar inductor motor/generator and high-frequency drive. *IEEE Transactions on Industry Applications*, 39(6):1710–1725.
- [183] Tuysuz, A., Meyer, F., Steichen, M., Zwyssig, C., and Kolar, J. W. (2017). Advanced Cooling Methods for High-Speed Electrical Machines. *IEEE Transactions on Industry Applications*, 53(3):1–1.
- [184] University, J. H. (2015). Johns Hopkins, DuPont join forces to produce improved Ebola protection suit. Available at <https://hub.jhu.edu/2015/09/28/hopkins-dupont-ebola-garment-partnership/>.
- [185] van der Geest, M., Polinder, H., and Ferreira, J. A. (2014). Influence of pwm switching frequency on the losses in pm machines. In *2014 International Conference on Electrical Machines (ICEM)*, pages 1243–1247.



- [186] van der Geest, M., Polinder, H., Ferreira, J. A., and Christmann, M. (2015). Power density limits and design trends of high-speed permanent magnet synchronous machines. *IEEE Transactions on Transportation Electrification*, 1(3):266–276.
- [187] Wang, Y., Zhu, Z.-Q., Feng, J., Guo, S., Li, Y., and Wang, Y. (2021). Rotor stress analysis of high-speed permanent magnet machines with segmented magnets retained by carbon-fibre sleeve. *IEEE Transactions on Energy Conversion*, 36(2):971–983.
- [188] Warberger, B. (2014). *Untersuchung von lagerlosen Aussenläufer-Motoren in hochreinen Rührprozessen*. PhD thesis, ETH Zürich.
- [189] Warberger, B., Reichert, T., Nussbaumer, T., and Kolar, J. W. (2010). Design considerations of a bearingless motor for high-purity mixing applications. In *SPEEDAM 2010*, pages 1454–1459.
- [190] Webster, J. (1999). *Wiley Encyclopedia of Electrical and Electronics Engineering, Volume 12*. Wiley. Chapter Electromagnetic Shielding.
- [191] Wiguna, C. A., Furqani, J., and Chiba, A. (2021). Improved current profile selection for noise reduction of switched reluctance motor at middle speed considering back emf. *IEEE Transactions on Industry Applications*, 57(5):4707–4719.
- [192] Yamazaki, K., Fukuoka, T., Akatsu, K., Nakao, N., and Ruderman, A. (2012). Investigation of locked rotor test for estimation of magnet pwm carrier eddy current loss in synchronous machines. *IEEE Transactions on Magnetics*, 48(11):3327–3330.
- [193] Yang, Y., Deng, Z., Yang, G., Cao, X., and Zhang, Q. (2010). A control strategy for bearingless switched-reluctance motors. *IEEE Transactions on Power Electronics*, 25(11):2807–2819.
- [194] Yao, J., Geng, H., and Zheng, W. (2020). Bearing selection of 20kw high speed motor and analysis of rotor dynamic characteristics. In *2020 IEEE International Conference on Mechatronics and Automation (ICMA)*, pages 1958–1962.
- [195] Yonnet, J.-P. (1981). Permanent Magnet Bearings and Couplings. *IEEE Transactions on Magnetics*, 17(1):1169–1173.
- [196] Zhang, P., Du, Y., Habetler, T. G., and Lu, B. (2011). A survey of condition monitoring and protection methods for medium-voltage induction motors. *IEEE Transactions on Industry Applications*, 47(1):34–46.
- [197] Zhao, G. F., Ying, J., Wu, L., and Feng, Z. H. (2019). Eddy current displacement sensor with ultrahigh resolution obtained through the noise suppression of excitation voltage. *Sensors and Actuators A: Physical*, 299:111622.
- [198] Zheng, S., Li, H., Peng, C., and Wang, Y. (2017). Experimental investigations of resonance vibration control for noncollocated amb flexible rotor systems. *IEEE Transactions on Industrial Electronics*, 64(3):2226–2235.

- [199] Zingerli, C. M. (2014). *Beiträge zu Axialventilatoren mit Homopolar-Magnetlager*. PhD thesis, ETH Zürich.
- [200] Zingerli, C. M., Imoberdorf, P., Kolar, J. W., and Nussbaumer, T. (2011). Rotor position measurement for a magnetically levitated 500'000 rpm permanent magnet machine. In *2011 IEEE Energy Conversion Congress and Exposition*, pages 1778–1784.
- [201] Zoethout, J. (2002). *Design and integration of position sensing systems*. PhD thesis, EPFL, Lausanne.
- [202] Zürcher, F., Nussbaumer, T., and Kolar, J. W. (2012). Motor torque and magnetic levitation force generation in bearingless brushless multipole motors. *IEEE/ASME Transactions on Mechatronics*, 17(6):1088–1097.
- [203] Zwyssig, C. (2008). *An Ultra-High-Speed Electrical Drive System*. PhD thesis, ETH Zürich.
- [204] Zwyssig, C., Member, S., Kolar, J. W., Member, S., and Round, S. D. (2009). Megaspeed Drive Systems : Pushing Beyond. *IEEE/ASME Transactions on Mechatronics*, 14(5):564–574.

# Patricio Peralta Fierro

## Curriculum Vitae

pato.peralta@gmail.com

 patricio-peralta-fierro



### Education

- 2017-2021 **Ph.D Microengineering, EPFL-LAI.**  
Mechatronics and Robotics.
- 2012-2014 **M.Sc. Electric Engineer, Politecnico di Torino, Double Degree.**  
Electric Drives and Power Electronics.
- 2012-2014 **Diplom Electric Engineer, Universidad Católica de Chile, Double Degree.**  
Focus on Energy.
- 2008-2012 **B.Sc. Electrical Engineer, Universidad Católica de Chile.**

### Experience

- 2014-2017 **Scientific Assistant, ETH Zürich, Power Electronic Systems Laboratory .**  
Two magnetically-levitated drives were successfully commissioned to pump at 250 °C fluid temperature: an improvement of 100 °C regarding its predecessor.  
In collaboration with Levitronix GmbH.

### Competences

Conception of mechatronic systems.  
Control of electric drives.  
Sensor systems.  
CAD Design.

### Scientific Publications

Journal and conference contributions in mechatronics, sensor technology and electromagnetic domains. [Link](#) to Google Scholar profile..

### Languages

Spanish    Mothertongue  
German    Fluent  
French    Fluent  
Italian    Fluent  
English    Fluent